SEVENTH FRAMEWORK PROGRAMME

THEME 6: Environment (including climate change)

Contract for: **Collaborative Project**

D.4.3
QA/QC Report

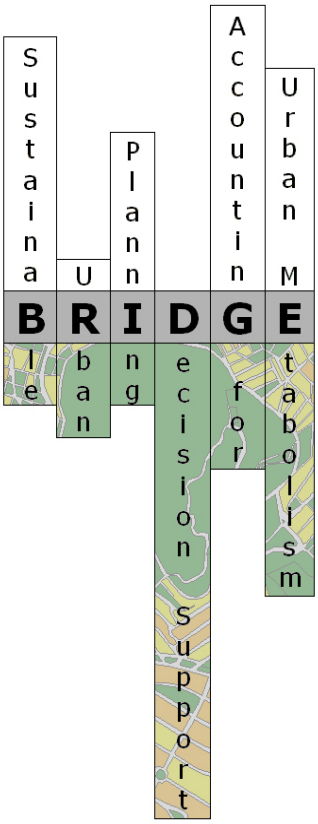

Project acronym:	BRIDGE
Project full title:	SustainaBle uRban planning Decision support accountinG for Urban mEtabolism
Contract no.:	211345
Date:	31/05/2011
Document Reference:	211345_018_TR_ UPM
Book Captain:	Roberto San José (UPM)
Authors:	Roberto San José (UPM), Juan Luis Pérez (UPM)
Contributors :	Donatella Spano (CMCC), Serena Marras (CMCC), David Pyles(CMCC), Matthias Falk (CMCC), Carlos Borrego (UAVR), Myriam Lopes (UAVR), Ana Isabel Miranda (UAVR), Jorge Humberto Amorim(UAVR), Pedro Cascão (UAVR), Joana Martins (UAVR), José Manuel Martins (UAVR), Anabela Carvalho (UAVR), Sue Grimmond (KCL), Mario Iamarino (USBa), Leena Järvi (UH, and KCL), Simone Kotthaus (KCL), Fredrik Lindberg (GU and KCL), D. Kolokotsa (NKUA), K. Gobakis (NKUA), A. Synnefa (NKUA), M. Santamouris (NKUA), Veldhuizen Ab (ALTERRA), Grégoire Pigeon (CNRM)
Issue:	1.0
Deliverable no.:	D.4.3
Dissemination Level:	RE

Document Status Sheet

Issue	Date	Author	Comments
1.0	Apr. 15/2011	R. San José & J.L. Pérez (UPM)	
	Apr. 30/2011	D. Spano & S. Marras , David Pyles, Matthias Falk (CMCC)	Added CMCC contribution on ACASA performance at local scale
	April 302011	Carlos Borrego, Myriam Lopes, Ana Isabel Miranda, Jorge Humberto Amorim, Pedro Cascão, Joana Martins, José Manuel Martins, Anabela Carvalho (UAVR)	Added contribution on UAVR model QA/QC
	17 june 2011	Cris Castillo (KCL), Sue Grimmond (KCL), Mario Iamarino (Università degli Studi della Basilicata), Leena Jarvi (UHEL and KCL), Simone Kotthaus (KCL), Fredrik Lindberg (University of Gothenburg and KCL)	
	21 June 2011	Sue Grimmond (KCL), Mario Iamarino Leena, Simone Kotthaus, Fredrik Lindberg	
	June24/2 011	R. Pyles (CMCC)	Added UCD/CMCC contribution on WRF-ACASA nested simulations (spatial domain re-design)

Table of Contents

Figures Table

1 Introduction

1.1 Definitions and Acronyms

Acronyms

ACASA Advanced Canopy-Atmosphere-Soil Algorithm (CMCC)

CAMO Cellular Automata Traffic Model (UPM)

CAMx Comprehensive Air quality Model with extensions (ENVIRON)

CMAQ Community Multiscale Air Quality Modelling System (US EPA)

EMIMO An emission model (UPM)

MICROSYS Microscale Air Quality Simulation System (UPM)

MM5 NCAR Mesoscale Meteorological Models (US NCAR)

TREM Transport Emission Model for Line Sources (UAVR)

URBAIR Urban air quality model (UAVR)

VADIS Microscale air quality model (UAVR)

WRF Weather Research & Forecasting Model (US NCAR, NCEP, FSL, AFWA, FAA, University of Oklahoma)

1.2 Purpose of the document

This document describes the **quality assurance** and **quality control** procedure which will be followed to guarantee the quality of the whole modelling process. It will define the limitations and the uncertainty of the results in the modelling task

1.3 Document References

Carlton, A.G., B. J. Turpin, K. Altieri, S. Seitzinger, R. Mathur, S. Roselle, R. J. Weber, 2008. CMAQ model performance enhanced when in-cloud SOA is included: comparisons of OC predictions with measurements, Environ. Sci. Technol. , 42, (23), 8799-8802,

Chen, F., and Coauthors, 1996: Modeling of land-surface evaporation by four schemes and comparison with FIFE observations. *J. Geophys. Res.*, **101**, 7251-7268.

Chen, F., Z. Janjic, and K. Mitchell, 1997: Impact of atmospheric surface layer parameterization in the new land-surface scheme of the NCEP mesoscale Eta numerical model. *Bound.-Layer Meteorol.*, **l85**, 391-421.

Chen, F., and J. Dudhia, 2001: Coupling an advanced land-surface/hydrology model with the Penn State/NCAR MM5 modeling system. Part I: Model implementation and sensitivity.

Mon. Wea. Rev., **129**, 569-585.

Chen, F, H. Kusaka, M. Tewari, J.-W. Bao, and H. Harakuchi, 2004: Utilizing the coupled WRF/LSM/urban modeling system with detailed urban classification to simulate the urban heat island phenomena over the Greater Houston area. Preprints, *Fifth Symp. on the Urban Environment*, Vancouver, BC, Canada, Amer. Meteor. Soc., 9-11. [Available online at http://ams.confex.com/ams.pdfpapers/79765.pdf.]

Chen, F., and Coauthors, 2007: Evaluation of the characteristics of the NCAR high-resolution land data assimilation system. *J. Appl. Meteor.*, **46**, 694-713.

Hamdi R & V. Masson. 2008. Inclusion of a Drag Approach in the Town Energy Balance (TEB) Scheme: Offline 1D Evaluation in a Street Canyon. *Journal of Applied Meteorology and Climatology*, 47 , 2627-2644

Hertel O., R. Berkowicz, J. Christensen, and O. Hov, 1993: Test of two numerical schemes foruse in atmospheric transport-chemistry models. *Atmos. Environ.*, **27A**, 2591–2611

Holt, T., and J. Pullen, 2007: Urban Canopy Modeling of the New York City Metropolitan Area: A Comparison and Validation of Single- and Multilayer Parameterizations. *Mon.Wea. Rev.*, 135, 1906–1930.

Jiang, W., S. Smyth, É. Giroux, H. Roth, and D. Yin, 2006: Differences between CMAQ fine mode particle and PM2.5 concentrations and their impact on model performance evaluation in the lower Fraser valley. *Atmos. Environ*., **40**, 4973–4985.

Jiang, X.Y., C. Wiedinmyer, F. Chen, Z.L. Yang, and J. C. F. Lo, 2008: Predicted Impacts of Climate and Land-Use Change on Surface Ozone in the Houston, Texas, Area. *J. Geophys. Res.*, **113**, D20312, doi:10.1029/2008JD009820.

Kusaka, H., H. Kondo, Y. Kikegawa, and F. Kimura, 2001: A simple single-layer urban canopy model for atmospheric models: Comparison with multi-layer and slab models. *Bound.-Layer Meteor.*, 101, 329-358.

Kusaka, H., and F. Kimura, 2004: Coupling a single-layer urban canopy model with a simple atmospheric model: Impact on urban heat island simulation for an idealized case. *J. Meteor. Soc. Japan*, **82**, 67-80.

Kusaka, H., and Coauthors, 2009: Performance of the WRF model as a high resolution regional climate model: Model intercomparison study. *Proc. ICUC-7 (in CD-ROM).*

Lemonsu, A.; Grimmond, C. S. B. & V. Masson. 2004. Modeling the surface energy balance of the core of an old Mediterranean city: Marseille. *Journal of Applied Meteorology*, 2004, 43, 312-327.

Lemonsu A., Bélair S., Mailhot, J. & S. Leroyer. 2010. Evaluation of the Town Energy Balance Model in Cold and Snowy Conditions during the Montreal Urban Snow Experiment 2005. *Journal of Applied Meteorology and Climatology*, 49, 346-362.

Lin, C-Y, and Coauthors, 2008: Urban Heat Island effect and its impact on boundary layer development and land-sea circulation over northern Taiwan, *Atmospheric Environment*, **42**, 5635-5649. doi:10.1016.

Marras, S., Spano, D., Pyles, R.D, Falk, M., Snyder, R.L., Paw U, K.T., 2010. Application of the ACASA model in urban environments: two case studies. AMS Conference on Ninth Symposium on the Urban Environment, Keystone, Colorado, USA, August 2-6 2010

Masson, V., Grimmond, C. S. B. & T.R. Oke. 2002. Evaluation of the Town Energy Balance (TEB) scheme with direct measurements from dry districts in two cities. *Journal of Applied Meteorology*, 41, 1011-1026.

Meyers, T.P., and Paw U, K.T., 1986. Testing of a higher-order closure model for modelling airflow within and above plant canopies. Bound. Lay. Meteorol. 31, 297-311

Miao, S., and F. Chen, 2008: Formation of horizontal convective rolls in urban areas. *Atm. Res.*, 89(3): 298-304.

Miao, S., F. Chen, M. A. LeMone, M. Tewari, Qingchun Li, and Yingchun Wang, 2009a: An observational and modeling study of characteristics of urban heat island and boundary layer structures in Beijing. *J. Appl. Meteorol. Climtol*, 48(3): 484–501.

Miao, S., F. Chen, Q. Li, and S. Fan, 2009b: Impacts of urbanization on a summer heavy rainfall in Beijing, The seventh International Conference on Urban Climate: Proceeding, June - 3 July 2009, Yokohama, Japan, B12-1.

Offerle, B.; Grimmond, C. S. B. & K. Fortuniak. 2005. Heat storage and anthropogenic heat flux in relation to the energy balance of a central European city centre. *International Journal of Climatology*, 25, 1405-1419.

Pigeon, G.; Moscicki, M. A.; Voogt, J. A. & V. Masson. 2008. Simulation of fall and winter surface energy balance over a dense urban area using the TEB scheme. *Meteorology and Atmospheric Physics*, 102, 159-171.

Pleim, J. E., A. Xiu, P. L. Finkelstein, and T. L. Otte, 2001: A coupled land-surface and dry deposition model and comparison to field measurements of surface heat, moisture, and ozone fluxes. *Water Air Soil Pollut. Focus*, **1**, 243–252.

Pyles, R.D., Weare, B.C., Paw U, K.T., 2000. The UCD Advanced Canopy-Atmosphere-Soil Algorithm: Comparison with observations from different climate and vegetation regimes. Q.J.R. Meteorol. Soc.,126: 2951-2980

Pyles, R.D., Weare, B.C., Paw U, K.T., Gustafson W., 2003. Coupling between the University of California, Davis, Advanced Canopy-Atmosphere-Soil Algorithm (ACASA) and MM5: Preliminary Results for July 1998 for Western –North America. J Appl. Meteorol. 42: 557-569

R. San José, J.I. Peña, J.L. Pérez, R.M. González, EMIMO: An Emission Model. ISBN: 3-540-00840-3, Springer-Verlag, 2003, pp. 292–298.

R. San José, J.L. Pérez, R.M. González, Advances on Real-Time Air Quality Forecasting Systems for Industrial Plants and Urban Areas by Using the MM5-CMAQ-EMIMO. Large-Scale Scientific Computing, Lecture Notes in Computer Science 2008. Springer Berlin / Heidelberg Start Page: 450 End Page: 457 Volume: 4818

Tewari, M., H. Kusaka, F. Chen, W. J. Coirier, S. Kim, A, Wyszogrodzki, T. T. Warner, 2010.Impact of coupling a microscale computational fluid dynamics model with a mesoscale model on urban scale contaminant transport and dispersion. Atmos. Res. In Press.

Wang, X. M., W. S. Lin, L. M. Yang, R. R. Deng, and H. Lin, 2007: A numerical study of influences of urban land-use change on ozone distribution over the Pearl River Delta Region, China. *Tellus*, 59B, 633-641.

Wang, X.M., and Coauthors, 2009: Impacts of weather conditions modified by urban expansion on surface ozone: Comparison between the Pearl River Delta and Yangtze River Delta regions, *Adv. in Atmos. Sci.*, 2009b,

1.4 Project Overview

This overview is an introduction to the BRIDGE Project. Who is familiar with the Project can skip this section because its content is already known.

BRIDGE is a joint effort of 14 European Organizations aiming at incorporating sustainability aspects in urban planning, accounting for relations between **urban metabolism** and **urban structure**. BRIDGE also aims at devising of innovative **strategies** for urban planning in Europe.

BRIDGE will provide the means to close the gap between bio-physical sciences and urban planners and to illustrate the advantages of accounting for urban metabolism issues on a routine basis in design decisions. BRIDGE will focus on the following components of urban metabolism: **Energy**, **water**, **carbon and pollutants**. There are many challenges of the sustainable urban planning with regards to the above components (for example to optimize energy efficiency of urban structure, to minimize primary water consumption, to minimize the emissions to atmosphere, etc.)

BRIDGE will exploit the advances in bio-physical sciences to develop a Decision Support System (**DSS**) which will be used to support the decision making needed to achieve the above challenges by proposing quantitative measures and guidelines for sustainable use of energy and materials in urban planning. This DSS will reflect the multidimensionality nature of the urban metabolism, as operationalised in intelligible and transferable **indicators** easily understood by a non-scientific public. Decision making means selecting among **alternatives**. The development of this DSS will be based on an analytical and a design component linking the bio-physical processes with socio-economic parameters in order to estimate the environmental impacts of urban metabolism components and the potential socio-economic implications related to these impacts.

The fluxes of each of the above urban metabolism components will be measured and modeled in BRIDGE case studies, in order to calculate the net-fluxes into or out of the city environment. The measured and simulated datasets will be integrated in the DSS and the environmental impacts of the respective physical flows will be assessed. A cost-benefit analysis will be used to contras the environmental impacts against the cost of “fixing” such impacts.

Five European cities have been selected as BRIDGE **case studies**: **Helsinki**, Finland; **Athens**, Greece; **London**, United Kingdom; **Firenze**, Italy and **Gliwice**, Poland. In order to develop a method that will be welcomed by local governments, it is important to involve them in the project from the beginning. The project uses a **Community of Practice** (CoP) approach, which means that in the **case studies**, local stakeholders and scientists of the BRIDGE project meet on a regular basis in order to learn from each other. The CoP will make clear what aspects are important for the future users of the BRIDGE products. This approach will also be used to create an “umbrella” CoP across the participating cities to exchange ideas and experience of BRIDGE on a European level.

2 QA/QC PROCESS

The objective of a QA/QC is to ensure that the modelling simulations are scientifically sound, robust and defensible. Evaluation procedures are commonly applied to measure model performance. However, an integrated system of activities should be established in order to guarantee and to improve the quality of modelling results.

The quality assurance plan for the output data of the models will include the following elements:

- Verification that correct configuration and science options are used. All configurations are included in the D4.2 document : “Model implementation”.
- We will verify the integrity of the all output files (e.g. no missing and/or corrupted files)
- We will create horizontal plots of different outputs, base case and alternatives, to assess whether the output fields are reasonable. Some of these images are included in the D4.2 document : “Model implementation”. Here we will see how sensible the modelling systems to changes are in the input data (alternatives).
- All base case simulation will be evaluated using observation from 2008 and summer 2010 to verify that the model outputs are reasonable and consistent with general expectations.

Model evaluation is an overall system of procedures designed to measure the model performance. The main task in the QA/QC is the model performance evaluation, where the modelled estimates are compared against observed values to access the model’s accuracy and provide an indication of its reliability. The emphasis is on assessing: how accurately the model predicts observed values and how accurately does the model predict responses of predicted value to changes in inputs (alternatives).

The most important goal of the evaluation is to determine whether the aggregate modelling systems (model codes plus input data sets and observational data for testing) offers sufficiently reliable and accurate results that public decision-makers may have reasonable confidence in using the models to help choose between different alternatives.

This evaluation will confirm that the modelling systems are performing consistent with its scientific formulation, technical implementation, and at a level that is at least as reliable as other currents state-of-science methods.

Definition of model quality is not a simple task and there is no universal approach. There are no “good” models or “poor” models, the model is suitable or nor for the specified objectives. Due to the complexity of the phenomena simulated, there are always uncertainties associated with modelling results. Model evaluation is complicated by the nature of atmospheric flow and the limited representatives of data collected in the real atmosphere.

Despite the wide application of mesoscale meteorological models, no procedures or protocols have been established at the European level that assures minimum requirements for the use of performance of meteorological model. Scientific principles that assure model consistency and robustness do exist, but are not organised or adopted globally according to a well-defined protocol.

Several statistical measures, graphical tools and related analytical procedures could be used in the evaluating process. The models evaluation will utilize numerous graphical displays to facilitate quantitative and qualitative comparisons between predictions and measurements. Together with the statistical metrics, the graphical procedures are indented to identify obviously flawed model simulations. For example we can use: spatial mean outputs time series plots, time series plots at monitoring locations, outputs maps, outputs scatter plots stratified by station, by time. The graphical displays will be generated, were appropriate for the full annual 2008 cycle as well as for monthly and seasonal periods, as summer 2010.

A number of statistical parameters are widely used to estimate the model performance, but within these parameters some indicator should be selected as more relevant, depending on the type of answers that the model has to supply .The definition of a quality indicator for modelling results is not a simple task. It should be taken into consideration that no single quality indicator is good enough to assess model performance, and that therefore a system of quantitative parameters has to be identified. Application of such indicators helps to understand model limitations.

The statistical measures most commonly used with numerical prediction models are showed below. In the following, predicted values are shortened by Pi and observer values con Oi. For each single site each time (i). All in all a dataset of N values is considered.

Average values: The average value of measurements and model results are calculated as:

$$\overline{O} = \frac{1}{N}\sum_{i=1}^{N} O_i$$

$$\overline{P} = \frac{1}{N}\sum_{i=1}^{N} P_i$$

The two averages should be the same for an ideal forecast.

Standard deviations: The standard deviation of measurements and model results are calculated as:

$$\sigma_O = \sqrt{\frac{1}{N}\sum_{i=1}^{N}(O_i - \overline{O})^2}$$

$$\sigma_P = \sqrt{\frac{1}{N}\sum_{i=1}^{N}(P_i - \overline{P})^2}$$

The two standard deviations should be the same for an ideal forecast.

Bias: The average difference (BIAS) for all error, for each forecast length is calculated as:

$$BIAS = \frac{1}{N}\sum_{i=1}^{N} E_i = \overline{P} - \overline{O}$$

The BIAS should be zero for an ideal forecast. BIAS gives a measure of the sign of the error of the simulations. This is particularly useful for model developers, as it point to weak parts of the model. In addition, BIAS is easily corrected with statistical post-processing. It is important to note that de BIAS can vary in time and space. Breaking up the data into time of the year and the day, and into single locations fives more information and better possibilities for correction. Moreover, the BIAS gives information of systematic model errors for particular observational values, e.g. low wind speed cases if the data are sorted when calculating the BIAS.

Standard deviation of error STDE: The standard deviation of error (STDE) evaluates the non-systematic part of the error and is a measure of model predictability.

$$STDE = \sqrt{\frac{1}{N}\sum_{i=1}^{N}[(P_i - \overline{P}) - (O_i - \overline{O})]^2}$$

The STDE should be zero for an ideal forecast. STDE usually increases with forecast length. When STDE has the same magnitude throughout the model simulation it can be interpreted as if the error is saturated initially due to model deficiencies.

Root mean square error RMSE: The total error (RMSE) results from STDE and BIAS:

$$RMSE = \sqrt{\frac{1}{N}\sum_{i=1}^{N}(P_i - O_i)^2} = \sqrt{BIAS^2 + STDE^2}$$

Root mean square error (RMSE) is simply a combination of BIAS and STDE and expresses the total model error. THE RMSE should be zero for an ideal forecast. It is useful measure for a comparison of e.g. two different models. One should bear in mind that the squaring implies that few large errors have relatively more impact on the measure than many small errors.

Correlation coefficient R: The correlation coefficient (R) is very similar al STDE. However R is dimensionless while STDE has the dimension of the measured parameter. There is a caution on using R on very long time series, e.g. years. The annual amplitude of the temperature is usually so large that R will be dominated by this large structure. This hides the smaller scale errors like diurnal cycles. Caution should also be given to R, because a large systematic error (BIAS) will not be expressed. It is calculated as:

$$R = \left[\frac{\frac{1}{N}\sum_{i=1}^{N}(O_i - \overline{O})(P_i - \overline{P})}{\sigma_O \sigma_P}\right]$$

The correlation coefficient r should be one for an ideal forecast.

Hit rate H: Hit rate (H) is defined as the fraction of the total simulation data that have a value which is inside an acceptable rage (for example 50%) of the simultaneous observations. H is particularly useful as an overall measure to evaluate model performance. H is one of the few measures that do not assume a Gaussian distribution of the errors. The hit rate H should be 100$ an ideal forecast.

$$H = \frac{1}{N}\sum_{i=1}^{N} n_i$$

with

$$n_i = \begin{cases} 1 \, for \left| E_i \le DA \right| \\ 0 \, else \end{cases}$$

In case of air pollution the maximum model uncertainty is defined by the UE directive 2008/50/CE. The uncertainty for modelling is defined as the maximum deviation of the measured and calculated concentration levels for 90% of individual monitoring points, over the period considered, by the limit value (or target value in the case of ozone), without taking into account the timing of the events. The fixed measurements that have to be selected for a comparison with modelling results shall be representative of the scale covered by the model.

MODELLING UNCERTAINTY 2008/50/CE				
PERIOD	SO2, NO2, NO, CO	BENZENE	PM10/PM25	OZONE
Hourly	50%	-	-	50%
8-hour averages	50%	-	-	50%
Daily averages	50%	-	-	-
Annual averages	30%	50%	50%	-

3 WRF/UCM-EMIMO-CMAQ. UPM MODELS.

3.1 WRF/UCM

Improvement of computational environment and physics in mesoscale model allows urban scale prediction with a larger domain using mesoscale model. It is implemented the parameterization of urban effect in the WRF mesoscale model which is developed in NCAR. NCAR coupled an urban canopy model (UCM) with Noah land surface model in the WRF model to realistically represent the urban by high resolution of land-use and building information. More information about WRF/UCM can be found in D4.1 “Model Selection Report” and D4.2 “Model Implementation Report”.

The coupled WRF/UCM model has been applied to major metropolitan regions (e.g. Beijing, Guangzhou/Hon Kong, New York City, Salt Lake City, Taipei, Tokyo and Madrid), and its performance was evaluated against surface observations, atmospherics soundings, wind profiler data, and precipitation data [Chen et al., 2004;Holt and Pullen, 2007;Jiand et al. 2008; Lin et al., 2008; Miao and Chen, 2008; Kusaka et al., 2009; Miao et al., 2009; Wang et al. 2009; Tewari et al. 2010}. Results show the coupled WRF/Noah/UCM modelling system is able to reproduce the observed features, reasonably well [Mia and Chen, 2008; Miao et al. 2009)]. Using WRF/Noah/UCM model significantly improved the simulation on the urban heat island effects, boundary-layer development, when compared to observations obtained from whether stations and lidar. [Lin et al. 2008].

3.2 EMIMO- CMAQ

The U.S. Environmental Protection Agency’s Community Multiscale Air Quality (CMAQ) model is a three-dimensional Eulerian (i.e., gridded) atmospheric chemistry and transport modeling system that simulates ozone, acid deposition, visibility, and fine particulate matter throughout the troposphere. Designed as a one-atmosphere model, CMAQ can address the complex couplings among several air quality issues simultaneously across spatial scales ranging from local to hemispheric. The CMAQ source code is highly transparent and modular to facilitate extensibility through community development.

CMAQ is a third-generation air quality model that is designed for applications ranging from regulatory and policy analysis to understanding the complex interactions of atmospheric chemistry and physics. Third-generation models, like CMAQ, treat multiple pollutants simultaneously up to continental or larger scales, often incorporating feedback between chemical and meteorological components. More information about CMAQ can be found in D4.1 “Model Selection Report” and D4.2 “Model Implementation Report”

The CMAQ system was designed to minimize the potential for model simulation error in several significant ways:

The formal CMAQ peer review process implemented by the EPA ensures that the model retains scientific credibility. Also, informal “review” of the modelling system occurs day-to-day as the

broad international user community applies CMAQ for a wide variety of scientific questions and in locations.

The modularity of the scientist processes in CMAQ makes modifications and adaptations to the user's needs more straightforward. The potential for error is minimized because the user is not required to change code or declare variables within program modules outside the one of immediate interest.

Many evaluation processes have been developed to measurement the performance of the CMAQ model. [Hetel et al., 1993; Pleim et al., 2001;Jiang et al., 2006;Carlotn et al. 2008;] Comparison of model predictions to observations at intensive field sites have been achieved, and sensitivity tests for comparison of chemical mechanisms.

Emissions quality assurance and quality control is the single most critical step in performing air quality modelling studies. Because emissions processing is tedious, time consuming and involves complex manipulations of many different types of data sets, it is not easy to detect errors. And the QA/QC responsibility is moved to the air quality model process. The emission model EMIMO have been evaluated to many applications, and the results of the chemical simulations were evaluated against observations, all cases the results show that de EMIMO – CMAQ system is able to reproduce the observed features, in a realistic way. [Roberto et al., 2003, 2008]

3.3 Applications

The last models have been run over 5 European cities, Athens, Firenze, Helsinki, Gliwice and London. WRF/UCM has been run for all cities and CMAQ to Athens and Firenze. Two domains have been set. First level: 37*37 grid cells, 5.4 km. grid resolution and the second level: 28*28 grid cells, 0.2 km.

3.3.1 Athens

The air pollution measurements contain data on air pollutants (CO, NO_2, NO, SO_2, O_3) on several stations close to the case study area. Hourly values for a whole year period are given. The data are provided by the Ministry of Environment, Energy and Climate change. More information can be found in D3.1.1 "Datasets of air quality, energy water, and carbon and pollutants fluxes/concentrations"

We can see the comparison between observed and modelled pollution data for the simulated domain, full year 2008. The performance of the modelling system is very good, with average values very close between measurements and modelled and correlation coefficients over 0.7.

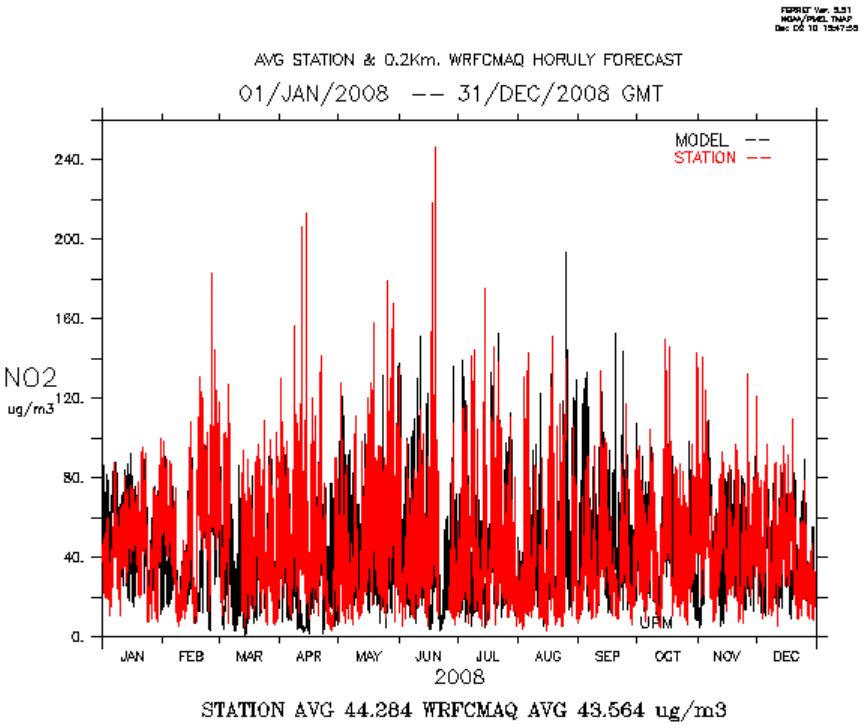

Figure 1: Time series comparison between WRF/UCM-EMIMO-CMAQ and stations Average, NO_2, Full year2008

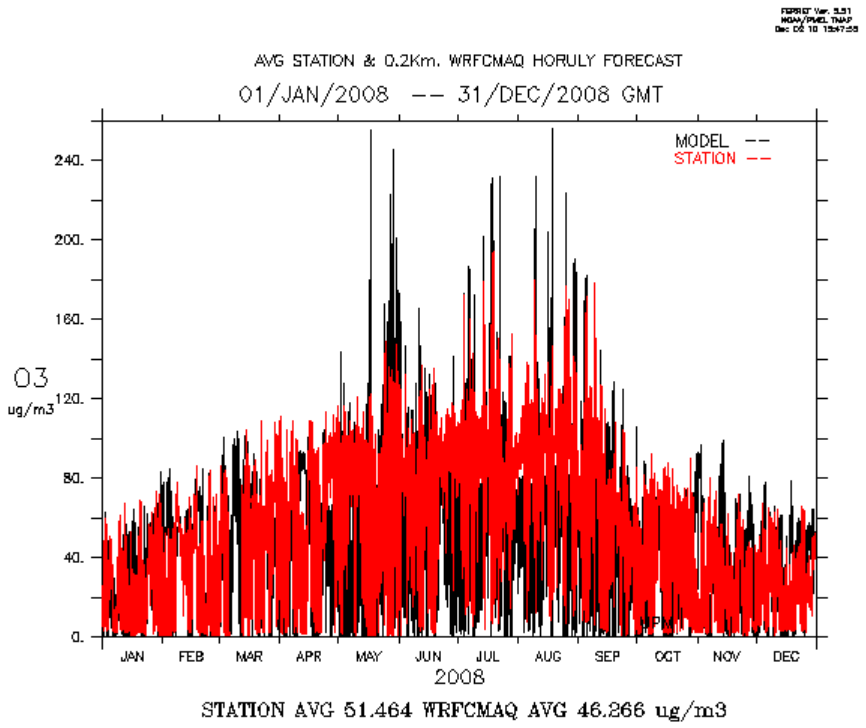

Figure 2: Time series comparison between WRF/UCM-EMIMO-CMAQ and stations Average, O_3, Full year2008

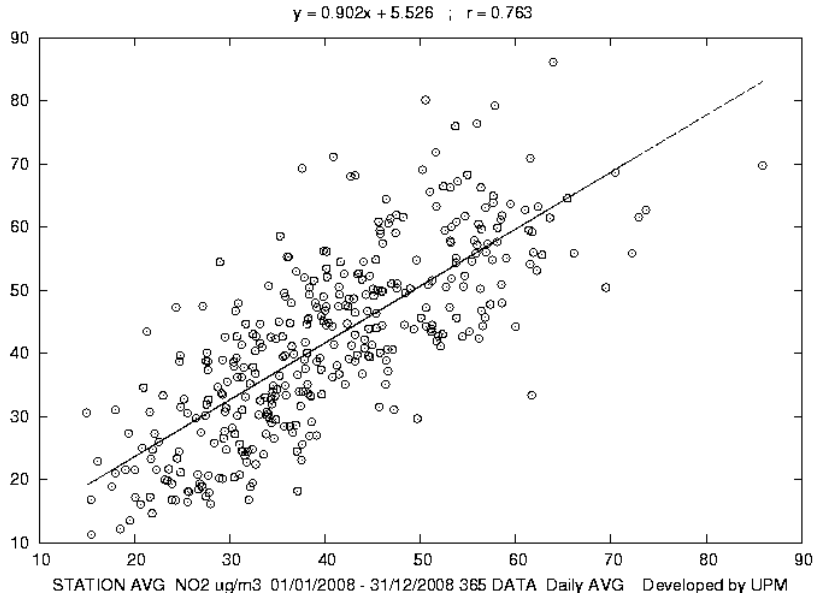

Figure 3: Lineal regression comparison between WRF/UCM-EMIMO-CMAQ and stations Average, NO_2, daily values, Full year2008

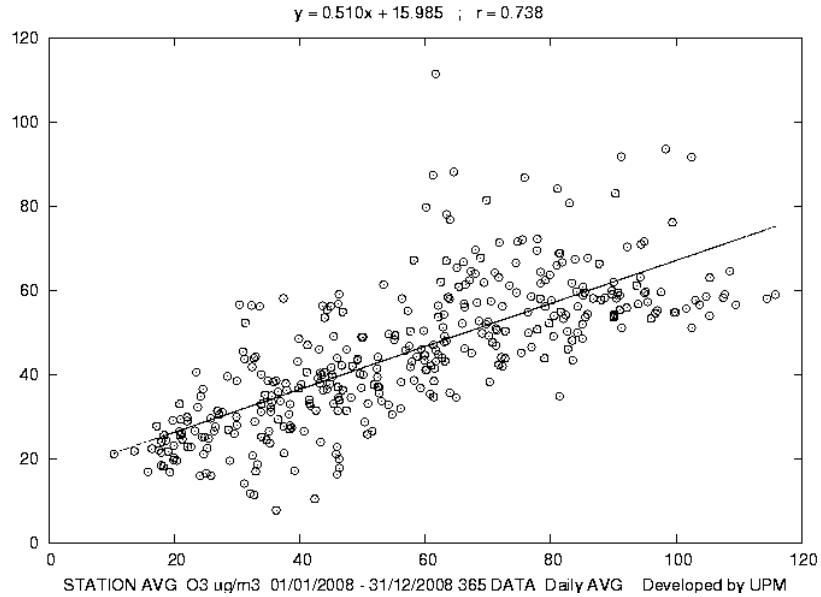

Figure 4: Lineal regression comparison between WRF/UCM-EMIMO-CMAQ and stations Average, O_3, daily values, Full year2008

3.3.2 Helsinki

Measurement data comes from Kumpula tower. UTM coordinates, X=217563 meters Y=2763551 meters. Height from sea level 57 meters. The measurement point is outside of the model domain of the 200 meters resolution, so the comparisons are with model data comes from simulation of the 5.4 km resolution domain.

The weather station is situated on the roof of one of the University of Helsinki buildings. The main variables are the solar radiation, temperature, winds and fluxes. The fluxes are measured with the eddy covariance technique on top de tower.

The commons periods between measurements and modelled data are 01/01/2008 – 31/12/2008 and 01/07/2010-30/09/2010

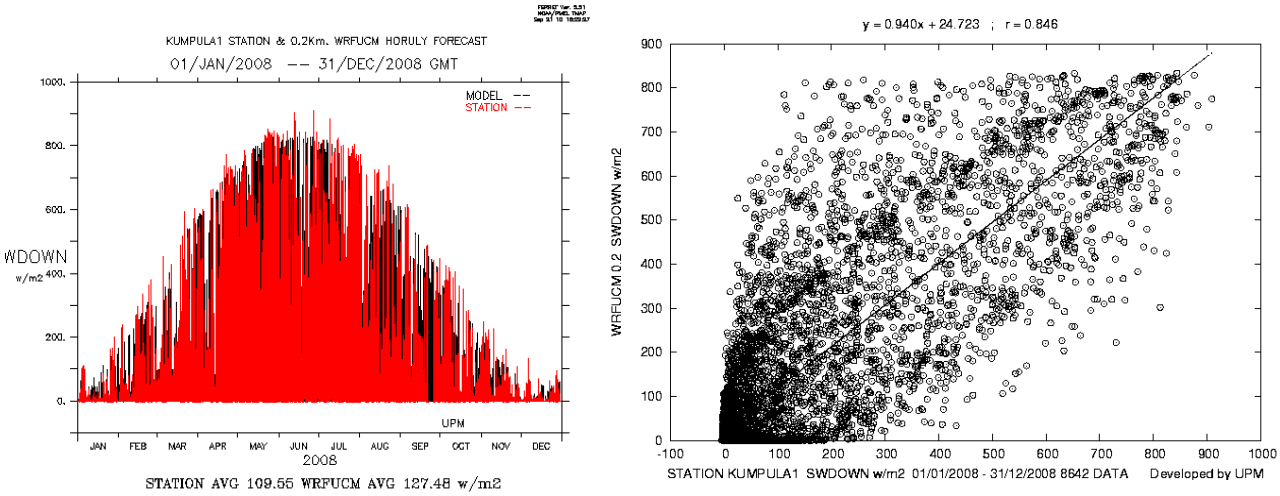

Figure 5: Time series comparison (left) and lineal regression (right) between WRF/UCM and Kumpula measurement, Solar radiation¸ Full year2008, 5.4 km resolution model domain

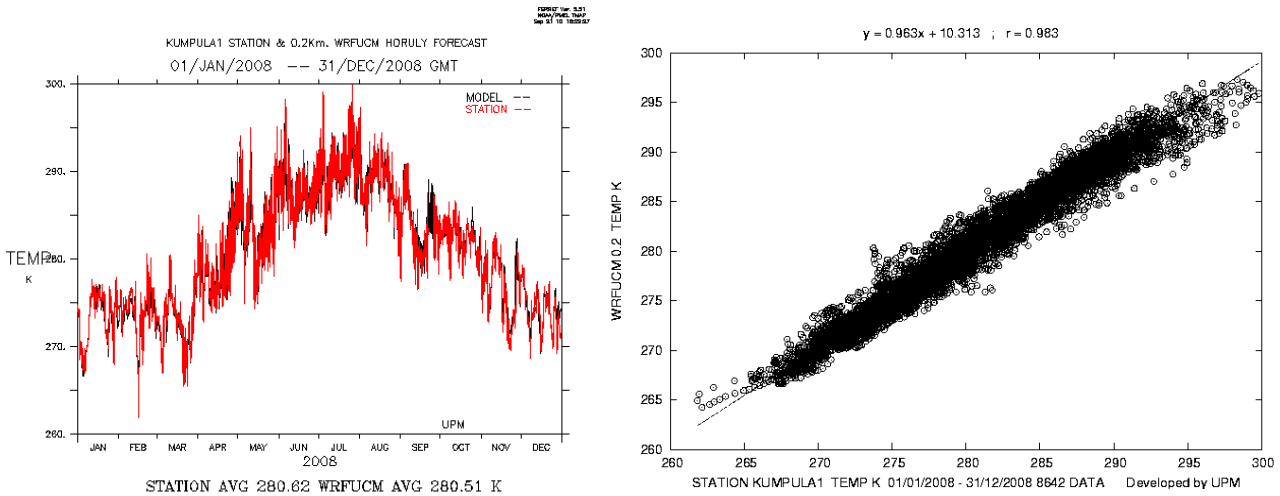

Figure 6: Time series comparison (left) and lineal regression (right) between WRF/UCM and Kumpula measurement, Air temperature¸ Full year2008, 5.4 km resolution model domain

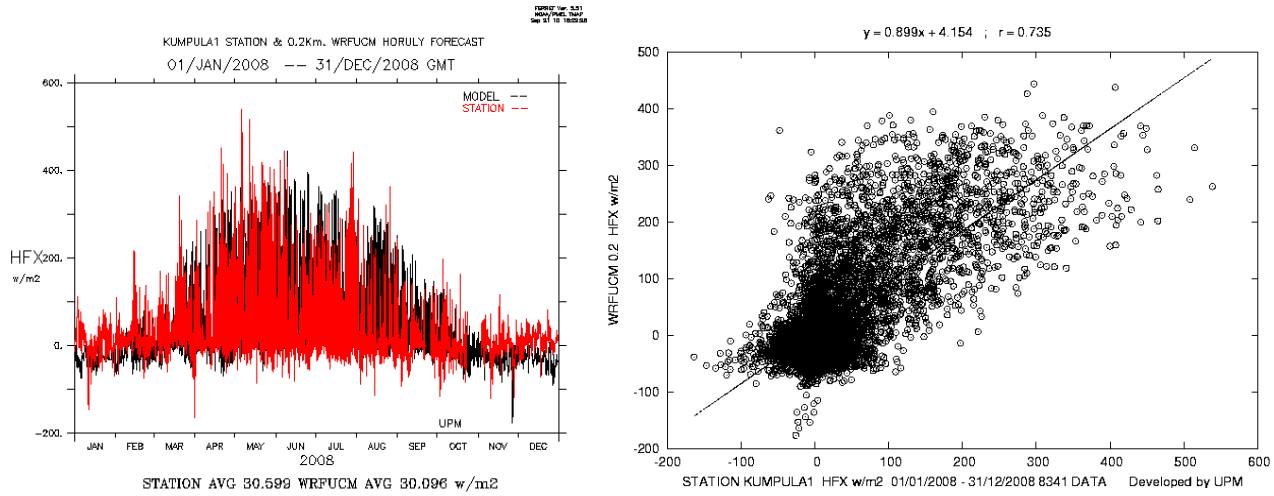

Figure 7: Time series comparison (left) and lineal regression (right) between WRF/UCM and Kumpula measurement, Sensible heat flux, Full year2008, 5.4 km resolution model domain

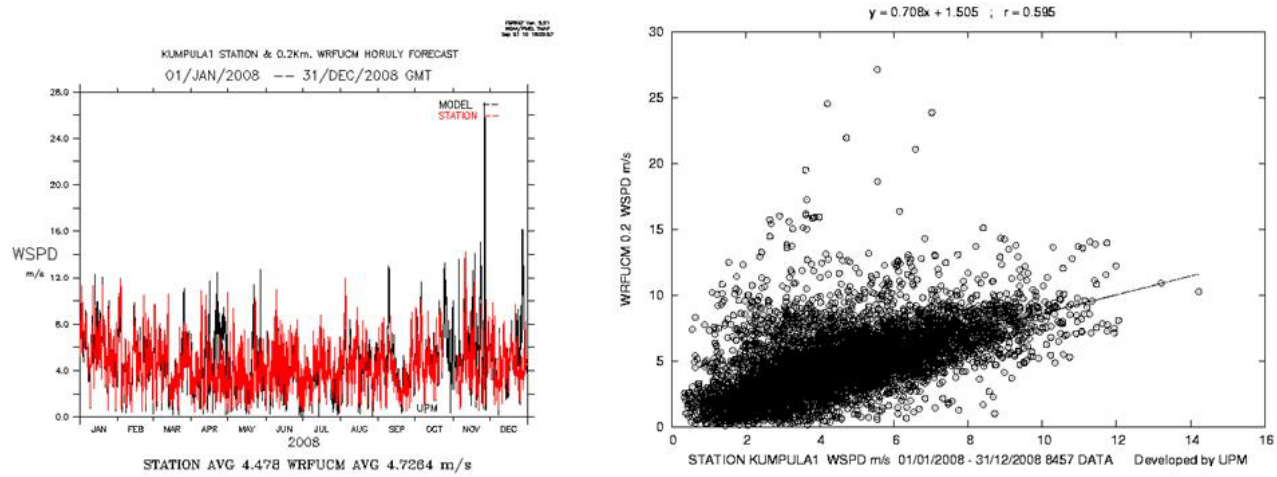

Figure 8: Time series comparison (left) and lineal regression (right) between WRF/UCM and Kumpula measurement, Wind Speed, Full year2008, 5.4 km resolution model domain

5.4 KM 01/01/2008 – 31/12/2008	TEMP	U	V	WSPD	SWDOWN	HFX
Observed mean	280.62	1.00	0.59	4.48	109.55	30.60
Calculated mean/Observed mean	1.00	0.83	0.83	1.04	1.17	1.03
Observed STD	6.89	3.54	3.16	1.98	194.24	76.23
Calculated STD/Observed STD	0.98	0.76	0.75	1.19	1.11	1.22
Bias	-0.14	-0.17	-0.10	0.20	18.13	1.05
Absolute Bias	0.94	1.76	1.27	1.34	62.44	43.49
R2	0.97	0.54	0.76	0.35	0.72	0.54
RMSE	1.26	2.42	1.60	1.99	117.02	63.59
RMSE/Observed Mean	0.00	2.42	2.72	0.45	1.07	2.08
PERCENTAGE within +/- 50	100.00	30.46	31.60	79.77	18.56	13.66

Table 1: Statistical parameters between WRF/UCM and Kumpula measurement, Full year2008, and 5.4 km resolution model domain

3.3.3 Gliwice

One measurement point is located at 50º 17´38.27”N 18º40´53.83”E. Measurement Meteorological parameters are: winds, air temperature, humidity, total radiation and atmospheric pressure. Turbulent flux measurements have been performed by UBAS, starting from January 2010. The common period between measurements and modelled data is 10/07/2010 – 30/09/2010

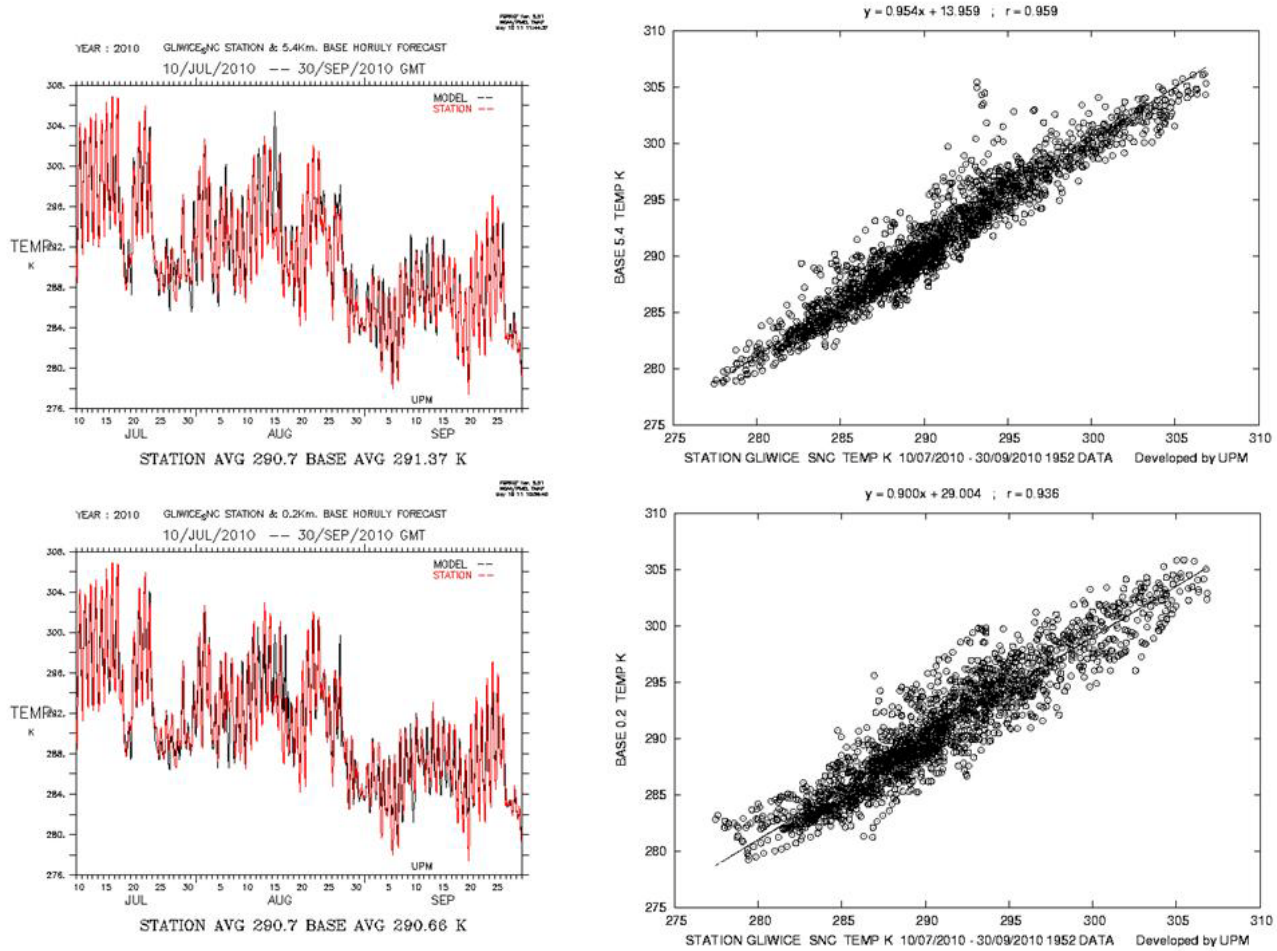

Figure 9: Time series comparison (left) and lineal regression (right) between WRF/UCM and Gliwice measurement, Air temperature, 10/07/2010 – 30/09/2010, 5.4km (top) and 0.2 km resolution (bottom)

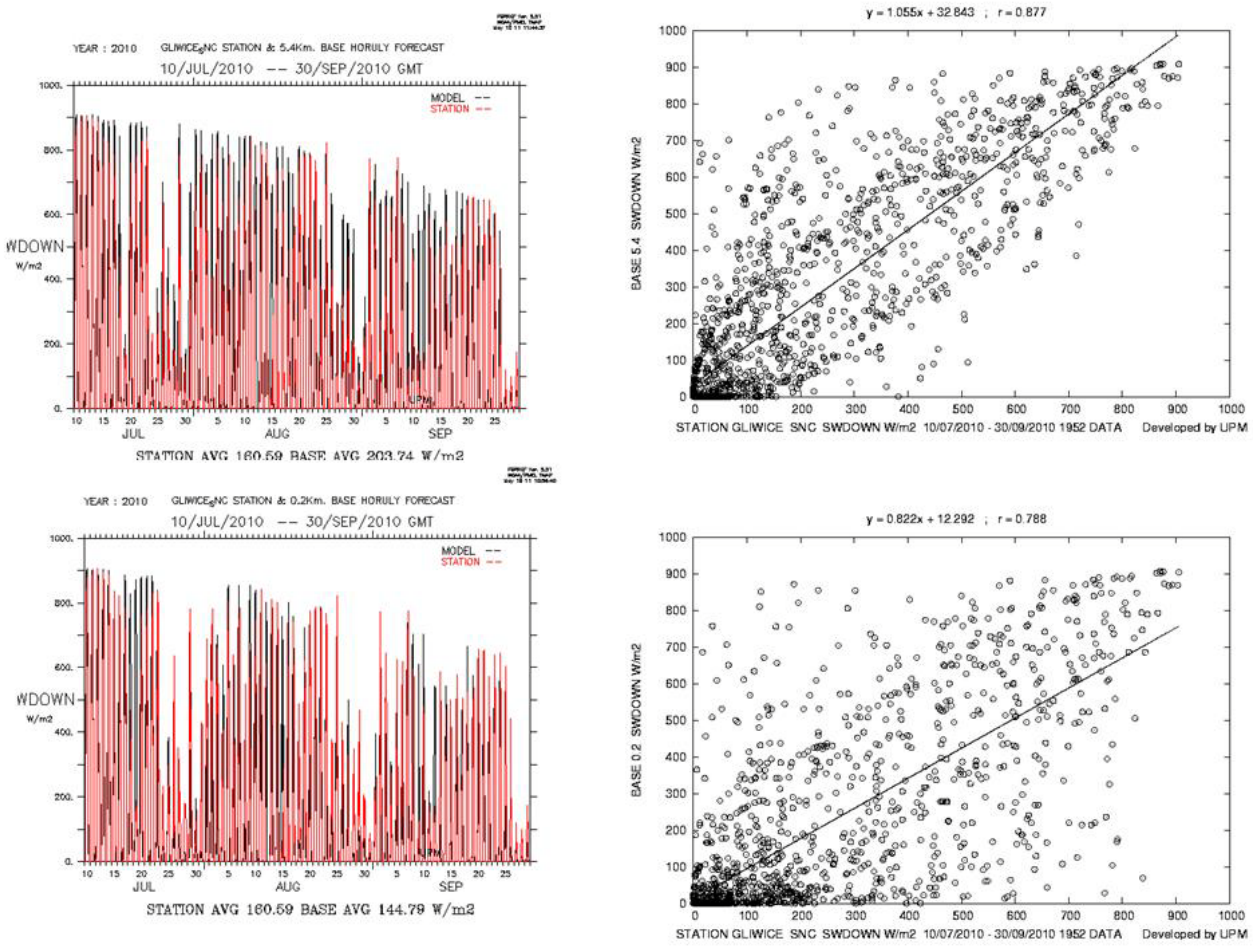

Figure 10: Time series comparison (left) and lineal regression (right) between WRF/UCM and Gliwice measurement, Short wave radiation, 10/07/2010 – 30/09/2010, 5.4km (top) and 0.2 km resolution (bottom)

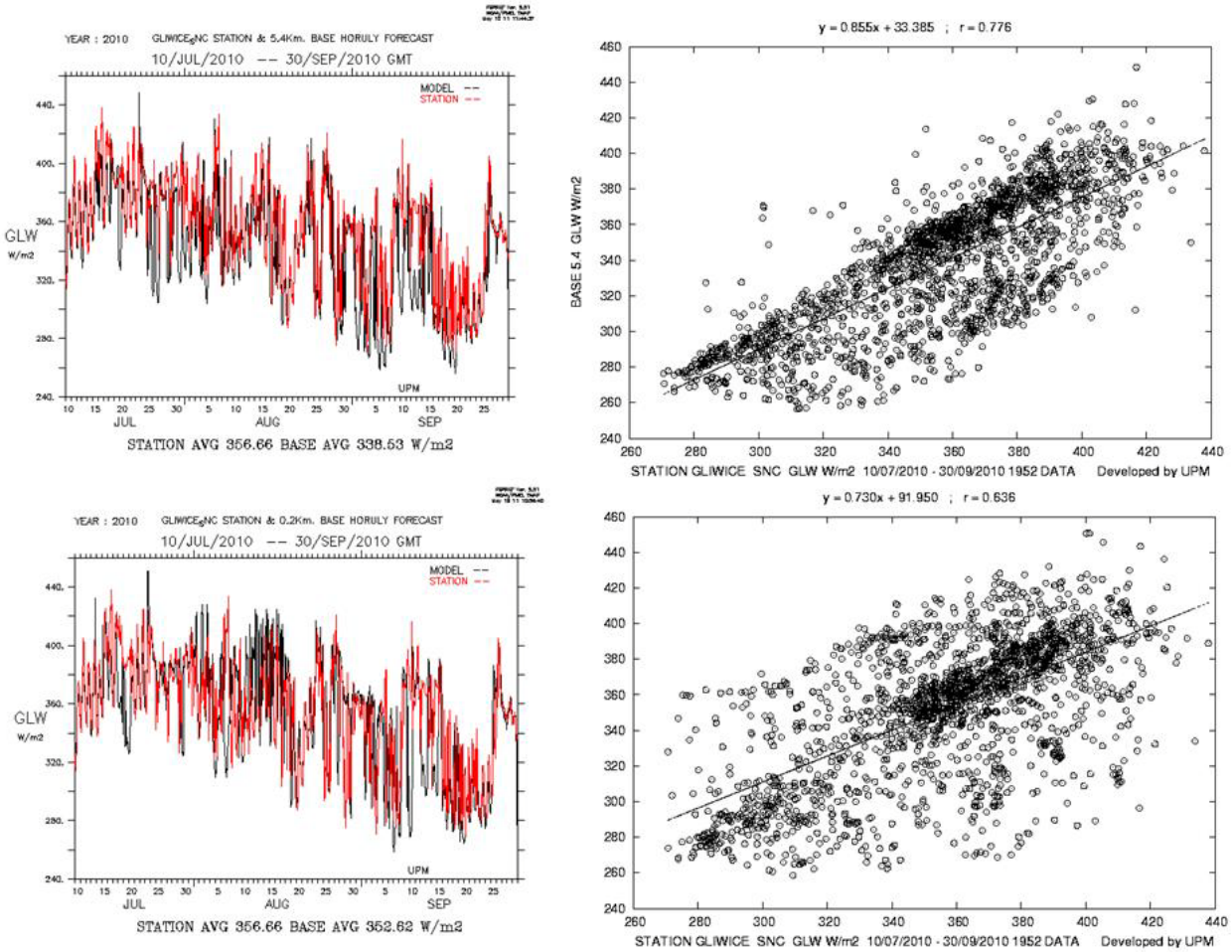

Figure 11: Time series comparison (left) and lineal regression (right) between WRF/UCM and Gliwice measurement, Long wave radiation, 10/07/2010 – 30/09/2010, 5.4km (top) and 0.2 km resolution (bottom)

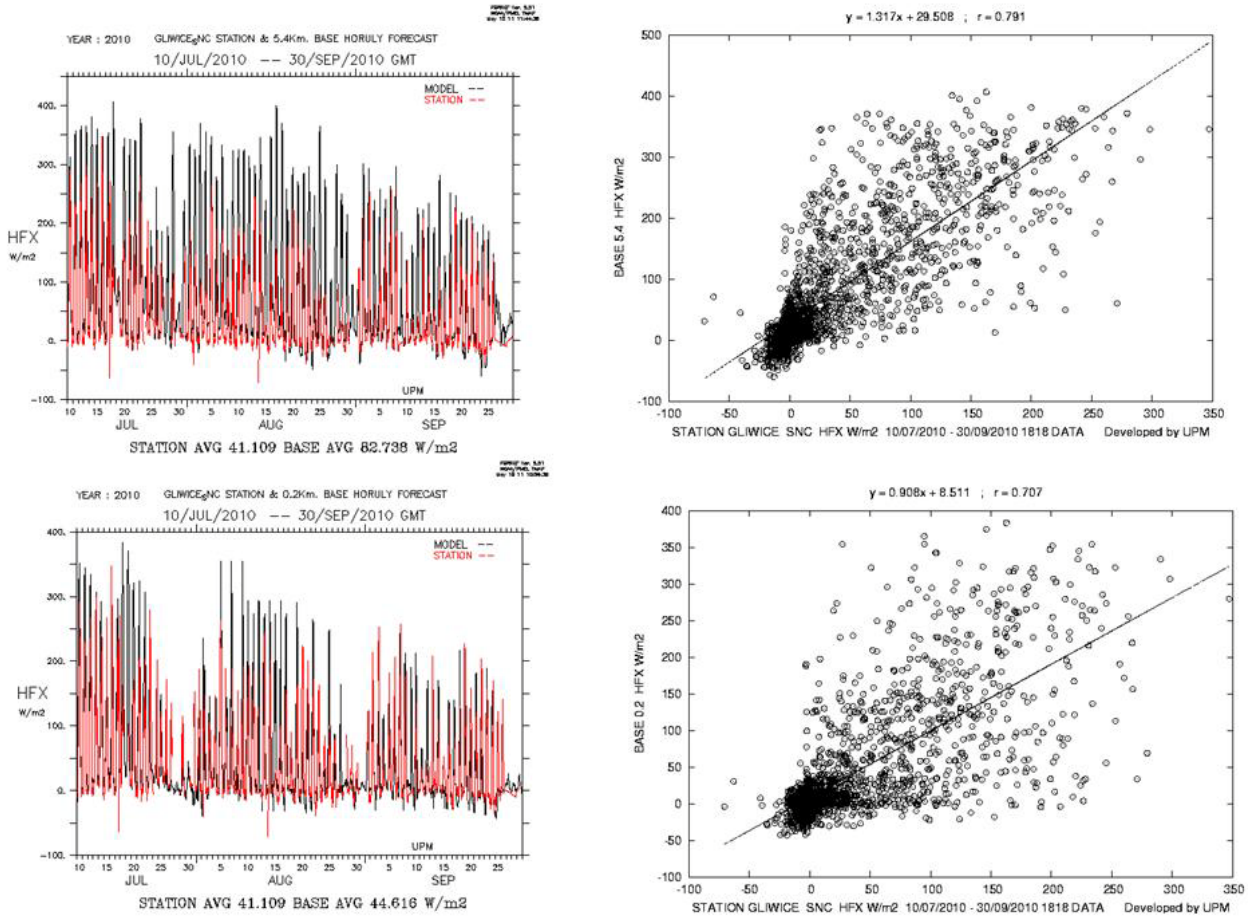

Figure 12: Time series comparison (left) and lineal regression (right) between WRF/UCM and Gliwice measurement, Sensible heat flux, 10/07/2010 – 30/09/2010, 5.4km (top) and 0.2 km resolution (bottom)

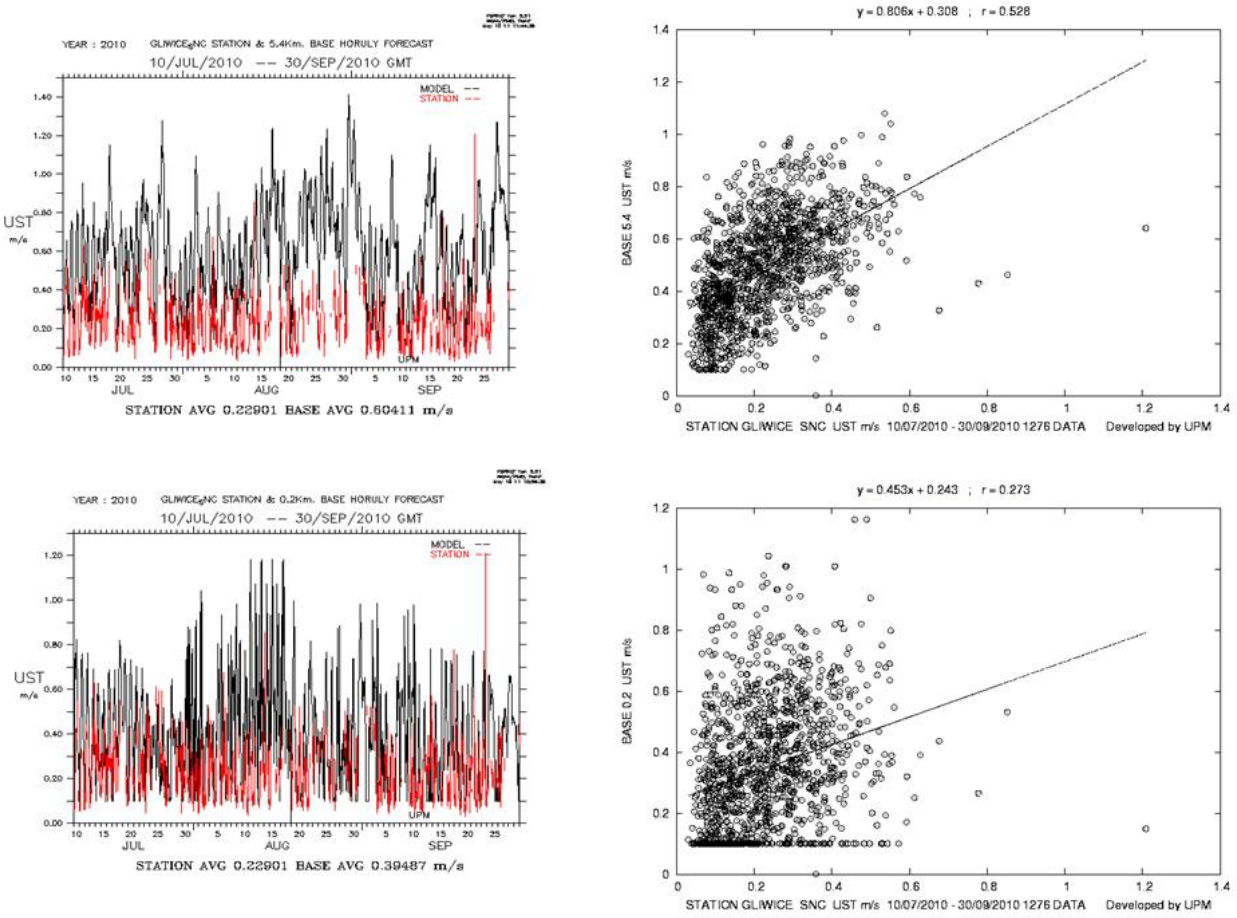

Figure 13: Time series comparison (left) and lineal regression (right) between WRF/UCM and Gliwice measurement, Fiction velocity, 10/07/2010 – 30/09/2010, 5.4km (top) and 0.2 km resolution (bottom)

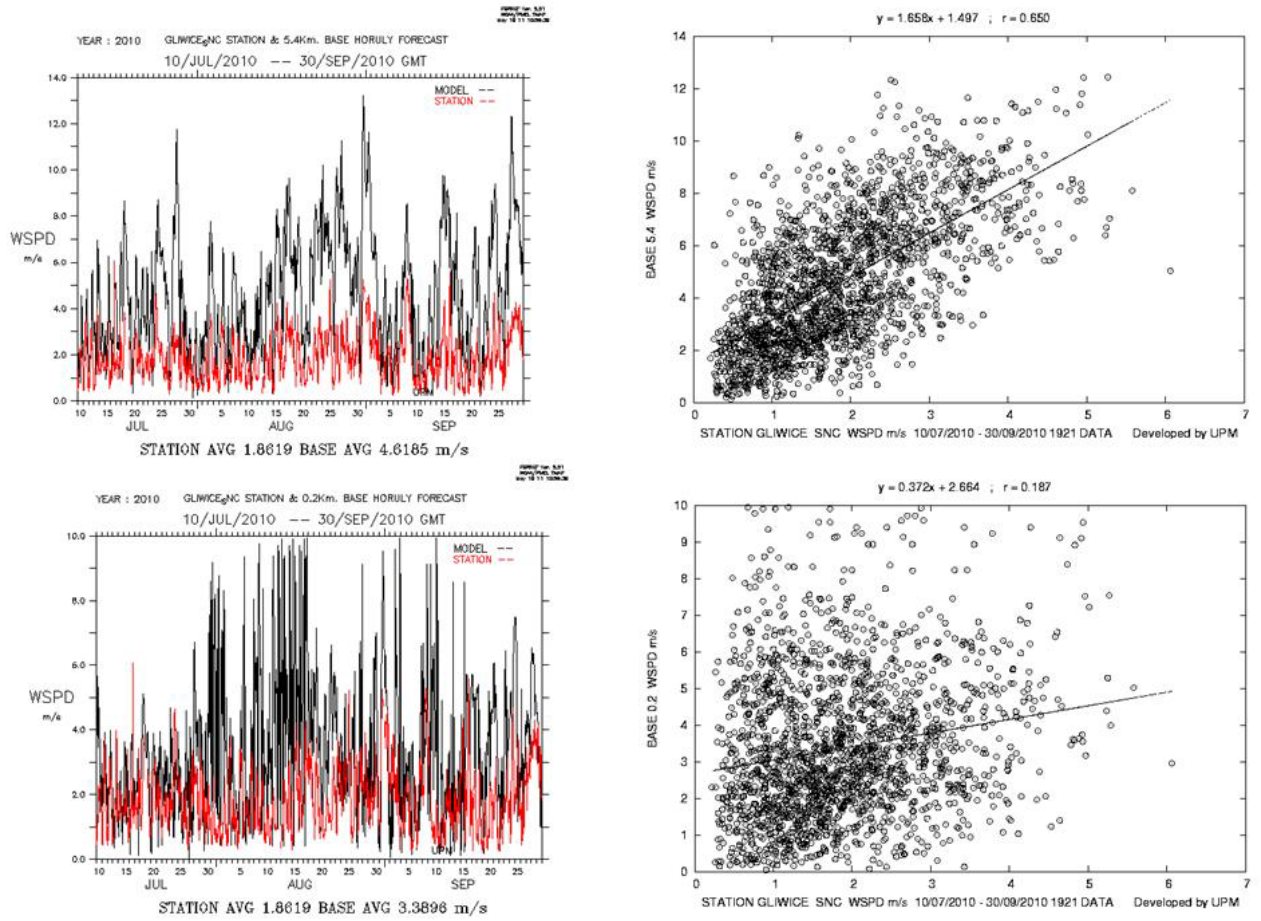

Figure 14: Time series comparison (left) and lineal regression (right) between WRF/UCM and Gliwice measurement, Wind Speed, 10/07/2010 – 30/09/2010, 5.4km (top) and 0.2 km resolution (bottom)

5.4 KM 10/07/2010 – 30/09/2010	HFX	UST	WSPD	SWDOWN	GLW	TEMP
Observed mean	41.11	0.23	1.86	160.59	356.66	290.70
Calculated mean/Observed mean	2.03	2.15	2.46	1.26	0.95	1.00
Observed STD	62.39	0.12	0.98	227.97	34.05	5.73
Calculated STD/Observed STD	1.67	1.53	2.55	1.20	1.10	0.99
Bias	42.54	0.26	2.72	41.70	-18.24	0.61
Absolute Bias	51.87	0.27	2.77	79.52	21.53	1.22
R2	0.63	0.28	0.42	0.77	0.60	0.92
RMSE	79.05	0.31	3.38	138.91	30.26	1.75
RMSE/Observed Mean	1.92	1.35	1.82	0.87	0.08	0.01
PERCENTAGE within +/- 50	16.83	18.81	16.14	60.50	100.00	100.00

Table 2: Statistical parameters between WRF/UCM and Gliwice measurement, 10/07/2010 – 30/09/2010, 5.4 km resolution model domain

0.2 KM 10/07/2010 – 30/09/2010	HFX	UST	WSPD	SWDOWN	GLW	TEMP
Observed mean	41.11	0.23	1.86	160.59	356.66	290.70
Calculated mean/Observed mean	1.12	1.51	1.80	0.90	0.99	1.00
Observed STD	62.39	0.12	0.98	227.97	34.05	5.73
Calculated STD/Observed STD	1.29	1.66	1.98	1.04	1.15	0.96
Bias	4.75	0.12	1.49	-16.34	-4.35	-0.09
Absolute Bias	35.29	0.18	1.86	84.61	22.44	1.53
R2	0.50	0.07	0.04	0.62	0.41	0.88
RMSE	57.20	0.24	2.50	152.69	31.79	2.02
RMSE/Observed Mean	1.39	1.05	1.34	0.95	0.09	0.01
PERCENTAGE within +/- 50	21.45	44.59	38.00	57.84	100.00	100.00

Table 3: Statistical parameters between WRF/UCM and Gliwice measurement, 10/07/2010 – 30/09/2010, 0.2 km resolution model domain

3.3.4 Firenze

An eddy covariance flux station is located at Ximeniano observatory (43º47´70”N, 11º15´E). On the roof there is a mast of 3 meters and measurements are at 33 meters above the street level. Meteorological variables: winds, humidity, temperature and solar radiation are available every 15 minutes and turbulent fluxes: sensible heat flux, latent heat flux and friction velocity every 30 minutes.

The common period between measurements and modelled data are 01/04/2008 – 01/05/2008 and 01/07/2010- 31/08/2010Air pollution data, SO2, NO2 and CO, are available every hour, for full year 2008 for a network of five air quality monitoring stations.

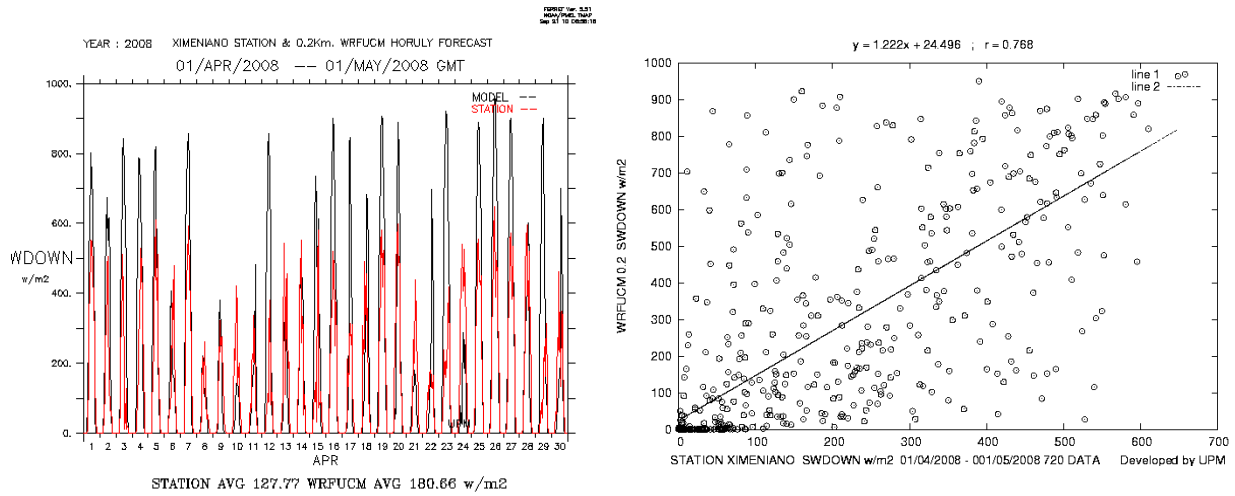

Figure 15: Time series comparison (left) and lineal regression (right) between WRF/UCM and Ximeniano measurement, Solar radiation¸ April, 2008, 0.2 km resolution model domain

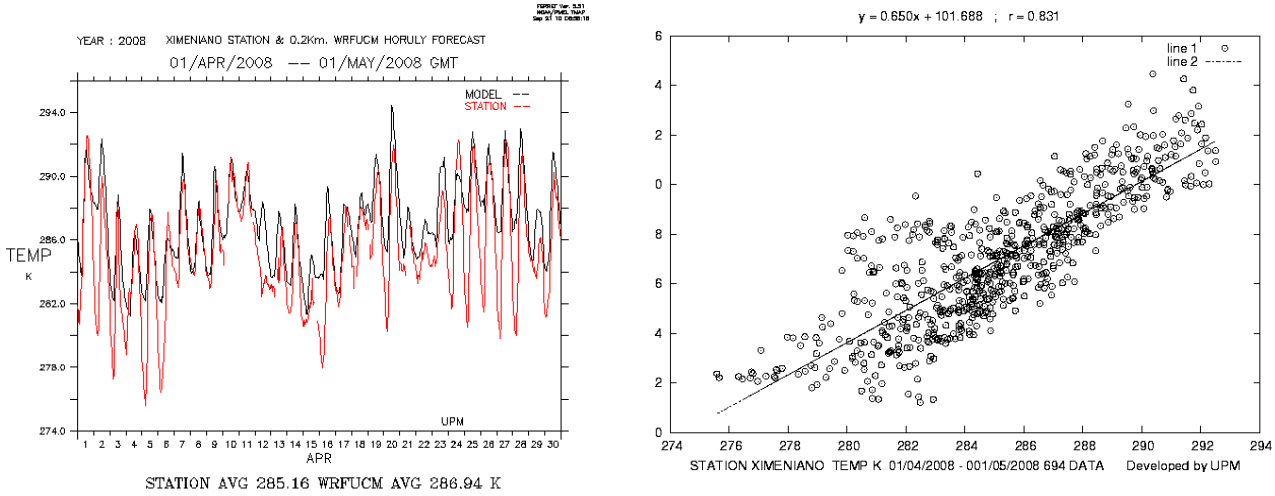

Figure 16: Time series comparison (left) and lineal regression (right) between WRF/UCM and Ximeniano measurement, Air temperature¸ April, 2008

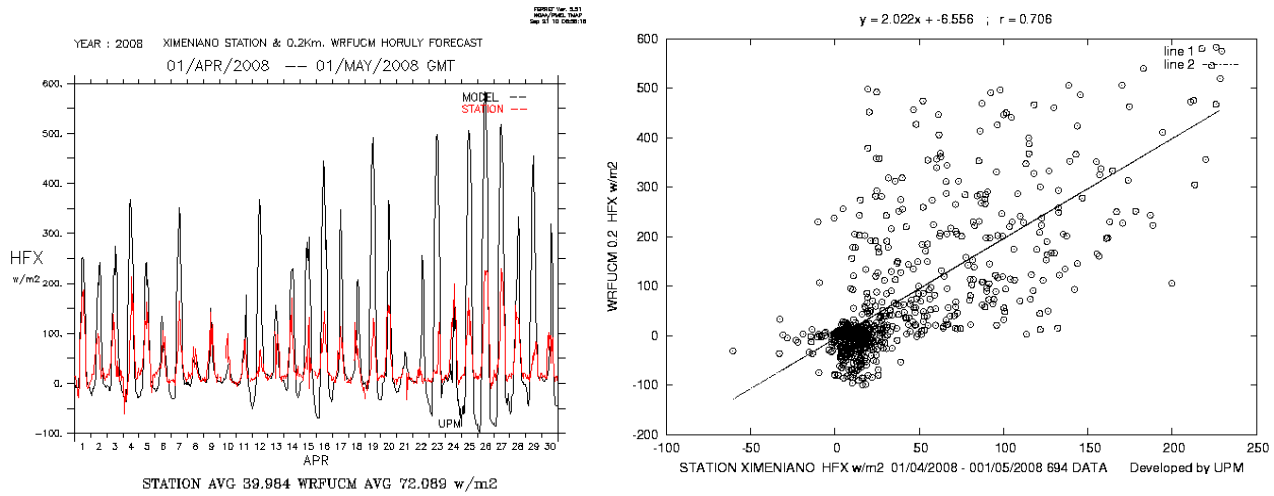

Figure 17: Time series comparison (left) and lineal regression (right) between WRF/UCM and Ximeniano measurement, Sensible heat flux¸ April 2008, 0.2 km resolution model domain

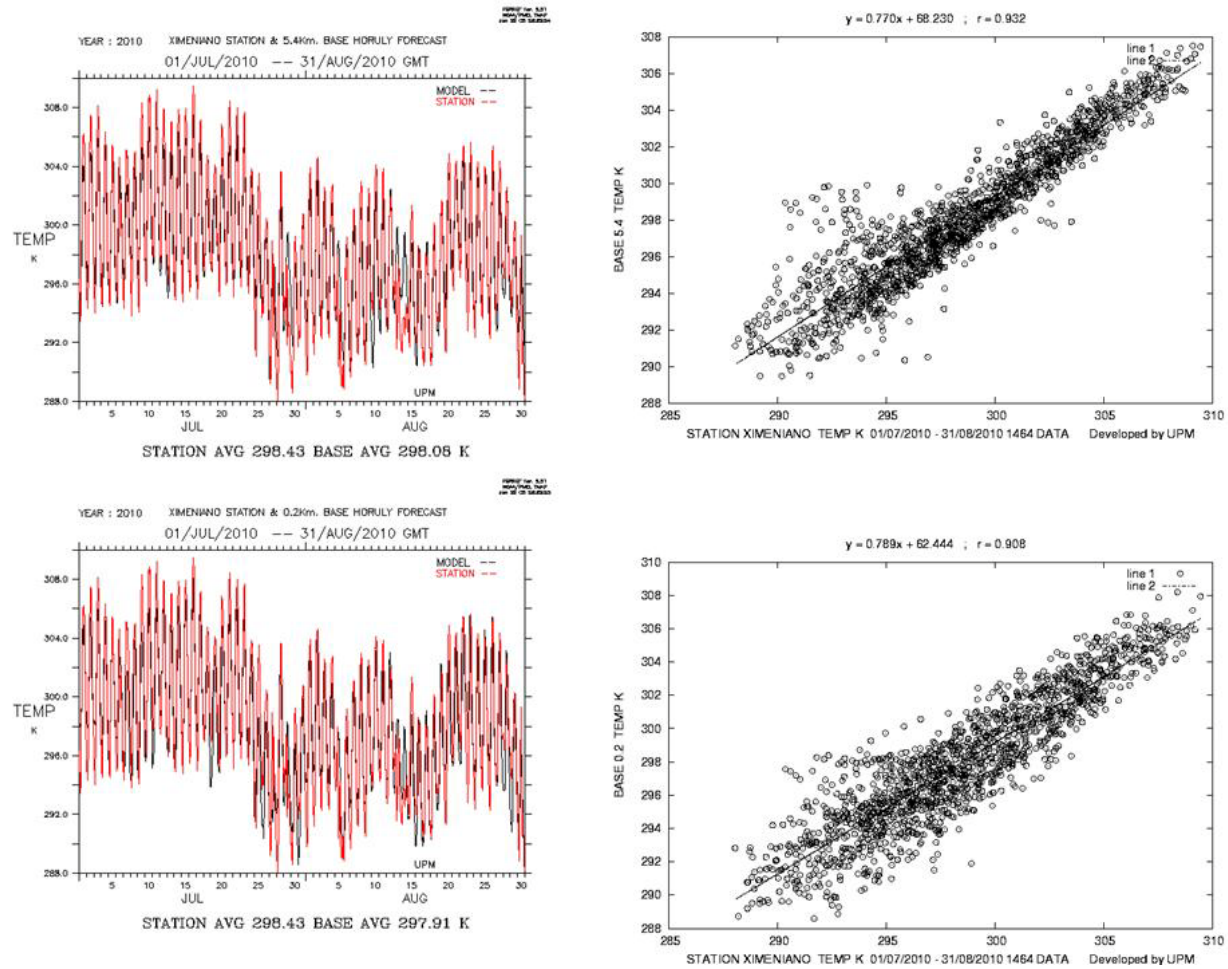

Figure 18: Time series comparison (left) and lineal regression (right) between WRF/UCM and Ximeniano measurement, Air temperature¸ 01/07/2010 – 31/08/2010, 5.4km (top) and 0.2 km resolution (bottom)

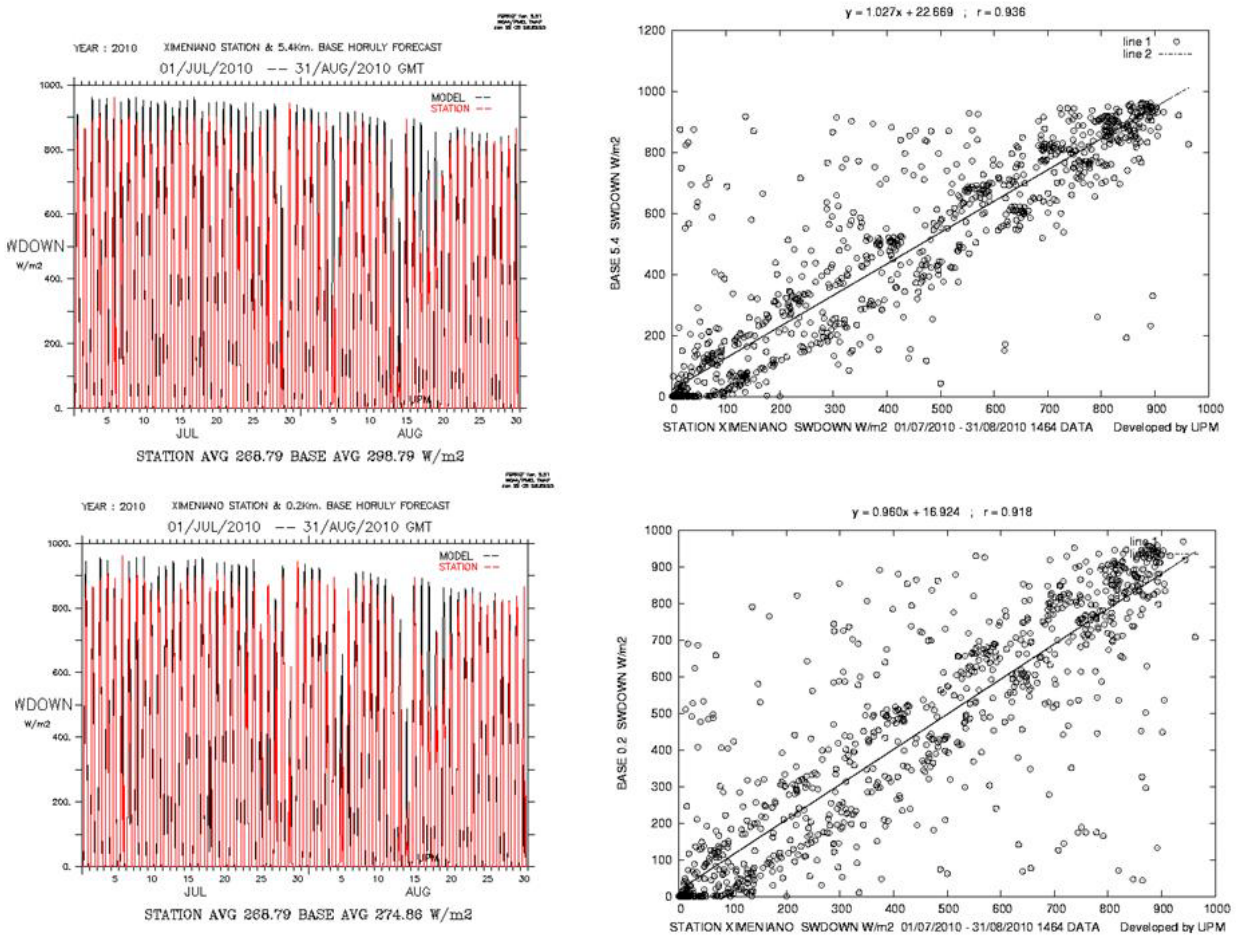

Figure 19: Time series comparison (left) and lineal regression (right) between WRF/UCM and Ximeniano measurement, Short wave radiation, 01/07/2010 – 31/08/2010, 5.4km (top) and 0.2 km resolution (bottom)

In the Figure 19, lineal regression of short wave radiation can see an ellipsoid form. This is due to a time shift. Model data are instant values every one hour and measurement data are 15 minutes temporal average. To compare model and station values, one hour (60 minutes) average has been done to convert 15 minutes station data in 1 hour data.

These temporal differences can be fixed if in the measurement data we use a 15 minutes temporal average from 44 to 59 minutes and the results are compared with the 1 hour instant value from the model.

In the Figure 21 , we can see how the ellipsoid has been avoided and the correlation coefficient is the same 0.918.

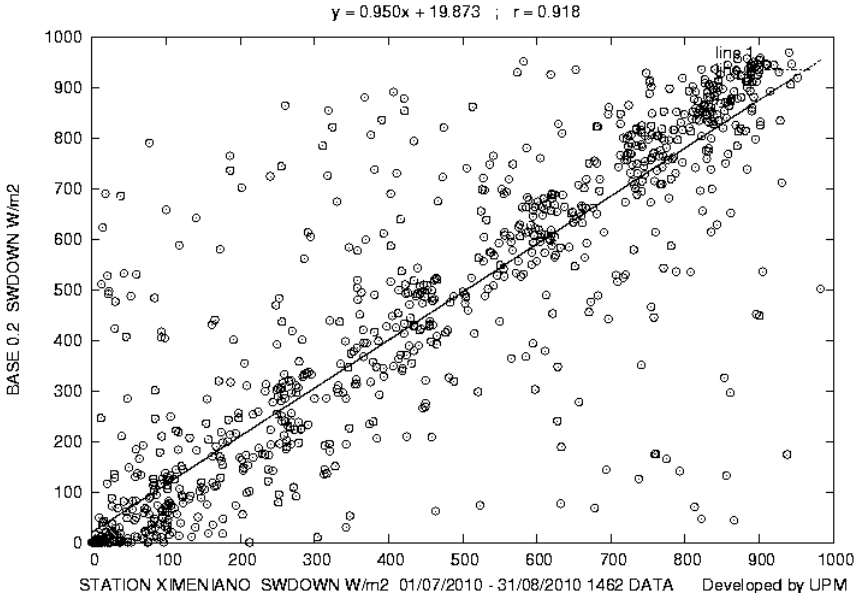

Figure 20: Lineal regression between WRF/UCM and Ximeniano measurement (15 minutes average), Short wave radiation¸ and 01/07/2010 – 31/08/2010, 0.2 km resolutions (bottom)

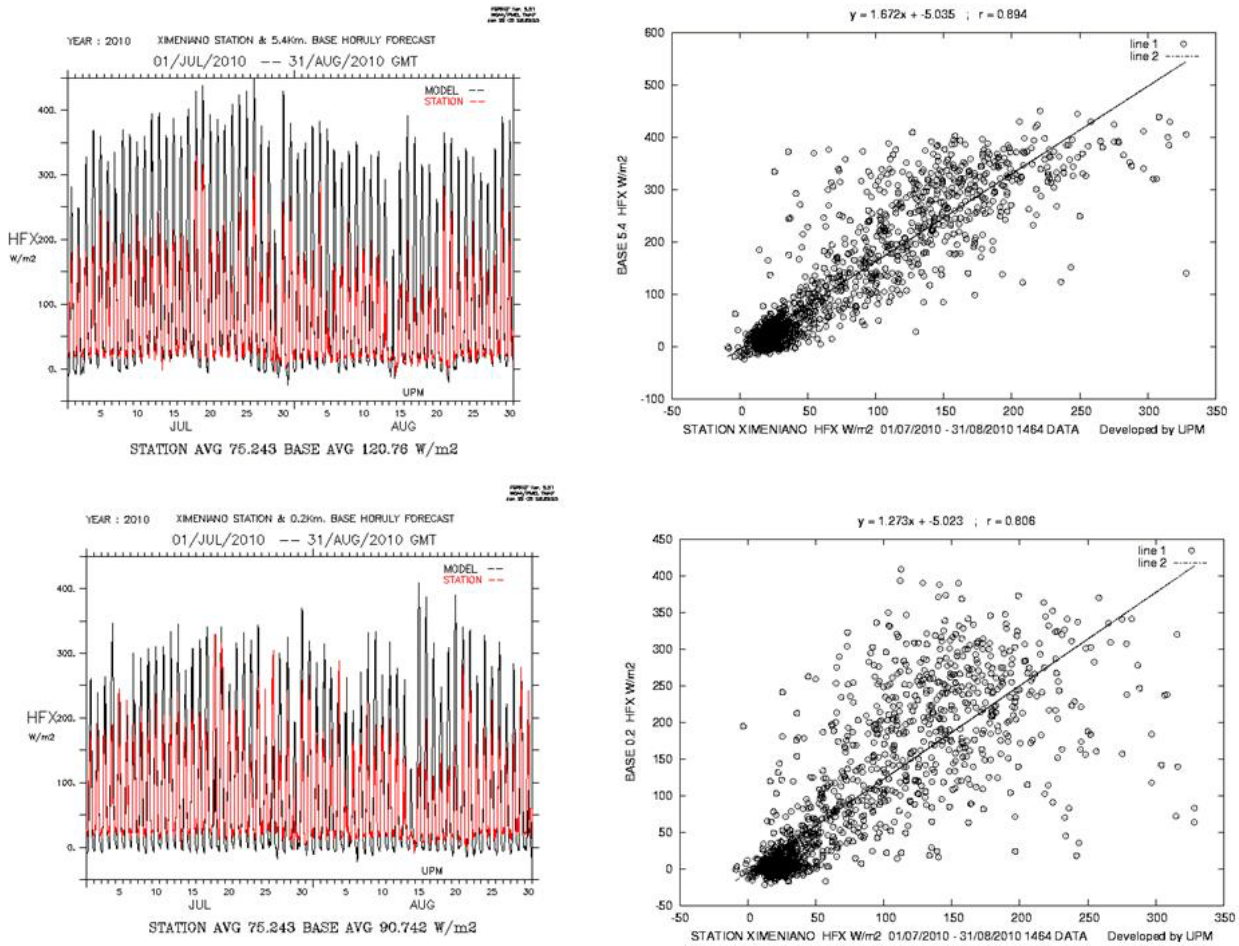

Figure 21: Time series comparison (left) and lineal regression (right) between WRF/UCM and Ximeniano measurement, Sensible Heat flux, 01/07/2010 – 31/08/2010, 5.4km (top) and 0.2 km resolution (bottom)

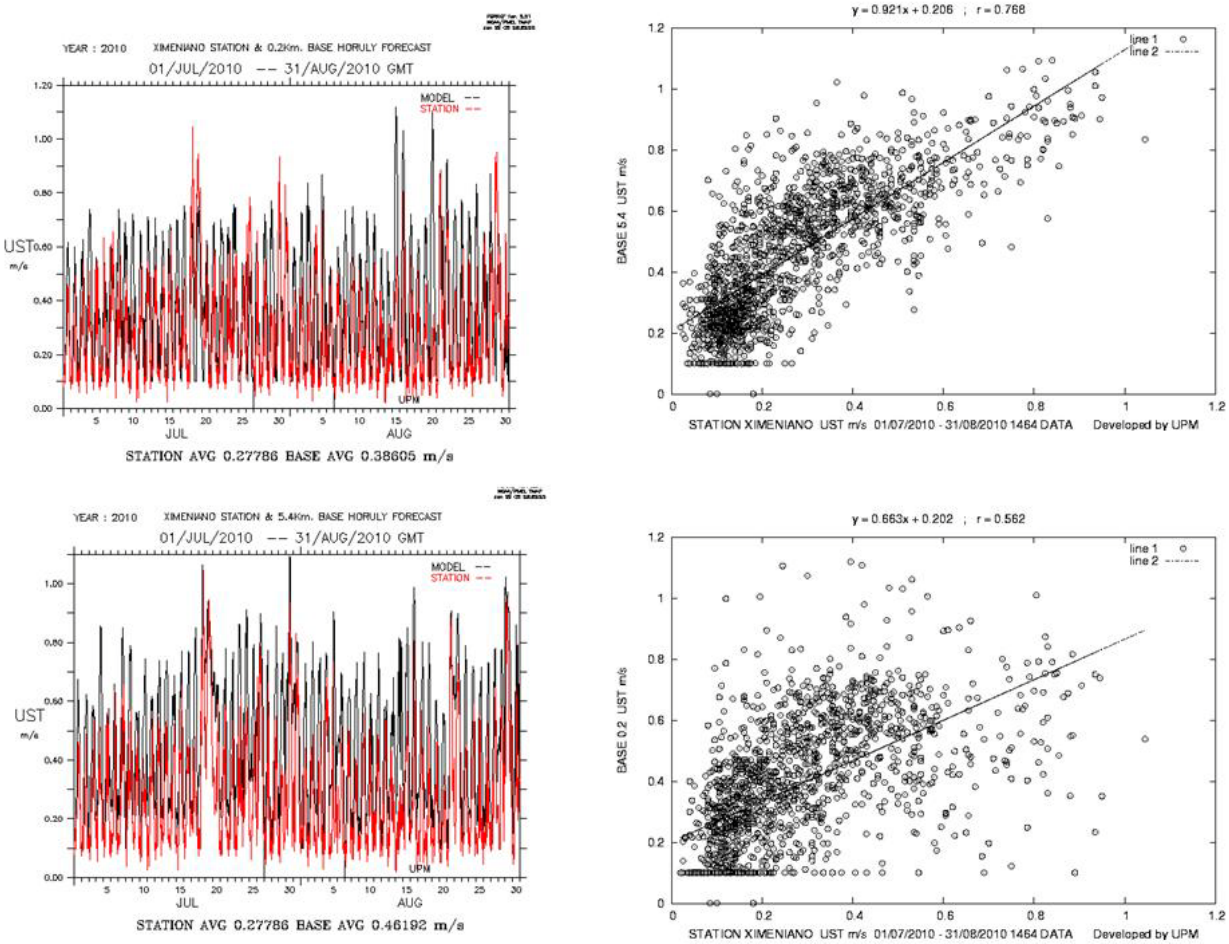

Figure 22: Time series comparison (left) and lineal regression (right) between WRF/UCM and Ximeniano measurement, Friction Velocity, 01/07/2010 – 31/08/2010, 5.4km (top) and 0.2 km resolution (bottom)

5.4 KM 01/07/2010 – 31/08/2010	WSPD	TEMP	SWDOWN	HFX	UST
Observed mean	1.60	298.43	268.79	75.24	0.28
Calculated mean/Observed mean	1.66	1.00	1.11	1.60	1.66
Observed STD	0.85	4.61	314.26	68.14	0.18
Calculated STD/Observed STD	2.14	0.83	1.10	1.87	1.20
Bias	1.05	-0.34	30.00	45.52	0.18
Absolute Bias	1.33	1.36	63.84	56.83	0.19
R2	0.25	0.87	0.88	0.80	0.59
RMSE	1.88	1.77	125.47	86.25	0.23
RMSE/Observed Mean	1.17	0.01	0.47	1.15	0.83
PERCENTAGE within +/- 50	45.70	100.00	79.10	38.52	34.29

Table 4: Statistical parameters between WRF/UCM and Ximeniano measurement, 01/10/2010 – 31/07/2010,5.4 km resolution model domain.

0.2 KM 01/07/2010 – 31/08/2010	WSPD	TEMP	SWDOWN	HFX	UST
Observed mean	1.60	298.43	268.79	75.24	0.28
Calculated mean/Observed mean	1.64	1.00	1.02	1.21	1.39
Observed STD	0.85	4.61	314.26	68.14	0.18
Calculated STD/Observed STD	1.59	0.87	1.05	1.58	1.18
Bias	1.02	-0.52	6.07	15.50	0.11
Absolute Bias	1.32	1.62	66.96	46.09	0.17
R2	0.10	0.82	0.84	0.65	0.32
RMSE	1.69	2.01	130.73	68.20	0.22
RMSE/Observed Mean	1.05	0.01	0.49	0.91	0.78
PERCENTAGE within +/- 50	38.73	100.00	77.73	35.72	48.02

Table 5: Statistical parameters between WRF/UCM and Ximeniano measurement, 01/10/2010 – 31/07/2010,0.2 km resolution model domain.

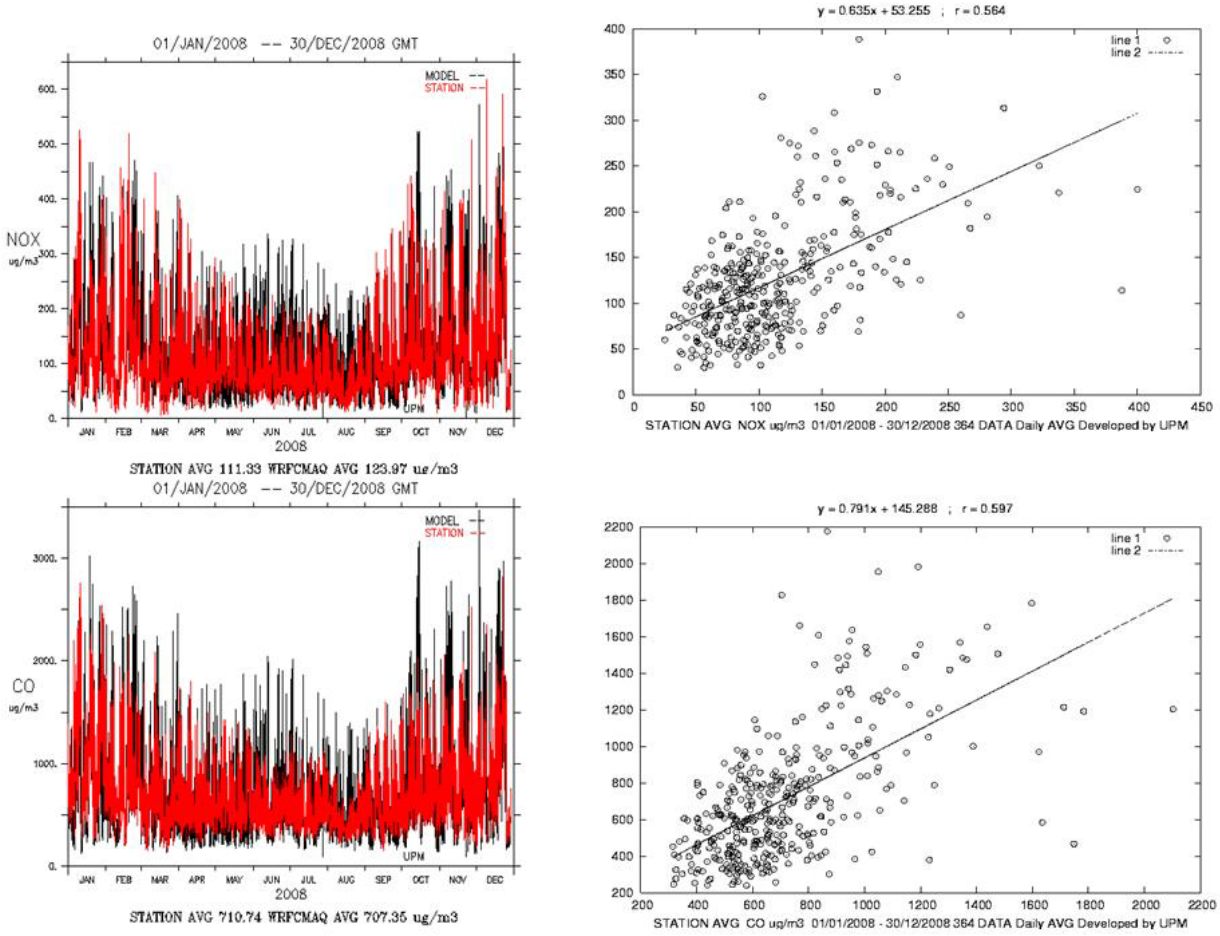

Figure 23 : Time series comparison (left) and lineal regression (right) between WRF/UCM-EMIMO-CMAQ and Average air pollution stations, 01/01/2008 – 31/12/2008, 0.2km. NOx (top) and CO (bottom)

01/01/2008 – 31/12/2008 AVG at 0.2 km	SO2	NOX	CO
Observed mean	1.44	111.33	710.74
Calculated mean/Observed mean	2.04	1.11	1.00
Observed STD	0.91	76.71	362.49
Calculated STD/Observed STD	2.68	1.13	1.34
Bias	1.50	12.69	-2.87
Absolute Bias	1.94	65.50	337.68
R2	0.02	0.17	0.19
RMSE	2.88	89.74	463.52
RMSE/Observed Mean	2.00	0.81	0.65
PERCENTAGE within +/- 50	35.71	50.76	63.28

Table 6: Statistical parameters between WRF/UCM-EMIMO-CMAQ and Average air pollution stations, 01/01/2008 – 31/12/2008,0.2 km resolution model domain.

3.3.5 London

Physical meteorology data is collected at KSK (King´s Strand King´s) located at 0.1161W 51.51146N. The data are available every 15 minutes. The data used are: winds, air temperature, pressure, short and long wave radiation.

The common periods between measurements and modelled data are 01/10/2008 – 31/12/2008 and 01/07/2010- 30/09/2010Additional air temperature measurements from Marylebone and Martins from London air quality stations networks for full 2008 year.

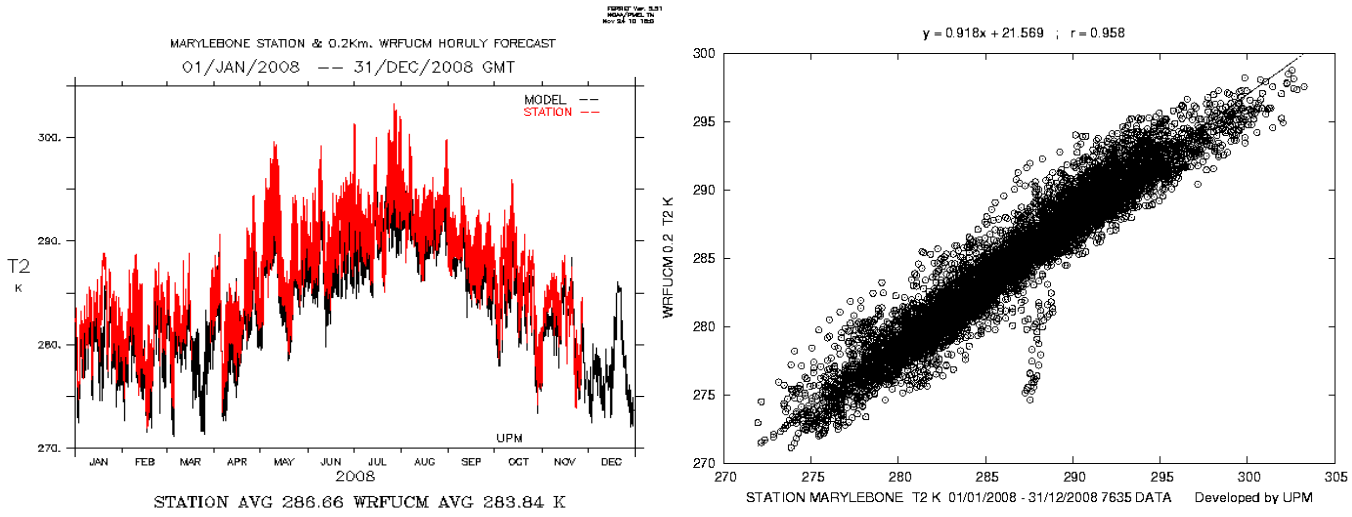

Figure 24: Time series comparison (left) and lineal regression (right) between WRF/UCM and Marylebone measurement, Air temperature, Full year2008, 0.2 km resolution model domain

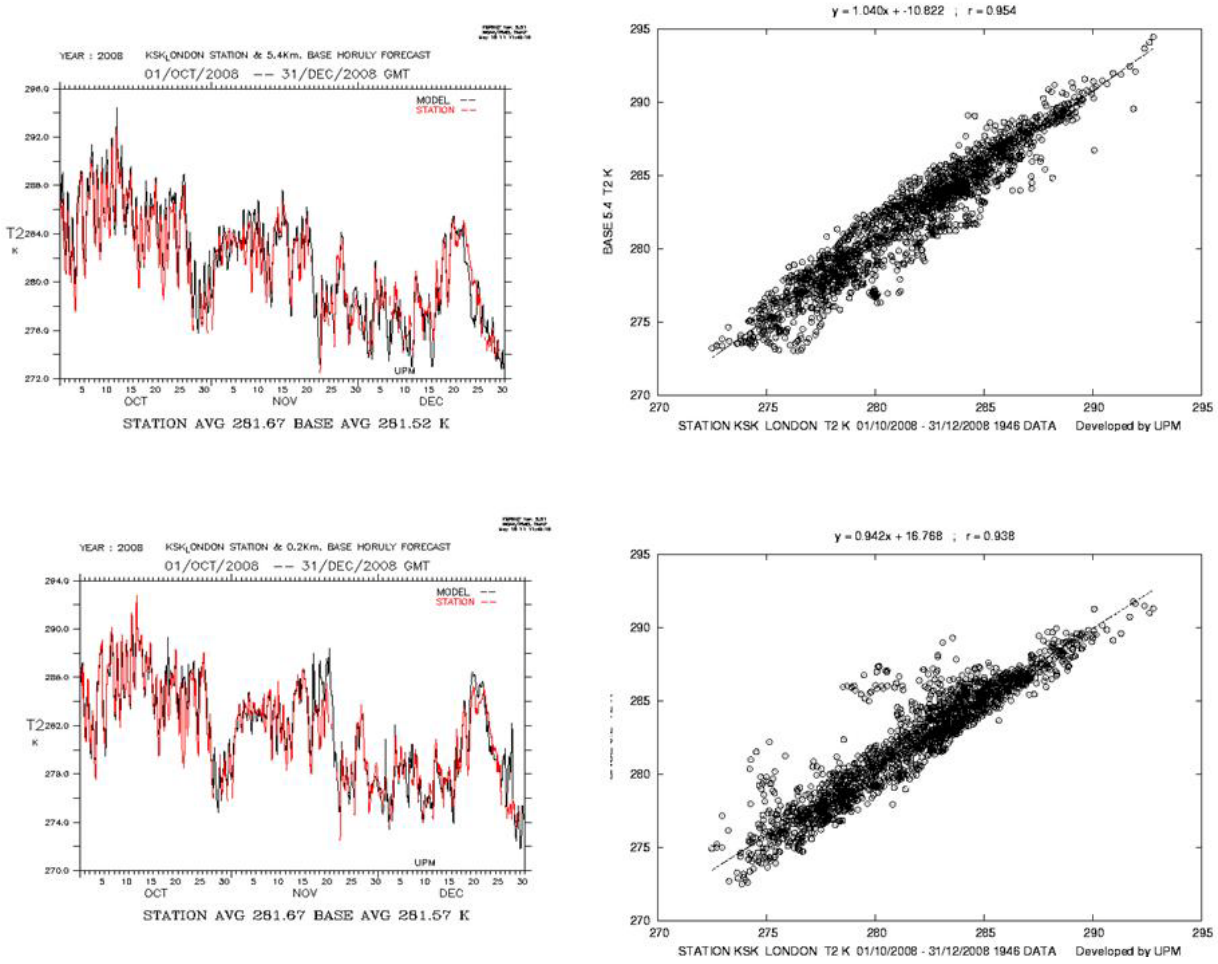

Figure 25: Time series comparison (left) and lineal regression (right) between WRF/UCM and KSK London measurement, Air temperature, 01/10/2008 – 31/12/2008, 5.4km (top) and 0.2 km resolution (bottom)

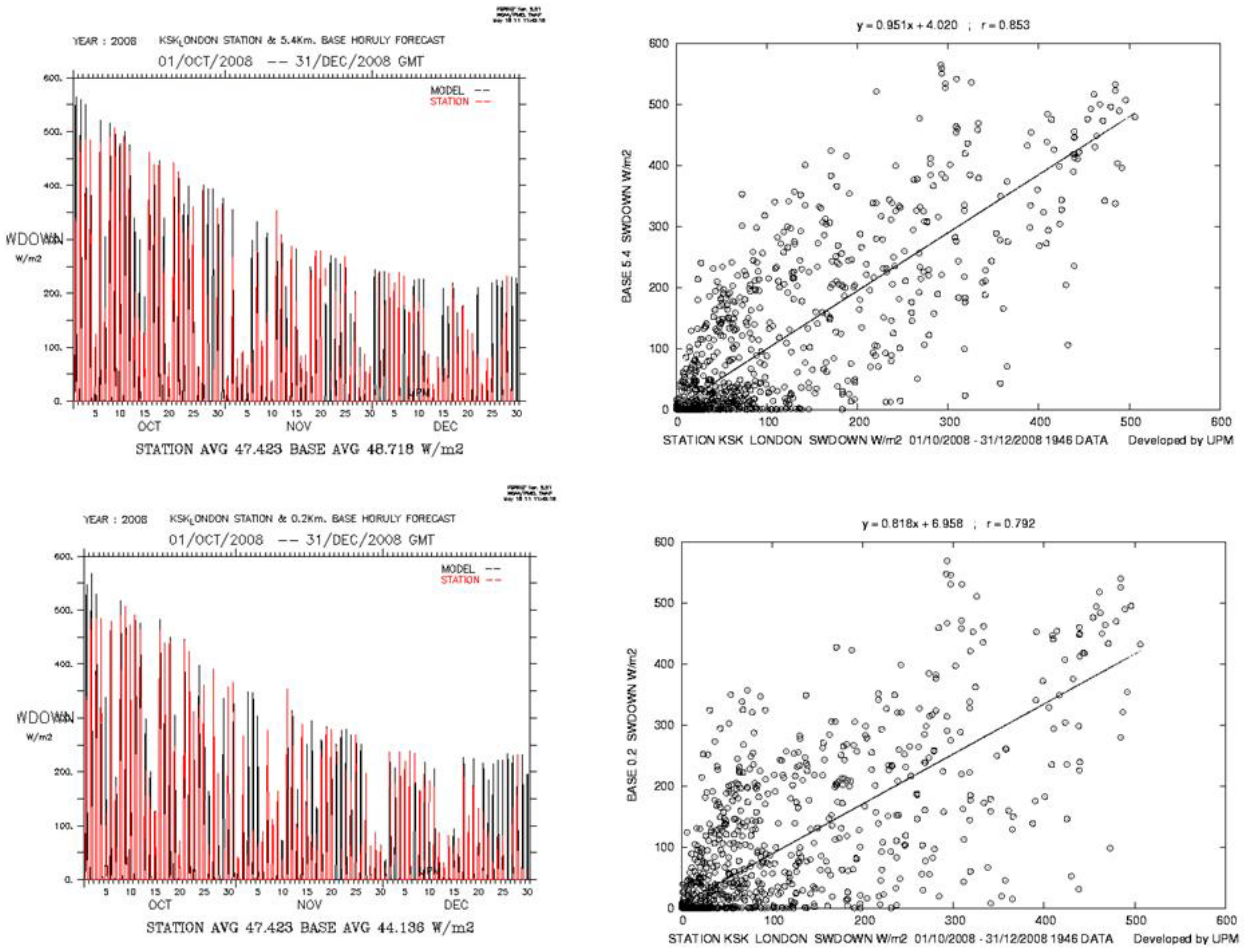

Figure 26: Time series comparison (left) and lineal regression (right) between WRF/UCM and KSK London measurement, Short wave radiation, 01/10/2008 – 31/12/2008, 5.4km (top) and 0.2 km resolution (bottom)

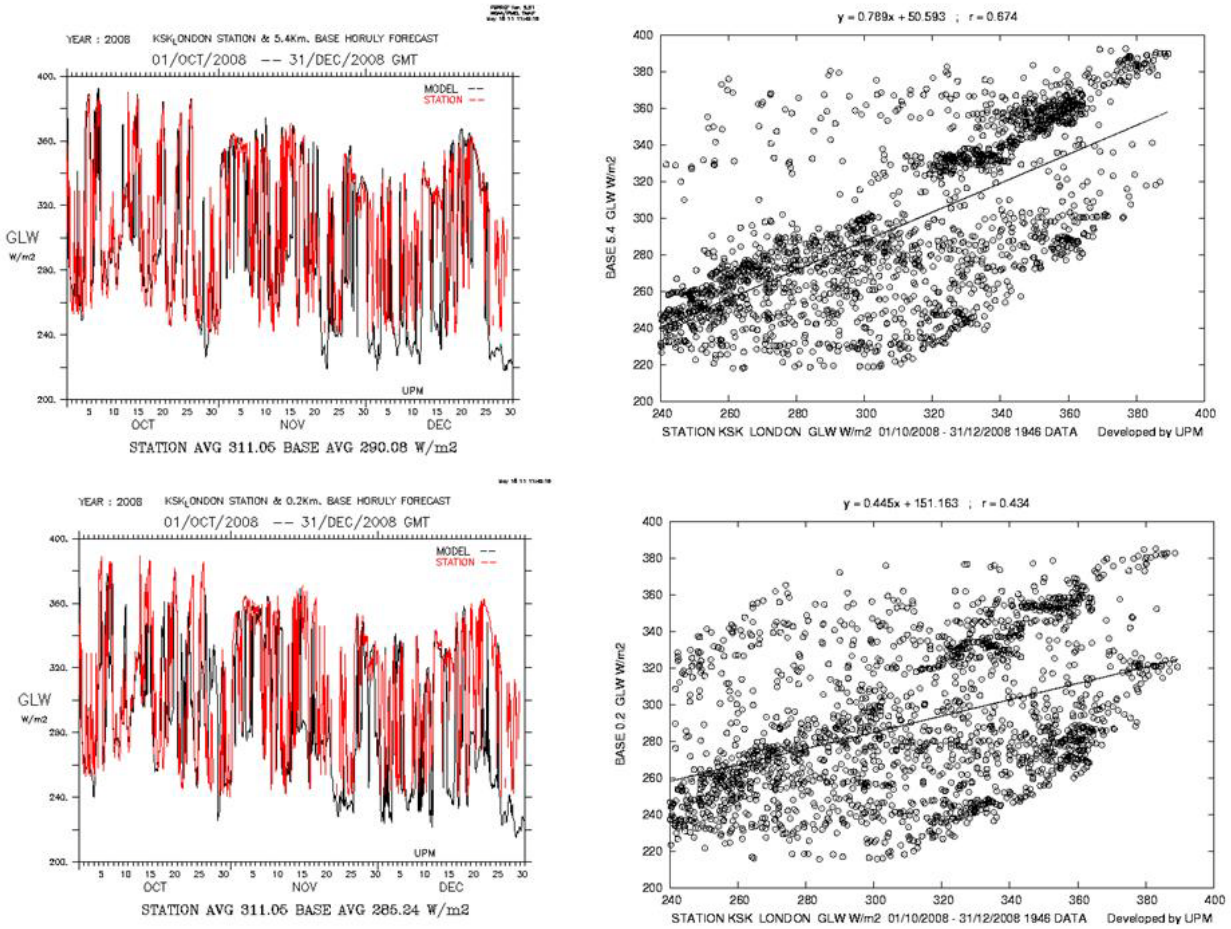

Figure 27: Time series comparison (left) and lineal regression (right) between WRF/UCM and KSK London measurement, Long wave radiation, 01/10/2008 – 31/12/2008, 5.4km (top) and 0.2 km resolution (bottom)

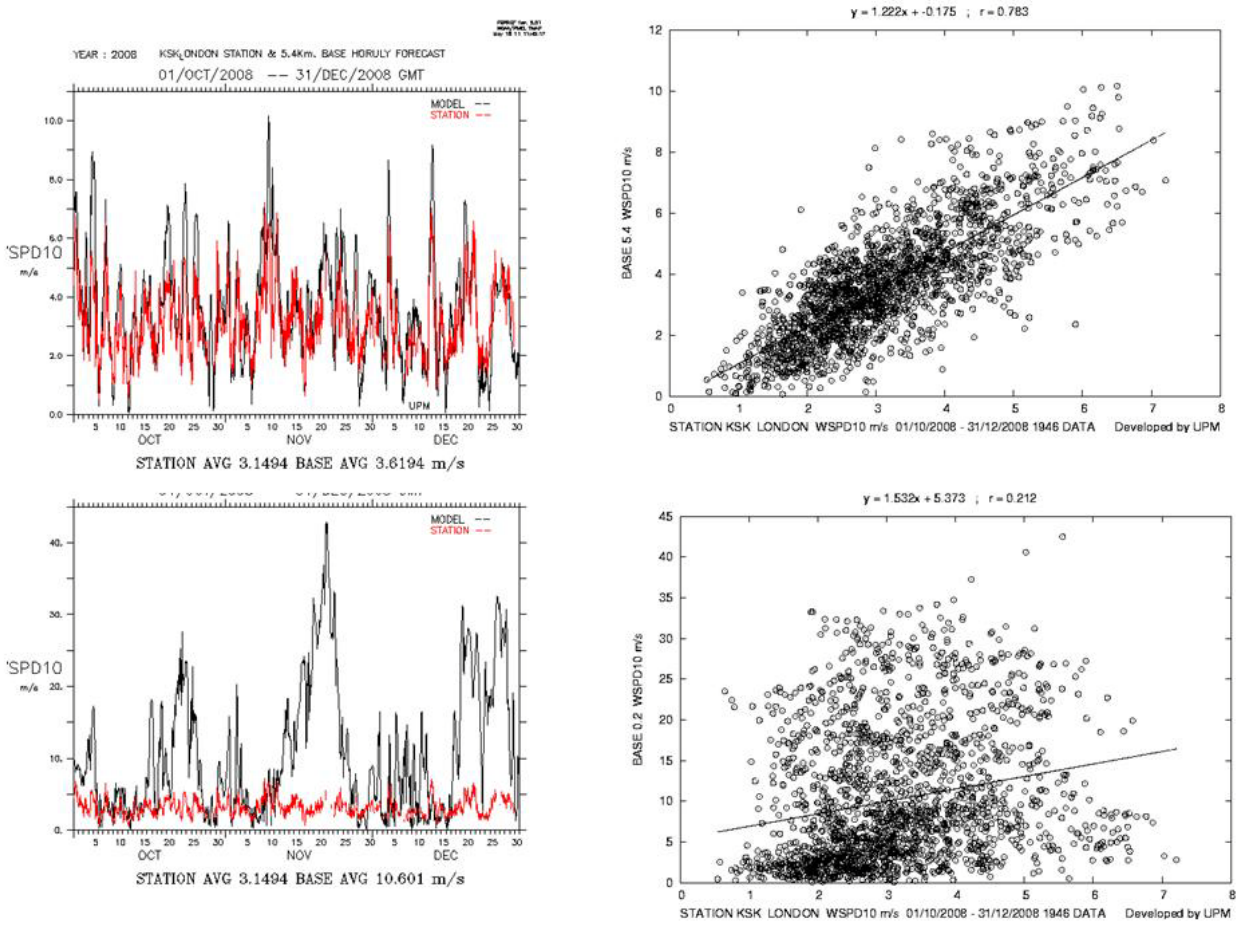

Figure 28: Time series comparison (left) and lineal regression (right) between WRF/UCM and KSK London measurement, Wind speed, 01/10/2008 – 31/12/2008, 5.4km (top) and 0.2 km resolution (bottom)

5.4 km 01/10/2008 – 31/12/2008	PSFC	WSPD10	SWDOWN	GLW	T2
Observed mean	100912.93	3.15	47.42	311.05	281.67
Calculated mean/Observed mean	1.00	1.17	1.04	0.95	1.00
Observed STD	1201.02	1.16	96.55	38.99	3.78
Calculated STD/Observed STD	0.98	1.56	1.12	1.17	1.09
Bias	240.43	0.52	1.70	-14.99	0.41
Absolute Bias	240.43	0.97	26.37	26.28	1.05
R2	1.00	0.61	0.73	0.45	0.91
RMSE	247.26	1.26	56.42	37.80	1.31
RMSE/Observed Mean	0.00	0.40	1.19	0.12	0.00
PERCENTAGE within +/- 50	100.00	78.67	70.55	100.00	100.00

Table 7: Statistical parameters between WRF/UCM and KSK London measurement, 01/10/2008 – 31/12/2008,5.4 km resolution model domain.

0.2 km 01/10/2008 – 31/12/2008	PSFC	WSPD10	SWDOWN	GLW	T2
Observed mean	100912.93	3.15	47.42	311.05	281.67
Calculated mean/Observed mean	1.00	3.24	0.96	0.93	1.00
Observed STD	1201.02	1.16	96.55	38.99	3.78
Calculated STD/Observed STD	0.99	7.22	1.03	1.03	1.00
Bias	-331.67	7.05	-1.68	-21.40	0.39
Absolute Bias	346.81	7.52	28.64	35.83	0.93
R2	0.98	0.04	0.63	0.19	0.88
RMSE	364.92	10.81	63.43	47.17	1.39
RMSE/Observed Mean	0.00	3.43	1.34	0.15	0.00
PERCENTAGE within +/- 50	100.00	25.64	70.81	100.00	100.00

Table 8: Statistical parameters between WRF/UCM and KSK London measurement, 01/10/2008 – 31/12/2008,5.4 km resolution model domain.

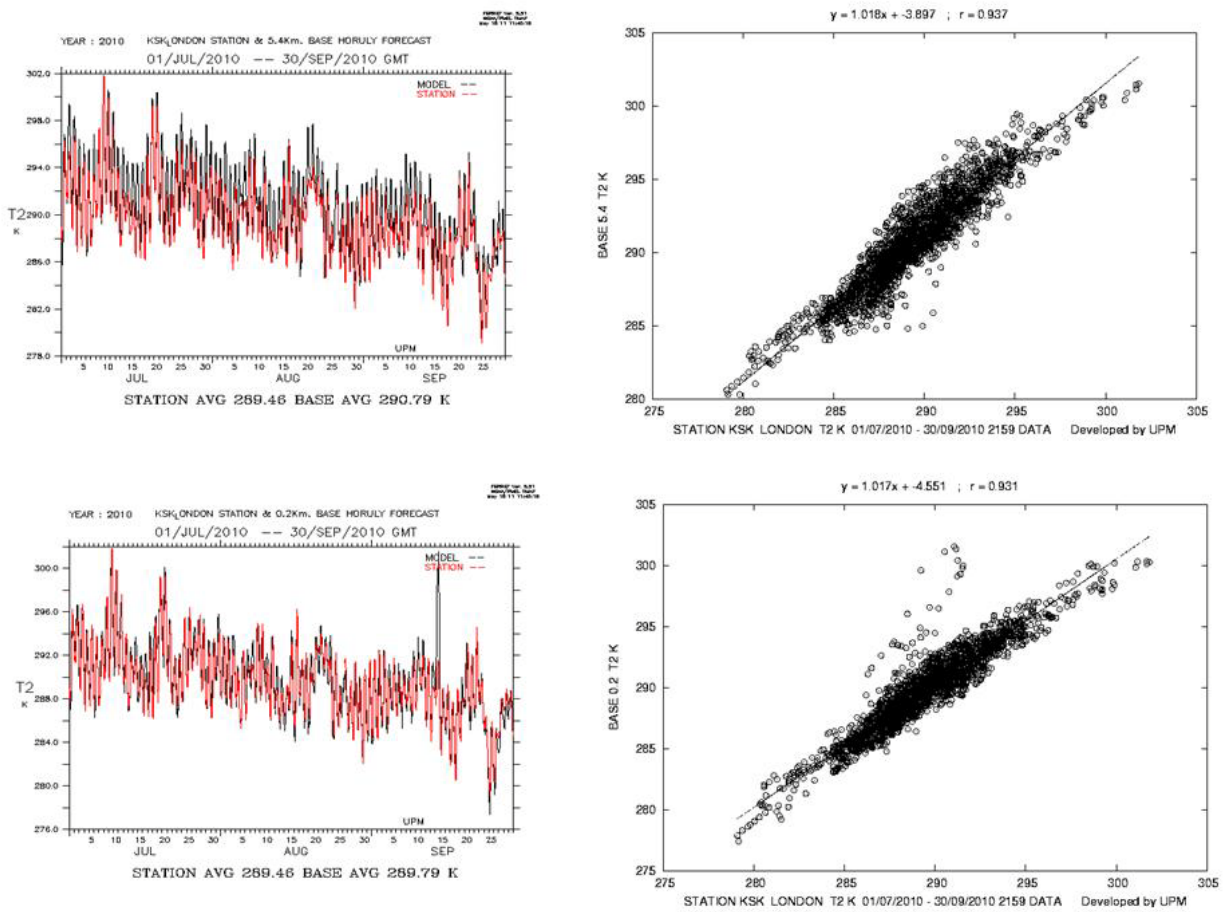

Figure 29: Time series comparison (left) and lineal regression (right) between WRF/UCM and KSK London measurement, Air temperature, 01/07/2010 – 30/09/2010, 5.4km (top) and 0.2 km resolution (bottom)

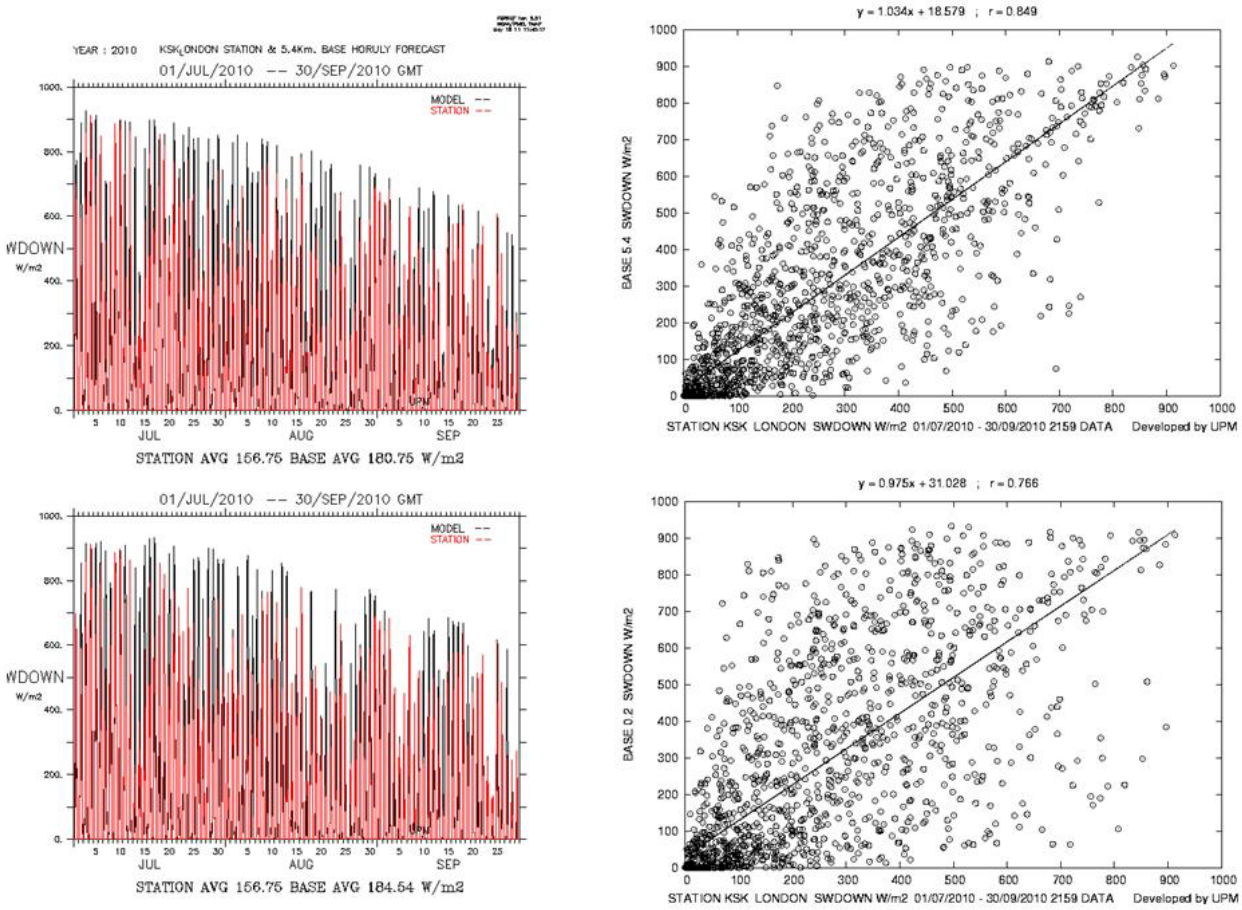

Figure 30: Time series comparison (left) and lineal regression (right) between WRF/UCM and KSK London measurement, Short wave radiation, 01/07/2010 – 30/09/2010, 5.4km (top) and 0.2 km resolution (bottom)

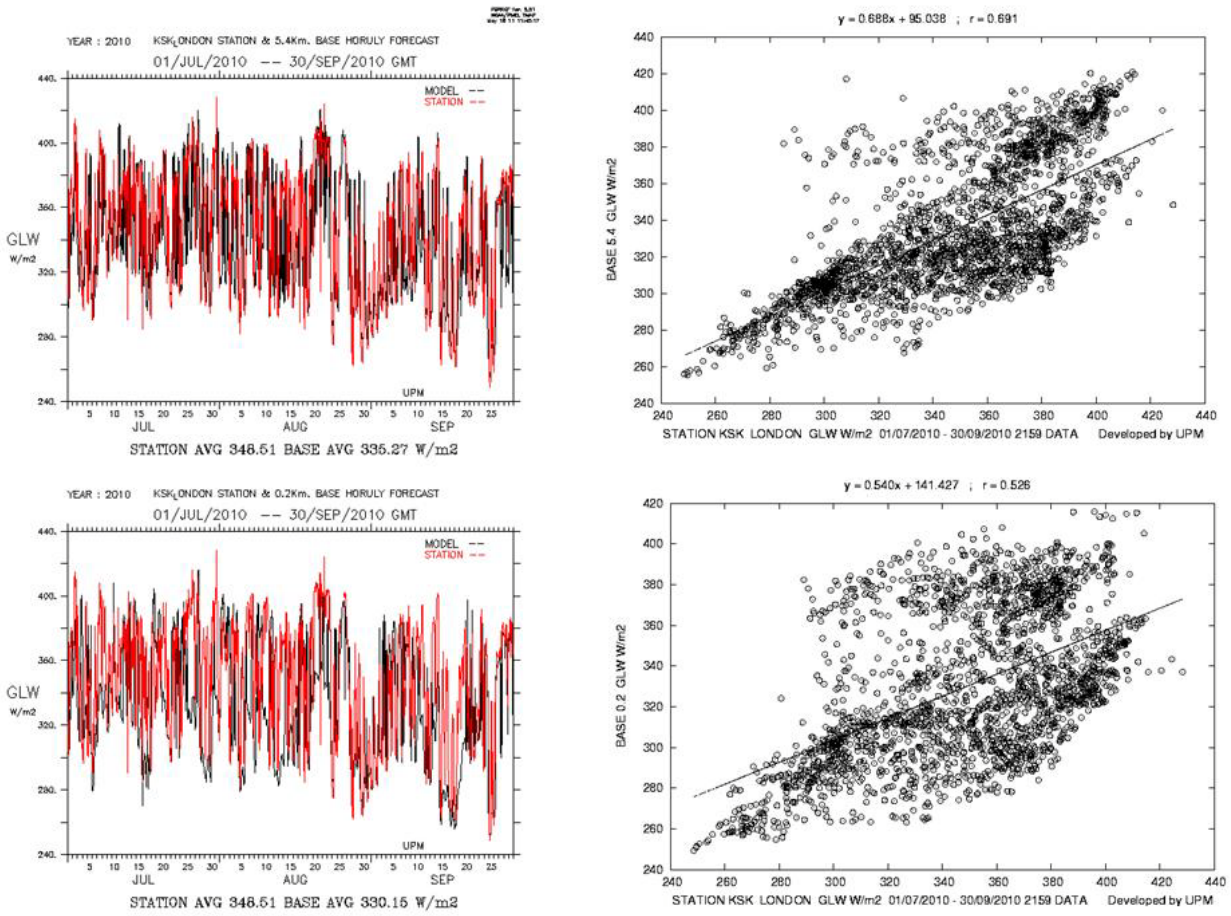

Figure 31: Time series comparison (left) and lineal regression (right) between WRF/UCM and KSK London measurement, Long wave radiation, 01/07/2010 – 30/09/2010, 5.4km (top) and 0.2 km resolution (bottom)

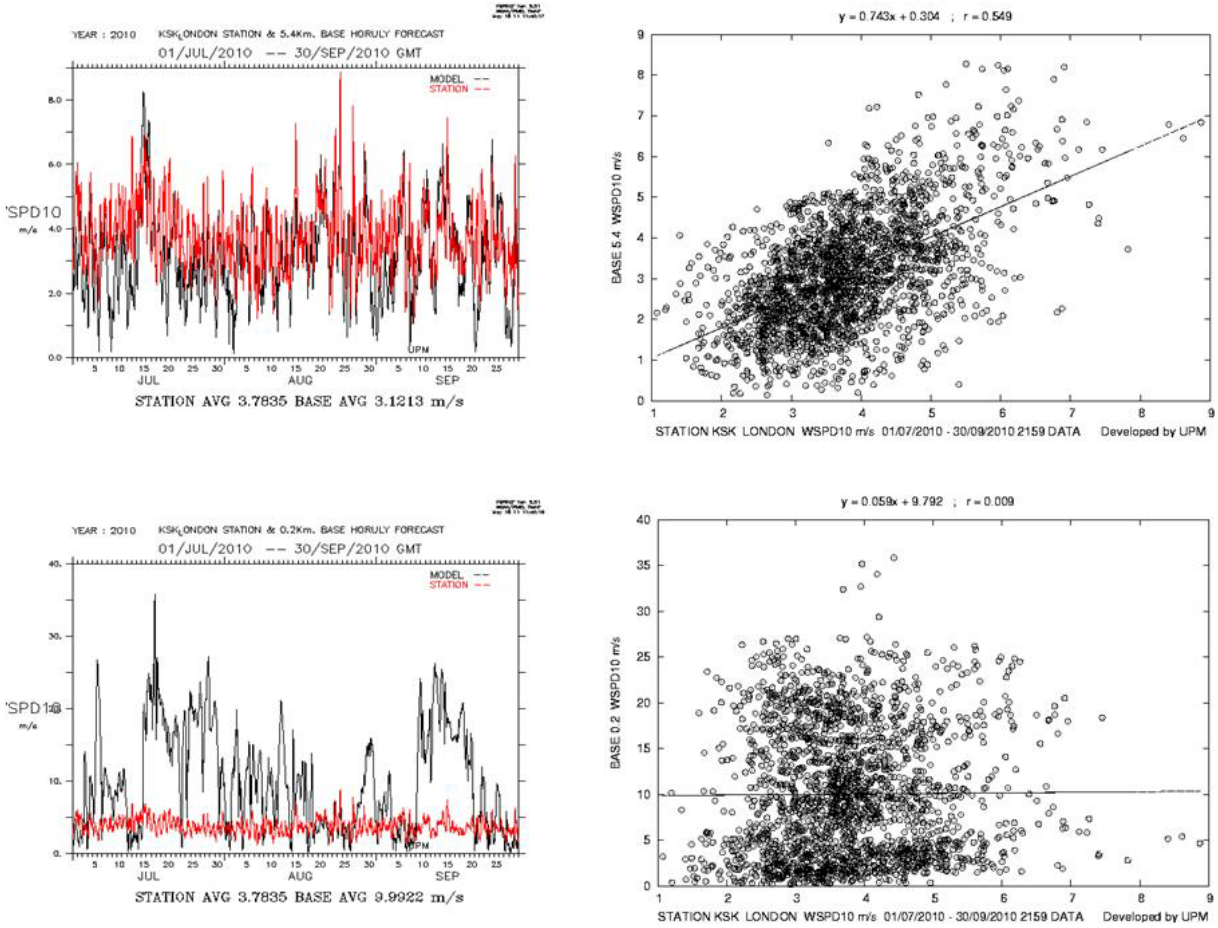

Figure 32: Time series comparison (left) and lineal regression (right) between WRF/UCM and KSK London measurement, Wind speed 01/07/2010 – 30/09/2010, 5.4km (top) and 0.2 km resolution (bottom)

5.4 km. 01/07/2010 – 30/09/2010	PSFC	WSPD10	SWDOWN	GLW	T2
Observed mean	100950.59	3.78	156.75	348.51	289.46
Calculated mean/Observed mean	1.00	0.82	1.15	0.96	1.00
Observed STD	572.41	1.02	205.52	36.07	3.15
Calculated STD/Observed STD	0.99	1.35	1.22	1.00	1.09
Bias	234.08	-0.67	23.88	-13.81	1.33
Absolute Bias	234.08	1.08	74.47	23.93	1.47
R2	1.00	0.30	0.72	0.48	0.88
RMSE	237.23	1.36	134.68	31.49	1.79
RMSE/Observed Mean	0.00	0.36	0.86	0.09	0.01
PERCENTAGE within +/- 50	100.00	82.49	64.47	100.00	100.00

Table 9: Statistical parameters between WRF/UCM and KSK London measurement, 01/07/2010 – 30/09/2010,5.4 km resolution model domain.

0.2 km 01/07/2010 – 30/09/2010	PSFC	WSPD10	SWDOWN	GLW	T2
Observed mean	100950.59	3.78	156.75	348.51	289.46
Calculated mean/Observed mean	1.00	2.65	1.17	0.95	1.00
Observed STD	572.41	1.02	205.52	36.07	3.15
Calculated STD/Observed STD	1.01	6.90	1.27	1.03	1.09
Bias	-299.31	6.23	27.14	-18.80	0.33
Absolute Bias	299.49	7.14	95.92	31.83	0.89
R2	0.97	0.00	0.59	0.28	0.87
RMSE	315.71	9.44	170.23	40.26	1.30
RMSE/Observed Mean	0.00	2.50	1.09	0.12	0.00
PERCENTAGE within +/- 50	100.00	23.95	59.19	100.00	100.00

Table 10: Statistical parameters between WRF/UCM and KSK London measurement, 01/07/2010 – 30/09/2010,0.2 km resolution model domain.

3.4 WRF/UCM vs. WRF/ACASA.

An intercomparison exercise of two models: WRF/UCM and WRF/ACASA has been developed. Both models have been run over the same domains in Firenze and Helsinki and with the same boundary and initial conditions supplied by UPM from the Global Forecast System (GFS). WRF/UCM has been run by UPM and WRF/ACASA has been run by the CMCC partner. Model description and implementation is available in the D4.1 and D4.2 documents. The common time period is the full year 2008.

We will show results of air temperature, sensible heat flux and latent heat flux, because they are the common variables for both models. Spatial and temporal differences have been calculated and finally in case of Firenze, both models have been compared with the Ximeniano station, throw lineal regressions (April 2008, common period between both model and measurements).

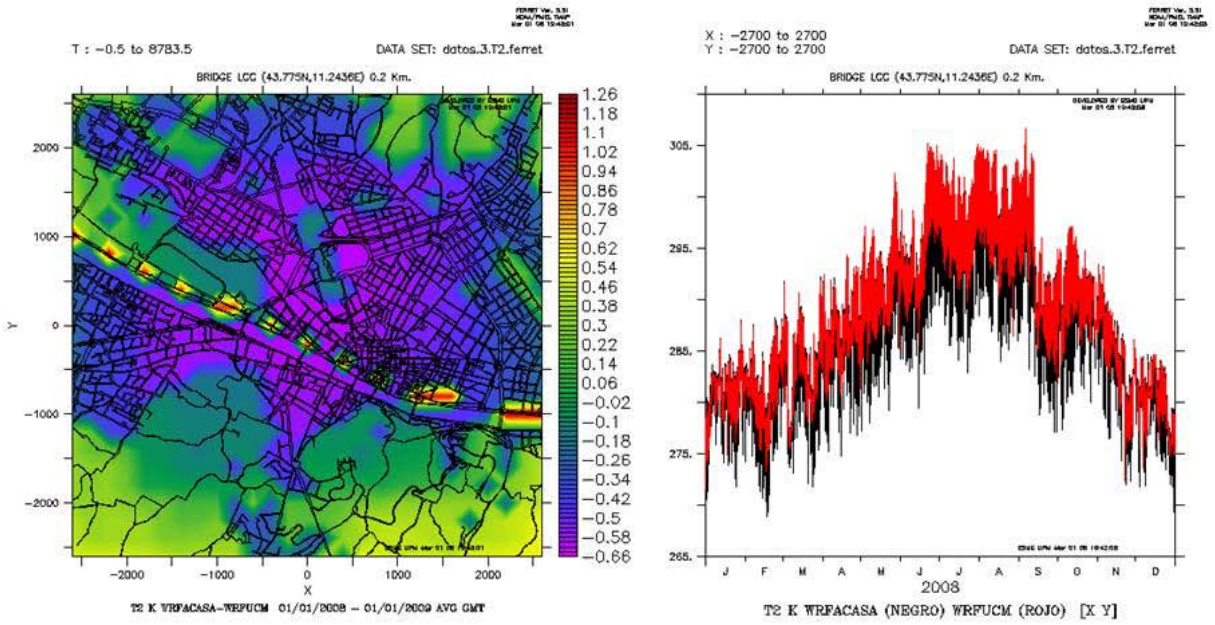

Figure 33: Air temperature, 2008 year, and 0.2 km domain resolution over Firenze, spatial differences (left): annual average WRFACASA -WRFUCM and temporal evolution (right): domain grid cells average WRFACASA (black) and WRFUCM (red).

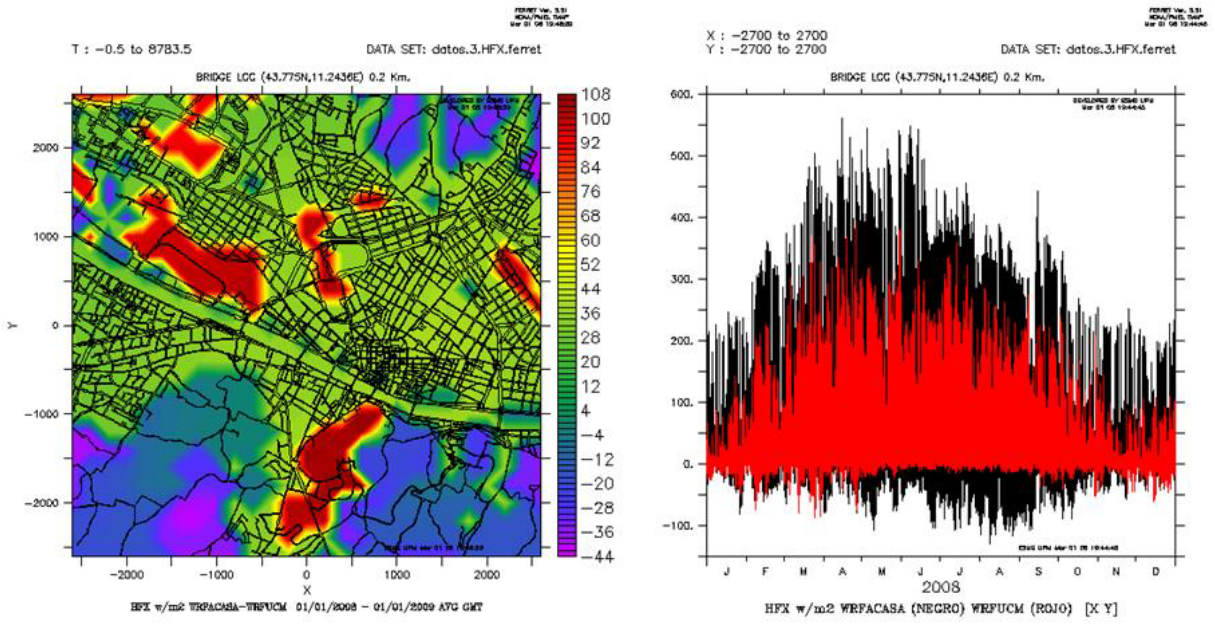

Figure 34: Sensible heat flux, 2008 year, 0.2 km domain resolution over Firenze, spatial differences (left) : annual average WRFACASA -WRFUCM and temporal evolution (right): domain grid cells average WRFACASA (black) and WRFUCM (red).

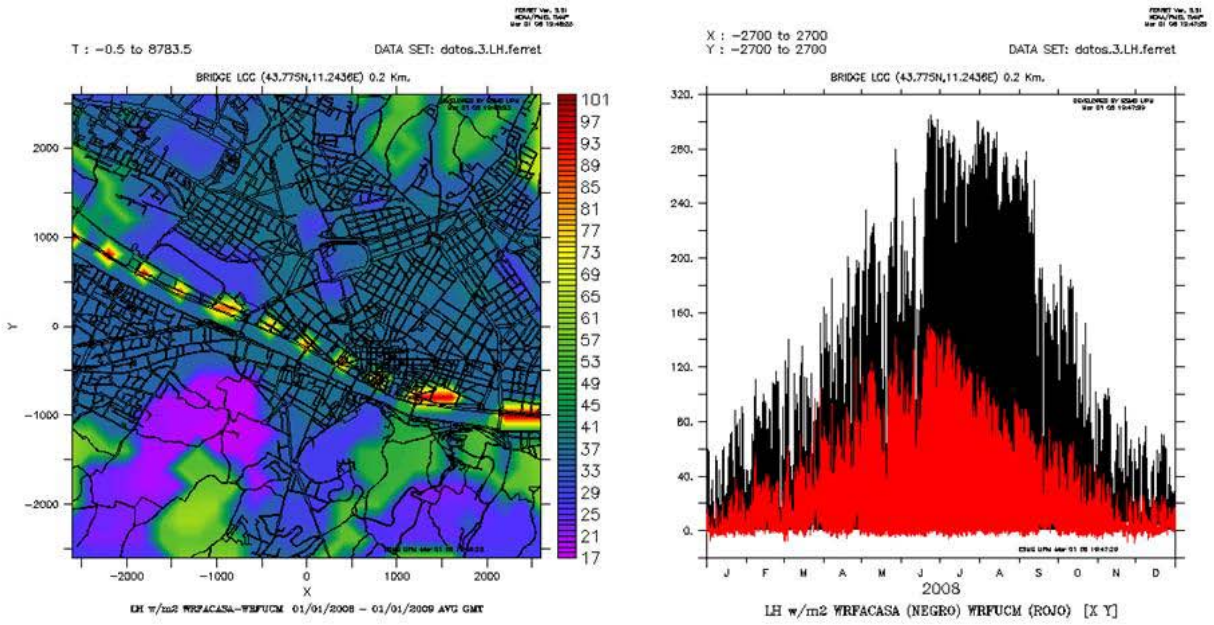

Figure 35: Latent heat flux, 2008 year, 0.2 km domain resolution over Firenze, spatial differences (left) : annual average WRFACASA -WRFUCM and temporal evolution (right): domain grid cells average WRFACASA (black) and WRFUCM (red).

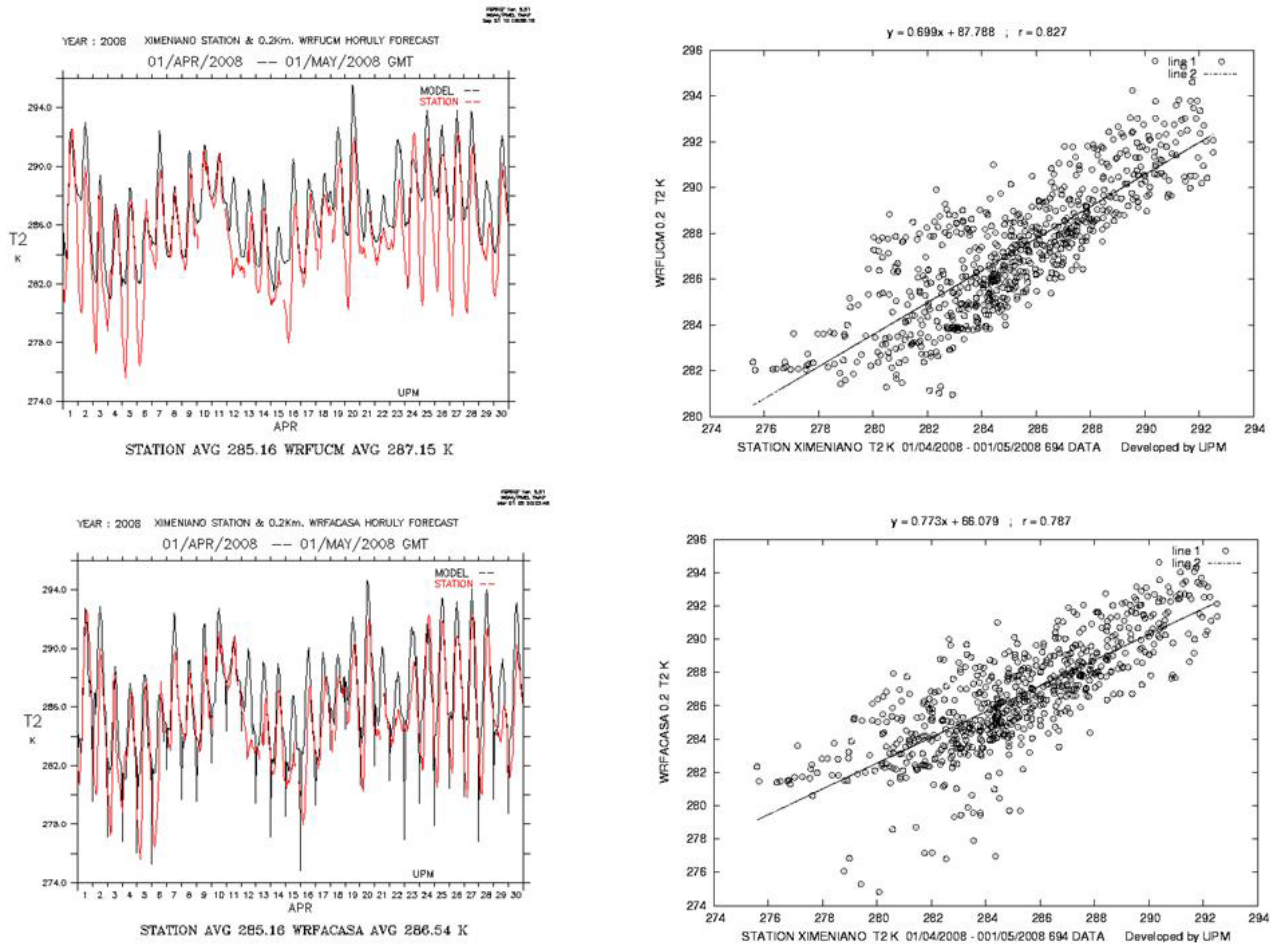

Figure 36: Time series comparison (left) and lineal regression (right) between WRF/UCM-Ximeniano (top) and WRF/ACASA-Ximeniano (bottom), Air temperature 01/04/2008 – 30/04/2008, 0.2km Firenze domain

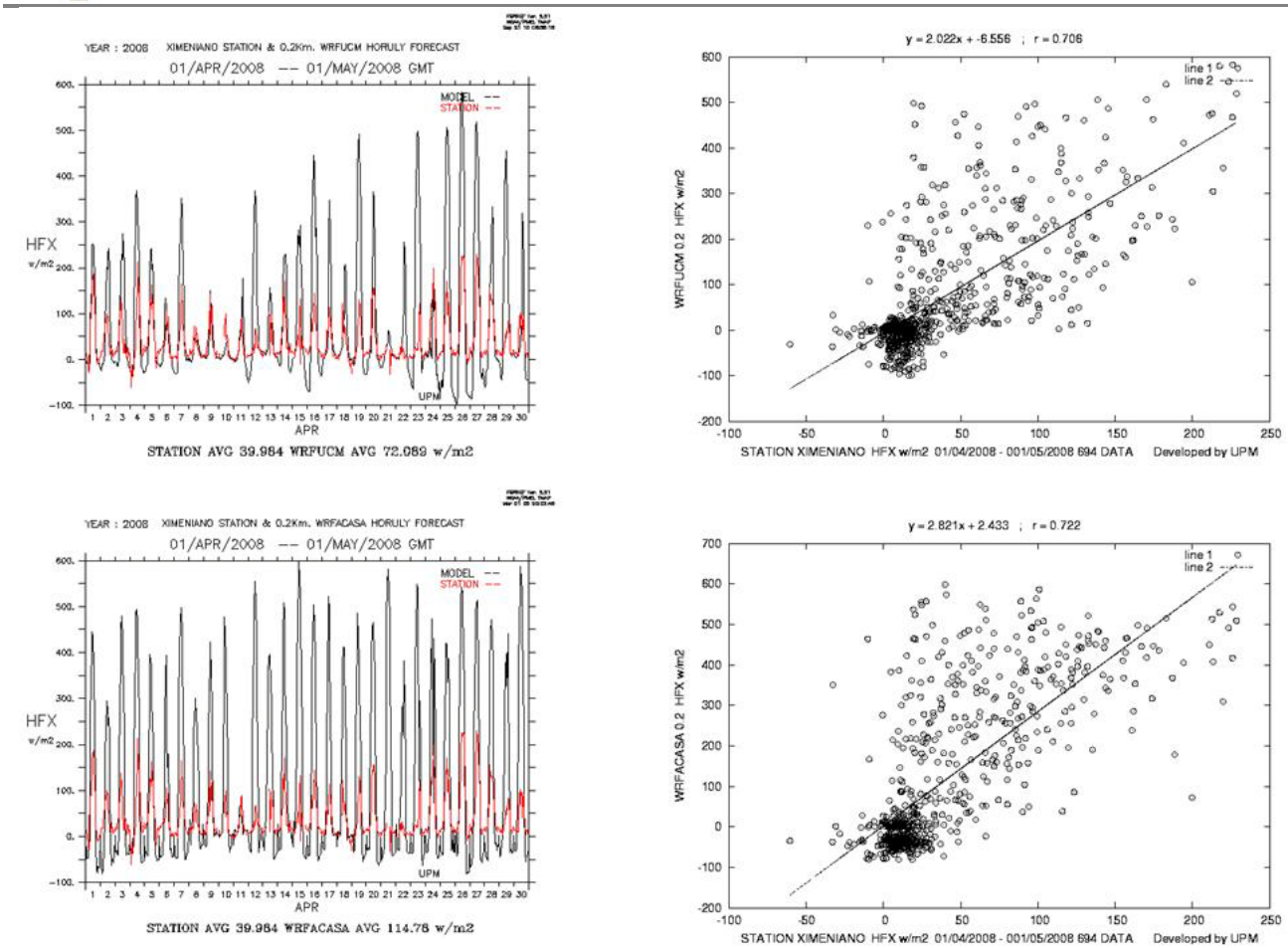

Figure 37: Time series comparison (left) and lineal regression (right) between WRF/UCM-Ximeniano (top) and WRF/ACASA-Ximeniano (bottom), Sensible Heat Flux 01/04/2008 – 30/04/2008, 0.2km Firenze domain

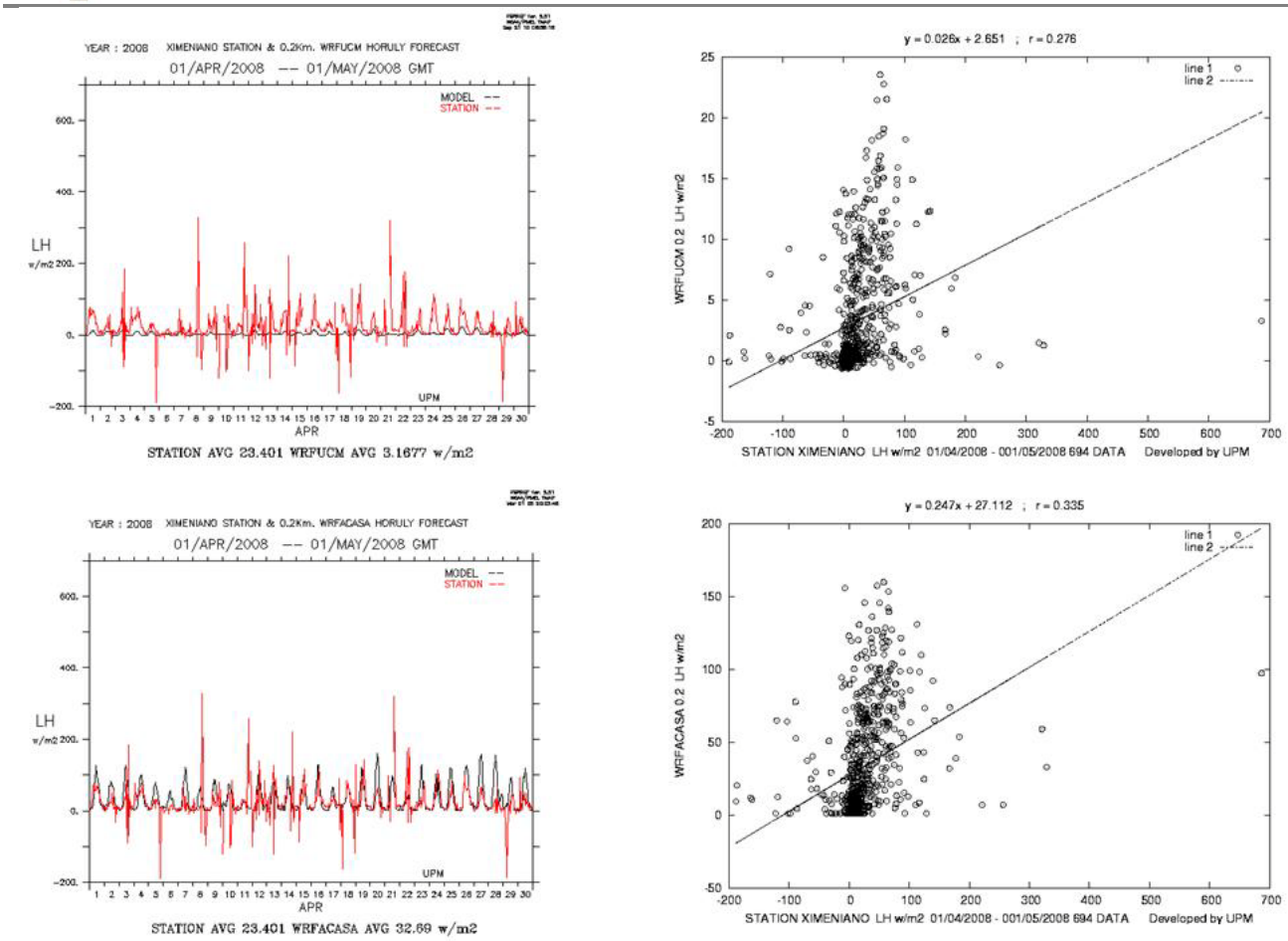

Figure 38: Time series comparison (left) and lineal regression (right) between WRF/UCM-Ximeniano (top) and WRF/ACASA-Ximeniano (bottom), Latent Heat Flux 01/04/2008 – 30/04/2008, 0.2km Firenze domain

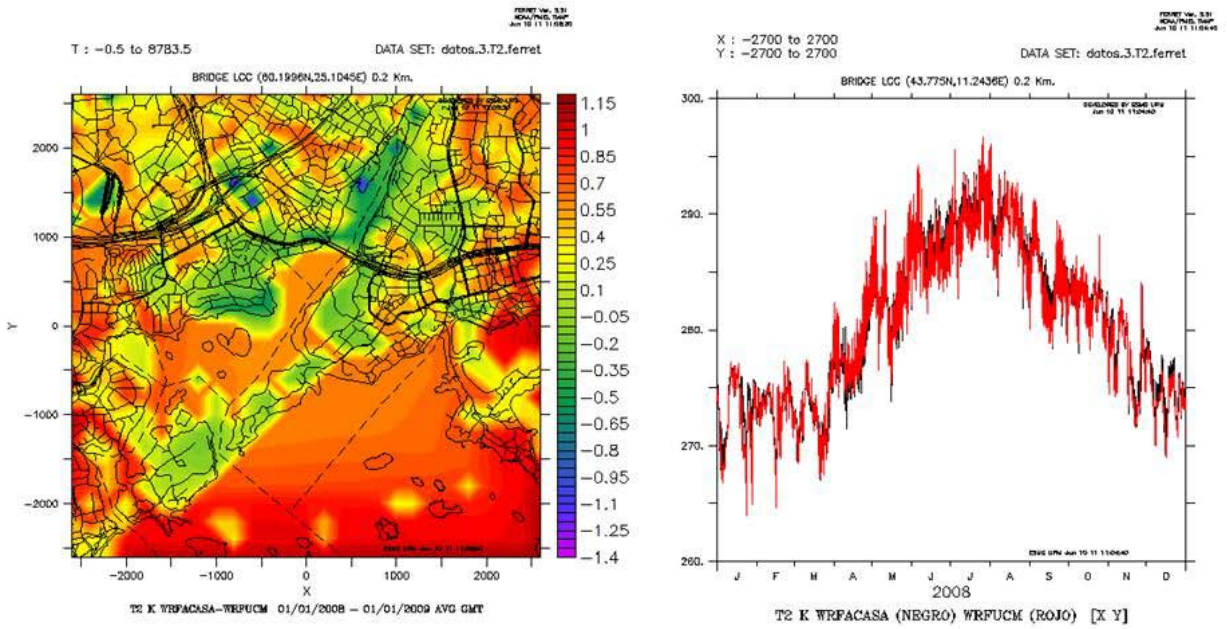

Figure 39: Air temperature, 2008 year, and 0.2 km domain resolution over Helsinki, spatial differences (left): annual average WRFACASA -WRFUCM and temporal evolution (right): domain grid cells average WRFACASA (black) and WRFUCM (red).

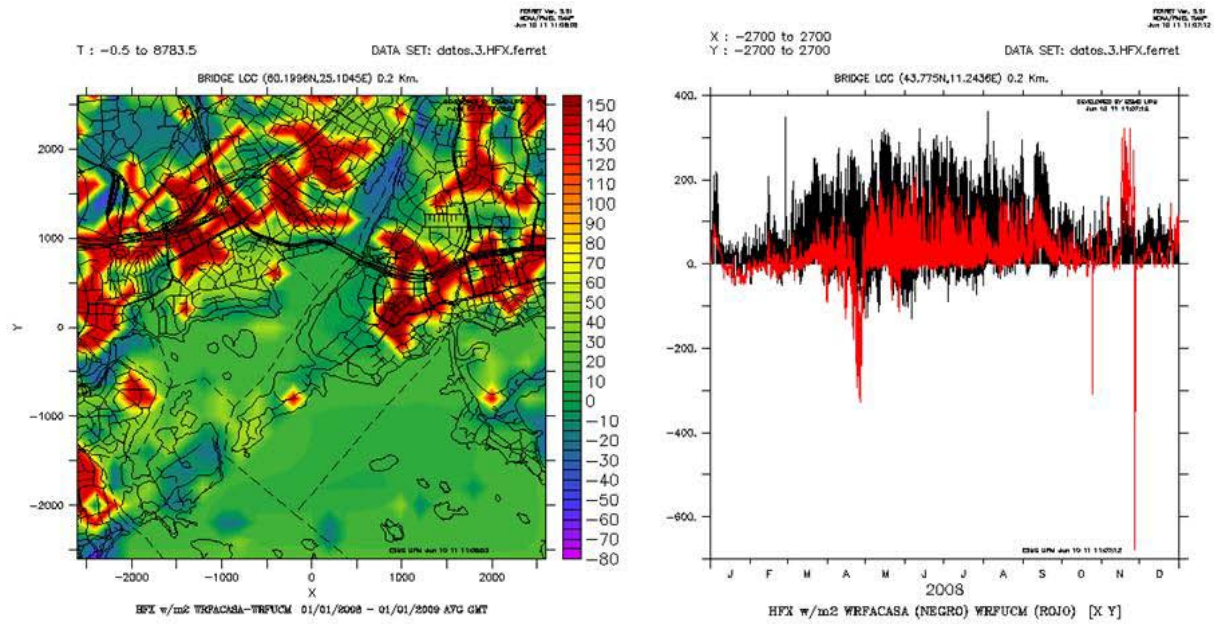

Figure 40: Sensible heat flux, 2008 year, 0.2 km domain resolution over Helsinki, spatial differences (left) : annual average WRFACASA -WRFUCM and temporal evolution (right): domain grid cells average WRFACASA (black) and WRFUCM (red).

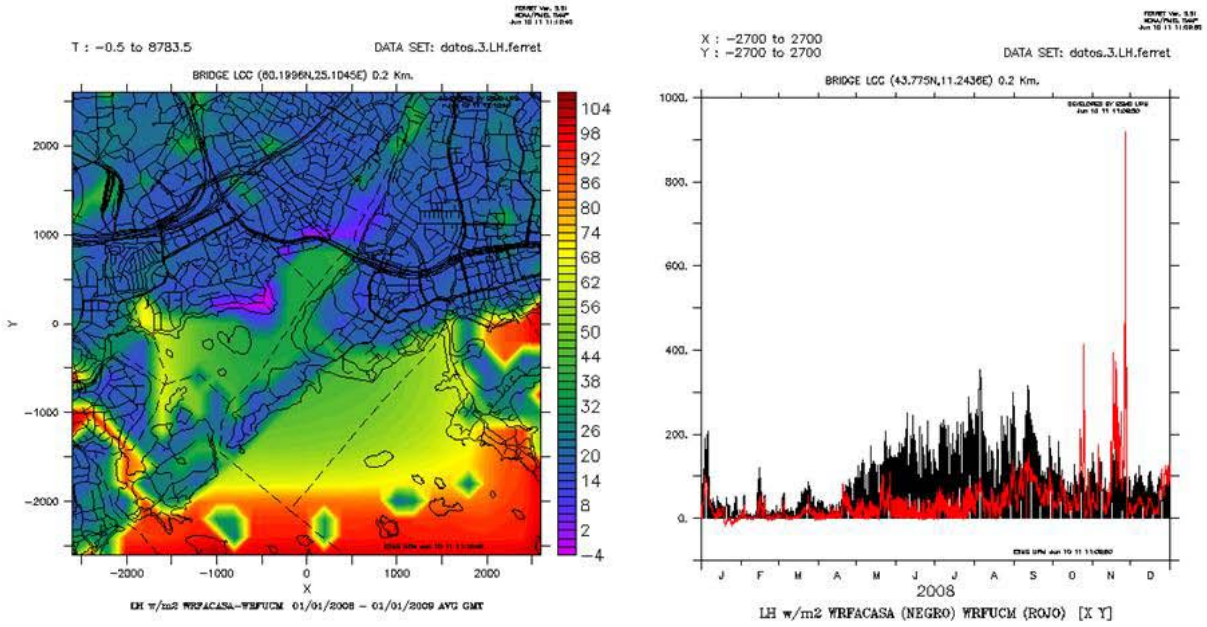

Figure 41: Latent heat flux, 2008 year, 0.2 km domain resolution over Helsinki, spatial differences (left) : annual average WRFACASA -WRFUCM and temporal evolution (right): domain grid cells average WRFACASA (black) and WRFUCM (red).

3.5 CONCLUSIONS

The comparison between observed and modelled results are excellent for several parameters such as temperature and heta fluxes. Wind speed comparisons are found to be poorer than for temperature and fluxes results. The limitations in computer time are the main cause for not having run the high spatial resolution runs (200 m) following the nesting rate approach as required for numerical and stability reasons (0.2 km, 0.6 km, 1.8 km, 5.4 km, 16.2 km, 48.6 km). The computer time required to fulfil these nesting cascade for several years, for five cities and for three different alternatives was out of the our supercomputer capabilities (Barcelona Supercomputer Center) as assigned for this EU project. An important controversy is actually in place for very high spatial resolution WRF runs (200 m, 600 m) and numerial issues are raised together with a substantial increase of vertical layers (higher than 100 vertical layers is suggested by several authors). In any case, we believe that due to the objectives of BRIDGE and the need to run the state-of-the-art meteorological models (WRF) with a very high resolution, the results are excellent. The 200 m spatial resolution seemed to be very appropriate since higher spatial resolution will lead to a completely unreasonable high computer time for performing the simulations and coarser than 200 m spatial resolution, will lead to grid-cells where the different alternatives proposed by the city authorities would not have any impact at all due to the coarse of the grid-cells.

In general the comparisons between observed data and modelled data is very good. In london during a few weeks, the wind speed is separately substantially to the observed wind speed. Previous difficulties appear when trying to run London area with the received topography and different interpolation procedure had to be applied in order to overcome the problem that the model did not even start to run. However, some numerical unstability could be present in this runs which is

probably due to the height of the buildings and abrupt changes in topography heights. More investigation is needed on the issue related to running WRF under super-high spatial resolution.

3.6 Acknowledgements

We have used the computer resources, technical expertise and assistance produced by the Centro de Supercomputación y Visualización de Madrid (CESVIMA) and the Spanish Supercomputer Network (BSC).

4 CAMx AND URBAIR. UAVR MODELS.

4.1 CAMx model.

As described in more detail in deliverables 4.1 and 4.2, the Comprehensive Air quality Model with extensions (CAMx) [Morris et al., 2004] is an Eulerian photochemical dispersion model that allows the integrated "one-atmosphere" assessment of gaseous and particulate air pollution over many scales ranging from sub-urban to continental.

CAMx was applied by UAVR Helsinki, Gliwice and London case studies to derive ambient concentrations of PM10, O3 and NO2, for the year 2008 (details of the applications are available in deliverable 4.2). In the present report, CAMx results obtained for Helsinki and Gliwice study cases are compared against observations coming from local air quality monitoring stations. A group of statistical indicators is also presented to allow the evaluation of the model's performance.

4.2

4.2.1 Statistical indicators

The following statistical indicators have been identified calculated (Tunis et al., 2010):

- The Correlation Coefficient (R): ranging from -1 to +1, indicates the strength of a linear relationship between two datasets (in this case, observed and modeled). A value of R near to zero indicates the absence of linear correlation between the variables.

$$R = \sum_{i=1}^{N}\left(M_i - \overline{M}\right)\cdot\left(O_i - \overline{O}\right) \Big/ \sqrt{\sum_{i=1}^{N}\left(M_i - \overline{M}\right)^2}\cdot\sqrt{\sum_{i=1}^{N}\left(O_i - \overline{O}\right)^2}$$

- The Index of Agreement (IOA): determines the extent to which magnitudes of observed mean values are related to the predicted deviations and allows for sensitivity toward differences in observed and modeled values; the perfect value of IOA is 1.

$$IOA = 1 - N \cdot RMSE^2 \Big/ \sum_{i=1}^{N}\left(\left|M_i - \overline{O}\right| + \left|O_i - \overline{O}\right|\right)^2$$

- The Mean Fractional Bias (MFB): is a useful indicator because it has the advantage of equally weighting positive and negative bias estimates and does not assume that observations are the truth (i.e. the denominator is the sum of observed and predicted); it ranges from -200% to +200%.

$$MFB = \frac{1}{N}\sum_{i=1}^{N}\frac{M_i - O_i}{\left(M_i + O_i\right)/2}$$

- The Mean Fractional Error (MFE): gives equal weight to under- and over-prediction and is not sensitive to a threshold in observed values ; it ranges from 0% to +200%.

$$MFE = \frac{1}{N}\sum_{i=1}^{N}\frac{\left|M_i - O_i\right|}{\left(M_i + O_i\right)/2}$$

- Factor of modeled values within a factor of two of observations (FAC2).

$$FAC2 = \frac{1}{N}\sum n_i \quad with \quad n_i = \begin{cases} 1 \; for \; 0.5 \le \left|M_i/O_i\right| \le 2 \\ 0 \; else \end{cases}$$

- The Relative Directive Error (RDE): defined in relation to the AQD, 2008 in order to give a mathematical expression of the "model uncertainty" term in the Air Quality Directive (AQD) (where O_{LV} is the closest observed concentration to the limit value concentration (LV) and M_{LV} is the correspondingly ranked modeled concentrations

$$RDE = \frac{\left|O_{LV} - M_{LV}\right|}{LV}$$

- The Relative Percentile Error (RPE): an alternative model error measure for the purposes of the AQD, defined as the concentration difference at the percentile p corresponding to the allowed number of exceedances of the limit value normalized by the observation.

$$RPE = \frac{\left|O_p - M_p\right|}{O_p}$$

Tunis et al. (2010) propose the model quality objectives presented in the next Table.

Table 11– Model quality objectives for O_3, PM10, NO_2 (Tunis et al., 2010).

	MFB	MFE	FAC2	R	IOA	RDE	RPE
O_3	<0.3	<0.45	>0.5	>0.65	>0.65	<0.5	<0.5
PM10	<0.6	<0.75	>0.5	>0.4	>0.6	<0.5	<0.5
NO_2	<0.4	<0.5	>0.5	>0.25	>0.5	<0.5	<0.5

4.2.2 Applications

4.2.2.1 Gliwice

CAMx results for Gliwice are compared against observations for 2008 obtained from AIRBASE (http://acm.eionet.europa.eu/databases/airbase/) for a local air quality monitoring station - Mewy (code PL0238A) - classified as urban background, which measures PM10 and NO_2, and is located at 18.7º East and 50.3º North.

The next figures present the time series and scatter plot for PM10 and NO_2, modeled and observed.

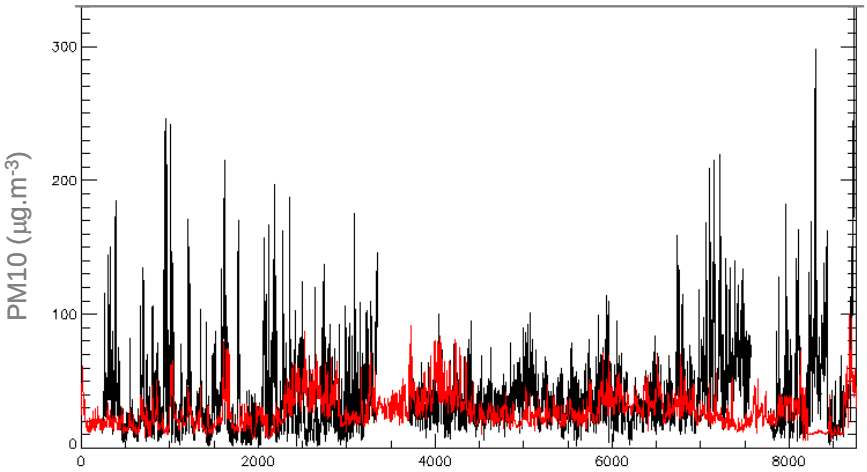

*Figure 42: PM10 time-series for Gliwice Mewy (observed in **black**, modelled in **red**).*

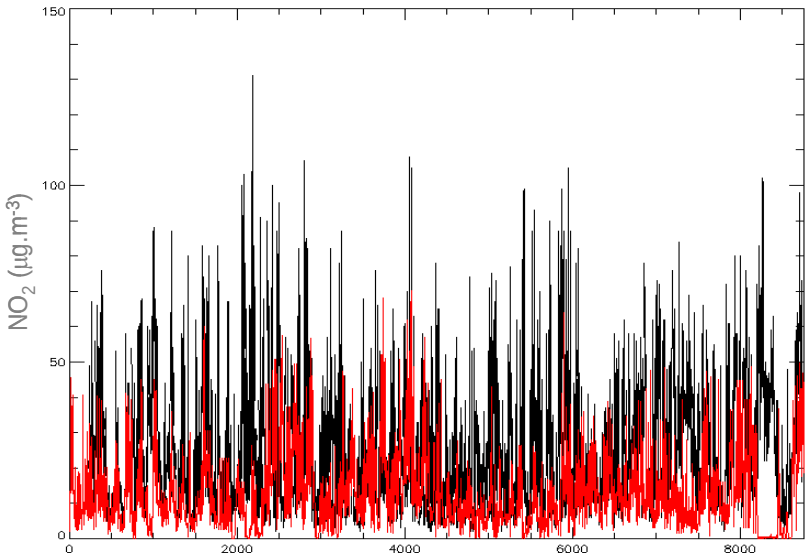

*Figure 43: NO2 time-series for Gliwice Menv(observed in **black**, modelled in **red**).*

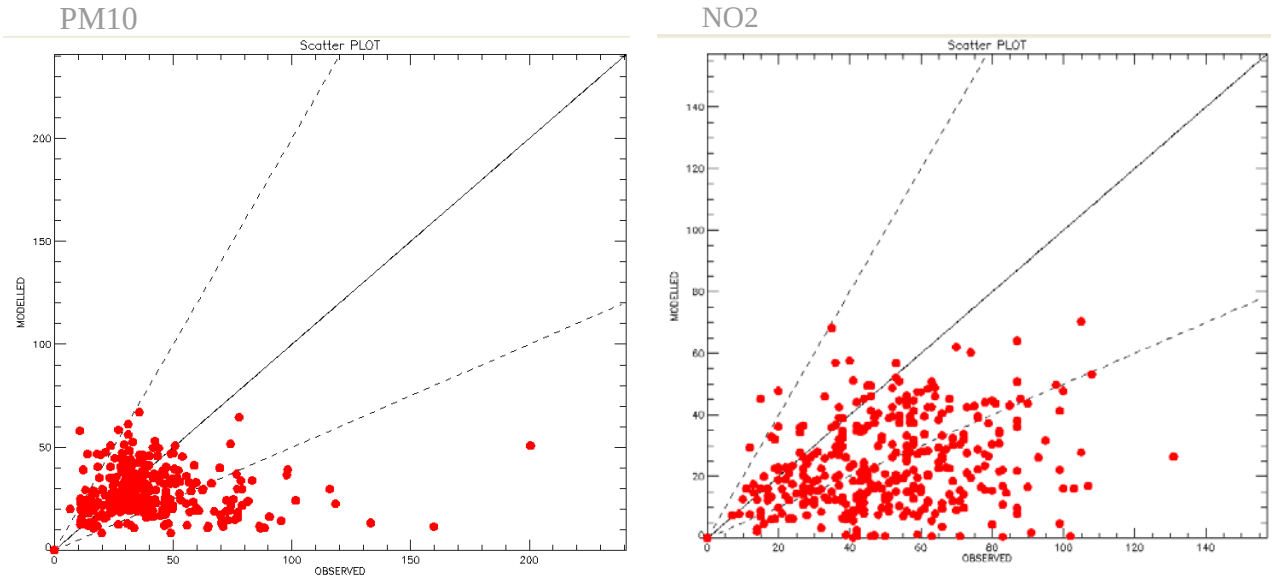

Figure 44: PM10 daily mean and NO_2 daily maximum scatter plot for Gliwice Menv.

The statistical parameters obtained with CAMx for PM10 and NO_2 are presented in the next table (values in green meaning that they accomplish the model quality objectives proposed by Tunis et al., 2010 presented in the previous table, and values in red meaning non-accomplishment with the same objectives). It is possible to conclude that for both pollutants the majority of the statistical parameters obtained the quality objective is accomplished, with a slightly better performance obtained for PM10.

Table 12– Statistical parameters obtained with CAMx for Gliwice Menv (values in green accomplish the quality objectives, values in red do not accomplish the quality objectives).

	MFB	MFE	FAC2	R	IOA	RDE	RPE
PM10	0.26	0.48	0.71	0.35	0.49	0.25	0.5
NO_2	0.5	0.57	0.5	0.3	0.47	0.30	0.46

4.2.2.2 Helsinki

CAMx results for Helsinki are compared against observations for 2008 obtained from AIRBASE (http://acm.eionet.europa.eu/databases/airbase/) for a local air quality monitoring station – Kalio (code FI00425) - classified as urban background, which monitors PM10, O_3 and NO_2. The next figures present the time series and scatter plot for PM10, O_3 and NO2, modeled and observed.

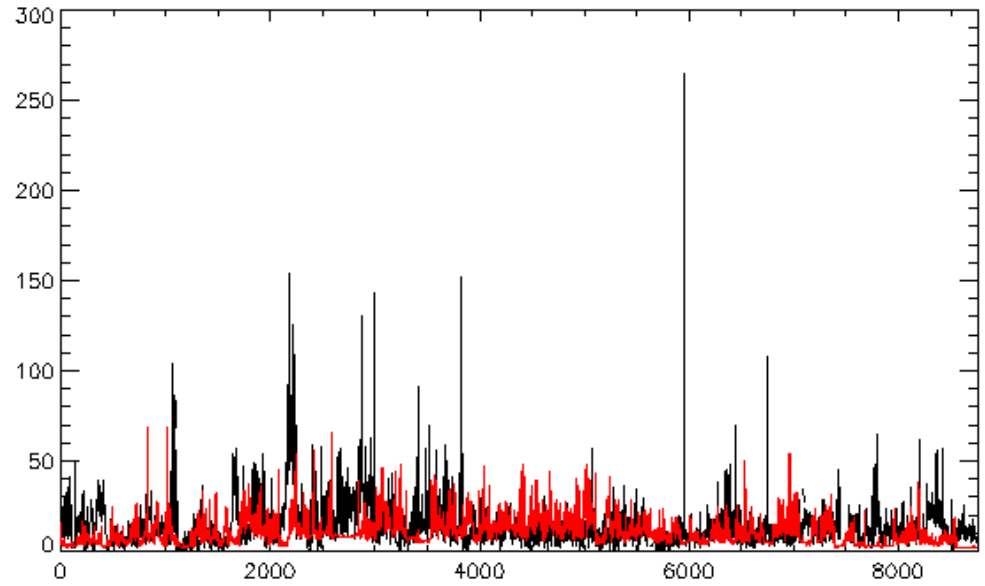

*Figure 45: PM10 time-series for Helsinki – Kalio (observed in **black**, modelled in **red**).*

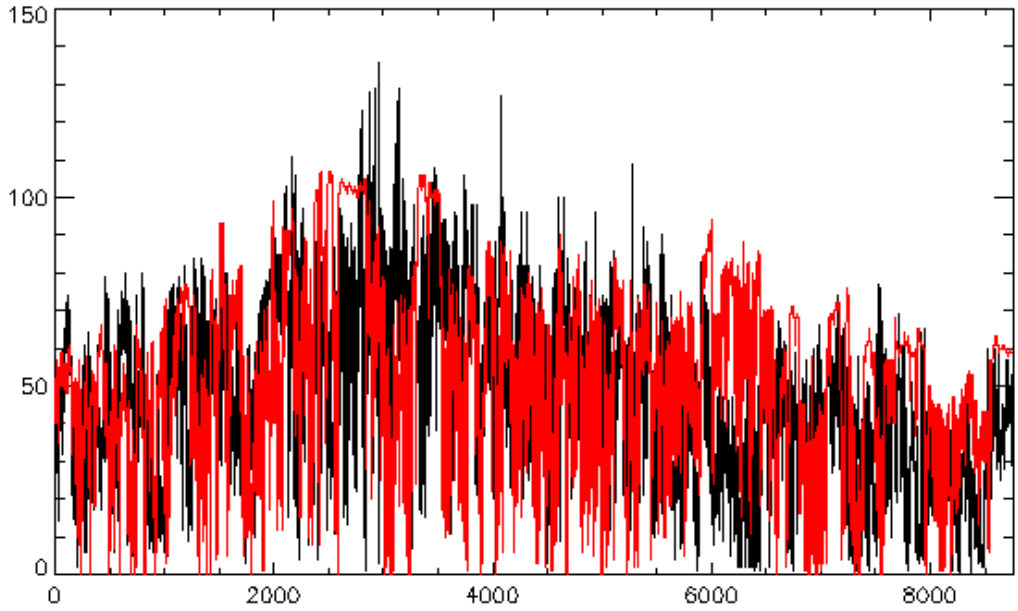

*Figure 46: O_3 time-series for Helsinki – Kalio (observed in **black**, modelled in **red**).*

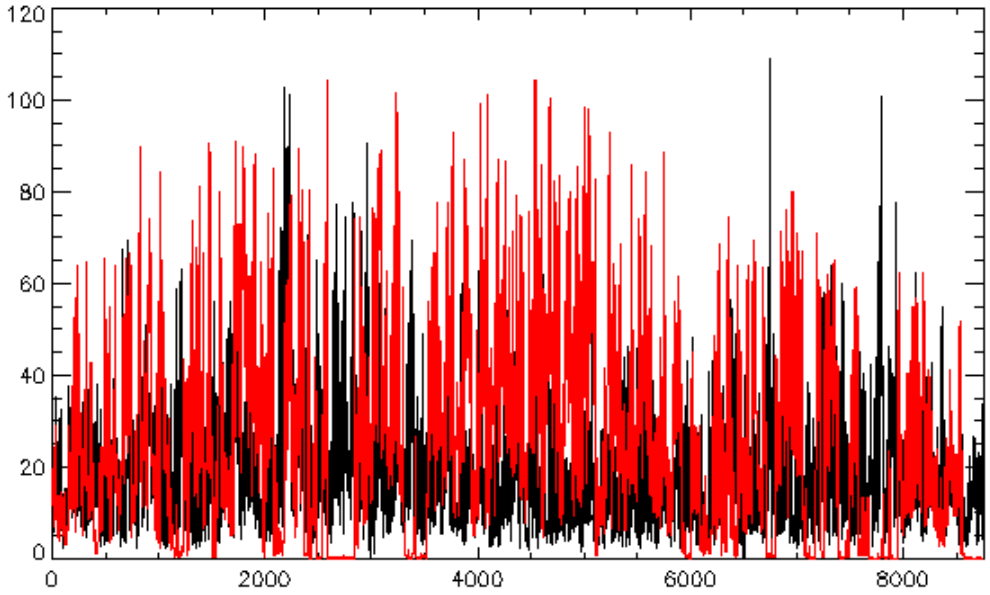

*Figure 47: NO_2 time-series for Helsinki – Kalio (observed in **black**, modelled in red).*

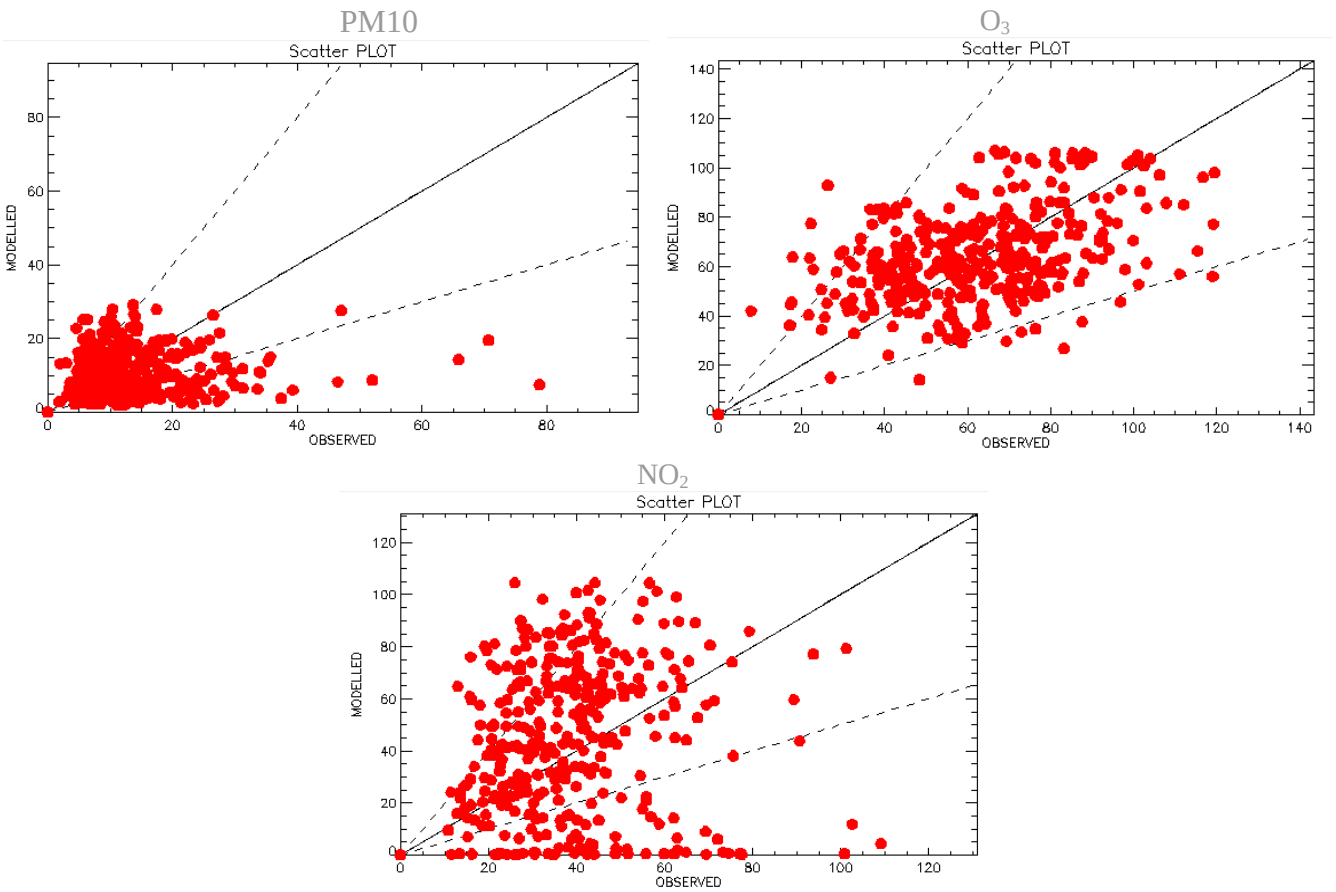

Figure 48: PM10 daily mean, O_3 daily 8-hour maximum and NO_2 daily maximum scatter plot for Helsinki – Kalio.

The statistical parameters obtained with CAMx for PM10, O_3 and NO_2 are presented in the next table (values in green meaning that they accomplish the model quality objectives proposed by Tunis et al., 2010 presented in the previous table, and values in red meaning non-accomplishment with the same objectives). All pollutants comply with the statistical parameters quality objectives, except for the correlation coefficient (R) and the index of agreement (IA). O3 is the pollutant for which the better performance is obtained.

Table 13– Statistical parameters obtained with CAMx for Helsinki – Kalio (values in green accomplish the quality objectives, values in red do not accomplish the quality objectives).

	MFB	MFE	FAC2	R	IOA	RDE	RPE
PM10	0.22	0.60	0.61	0.2	0.4	0.49	0.50
O_3	0.05	0.29	0.92	0.5	0.65	0.1	0.1
NO_2	0.06	0.65	0.59	0.15	0.42	0.02	0.02

4.2.2.3 Indicators

Deliverable 5.3 (Indicators Definition Report) defined the set of indicators of environmental, socio-economic and sustainability impacts. The next table presents the air quality indicator values obtained with CAMx for its three study cases and the observed values at the local air quality monitoring stations.

Table 14 – Air quality indicators produced by CAMx and observed for Helsinki, Gliwice and London ("-" means the pollutant is not measured in the monitoring station).

Indicator Name	Indicator value Modelled / Observed			
	Helsinki	Gliwice	London	*Threshold*
annual [NO_2] ($\mu g.m^{-3}$)	25 / 19	20 / 26	n.a.	*50 $\mu g.m^{-3}$*
annual [PM10] ($\mu g.m^{-3}$)	11 / 14	28 / 40	14 / 25	*48 $\mu g.m^{-3}$*
annual [PM2.5] ($mg.m^{-3}$)	9 / 9	24 / -	9 / 13	*No limit defined*
maximum 8-hour [O_3] ($\mu g.m^{-3}$)	107 / 119	113 / -	149	*120 $\mu g.m^{-3}$ for 8- hour averages*
No. of NO_2 exceedances	0 / 0	0 / 0	n.a.	*200 $\mu g.m^{-3}$ not to be exceeded more than 18 times a year*
No. of PM10 exceedances	2 / 4	13 / 65	7 / 10	*50 $\mu g.m^{-3}$ not to be exceeded more than 35 times a year*
No. of O_3 exceedances	0 / 0	0 / -	3 / 0	*120 $\mu g.m^{-3}$ for 8- hour averages no more that 25 times a year*

4.3 URBAIR model.

As described in more detail in deliverables 4.1 and 4.2, the Urban Air Quality (URBAIR) model is an on-line second generation Gaussian model. It integrates a number of functionalities, namely the estimation of road traffic emissions, and the simulation of the resulting air quality patterns for a given spatial domain and time period (usually one year, in compliance with the Directive) for a number of air pollutants, namely: particulate matter with aerodynamic diameter smaller than 10 µm (PM10), nitrogen dioxide (NO_2), sulfur dioxide (SO_2) and carbon monoxide (CO). Because of the capability to simulate the effect of buildings on air pollutants dispersion, URBAIR offers the possibility to assess the impact of urban planning strategies and traffic management scenarios on air quality.

Within the current report, the air quality results obtained with URBAIR for the baseline situation for the 5 study cases were analyzed and evaluated, namely using available observed data.

4.3.1 Athens

Figure 49 and Figure 50 presents a time series of simulated and measured PM10 and NO_2 concentrations for the year of 2008. Observed air quality levels were acquired at the Aristotelous air quality monitoring station. The simulated values were extracted from a specific cell of the domain which corresponds to the location of the referred air quality station. In this study case, the background concentrations monitored in an air quality station outside the study domain were added to the URBAIR simulated concentrations.

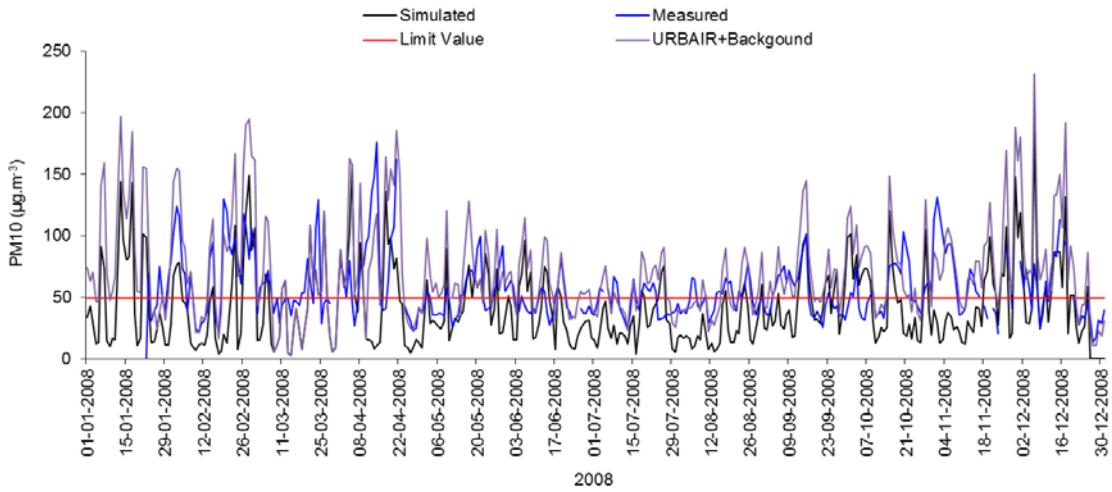

Figure 49 - Comparison of measured vs. simulated PM10 concentration for the 2008 year for a specific cell of the Athens domain (XY=2800, 2000).

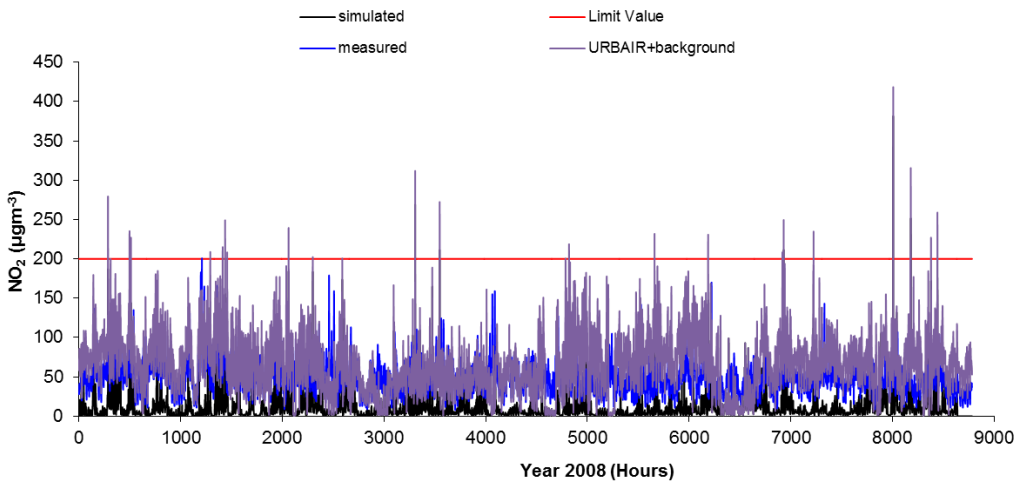

Figure 50 - Comparison of measured vs. simulated NO_2 concentration for the 2008 year for a specific cell of the Athens domain (XY=2800, 2000).

In general, simulated values reasonably follow the trend of measured concentrations. However, some underestimation tendency was observed, which can be originated by the lack of information relating background concentrations and local emission point sources, and, in the case of particulate matter, no ressuspension was considered since the model accounts exclusively for direct exhaust emissions.

In terms of air quality it can be inferred from the analysis of Figure 49 that both measured and simulated PM10 concentrations show several exceedances to the legislated value of 50 $\mu g.m^{-3}$, while for NO_2 the number of simulated exceedances surpasses the ones observed.

Three quality indicators have been used to evaluate the URBAIR performance over the study region, namely: Index of Agreement (IOA), Measures of Skill (SKILLr) and BIAS. The IOA gives the difference between the predicted values and the observed ones. If IOA is higher than 0.5 the model has a good performance. RMSE values lower than the standard deviation of the observed values also indicates a good performance of the model. The BIAS indicates if the model follows the variations of the observed values: if positive, the model overestimates the results, and if negative the model underestimates the results.

In Table 15 and Table 16 the statistical parameters obtained for the pollutants PM10 and NO_2 are presented for the Athens study case.

Table 15– URBAIR performance statistics for PM10 and NO_2 in Athens.

Study case	Pollutant	Average		Standard Deviation		BIAS	STDE	RMSE	R	IOA	SKILLr
		Observed	Predicted	Observed	Predicted						
Athens	PM10	56.4	41.9	27.7	31.4	-13.3	36.5	38.6	0.28	0.52	1.4
	NO_2	49.3	11.3	19.7	17.1	-37.9	24.7	45.2	0.098	0.39	2.3

Analysing the PM10 results from Table 15 it can be concluded that the simulations for Athens study case are slightly underestimated by comparing the average observed and simulated values which is also confirmed by the BIAS. The RMSE and the IOA indicate a good model performance although the correlation (given by the parameter R) is low. Regarding NO_2, there is a significant underestimation of concentrations in comparison with the observations. In order to assess the effect of adding the background concentrations to modelling results in the overall accuracy of the model, values measured in an air quality station located outside the computational domain that should be representative of the area around the study domain, without being affected by the emissions inside this specific area. In the case of PM10 and NO_2, the results presented in Table 16 show an improvement in some of the evaluation metrics, namely the R and the IOA.

Table 16 – URBAIR performance statistics obtained for PM10 using background measurements.

Study case	Pollutant	Average		Standard Deviation		BIAS	STDE	RMSE	R	IOA	SKILLr
		Observed	Predicted	Observed	Predicted						
Athens	PM10	56.4	71.2	27.7	39.4	16.5	35.6	39.3	0.57	0.62	1.41
	NO_2	49.3	65.6	19.7	35.6	16.3	33.7	37.5	0.39	0.51	1.90

4.3.2 Helsinki

For the Helsinki case study quality indicators were not calculated because of the inexistence of an air quality monitoring station.

4.3.3 Gliwice

Although there is an air quality station inside the Gliwice domain its location is too close to the boundaries to allow an adequate comparison between simulated and measured concentrations. For this reason it was decided not to use the observed data for QA/QC purposes.

4.3.4 Firenze

Figure 51 presents a time series of simulated and measured PM10 concentrations for the year of 2008. Observed air quality levels were acquired at the Gramsci air quality monitoring station. The simulated values were extracted from a specific cell of the domain which corresponds to the location of the referred air quality station. In this study case, the background concentrations monitored in an air quality station outside the study domain were added to the URBAIR simulated concentrations following the procedure already described in the Athens city case.

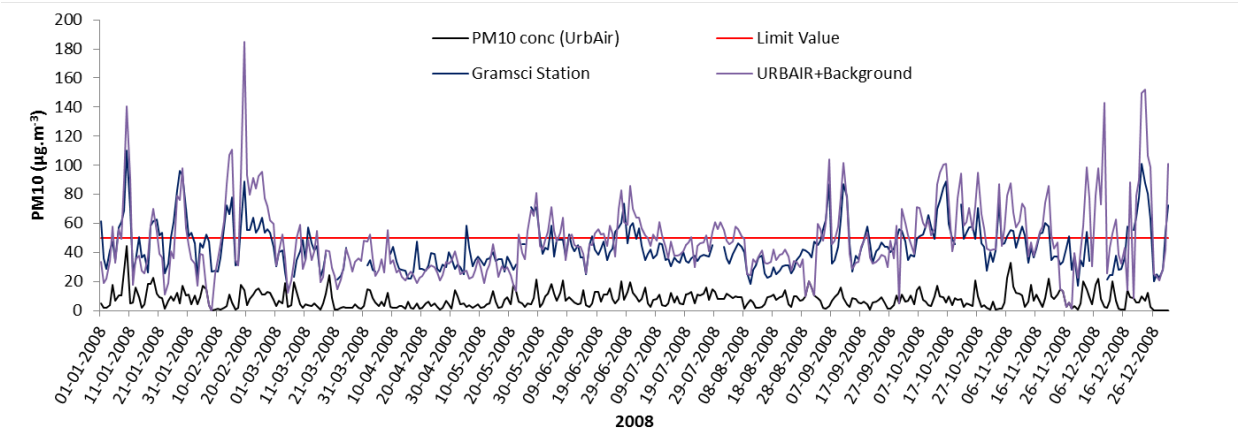

Figure 51- Comparison of measured vs. simulated PM10 concentration for the 2008 year for a specific cell of the Firenze domain (XY=2800, 3500).

The simulated values present a significant underestimation compared to the values acquired in the Gramsci air quality monitoring station as shown by the analysis of Table 17.

Table 17 – URBAIR performance statistics for PM10.

Study case	Pollutant	Average		Standard Deviation		BIAS	STDE	RMSE	R	IOA	SKILLr
		Observed	Predicted	Observed	Predicted						
Firenze	PM10	44	7.89	19.8	5.8	-36.4	18.7	40.9	0.28	0.47	2.06

By adding the contribution of urban background concentration it can be shown that results accuracy is greatly improved (see Table 18).

Table 18 – URBAIR performance statistics for PM10 (considering background concentrations).

Study case	Pollutant	Average		Standard Deviation		BIAS	STDE	RMSE	R	IOA	SKILLr
		Observed	Predicted	Observed	Predicted						
Firenze	PM10	44	48.6	19.8	24.9	3.9	21.5	21.8	0.78	0.71	1.1

4.3.5 London

In Figure 52 the simulated and measured PM10 concentrations at the location of the Marylebone air quality monitoring station are presented for year of 2008. As before, background concentrations monitored in an air quality station outside the study domain were added to the URBAIR simulated concentrations.

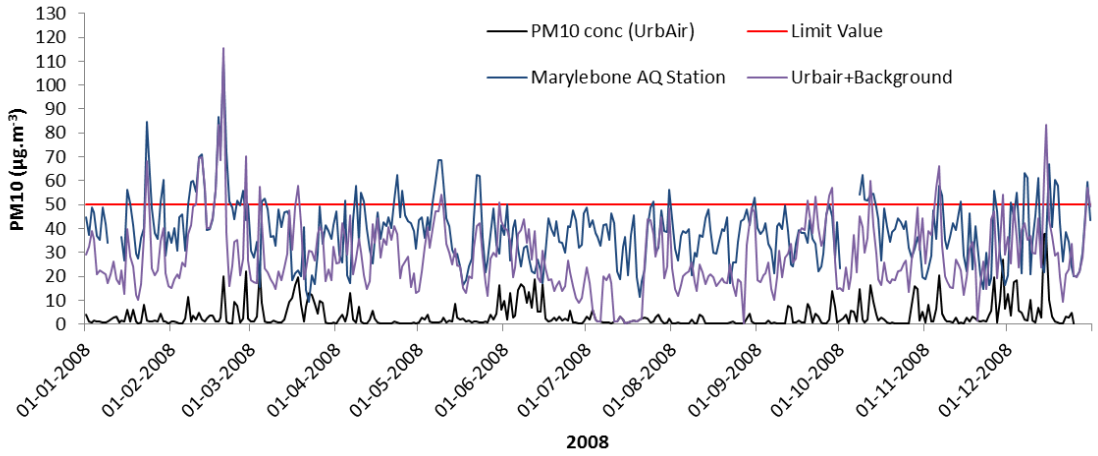

Figure 52 - Comparison of measured vs. simulated PM10 concentration for the 2008 year for a specific cell of the London domain (XY=500, 5300).

There is a clear underestimation of the simulated concentrations when comparing with the PM10 concentrations measured in the air quality station, as can be also concluded by the analysis of the QA/QC statistical parameters presented in Table 19.

Table 19 – URBAIR performance statistics for PM10.

Study case	Pollutant	Average		Standard Deviation		BIAS	STDE	RMSE	R	IOA	SKILLr
		Observed	Predicted	Observed	Predicted						
London	PM10	39.1	3.5	14.7	5.3	-35.5	16.0	38.9	-0.12	0.36	2.64

As stated before, there are several reasons that justify this underestimation: no background concentrations are being considered with URBAIR simulations, local points sources are not taken into account, hourly traffic fluxes were calculated from annual values (since no information on hourly traffic is available), and only exhaust emissions are being considered (i.e., no ressuspension). Traffic jams can also be responsible for an

underestimation of PM10 emissions since traffic emissions are estimated based on vehicle counting and average speed. Consequently, by adding the urban background contribution simulated values are in much better agreement with the values measured at the Marylebone air quality monitoring station, as shown in Table 20.

Table 20 – URBAIR performance statistics for PM10 (considering background concentrations).

Study case	Pollutant	Average		Standard Deviation		BIAS	STDE	RMSE	R	IOA	SKILLr
		Observed	Predicted	Observed	Predicted						
London	PM10	39.1	28.7	14.7	14.8	-10.5	15.9	18.6	0.44	0.61	1.26

5 KCL MODELS

5.1 Introduction [Author: Grimmond]

King's College London, in association with others, has developed and tested a series of models (Table 21) that are incorporated into the Decision Support System (DSS). In this report we summarize this work. A large amount of this work has been submitted for publication so in these cases the material is not presented in full here. The main emphasis is on the evaluation and use of SUEWS in London and Helsinki. However two other general topics are presented briefly prior to this:

(1) Modelling of Anthropogenic heat flux

(2) Other Urban Land surface models

Table 21: Modelling sub-projects that King's College London (with others) have been associated with that relate to the BRIDGE project.

Model Name/Sub-Project	*Description*	*Publications*[1]
LUCY	Anthropogenic Heat flux for all cities globally	Allen et al. (2010)[2]
GreaterQF v3.2	Anthropogenic heat flux for London	Iamarino et al. (2011)[3]
LUMPS	Radiation and energy balance model	Loridan et al. (2011)[4]
SUEWS	Radiation, energy and water balance model	Jarvi et al. (2011)[5] in review
SLUCM/WRF	Single Layer Urban Canopy Model/ WRF Radiation and energy balance Model	Loridan et al. (2010)[6] Chen et al. (2011)[7] Loridan and Grimmond (2011)[8] in review
Urban-PILPS	Urban energy balance Model comparison	Grimmond et al. (2010)[9] Grimmond et al. (2011)[10]

[1] For copies of papers please contact Prof Sue Grimmond (Sue.Grimmond@KCL.ac.UK)

[2] Allen L, F Lindberg, CSB Grimmond (2010) Global to city scale model for anthropogenic heat flux, International Journal of Climatology doi: 10.1002/joc.2210 http://onlinelibrary.wiley.com/doi/10.1002/joc.2210/pdf

[3] Iamarino M, Beevers S, CSB Grimmond High Resolution (Space, Time) Anthropogenic Heat Emissions: London 1970-2025*International Journal of Climatology* doi 10.1002/joc.2390

[4] Loridan T, CSB Grimmond, BD Offerle, DT Young, T Smith, L Jarvi, F Lindberg. Local-Scale Urban Meteorological Parameterization Scheme (LUMPS): longwave radiation parameterization & seasonality related developments Journal of Applied Meteorology&Climatology.**50**: 185-202. doi: 10.1175/2010JAMC2474.1

[5] JärviL, CSB Grimmond, A ChristenThe**S**urface**U**rban **E**nergy and **W**ater Balance **S**cheme (SUEWS): Evaluation in Vancouver and Los Angeles. *Journal of Hydrology (in review)*

[6] Loridan T, CSB Grimmond, S Grossman-Clarke, F Chen, M Tewari, K Manning, A Martilli, H Kusaka,M Best (2010)Trade-offs&responsiveness of the single-layer urban canopy parameterization in WRF: an offline evaluation using the MOSCEM optimization algorithm&field observations. *Quarterly Journal of the Royal Meteorological Society*, 136: 997-1019.doi: 10.1002/qj.614

[7] Chen F, H Kusaka, R Bornstein, J Ching, CSB Grimmond, S Grossman-Clarke, T Loridan, KW Manning, A Martilli, S Miao, D Sailor, FP Salamanca, H Taha, M Tewari, X Wang, AA Wyszogrodzki, C Zhang (2010) The integrated WRF/urban modeling system: development, evaluation,&applications to urban environmental problems, International Journal of Climatology 31, 273- 288doi: 10.1002/joc.2158

[8] Loridan T&CSB Grimmond (2011) Multi-site evaluation of an urban land-surface model: intra-urban heterogeneity, seasonality and parameter complexity requirements.*Quarterly Journal of the Royal Meteorological Society (in review)*

[9] ***Grimmond CSB, M Blackett, M Best, J Barlow, JJ Baik, S Belcher, SI Bohnenstengel, I Calmet, F Chen, A Dandou, K Fortuniak, ML Gouvea, R Hamdi, M Hendry, T Kawai, Y Kawamoto, H Kondo, ES Krayenhoff, SH Lee, T Loridan, A Martilli, V Masson,S Miao, K Oleson, G Pigeon, A Porson, YH Ryu, F Salamanca, GJ Steeneveld, M Tombrou, J Voogt, D Young, N Zhang (2010) The International Urban Energy Balance Models Comparison Project: First results from Phase 1* Journal of Applied Meteorology & Climatology, *49, 1268-92, doi: 10.1175/2010JAMC2354.1***

[10] Grimmond CSB, M Blackett, MJ Best, J-J Baik, SE Belcher, J Beringer, SI Bohnenstengel, I Calmet, F Chen, A Coutts, A Dandou, K Fortuniak, ML Gouvea, R Hamdi, M Hendry, M Kanda, T Kawai, Y Kawamoto, H Kondo, ES Krayenhoff, S-H Lee, T

5.2 Anthropogenic Heat Flux [Author: Grimmond]

Two different models for anthropogenic heat flux have been developed:

a) Global model (LUCY)

b) Model for London (GreaterLondon)

In the former case the output for all of the BRIDGE cities can be modelled and used by all the modelling groups. In the latter case the model has higher spatial and temporal resolution but is only for London. For both of these models the software is available at
http://geography.kcl.ac.uk/micromet/index.htm
Manual:http://geography.kcl.ac.uk/micromet/Manuals/LUCY_v22-UserManual.pdf
GreaterLondon – Manual is part of software

5.2.1 Global Model of Anthropogenic Heat Flux[11] [Author: Lindberg, Allen, Kotthaus, Grimmond]

The **L**arge scale **U**rban **C**onsumption of energ**Y** model (LUCY) simulates all components of anthropogenic heat flux (Q_F) from the global to individual city scale at 2.5 x 2.5 arc-minute resolution. This includes a database of different working patterns and public holidays, vehicle use and energy consumption in each country. The databases can be edited to include specific diurnal and seasonal vehicle and energy consumption patterns, local holidays and flows of people within a city. If better information about individual cities is available within this (open-source) database, then the accuracy of this model can only improve, to provide the community data from global-scale climate modelling or the individual city scale in the future.

Allen et al. (2010) provides the detail of the procedures used to model the three components of anthropogenic heat flux (Figure 53): heat emissions from vehicles, heat released from buildings and heat released from metabolism.

The results for anthropogenic heat flux are very dependent on spatial and temporal scale. With greater spatial variability being expected as the spatial resolution becomes smaller. When the annual mean anthropogenic heat flux for a central part of Europe is plotted it is very evident where the major urban locations are located (Figure 54).

Tokyo is renowned for its very large anthropogenic heat flux values which are typically cited as being the largest for any urban area (Ichinose et al. 1999). Here we compare the fluxes obtained for London and Tokyo for comparative purposes at the 2.5 x 2.5 arc-minute scale. First considering the temporal pattern through the year the mean flux for the whole urban area 2-3 times greater than London at all times of the year (Figure 55). The temporal pattern for one day for the two cities is shown in Figure 56. The smallest fluxes occur at 3 am in the morning across both cities. The locations of the central business districts are clear (Figure 56).

Loridan, A Martilli, V Masson S Miao, K Oleson, R Ooka, G Pigeon, A Porson, Y-H Ryu, F Salamanca, G-J Steeneveld, M Tombrou, JA Voogt, D Young, N ZhangInitial Results from Phase 2 of the International Urban Energy Balance Comparison Project, *International Journal of Climatology*31, 244-272

[11] This section comes from the published paper by Allen et al. (2010 early view).

Subsequent to the publication of the Allen et al. (2010) paper further developments have been made of LUCY[12].

In version 1.0 of LUCY (Allen et al. 2010) the mean monthly temperature was used to estimate an energy scaling factor (T_F) which was used to calculate heat emissions from buildings. Willmott et al.'s (1998) global monthly average temperature was used to compute T_F using a balance point temperature of 12°C (Nicol and Humphreys, 2002). From that temperature a 5% increase in T_F was assumed for each decrease of 1°Cin air temperature (Amato et al., 2005). In the hottest months, air conditioning was taken into account by increasing the multiplication factor by 3% for each 1°C increase (as determined by Kondo and Kikegawa, 2003). The limitations of this include: (1) that the increase of T_F was capped at -4°C reverting back to T_F=1 which led to unreasonably low heat emission from buildings at very low temperature foremost at high latitudes; and (2) using the long term monthly average temperatures means that the model is not responsive to actual conditions (e.g. warm or cold days).

In version 2.0 (v2.0), we introduced dynamic behaviour to T_F, which takes into account the expected monthly temperature for different latitudes by time (month) of year. The earlier lower limit of -4°C is replaced with a minimum temperature that varies with latitudinal band (i.e. 85N to 75N). Thus for higher latitudes where monthly mean temperatures are likely to be less than -4°C, T_F does not revert to 1, thus ensuring a more appropriate response. Here the minimum temperatures used are computed from Willmott et al.'s (1998) global monthly average temperature datasets. When the minimum average temperature is warmer than -4°C for a latitudinal band and month, then the previously used function is used to scale the increase in T_F (i.e. 5% increase in T_F/ 1°C decrease in temperature below the comfort threshold). The fixed increase of 3% in T_F with every 1°C increase in temperature is still used in v2.0. However, the response to temperatures above 36°C is changed so that T_F continues to increase at the same rate above 36°C. In addition, v2.0 includes the possibility to consider daily temperature patterns resulting in a more dynamic model that is sensitive to relatively rapid changes in temperature. Given that heat waves or extremely cold periods are normally considerably shorter than a month, this will allow a more appropriate response.

Figure 57 shows results after using LUCYv2.0 for a latitudinal transect in Europe (Helsinki, Firenze, Athens and Glwice are present). Both the modelled anthropogenic heat fluxes are shown (left) and the differences (0 - 20 W m^{-2}) from the version 1 (right). Significant differences are found in major urban settings in the northern areas such as Stockholm, Sweden (59°20'N, 18°03'E). However, other urban areas in northern Europe e.g. Helsinki (60°10' N, 25°0' E) shows no differences between the two versions. This is because Helsinki is located in an area where the multiplication factor (v1.0) reverted back to 1 since the monthly mean air temperatures is below -4° (not shown).

[12]Lindberg F, S Kotthaus, J He, Lucy Allen, CSB Grimmond (in preparation) Development of a more dynamic global anthropogenic heat flux model (LUCY) through linkage to an open source database (KUMA)

In upcoming version 3 (v3.0) we introduce the possibility to theoretically examine any day or number of sequential days between 1900 and 2100. However, the success of the execution is highly dependent on the datasets available for the specific time of interest. Data sources needed for the model to make accurate assumptions on anthropogenic heat flux are: population density, air temperature, energy consumption and traffic data in the form of number of cars, freights and motorbikes per 1000 people by country (Allen et al. 2010). Population and temperature are spatial grids whereas energy and traffic data are stored as text files including statistics for each county and year. In order to manage the data sources a database system, the **K**ing's College London **U**rban **M**icrometeorology data **A**rchive (KUMA), for storing and selecting input data for LUCY is used.

Software: Available fromhttp://geography.kcl.ac.uk/micromet/
Manual: http://geography.kcl.ac.uk/micromet/Manuals/LUCY_v22-UserManual.pdf

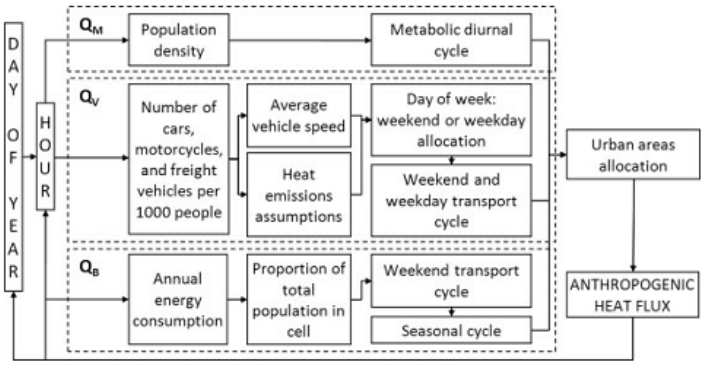

Figure 53: Flowchart of the LUCY global anthropogenic heat flux model (Allen et al. 2010).

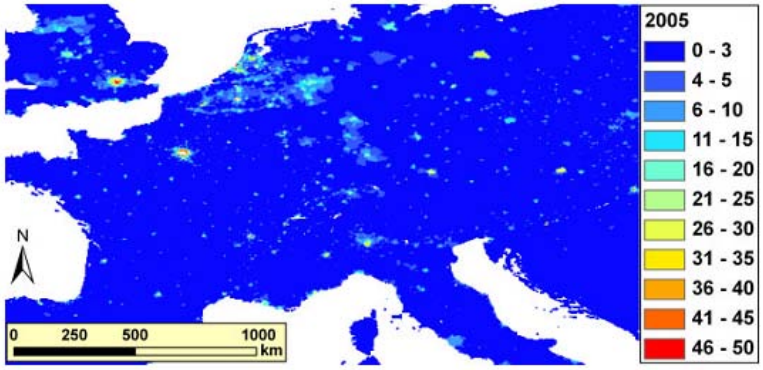

Figure 54: Annual average anthropogenic heat flux (W m^{-2}) for Central Europe in 2005 (2.5 X 2.5 arc minute resolution).

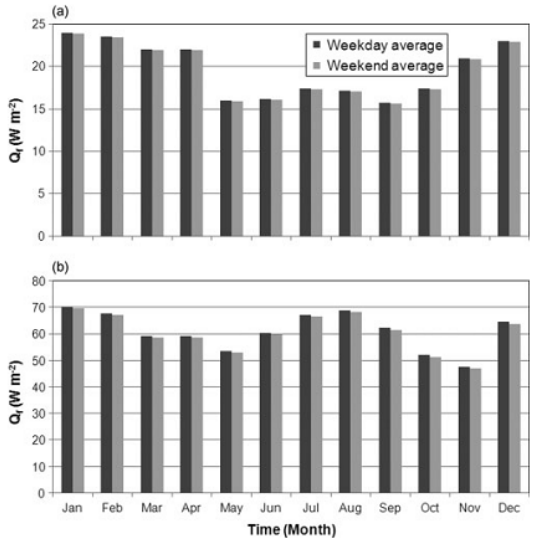

Figure 55: Monthly average anthropogenic heat emissions in (a) London and (b) Tokyo during 2005 (Allen et al. 2010).

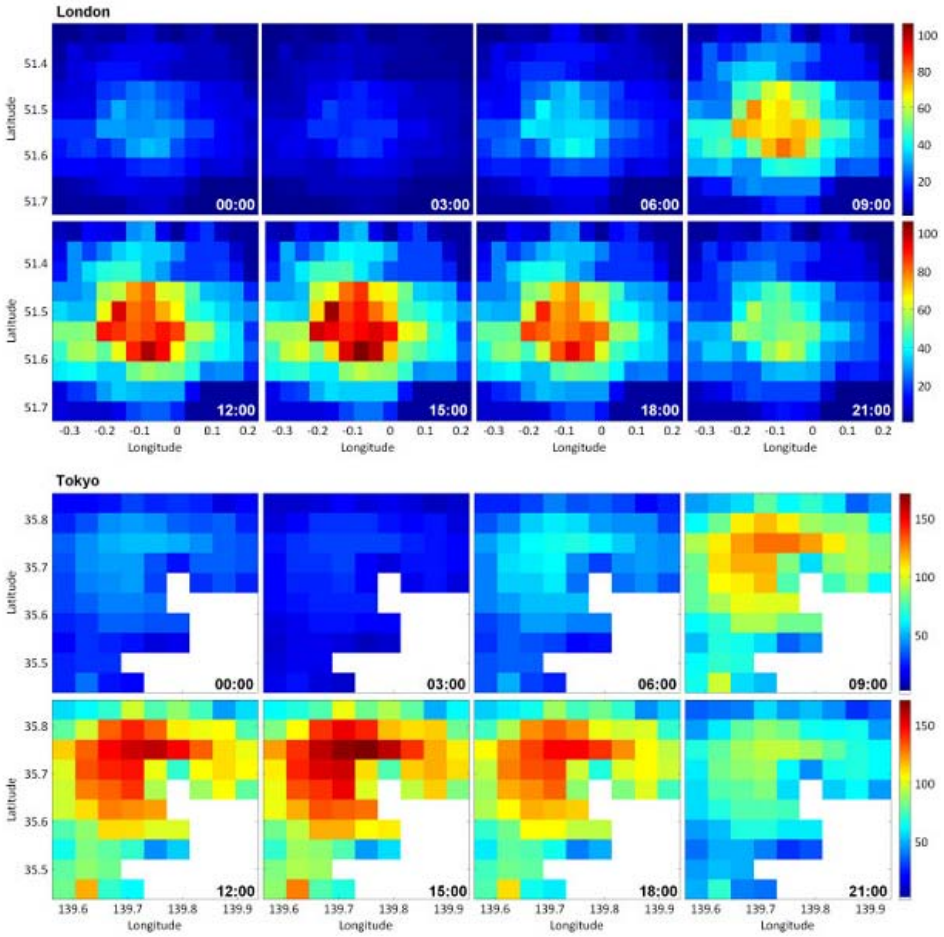

Figure 56: Diurnal patterns of the anthropogenic heat flux in London and Tokyo on Monday 14 February 2005 (Allen et al. 2010).

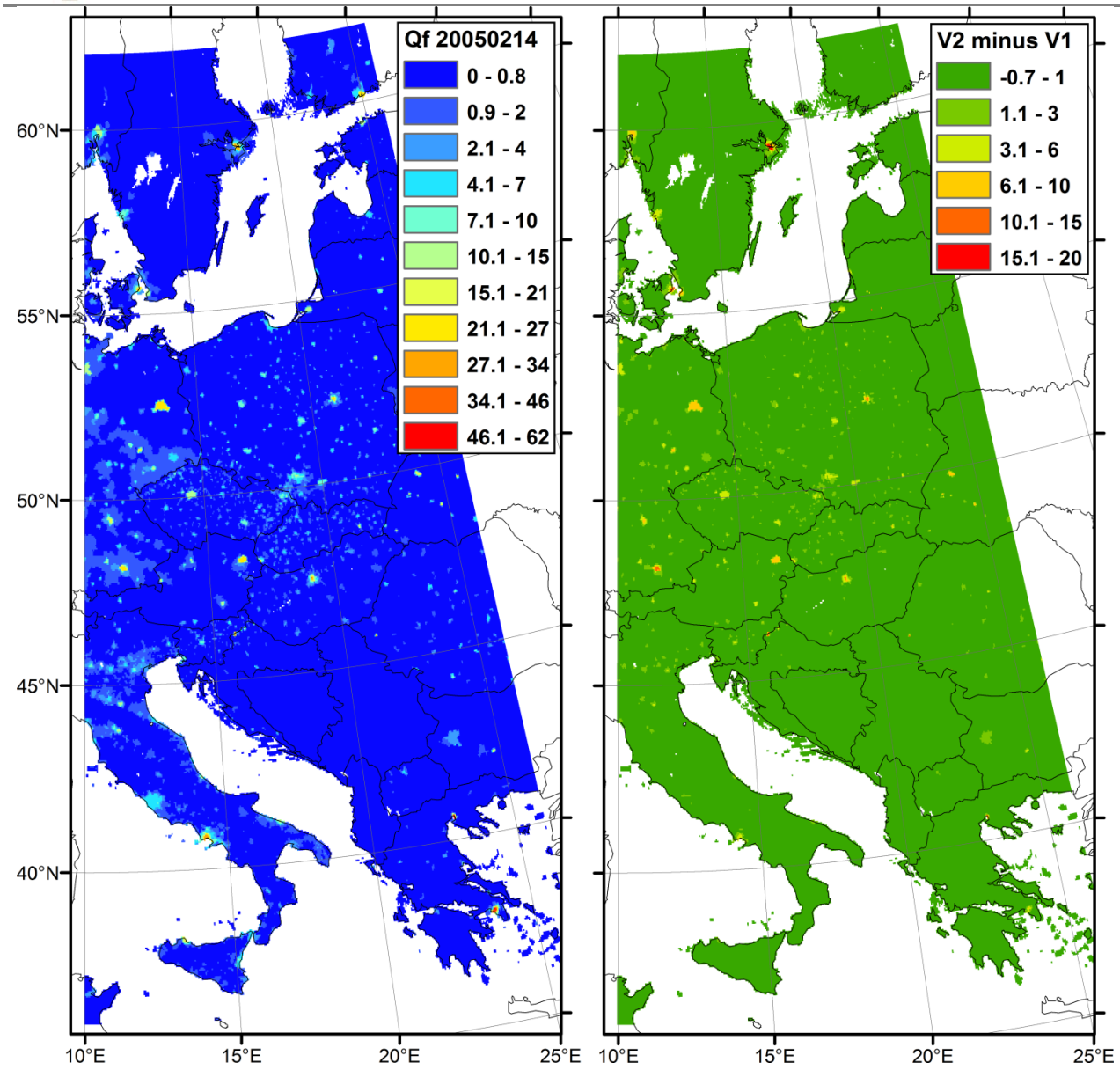

Figure 57: A snapshot of anthropogenic heat flux (Q_F W m^{-2}) for a latitudinal transect across Europe 14 February 2005. The pixel resolution is 2.5 × 2.5 arc-minutes: (left) calculations with LUCY v2.0 with KUMA (right) difference in results with version of LUCY used (v2.0 – v1.0).

5.2.2 Greater London[13][Authors: Iamarino, Beevers, Grimmond]

Iamarino et al. (2011) describe the components of the model (GreaterQF) which simulates the anthropogenic energy released by human activities across Greater London. To this goal, the main contributions considered by this model are heat emissions from buildings, road traffic and human metabolism. For the building sector, heat emissions have been classified by energy source (natural gas, electricity, other fuels) and by sector (domestic, industrial). Here, industrial heat emissions refer to emissions arising from energy consumption in the service industry (commerce, business, administration, etc.) rather than the manufacturing industry. As concerns road traffic, emissions are classified by type of transportation: cars, buses, taxi, motorcycles, light good vehicles (LGV), rigid heavy good vehicles (HGV), articulated HGV. For each source and sector, emissions have been computed in terms of sensible heat, latent heat and heat lost in the wastewater collecting system.

To ease computing and visualization of spatial and temporal profiles of QF in Greater London, the software GreaterQF (version 3.2) has been developed and made available (http://geography.kcl.ac.uk/micromet/). It is an executable Microsoft Windows application built within the development environment Embarcadero Delphi® XE. Results can be obtained as total QF or fraction (sensible, latent and heat-to-wastewater), individually for all sources considered in this work, with the desired spatial resolution (200 × 200 m^2 grid or any of the NeSS units) and temporal resolution (from 30 min up to 1 year). Output is graphical or as a textfile suitable for GIS analysis or for import to other models.

For the years 2005-2008, the average total anthropogenic flux over Greater London was 10.9 W m^{-2}. Energy flows classified by source, sector and sink are shown in the Sankey diagram of Figure 58. The largest contribution is from the building sector as a whole, with 8.7 W m^{-2} (80% of total, of which 42% is domestic and 38% industrial sector). This is followed by the transportation sector, which contributes 1.65 W m^{-2} (15%), where cars are by far the most important source of heat emissions (accounting for 64% of the transportation sector and 10% of total Q_F), followed by large good vehicles (LGV), rigid heavy goods vehicles (HGV) and buses and coaches. The impact of taxi, motorcycles and articulated HGVs is negligible since they are all less than 0.1 W m^{-2}. Finally, human metabolism contributes 0.55 W m^{-2} (5.1%). As concerns the sinks, the largest fraction of total Q_F is emitted as sensible heat to atmosphere (8.8 Wm^{-2}, 81% of total), while only small fractions are emitted as latent heat through the release of water vapor (0.79 W m^{-2}, 7.3%) or lost in the wastewater system (1.3 W m^{-2}, 12%). The average fluxes in Figure 58 appear modest, but they correspond to a very large final amount of energy (150 TWh) annually released by human activities into the environment across Greater London. Moreover, these fluxes are very unevenly distributed in time and space with peaks up to orders of magnitude greater than the average values.

The spatial variability of Q_F by sector is shown in Figure 59 with 200 m × 200 m resolution (compare to Figure 56). The domestic heat emissions (Figure 59a) appear rather homogeneously distributed in space, with peak values up to 36.5 W m^{-2}, while industrial (all non-residential buildings) emissions (Figure 59b) are very concentrated in Central London (peaks up to 197 W m^{-2}). Emissions from road traffic (Figure 59c) follow, as expected, the London road network and

[13] This section is from: Iamarino M, Sean Beevers, C. S. B. Grimmond (2011). High-Resolution (Space, Time) Anthropogenic Heat Emissions: London 1970 – 2025. *International Journal of Climatology*. n/a. doi 10.1002/joc.2390

reflect more clearly the routes of major roads which are easily identifiable. In some cells with major road junctions, peak emissions are up to 48 W m^{-2}. Metabolic heat emissions (Figure 59d) have a spatial distribution similar to industrial energy with higher values in central areas (peaks up to 6.4 W m^{-2}), where people are more concentrated in the daytime. The resulting total Q_F (Figure 59e) cumulative distribution function (Figure 59f) has been folded to highlight its positive skewness, as evidenced by the long tail on the right of the median value, 8.0 W m^{-2}. It follows that 50% of London surface experiences annual total heat emissions < 8.0 W m^{-2} and only 2.5% has values > 50 W m^{-2}. Most of these high values fall within a restricted area of Central London defined in the London Plan of the Greater London Authority (GLA/3, Table 22) as the Central Activities Zone (CAZ, indicated with dashed boundaries in Figure 59e). The CAZ surface (33.5 km^2) is just 2% of Greater London, but it accounts for one third of the total industrial energy consumption due to the very high concentration of service industry (government offices and other institutions, financial and business services, large shopping quarters, extensive activities associated with tourism, entertainment, education, communication and so on).

The largest emissions in the CAZ are within the City of London, the smallest London borough (3.2 km^2, continuous boundaries in Figure 59e). This area contains some of the largest and most high-standard office buildings in London where a very large number of people work (348,000 people in 2007). The average Q_F is 140 W m^{-2} with local peaks up to 210 W m^{-2}. Other extreme values within the CAZ can be found along the route Oxford Street – Regents Street – Piccadilly Circus (values up to 146 W m^{-2}), along Victoria Street (160 W m^{-2}), around Euston Square (181 W m^{-2}) and Knightsbridge (143 W m^{-2}). Outside the CAZ, it is worth noting the 145 W m^{-2} in the Canary Wharf area located a few kilometers eastwards: heat emissions in this business and financial district, which hosts the three tallest skyscrapers in the UK, is expected to grow in the future due to the completion of more large office buildings.

For practical or predictive purposes, a first order estimate of the total heat released by buildings (domestic + industrial) in an area is given by:

$$Q_{F,B} = k d_c \quad (1)$$

where k is a proportionality constant, d_c [person m^{-2}] is a corrected population density calculated as weighted average of the workplace (d_w) (weight w_d) and resident (d_r) population density of the given area:

$$d_c = w_d d_w + (1-w_d) d_r \quad (2)$$

This type of correlation directly follows from the use of resident and workplace population densities to scale energy consumption in buildings. The best fit for entire Greater London is obtained when k = 2160 W $person^{-1}$ and w_d = 0.58 (R^2 = 0.92); evidently, this also corresponds to using a constant heat emission factor per workplace population, kw_d = 1253 W $person^{-1}$, and a constant heat emission factor per resident population, $k(1-w_d)$ = 907 W $person^{-1}$. A similar empirical relation cannot be given for $Q_{F,T}$ since road traffic cannot be easily correlated with population, land-use or other indicators.

Over the 2005-2008 period there is a small decreasing trend of Q_F in Greater London (Figure 60). From the daily average values and daily minimum/maximum range the seasonal variability is clear, with higher values in winter due to increased energy load for space heating. Moreover, there is no clear evidence of summer energy consumption peaks (*e.g.*, due to air conditioning) as it is typical in warmer climates (Psiloglou et al., 2007). The maximum relative deviation of winter Q_F with respect to summer is around 80% which is much less than expected at London's latitude (51°N) (Ferreira *et*

al., 2010). This can be explained partly by London's climate that has smaller temperature fluctuations between summer and winter compared to continental cities at similar latitude.

The daily minima (usually between 2:00 and 5:00) have a smaller seasonal oscillation compared to the range in the maxima (reached between 12:00 and 19:00 depending on season and day of week). The 24-h range has a mean of 15 W m^{-2} in winter and 7 W m^{-2} in summer. However, for some grid cells in the CAZ, the difference is up to 300 W m^{-2} in winter.

Examples of the half-hourly profiles for a typical week in January 2008 (Monday 14 to Sunday 20) are shown in Figure 61 for two representative grid cells: cell ID 22030 in the City of London with predominant emissions from the industrial sector and ID 22642 in a residential neighborhood (Southwark) with predominant emissions from the domestic sector. In both, the residential emission profile on working days has two peaks (Figure 61a), a lower one in the morning (between 8:00 and 9:00) and a second, higher one in the evening (18:00 - 19:00). This reflects the pattern of occupancy of dwellings and the corresponding energy needs. In contrast, industrial emissions peak only once between 11:00 and 12:00 (Figure 61b), when activities in the service industry are at their maximum. The situation is different at weekends, when industrial emissions drop and domestic emissions increase slightly. With respect to road traffic, emission profiles for personal transportation (Figure 61c) have two peaks on working days (at 8:00–9:00 and at 16:30–17:30) corresponding to the main movements of people to/from their workplace/schools etc, with smoother profiles during weekends. Freight transport (Figure 61d) emissions are also double-peaked during the week with highest values in the early morning and at around midday, with large reductions on Sunday. Emissions from human metabolism also reflect movement of people (Figure 61e): in the CAZ cell, metabolic emissions are very high during working days and fall during the night and on weekends when most people are not present. While in the residential cell the profile has the typical double peak during working days when the presence of people at home is greater and a plateau on weekends due to occupancy throughout the day. The lower values during the night are due to the reduced metabolic rates. The total Q_F (Figure 61f) are consequently shaped by the predominant emitting sector (domestic and industrial buildings, respectively).

Across the temporal and spatial domain considered, the Q_F partitioning does not differ significantly from the proportions in Figure 58. The sensible heat fraction occasionally can be lower in residential areas, due to the higher hot water needs (which increases the heat-to-wastewater fraction) and the greater importance of natural gas consumption (which increases the latent heat fraction). It is slightly higher in areas with consumption dominated by the service industry due to the more extensive use of electricity (which does not produce latent heat).

However, the use of evaporative cooling towers in large A/C centralized systems can significantly change the sensible-to-latent heat ratio with respect to predictions of the present model. In London, where summers are mild, artificial cooling is almost completely absent in the domestic sector and is used only by the high-standards service industry. According to the cooling towers registers held by the London Borough Councils, more than half of the around 2000 cooling towers in operation in Greater London are concentrated within the CAZ and Canary Wharf. To assess the impact of such high concentration, the case of output area (OA) 00AAFZ0001 (0.39 km^2) within the City of London is addressed. This area has large office buildings and its business nature is evident from the contrasting workplace population (39,000 people) to the few residents (141). 77 evaporative cooling towers are in operation in this OA and serve 28 buildings, corresponding to 29% of the total OA

building volume. Assuming that cooling involves the entire volume of these 28 buildings, the typical summer day profile of latent heat flux generated by the cooling towers can be estimated as:

$$Q_{lat}(t) = (1 + COP)E_c(t)\frac{A_c}{A_{OA}}$$

where $E_c(t)$ is the average time profile of electrical power consumption [W m^{-2}] for cooling in a UK office in summer[14](based on data from Knight and Dunn, 2002), *COP* is the coefficient of performance corresponding to the energy transferred to the outside per unit of electrical energy spent (4.0 has been used as typical value for modern water cooled chillers)[15], A_c is the estimated total cooled floor area ($4.1 \cdot 10^5$ m^2), and A_{OA} is the surface of the output area ($3.9 \cdot 10^5$ m^2). The resulting Q_{lat} is ~70 W m^{-2} daily, with an afternoon peak of 170 W m^{-2} (Figure 62) and this is much larger than the total $Q_{F,B}$ (sensible+latent) estimated for the buildings served by these cooling towers (evaluated as 29% – *i.e.*, the same proportion as building volume – of $Q_{F,B}$ for the entire OA). This agrees with previous findings (*e.g.*, Sailor *et al.*, 2007) and is due to the fact that Q_{lat} also includes a large part of the solar radiation absorbed by the buildings during the day. Hence, this flux represents a particular contribution to the total heat flux $Q_{ex,B}$ (Figure 64) leaving the building, and introduces the need for a more complete building modelling approach if the building-atmosphere interaction is to be described in detail.

The short-term trends obtained for 2005-2008 have been extended backwards to 1970 and forwards until 2025. For the building sector, this is achieved by applying the same long-term trends proposed by DECC as baseline for the entire UK (see DECC/2 for 1970-2004 and DECC/4 for 2009-2025, Table 22). An annual correction factor has been introduced in order to account for differences in London population dynamics relative to the UK, based on population history and projections (ONS/2, Table 22). For road traffic, reconstruction in the past is consistent with the London LAEI emissions inventory (GLA/2, Table 22) and future forecasts have been provided by Transport for London (personal communication).

With reference to the building sector (Figure 63a), $Q_{F,B}$ during 1970-90 oscillated around 7.7 W m^{-2} as the slowly increasing UK per-capita energy consumption over this period was balanced by a decrease in London population which reached a minimum in 1982. After that, emissions have increased and peaked in 2001 (9.3 W m^{-2}). From 2002, the gradually increasing price of fuels and, more recently, the slowing down of UK economic growth have caused a continuous decrease in energy consumption. The minimum is expected to have been reached in 2009 and a slow recovery is forecast from 2010 with a return to pre-crisis levels by 2020 (if expectations of fuel prices, national gross domestic product and population dynamics are met). Heat emissions from the transportation sector (Figure 63b) have been constantly increasing from 1970 until the mid-90's, with values almost doubling during this period. The subsequent decreasing trend, which is counter to the trend of continuously increasing level of road traffic in the rest of the UK, is a result of measures undertaken by the Greater London Authority to control traffic-related pollution and is expected to continue in the coming two decades. The resulting total Q_F (Figure 63c), which includes metabolic $Q_{F,M}$ adjusted according to population dynamics, has a long-term trend that closely follows $Q_{F,B}$, with a maximum of 11.7 W m^{-2}in 2001 and a recent relative minimum of 10.2 W m^{-2} in 2009.

[14] Knight I, Dunn G. 2002. A/C energy efficiency in UK office environment. Proceedings of 2nd International Conference on Electricity Efficiency in Commercial Buildings, 27–29 May 2002, Nice, France.
[15] Stanford HW, III. 2003. *HVAC Water Chillers and Cooling Towers*. Marcel Dekker: New York.

Interestingly, for the years 1971-76, poor agreement is found with road traffic emissions of 2.5 W m^{-2} estimated over Greater London by Harrison *et al.* (1984)[16], which is double the value suggested here (1.2 W m^{-2} mean for same years). However, estimates for the building sector are closer (8.5 versus 7.6 W m^{-2}). Better agreement is found with the more recent work of Hamilton *et al.* (2009) [17] for $Q_{F,B}$ in 2005 since same DECC data for that year have been used.

The trend for the next 25 years is encouraging in that no dramatic increases of London Q_F are forecasted in the medium term. This might not be true locally, especially in the CAZ area and in its financial core City of London, which will experience further concentration of activities in coming years. Projections of workplace population in the City of London have been recently addressed by the Greater London Authority (GLA/4,Table 22) and are based on planned availability of office space, area's accessibility and employment trends. According to this analysis, 80000 additional workers are expected by 2025 in the City, bringing to 430000 the total number of people working in an area of just 3.2 km^2. Projections for the City of London can be made, for the building sector, by applying eq. (1) and (2) after determination of k and w_d using GLA projections of d_w and d_r, and by correcting for the expected national trend in domestic and industrial energy consumption. The $Q_{F,M}$ can be estimated based on expected resident and workplace population dynamics, and $Q_{F,T}$ can be projected using the overall London trend of Figure 63b. The resulting total Q_F in the City of London is expected to recover much faster and to reach 165 W $m^{-2}$by 2025 (with 16% increase with respect to 2005) (Figure 63d). Analogous situations are expected in other expansion areas, in particular Canary Wharf, where the workplace population is projected to double by 2025.

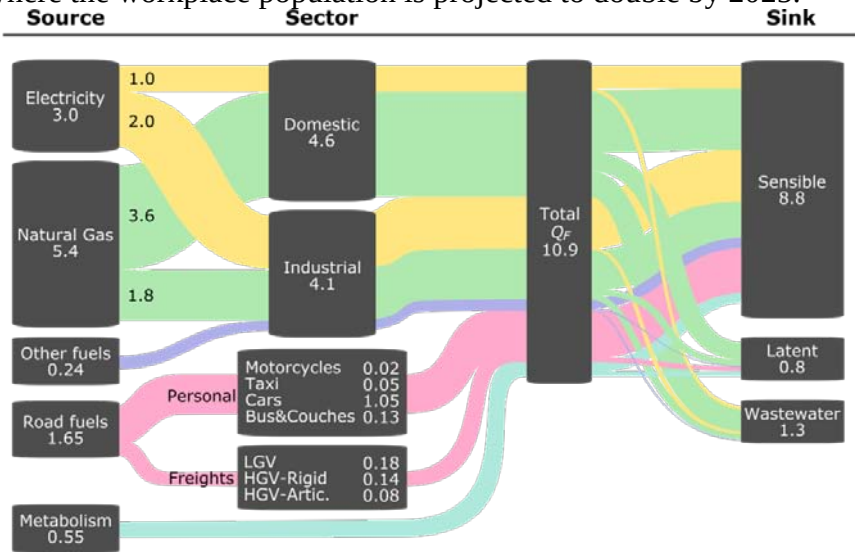

Figure 58: Anthropogenic heat flux for Greater London by source, sector and sink (2005 -2008)(Iamarino et al. 2011)

[16] Harrison R, McGoldrick B, Williams CGB. 1984. Artificial heat release from Greater London, 1971–1976. *Atmospheric Environment* **18**: 2291–2304, DOI:10.1016/0004-6981(84)90001-5.

[17] Hamilton IG, Davies M, Steadman P, Stone A, Ridley I, Evans S. 2009. The significance of the anthropogenic heat emissions of London's buildings: a comparison against captured shortwave solar radiation. *Building and Environment* **44**: 807–817, DOI: 10.1016/j.buildenv.2008.05.024.

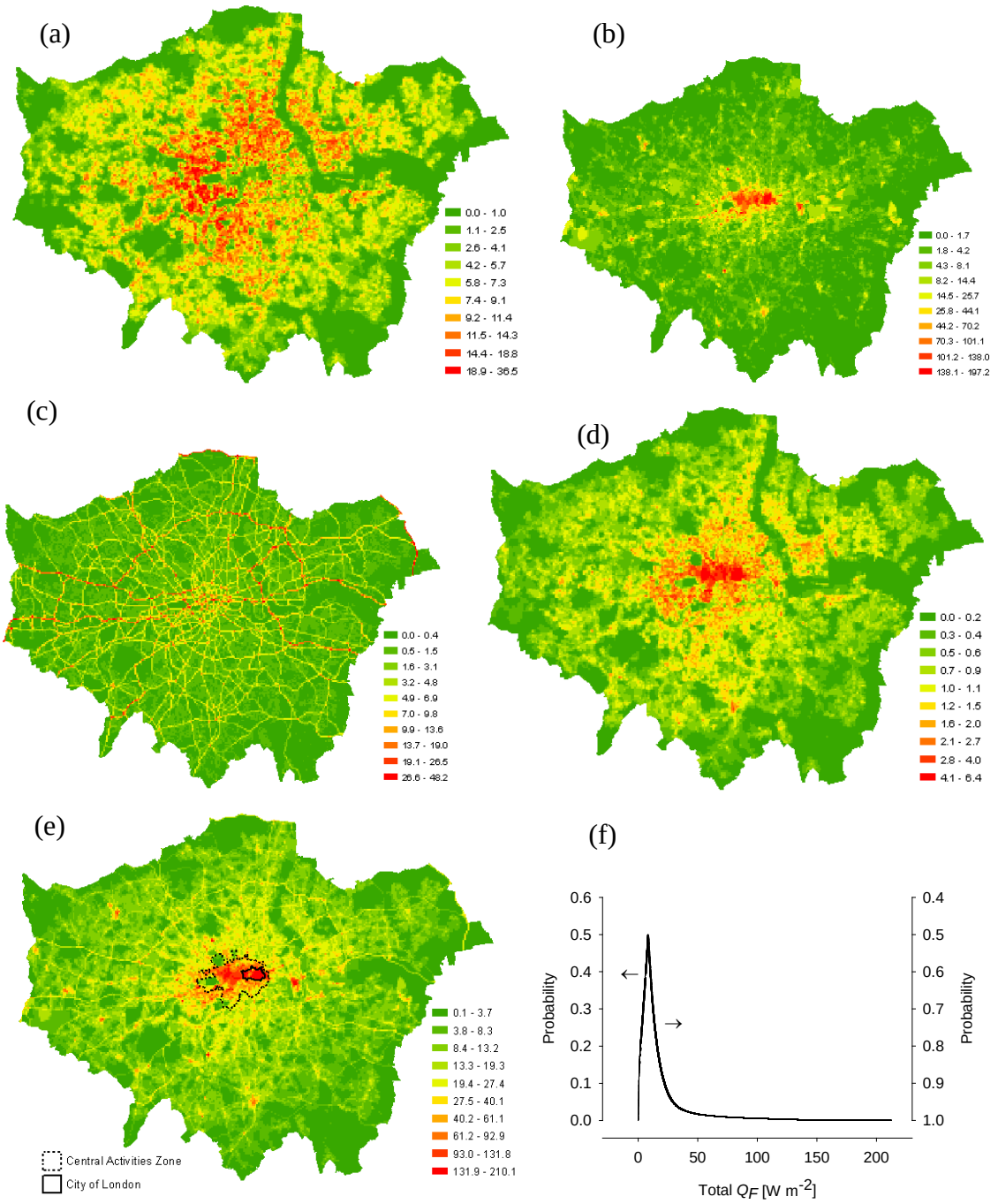

Figure 59: Spatial variability of heat emissions (average for 2005-2008) at 200 m × 200 m resolution by sector: (a) domestic, (b) industrial, (c) road traffic, (d) metabolism and (e) total (classes by Jenks natural breaks); and (f) folded cumulative distribution function of total Q_F *(f). Values in W m^{-2}.(Iamarino et al. 2011)*

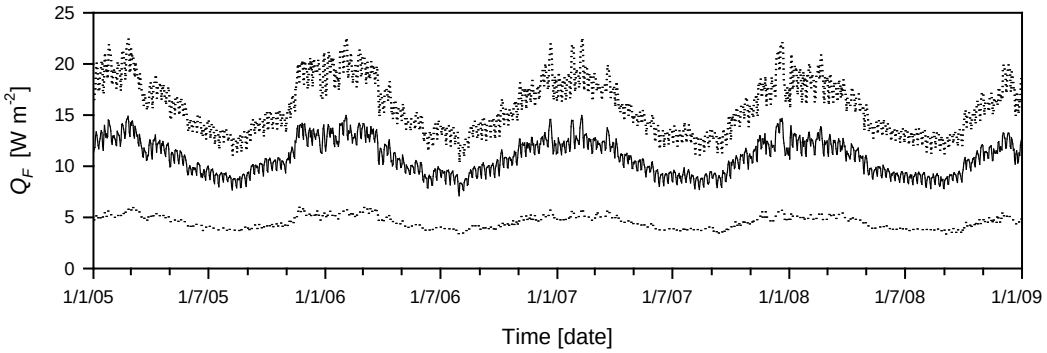

Figure 60: Temporal variation (2005-8) of total Q_F for Greater London as average (solid) and minimum/maximum (dotted lines) daily values.(Iamarino et al. 2011)

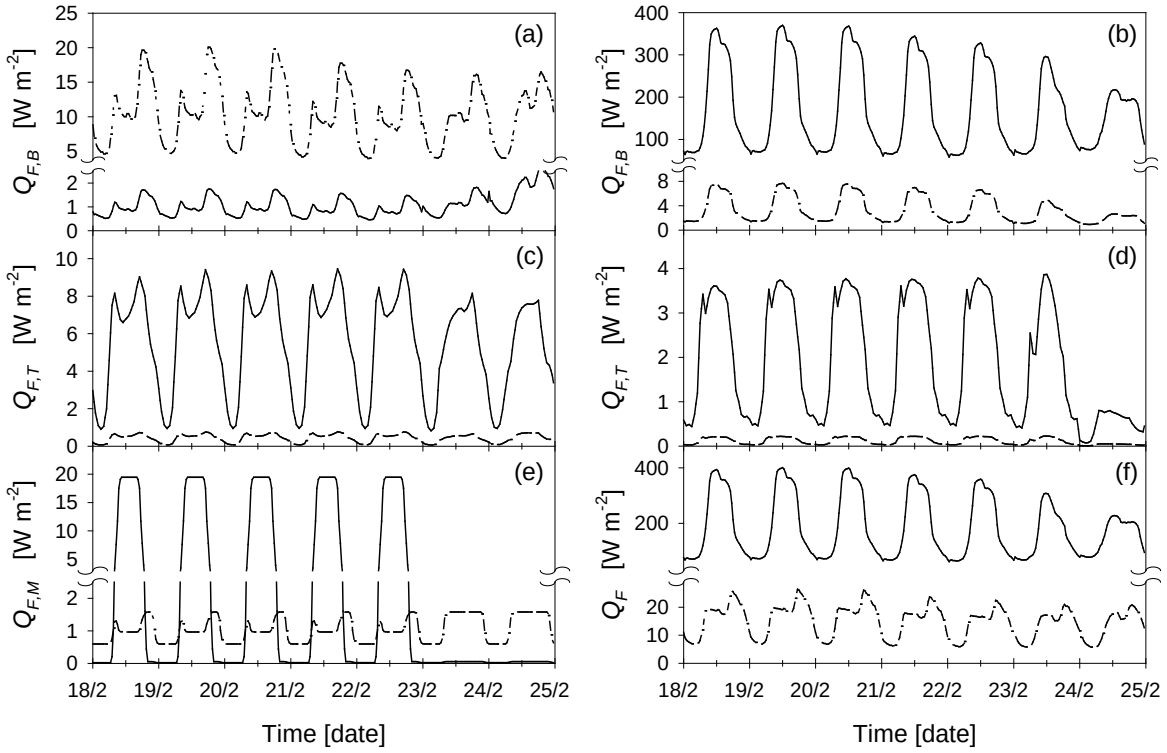

Figure 61: Half-hourly heat emissions during February 18-24, 2008 (Monday to Sunday) for cell ID 22030 (solid) and 22642 (dashed) from: buildings (a: domestic, b: industrial), road traffic (c: personal, d: freight), (e) metabolism and (f) total Q_F. Note the vertical axis is broken and is different between graphs.(Iamarino et al. 2011)

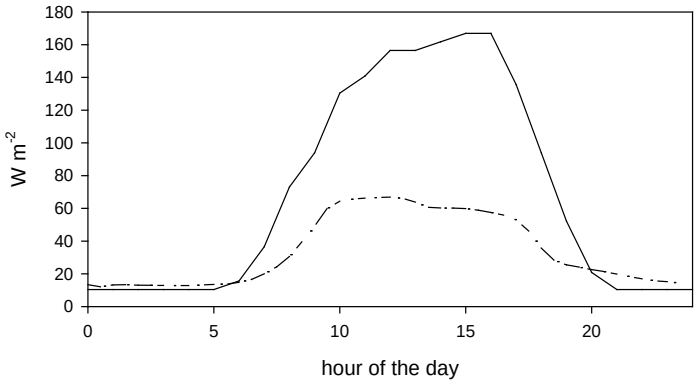

Figure 62: Summer day latent heat emissions from buildings with cooling towers in output area 00AAFZ0001 (solid) and $Q_{F,B}$ from same buildings (dashed).(Iamarino et al. 2011)

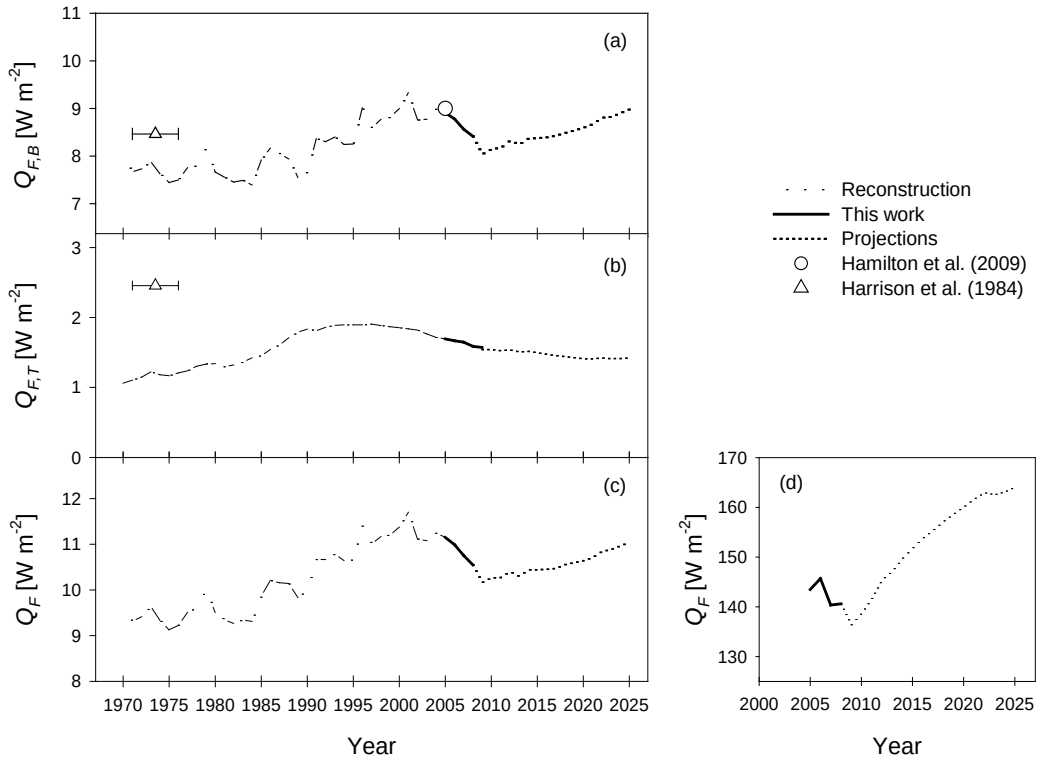

Figure 63: Heat emissions in Greater London from 1970 to 2025 for (a) building sector, (b) road traffic (b) and (c) total; and (d) total emissions in the City of London for 2005-2025.(Iamarino et al. 2011)

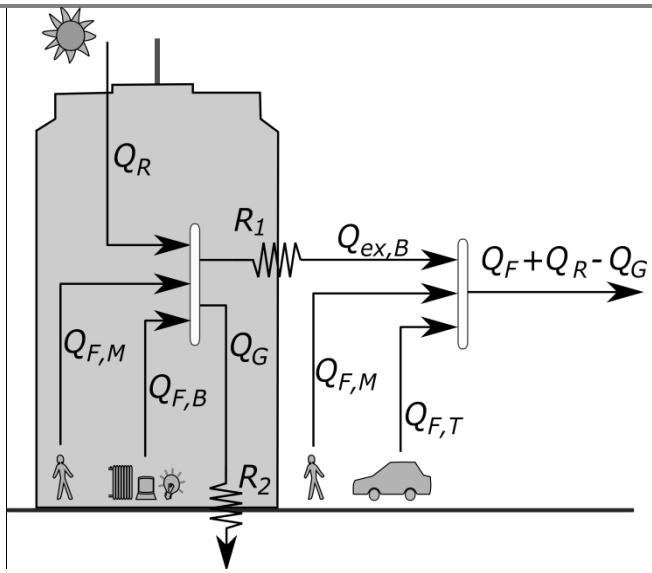

Figure 64: Anthropogenic heat and environmental loads (Iamarino et al. 2011)

Table 22: Data sources used in the Greater London (Iamarino et al. 2011).

Source	Description		Direct access	Last retrieved
DECC (Department of Energy and Climate Change)	1	Greater London gas, electricity and other fuel consumption	http://www.decc.gov.uk/en/content/cms/statistics/regional/regional.aspx	06/08/2010
	2	History of UK energy demand (1970-2009)	http://www.decc.gov.uk/publications/basket.aspx?filetype=4&filepath=Statistics%2fpublications%2fecuk%2f266-ecuk-overall-2010.xls	06/08/2010
	3	Calorific values of UK fuels	http://www.decc.gov.uk/en/content/cms/statistics/source/cv/cv.aspx	04/10/2010
	4	Projections of UK energy demand (2010-2025)	http://www.decc.gov.uk/en/content/cms/statistics/projections/projections.aspx	04/10/2010
DEFRA (Dept. for the Environment, Food and Rural Affairs)	1	Hourly traffic data – method document	http://www.airquality.co.uk/reports/cat05/1004010934_MeasurementvsEmissionsTrends.pdf	09/11/2010
DfT(Department for Transport)	1	Manual Classified Count and Automatic Count Data	http://www.dft.gov.uk/matrix/	09/11/2010
ERC (Energy Research Center)	1	Buildings energy load profiles	http://data.ukedc.rl.ac.uk/browse/edc	06/08/2010
GLA (Greater London Authority)	1	LEGGI 2008	http://data.london.gov.uk/datastore/package/leggi-2008-database	09/11/2010
	2	LAEI 2008	http://data.london.gov.uk/laei-2008	09/11/2010
	3	Central Activities Zone Boundaries	http://data.london.gov.uk/datastore/	22/11/2010

		(London Plan)	package/central-activities-zone-boundary-london-plan-consultation-2009	
	4	Projections of workplace and resident population in City of London	http://www.london.gov.uk/who-runs-london/mayor/publications/business-and-economy/employment-projections-2031	26/11/2010
NG (National Grid plc)	1	UK daily gas demand	http://marketinformation.natgrid.co.uk/gas/DataItemExplorer.aspx	06/08/2010
	2	UK half-hourly electricity demand	http://www.nationalgrid.com/uk/Electricity/Data/Demand+Data/	06/08/2010
ONS (Office for National Statistics)	1	NeSS hierarchy	http://www.neighbourhood.statistics.gov.uk/HTMLDocs/downloads/NeSS_Data_Exchange_Hierarchy_Diagrams_v0.1.pdf	09/08/2010
	2	Residents, workplace and daytime population – UK 2001 National Census	http://neighbourhood.statistics.gov.uk/dissemination/	01/07/2010
	3	Time use survey 2005	http://www.statistics.gov.uk/cci/article.asp?id=160	09/08/2010

5.3 Evaluation of Urban Land Surface Models[18]

A large number of urban land surface models (LSM) now exist with different assumptions about the important features of the surface and exchange processes that need to be incorporated. To date, no comparison of these models has been conducted; in contrast, models for natural surfaces have been compared extensively as part of the Project for Intercomparison of Land Surface Parameterisation Schemes.

The decision support system will incorporate a large number of different urban LSM (Table 23) with varying characteristics but not the complete range of models that are currently available. The DSS will also include results from models but not that are not available for rerunning by the user (e.g. the Single Layer Urban Canopy Model (SLUCM) has been used within the WRF simulations but is not being incorporated into the DSS. Urban land surface schemes have been developed to model the distinct features of the urban surface and the associated energy exchange processes. These models have been developed for a range of purposes, and make different assumptions related to the inclusion and representation of the relevant processes.

[18] This section is from these two papers:

Grimmond CSB, M Blackett, M Best, J Barlow, JJ Baik, S Belcher, SI Bohnenstengel, I Calmet, F Chen, A Dandou, K Fortuniak, ML Gouvea, R Hamdi, M Hendry, T Kawai, Y Kawamoto, H Kondo, ES Krayenhoff, SH Lee, T Loridan, A Martilli, V Masson,S Miao, K Oleson, G Pigeon, A Porson, YH Ryu, F Salamanca, GJ Steeneveld, M Tombrou, J Voogt, D Young, N Zhang (2010) The International Urban Energy Balance Models Comparison Project: First results from Phase 1*Journal of Applied Meteorology & Climatology*, ***49****, 1268-92, doi: 10.1175/2010JAMC2354.1*

Grimmond CSB, M Blackett, MJ Best, J-J Baik, SE Belcher, J Beringer, SI Bohnenstengel, I Calmet, F Chen, A Coutts, A Dandou, K Fortuniak, ML Gouvea, R Hamdi, M Hendry, M Kanda, T Kawai, Y Kawamoto, H Kondo, ES Krayenhoff, S-H Lee, T Loridan, A Martilli, V Masson S Miao, K Oleson, R Ooka, G Pigeon, A Porson, Y-H Ryu, F Salamanca, G-J Steeneveld, M Tombrou, JA Voogt, D Young, N ZhangInitial Results from Phase 2 of the International Urban Energy Balance Comparison Project, *International Journal of Climatology*31, 244-272

In the urban LSM comparison 33 models participated in Phase 1 and 31 models (Grimmond et al. 2010) in all four stages of Phase 2 (Grimmond et al. 2011). The aim of the comparison is two-fold: to identify those modelling approaches that minimise the errors in the simulated fluxes of the urban energy balance and to determine the degree of model complexity required for accurate simulations.

In Phase 1 evaluation is based on a dataset containing net all-wave radiation, sensible heat and latent heat flux observations for an industrial area in Vancouver.There is evidence that some classes of models perform better for individual fluxes but no model performs best or worst for all fluxes. In general, the simpler models perform as well as the more complex models based on all statistical measures.Generally the schemes have best overall capability to model net all wave radiation and least capability to model latent heat flux.

In Phase 2 evaluation of 32urban land surface schemes was conducted (Grimmond et al. 2011). In four stages, participants were given increasingly detailed information about an urban site for which urban fluxes were directly observed. At each stage, each group returned their models' calculated surface energy balance fluxes. Wide variations are evident in the performance of the models for individual fluxes. No individual model performs best for all fluxes. Providing additional information about the surface generally results in better performance. However, there is clear evidence that poor choice of parameter values can cause a large drop in performance for models that otherwise perform well. As many models do not perform well across all fluxes there is need for caution in their application and users should be aware of the implications for applications and decision making.

The results from the model comparison allow for the sizes of errors to be considered relative to the measurements. These errors are probably important to be aware of for determining what the impact of a difference between model runs/outputs are.

Conclusions that were drawn from Phase 2 after groups from around the world ran various urban land surface models in offline mode[19]over four stages, with increasing information about the site provided. Initially the groups knew only that the site was urban, but by Stage 4 detailed surface materials characteristics had been provided. In Grimmond et al. (2011) the ability to model the radiation and energy balance fluxes on average for a year is evaluated. It should be remembered that observations also have errors which vary with time of day, season, latitude, local geography and land cover. In the process of running the models, a small number of models improved for an individual flux at each stage as new information was provided (2, 2, 2, 5, 4; foroutgoing shortwave radiation $K\uparrow$,outgoing longwave radiation $L\uparrow$, net all wave radiation Q^*,turbulent sensible heat flux Q_H, turbulent latent heat flux Q_E respectively). However, there are other models that have a drop in performance with the addition of more complete information, and cases where there is a systematic decline at all stages (0, 1, 4, 0, 1; for $K\uparrow$, $L\uparrow$, Q^*, Q_H, Q_E respectively).

From the analysis of the data returned from the modelling groups in relation to the observed flux data the following conclusions are drawn (Grimmond et al. 2011):

- A wide range of model performance is evident for each flux. No individual model does best for every flux modelled. Clearly this finding has very significant implications for the application of any model. It may

[19] In this context this means the model is not linked to a large scale 3-d meteorological model, rather forcing is provided by observed data. By doing this the performance of the ULSM is separated from the impact of the 3-d model which may change the data provided to the surface scheme.

also imply that in some cases models perform well but for the wrong physical reasons. For example, if a model overestimates the net shortwave radiation, but accurately models the sensible heat flux, then it may indicate a problem also in the physical representation of the heat exchanges between the surfaces and the atmosphere (since it needs to "absorb" more energy to get the right sensible heat flux).

- Taking vegetation cover into account (or not) significantly impacts model performance. This conclusion is in agreement with those of Phase 1 (Grimmond et al. 2010) where the site had a much lower plan area fraction of vegetation than the Phase 2 site. Data provided at Stage 2 (surface cover fractions) usually had the largest impact on model performance. Moreover, the fact that the RMSE for the latent heat flux is of the same order as the latent heat flux itself, indicates that work needs to be done to improve simulations of this flux.
- Closure of the radiation balance is not a good measure of the ability to calculate a particular radiative flux. Comparing the performance of the components of the radiation balance to the net all wave radiation shows a clear re-ranking between fluxes. Notably those that perform poorly for an individual component flux are not the poorest for Q* (see Grimmond et al. 2011 Figures 2, 5, 8). This means it is important that when a user applies a model they are aware of the performance of the ULSM not only for the initial flux of interest but also for the other fluxes for which the user may wish to infer impact. Given the increasing use of ULSM for assessing mitigation and adaptation strategies this is very important.
- Overall the ULSM generally model $K_{\uparrow}$well and additional surface information does result in an improvement of performance. The models are able to estimate reasonably well the amount of energy absorbed by the urban fabric, but have bigger problems in partitioning it between longwave, sensible, latent and storage heat fluxes.
- Overall $L_{\uparrow}$ is not as well modelled as $K_{\uparrow}$. The set of model characteristics that minimise the errors in the outgoing longwave radiation change with the time of day. Generally performance improved when the pervious/impervious fraction became known but did not when heights and further information on surface fractions were provided. The performance of most models deteriorated when building material information was provided; typically back to the levels at Stage 1 but in many cases even poorer. Given the difficulty to gather appropriate values of material characteristics, their provision may not currently be worth the effort given how models then perform. Alternatively, there is a need to ensure that the data are of much better quality than is currently 'easily' obtainable.
- Net all wave radiation is modelled better than either $K_{\uparrow}$or$L_{\uparrow}$. In general the radiative fluxes are modelled better than the turbulent fluxes. The net all wave radiation is clearly the best modelled flux which is in agreement with Phase 1 results (Grimmond et al. 2010). There is clear trade off in performance between net all wave radiation (Q*) and turbulent sensible heat flux (Q_H) which is in agreement with Loridan et al. (2010a).
- The errors from the models were smaller during the night than they were during the daytime, although this might be expected as the surface energy balance is not dominated by the solar radiation during this period.
- For the net radiation, simple characteristics give the best results for both daytime and night-time, although there is much greater variability between the classes than for the outgoing longwave radiation.
- The models that perform best, for individual characteristics, are those that are the simplest as they can be assigned one parameter that is close to the observed value. Based on overall complexity the simplest and the most complex have similar results which are better than the medium complexity models.

- Additional surface information is important in improving model performance. However, there is evidence that good model physics is not enough to prevent the users' choice of parameter values from significantly influencing the outcome. Therefore it is essential when models are being used for scenario testing that appropriate parameter values are used.
- Simpler models often showed a net improvement with additional information; the more complex models did not. This may be because there was not enough additional detailed information provided so it was more difficult for the users to decide how to use this information appropriately. It is important to note that parameters specified for simpler models (e.g. overall albedo) often equate to empirical aggregations of processes in more complex models (e.g., the net effect of reflections due to facet albedos). Nevertheless, the results here suggest that increased model complexity does not necessarily increase model performance.
- It is expected that more complex models may have more potential for future improvements as they are able to resolve more details without deteriorating their performance. The most complex models are more flexible and have the potential to describe the biophysical interactions between the atmosphere and urban surfaces. Although the ability to do this has not been tested here, these models can provide vertical profiles of atmospheric variables within the urban canopy layer. If the simulation is for weather forecasting, a good estimate of the heat fluxes at the top of the urban canopy is probably sufficient, and, consequently, a simple scheme may be the appropriate choice. Whereas if air quality is the focus, the atmospheric behaviour within the urban canopy layer may be important, and a more complex scheme can be useful. An important finding of PILPS-urban is that in many cases, work is needed to improve the complex schemes (both in terms of physics and definition of numerical constants), in order to have skills comparable to those of the more simple schemes in estimating energy fluxes at the top of the urban canopy. More complicated models are generally more difficult to use and it is even difficult for modellers to identify which are the most critical points of their model.
- As a community it is clear that in terms of surface characteristics, the information up to Stage 3 benefited a large number of models. The albedo and emissivity were also beneficial (Stage 4) but the provision and acquisition of the most appropriate wall, roof and road thermal properties need further thought and development from the modelling community. This model comparison has already generated a suggested improved method for thermal parameter specification that accounts for the high degree of heterogeneity of such parameters in cities (Salamanca et al. 2009). Hopefully additional analyses will shed more light on this issue.
- Using an ensemble of models rather than one model is generally better than any individual model for an individual flux. In general the medium complexity ensemble performs least well and the simple performs best. The 'all' ensemble is always better than the medium complexity. Given the overall better performance of the ensembles they may be better than using one individual model when considering all of the fluxes.

Table 23: Urban Land Surface Models that are being used in the BRIDGE DSS and whether they participated in the urban model comparison.

Model Name	Group	Participated in model comparison
Surfex(TEB)	Meteo – France	Yes
LUMPS	KCL	Yes
SUEWS	KCL/UH	No
ACASA	UNISS	No
SLUCM	UPM	Yes
SimGro	WU	No

5.4 LUMPS/SUEWS[20]: overview [Author: Järvi, Loridan &Grimmond]

Loridan et al. (2011) provides an overview of recent developments to the Local-scale Urban Meteorological Parameterization Scheme (LUMPS), a simple user-friendly model able to simulate the urban energy balance. The major development is the coupling of LUMPS to the Net All-Wave Radiation Parameterization (NARP). Others include that the model now accounts for: changing availability of water at the surface; seasonal variations of active vegetation; and the anthropogenic heat flux; while maintaining the need for only commonly available meteorological observations and basic surface characteristics. The incoming component of the longwave radiation (L↓) is improved through a simple relation derived using cloud cover observations from a ceilometer collected in central London.

Järvi et al. (2011) describe and evaluate the urban energy and water balance model (SUEWS),which uses a small number of commonly measured meteorological variables (Table 24) and information about the surface cover (Table 25).The models contains LUMPS within it and then a more biophysically responsive evaporation-interception model for a single layer with multiple surface types (paved (PAV), buildings (BLD), coniferous trees and/or shrubs (CT), deciduous trees and/or shrubs (DT), irrigated grass (GI), non-irrigated grass (GU) and water (W)). Below each surface type, except water, there is a single soil layer. At each time step the moisture state of each surface is calculated. Horizontal water movements at the surface and in the soil are incorporated.

[20] This section is drawn from:

Loridan T, CSB Grimmond, BD Offerle, DT Young, T Smith, L Jarvi, F Lindberg. Local-Scale Urban Meteorological Parameterization Scheme (LUMPS): longwave radiation parameterization & seasonality related developments Journal of Applied Meteorology&Climatology.**50**: 185-202doi: 10.1175/2010JAMC2474.1

JärviL, CSB Grimmond, A ChristenThe**S**urface**U**rban **E**nergy and **W**ater Balance **S**cheme (SUEWS): Evaluation in Vancouver and Los Angeles. *Journal of Hydrology (in review)*

Table 24: Required (a) meteorological input and (b) output variables of the model. (Järvi et al. 2011)

Variable	Units
(a) Input	
Mean wind speed (u)	m s^{-1}
Relative humidity (RH)	%
Air temperature (T)	°C
Air pressure	kPa
Precipitation (P)	mm h^{-1}
Incoming short wave radiation ($K\downarrow$)	W m^{-2}
(b) Output	
Net all-wave radiation (Q^*)	W m^{-2}
Radiation components: K↑, L↑,L↓	W m^{-2}
Surface temperature	°C
Sensible heat flux - LUMPS (Q_H)	W m^{-2}
Latent heat flux - LUMPS (Q_E)	W m^{-2}
Storage heat flux (ΔQ_S)	W m^{-2}
Sensible heat flux -SUEWS (Q_H)	W m^{-2}
Latent heat flux - SUEWS (Q_E)	W m^{-2}
Evapotranspiration (E)	mm h^{-1}
External water use (I_e)	mmh^{-1}
Drainage (D)	mm h^{-1}
State of the surface storages (C_i)	mm
State of the soil storages ($C_{soil,i}$)	mm
Surface and soil runoff (r)	mm h^{-1}
Aerodynamic resistance (r_a)	s m^{-1}
Surface resistance (r_s)	s m^{-1}
Friction velocity (u_*)	m s^{-1}
Obukhov length (L)	m
Soil moisture deficit ($\delta\theta$)	mm
Leaf area index (LAI)	m^2 m^{-2}
Total runoff (r)	mm
Runoff to sewers (r_{sew})	mm
Above ground runoff (r_{agr})	mm
Soil runoff (r_{soil})	mm

Table 25: Parameters in alphabetical order that need to be specified in order to run SUEWS. All are given a default value - those in **bold** *are the ones that site specific values are most critical for. Equation number referred to are in Järvi et al. (2011).*

Name	Units	Description
α_i	-	Effective surface albedo for *i*th surface
α_{snow}	-	Effective surface albedo for snow (used in NARP)
$\lambda_{g,irr}$	-	Fraction of irrigated grass (LUMPS)
$\lambda_{pav,irr}$	-	Fraction of irrigated paved areas (LUMPS)
$\lambda_{t,irr}$	-	Fraction of land in which trees are irrigated (LUMPS)
ε_i	-	Effective bulk surface emissivity for *i*th surface
ε_{snow}	-	Effective surface emissivity for snow
$\boldsymbol{\Delta F_w}$	**Mm**	Difference in input and output flows for the water surface type
$a_{0,\{wd,we\}}$	W m^{-2} (capita ha^{-1})$^{-1}$	Parameterdefining the base Q_F per capita in (3)
$a_{1,\{wd,we\}}$	W m^{-2} K^{-1} (capita ha^{-1})$^{-1}$	Parameter related to CDD in (3)
$a_{2,\{wd,we\}}$	W m^{-2} K^{-1} (capita ha^{-1})$^{-1}$	Parameter related to HDD in (4)
$\boldsymbol{A_s}$	**Ha**	**Surface area of the study area**
B	-	Empirical coefficient in (T2.1-T2.2)
b_0(a,m)	Mm	Parameter related to daily I_e in (10)
b_1(a,m)	mm K^{-1}	Parameter related to daily I_e in (10)
b_2(a,m)	mm d^{-1}	Parameter related to daily I_e in (10)
$\boldsymbol{C_i}$	**Mm**	**Initial wetness state for *i*th surface type**
$\boldsymbol{C_{soil,i}}$	**Mm**	**Initial state of the soil storage of *i*th surface type**
Cap_{Sew}	Mm	Maximum capacity of sewers
$D_{0,i}$	Mm	Drainage rate of ith surface in maximum wetness state
$\mathbf{DLT_{start}}$	**Doy**	**Start of the daylight savings time (used for I_e and Q_F)**
$\mathbf{DLT_{end}}$	**Doy**	**End of the daylight savings time (used for I_e and Q_F)**
$\boldsymbol{f_{aut}}$	-	**Fraction of irrigated area using automatic irrigation**
G_1	mm s^{-1}	Parameter related to the maximum surface conductance
G_2	W m^{-2}	Parameter in $g(K\downarrow)$
G_3	kg g^{-1}	Parameter in $g(\delta q)$
G_4	g kg^{-1}	Parameter in $g(\delta q)$
G_5	°C	Parameter in $g(T)$
G_6	mm^{-1}	Parameter in $g(\delta\theta)$
GDD_i	-	Growing degree days when leaf-on for *i*th vegetation surface
$\boldsymbol{I_{e,start}}$	**doy**	**Starting day for external irrigation**
$\boldsymbol{I_{e,end}}$	**doy**	**Ending day for external irrigation**
km	mm s^{-1}	Hydraulic conductivity of soil
$K\downarrow_m$	W m^{-2}	Maximum of $K\downarrow$in surface conductance equation
$LAI_{Max,i}$	m^2 m^{-2}	Maximum LAI for *i*th vegetation surface
$LAI_{Min,i}$	m^2 m^{-2}	Minimum LAI for *i*th vegetation surface
lat	°	**Latitude of the site**
lng	°	**Longitude of the site**
$\boldsymbol{p}$	**inh ha^{-1}**	**Population density in the area**
P_c		Water capacity of sewers
res_{drain}	mm h^{-1}	Drainage rate of the surface (LUMPS)
R_C	mm	Limit when the total surface is totally covered with water (LUMPS)
res_{cap}	mm	Capacity of the surface to hold water (LUMPS)
S_1	mm	Fitted parameter in calculation of surface resistance
S_2	mm	Fitted parameter in calculation of surface resistance
S_i	mm	Storage capacity for *i*th surface
$S_{soil,i}$	mm	Soil storage of *i*th surface type
SDD_i	°C	Senescence ending degree day for *i*th vegetation surface
tt	-	Atmospheric transmissivity
$T_{BaseGDD}$	°C	Base temperaturefor vegetation growth of *i*th vegetation surface

T_{BaseSDD}	°C	Base senescence temperaturefor vegetation of *i*th vegetation surface
T_{BaseQF}	°C	Base temperature for Q_F
$\boldsymbol{T_H}$	**°C**	**Maximum temperature limit**
$\boldsymbol{T_L}$	**°C**	**Minimum temperature limit**
$\boldsymbol{T_{\mathrm{step}}}$	**s**	**Timestep**
$\boldsymbol{T_{ZONE}}$	**h**	**Time zone relative to UTC**
$\boldsymbol{z_h}$	**m**	**Mean height of buildings**
$\boldsymbol{z_m}$	**m**	**Measurement height of meteorological input variables**
z_{soil}	mm	Soil depth of the modeled soil moisture
z_{tr}	m	Mean height of trees

5.4.1 LUMPS/SUEWS evaluation: non-BRIDGE sites **[Grimmond]**

LUMPS has been evaluated at a number of sites. First using observed net all wave radiation to drive the model was evaluated in nine North American sites (Grimmond and Oke 2002).The radiation model was tested independently in Offerle et al. (2003). The new combined version of LUMPS is evaluated by Loridan et al. (2011).The new L↓ formulation is evaluated with two independent multi-year datasets (Łódź, Poland and Baltimore, USA) and compared to alternatives that include: the original NARP and a simpler one using the U. S. National Climatic Data Center cloud observation database as input. The performance for the surface energy balance fluxes is assessed using a two year dataset (Łódź). Results have an overall RMSE < 34 W m^{-2} for all surface energy balance fluxes over the two year period when using L↓ as forcing, and RMSE < 43 W m^{-2} for all seasons in 2002 with all other options implemented to model L↓.

Järvi et al. (2011) test SUEWS/ LUMPS against direct flux measurements carried out over a number of years in Vancouver, Canada and Los Angeles, USA. At all measurement sites the model is able to simulate the net all-wave radiation and turbulent flux densities of sensible and latent heat well (rmse = 25-47 W m^{-2}, 30-59 and 20and 55 W m^{-2}, respectively). SUEWS reproduces the diurnal cycle of the turbulent fluxes but underestimates latent heat flux and overestimates sensible heat flux in the day time. The model tracks measured surface wetness and simulates the variations in soil moisture content. It is able to respond correctly to short-term events as well as annual changes. The largest uncertainty relates to the determination of roughness length for heat and surface conductance.

5.4.2 SUEWS evaluation: BRIDGE **[Author: Grimmond]**

Using the observations collected as part of the BRIDGE project SUEWS is evaluated. It is evaluated at two sites[21] (London and Helsinki). The fluxes evaluated consist of the following:

a) Radiation components (London, Helsinki)
b) Sensible and Latent heat flux(London, Helsinki)
c) Soil moisture (London)
d) Surface temperature (London)
e) Runoff (Helsinki)
f) Water Use (Helsinki, summer 2011)

[21] If time permits data from the other sites may also be used for evaluation purposes.

The evaluation and results for the model runs are split by site. Prior to the model results the site characteristics and the forcing data are briefly described for each site.

5.4.3 Site Characteristics: London **[Author: Lindberg &Grimmond]**

To characterize the London site the databases described in D.3.4: London Case Study are used. The key data sources are given in Table 26. The areas of interest for modelling purposes in London are (Figure 65):

a) Central Activity Zone (CAZ)
b) Locations of the flux towers (KSS, KSK)
c) Soil moisture sites (HAN, EMB, JUB,TEM)

The current vegetation, the heights of buildings and the topography in the CAZ can be seen in Figure 66. The modelling is done initially using the grids shown in this Figure. The flux towers are in grid 3004 so this is used as the initial basis for surface characterization.

Table 26 : Data sets used to characterize London surface characteristics

Code	Source	Description
LI58	GLA	Infoterra LiDAR datasummer 2008 and summer 2005 (1 m^2 resolution)
VL	GLA/ ERG[22] – KCL	Virtual London calculated from LiDAR data – has the building characteristics
OS	KCL	OS MasterMap® Topography Layer data
STI	Individual Boroughs, via the Forestry Commission	Street Tree Inventory data
GRP	Matthew Thomas, GLA	ArcGIS Layer with slopes and area of roofs that are potential locations for installinggreen roofs calculated from LiDAR data- UCL
LCC	Lindberg and Grimmond (2011)	Land cover data set created with surface characteristics

[22] ERG – KCL: Environmental Research Group – King's College London

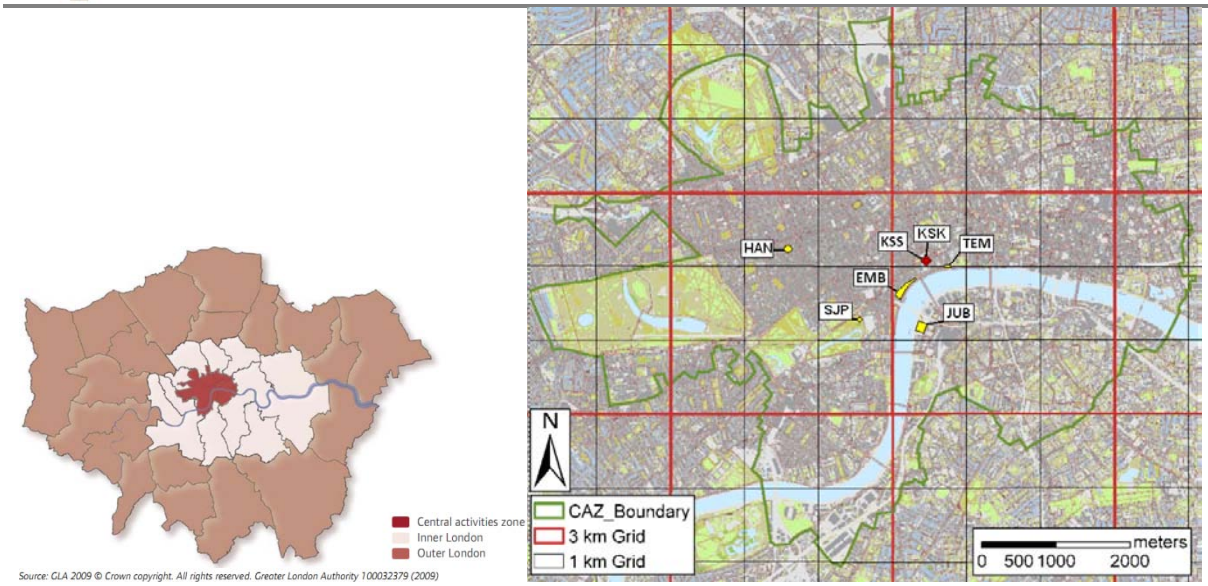

Figure 65: (left) Location of Central Activity Zone[23] (CAZ) within Greater London (lines are the 33 Boroughs, blue River Thames) and (right) CAZ with a 1 km and 3 km grid. Location of tower sites (KSS, KSK) and soil moisture sites (HAN, EMB, JUB, TEM) and St. James's Park meteorological enclosure are indicated.

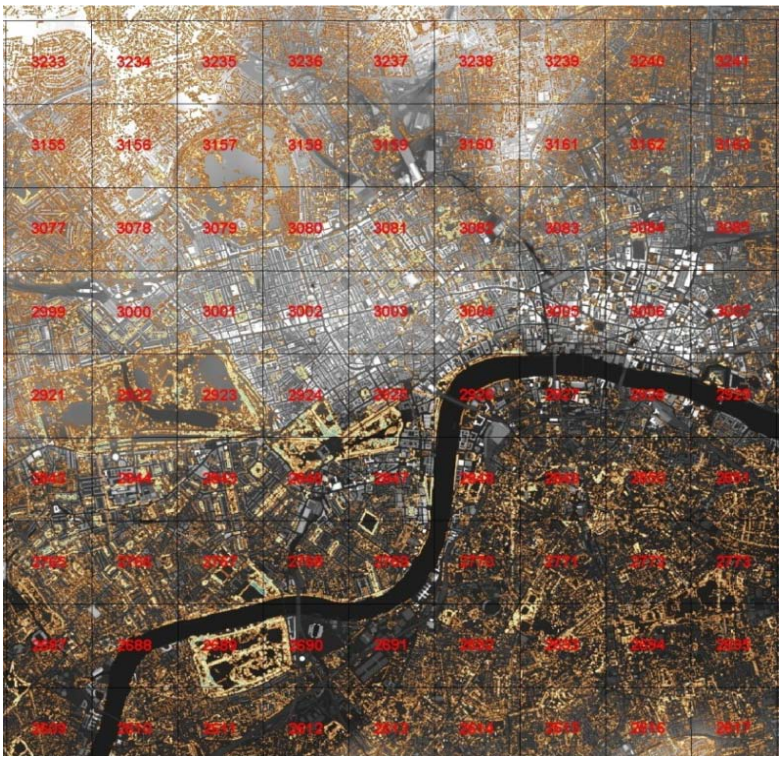

Figure 66: Central Activity Zone of London (with 1 km grid). Grid 3004 is where KCL is located. Topography and building height shown in black and white (white higher). Trees shown in brown to green scale with green being taller.

[23]http://www.london.gov.uk/shaping-london/london-plan/docs/london-plan.pdf

5.4.4 SUEWS: Results London [Author: Castillo, Järvi, Kotthaus, Grimmond]

The forcing data used to run the model is from instruments mounted on KSS tower for the period January 1 2010 to December 31, 2010.To create a complete forcing data set it was necessary to gap fill some missing time periods (

Table 27). The techniques used to gap-fill are the following:

M1) Linear interpolation between missing data points if less than 3 time periods;

M2) Replace with data from KSK for missing period;

M3) Average data from previous and next days because period missing for an individual day larger than M1 method.

To evaluate the model performance the following data are used:

a) Radiation flux data;
b) Turbulent heat fluxes;
c) Surface temperatures;
d) Soil moisture.

Like the forcing data these data sets are not complete. Table 28 provides the amount of data that are available for the evaluation. For both surface temperature and soil moisture these measurements are micro-scale point measurements (see D.3.4 London Observation Case Study report). For evaluation purposes these data are averaged together to provide a mean value.

Table 27: Forcing data used for model runs. Number of 30-minute periods and method used for gap filling.

Variable	**KSS 2010 (30 min) Total: 17520**
K↓	M2: 169 ; M3: 54
L↓	M1: 4; M2: 338; M3: 54
Air temperature	M1: 2; M2: 217
Relative humidity	M1: 2; M2: 217
Station pressure	M1: 2; M2: 217
Wind speed	M1: 2; M2: 217
Precipitation	M2: 982 (ARG100 data used)

Table 28: Amount of data available to evaluate the model performance

Variable	**KSS 2010 (30 min) Total: 17520**
Q*	17300
L↓	17290
K↑	7778
L↑	17300
Soil moisture	7415
Surface temperature	10320

SUEWS (version 1.0) was run for London using Grid 3004 (Figure 66) and meteorological forcing data for 2010. The model results, which include the components for radiative fluxes, energy balance, and water balance; are presented here along with their evaluation against observed radiation, turbulent heat fluxes, soil moisture, and surface temperature. The settings for the model options are given in Table 29, while the values for the input parameters used are in

Table 30.

Table 29 : Settings for SUEWS v1.0 run options for London (Grid 3004Figure 66; 2010 KUMA data)

Model Run Options	**Value**	**Description**
Anthropogenic heat choice	2	Q_F was calculated
GIS input type	3	Land cover data stays constant with time
Net radiation choice	2	Net radiation was modelled using NARP
ΔQ_S choice	1	Modelled using OHM; based on surface types
SUEWS status	1	SUEWS part was calculated
Vegetation type (fraction)	1	For turbulent fluxes: sum of all vegetation from total surface area
z_0 method	2	$z_0$and *d* calculated from mean building height with "Rule of Thumb"
Roughness length for heat	2	According to Kawai *et al*., 2009
Soil moisture deficit	0	Modelled
Stability method	2	Momentum: Unstable – Dyer 1974, modified by Högstrom 1988; Stable – Van Ulden & Holstag 1985Heat: Dyer, modified by Högstrom 1988
External water use choice	0	Modelled
OHM options: canyons	2	Canyons were not included
OHM options: vegetation	2	Separated to grass/ tree & shrubs/water
OHM options: veg. coefficients	3,4	Short grass (Doll *et al*., 1985) and bare soil (Novak 1982)
OHM options: roof coefficients	1	Mean for all
OHM options: impervious areas	2	Separated to concrete and asphalt
OHM options: imp. coefficients	2,4	Concrete (Doll *et al*., 1985) and asphalt (Narita *et al*., 1984)

Table 30: Parameter values used in the London runs (defined in Table 25)

Name	Units	Value
α_{snow}	-	0.35
$\lambda_{g,irr}$	-	0.8
$\lambda_{pav,irr}$	-	0
$\lambda_{t,irr}$	-	0
ε_i	-	(Pav) 0.95; (Bld) 0.91; (CT) 0.98; (DT) 0.98; (GI) 0.93; (GU) 0.93; (W) 0.95; (Snow) 0.99
ΔF_w	mm	0
$a_{0,\{wd,we\}}$	W m^{-2} (capita ha^{-1})$^{-1}$	0.014711
$a_{1,\{wd,we\}}$	W m^{-2} K^{-1} (capita ha^{-1})$^{-1}$	0.00044444
$a_{2,\{wd,we\}}$	W m^{-2} K^{-1} (capita ha^{-1})$^{-1}$	0.00048889
A_s	Ha	100
C_i	mm	(all) 0
$C_{soil,i}$	mm	(Pav) 95; (Bld) 65; (CT) 140; (DT) 140; (GI) 140; (GU) 140
Cap_{Sew}	mm	700
$D_{0,i}$	mm	(Pav) 10; (Bld) 10; (CT) 0.013; (DT) 0.013; (GI) 10; (GU) 0.013
DLT_{start}	Doy	87 (28 March 2010)
DLT_{end}	Doy	304 (31 October 2010)
f_{aut}	-	0.1
G_1	mm s^{-1}	14.5
G_2	W m^{-2}	484.93
G_3	kg g^{-1}	0.222
G_4	g kg^{-1}	3.27
G_5	°C	10.92
G_6	mm^{-1}	0.019
GDD_i	-	(all) 300
$I_{e,start}$	doy	100
$I_{e,end}$	doy	270
km	mm s^{-1}	0.0005
$K\downarrow_m$	W m^{-2}	950
$LAI_{Max,i}$	m^2 m^{-2}	(CT) 5.1; (DT) 5.5; (GI) 5.9; (GU) 5.9
$LAI_{Min,i}$	m^2 m^{-2}	(CT) 4; (DT) 1; (GI) 1.6; (GU) 1.6
lat	°	51.5153
lng	°	0.11453
p	inh ha^{-1}	30
res_{drain}	mm h^{-1}	0.25
R_C	mm	1
res_{cap}	mm	10
S_i	mm	(Pav) 0.25; (Bld) 0.48; (CT) 1.2; (DT) 0.3; (GI) 1.9; (GU) 1.9
$S_{soil,i}$	mm	(Pav) 100; (Bld) 70; (CT) 150; (DT) 150; (GI) 150; (GU) 150
SDD_i	°C	(all) -450
tt	-	1

$T_{BaseGDD}$	°C	(all) 5
$T_{BaseSDD}$	°C	(all) 13
T_{BaseQF}	°C	18.2
T_H	°C	28
T_L	°C	-4
T_{step}	s	1800
T_{ZONE}	h	0
z_h	m	19.559
z_m	m	31
z_{soil}	mm	250
z_{tr}	m	14

The runs of SUEWS v1.0analysed for London (Table 31) have the following main differences: incoming longwave radiation (L↓) option and albedo values. The L↓ was either calculated from air temperature and relative humidity (Runs 1 and 3), or was an input variable (Runs 2 and 4). Albedo values for Runs 1 and 2 were the default values, while those for Runs 3 and 4 were lowered based on the observed albedo at KSS.

Table 31 also lists the level of data processing for the variables used as input for SUEWS v1.0 and for evaluation. Generally, level 0 (L0) pertains to raw data, level 1 (L1) time averaged data, level 2 (L2) preliminary correction (e.g. correcting any known incorrect timestamps), level 3 (L3) secondary corrections (e.g. adjustments for calibration), and level 4 (L4) gap-filled data. The SUEWS v1.0 results use a subscript to indicate which run it is associated with (e.g.; Q^*_1 for Run 1). As we have a number of versions of data and the processing is continuing, the data used from the KUMA archive[24] is indicated

Table 31).

Table 31 : Parameter settings and values for all London runs

Parameters	Run 1	Run 2	Run 3	Run 4
L↓	Calc from T& RH	Input	Calc from T& RH	Input
α_{PAV}	0.12	0.12	0.10	0.10
α_{BLD}	0.15	0.15	0.10	0.10
α_{CT}	0.10	0.10	0.10	0.10
α_{DT}	0.18	0.18	0.15	0.15
α_{GI}	0.21	0.21	0.17	0.17
α_{GU}	0.21	0.21	0.18	0.18
α_W	0.10	0.10	0.10	0.10
	Level of data processing for variables; date of processing			
K↓ input	L4; 2011-06-15	K↑ evaluation		L2; 2011-06-14
L↓ input	L4; 2011-06-15	L↓ evaluation		L2; 2011-06-14
Wind speed	L2; 2011-01-12	L↑ evaluation		L2; 2011-06-14
Relative humidity	L2; 2011-01-12	Surface temperature		L2; 2011-02-11
Air temperature	L2; 2011-01-12	Soil moisture		L0; 2011-04-15
Air pressure	L2; 2011-01-12	Rainfall		L0; 2011-01-28

[24]http://geography.kcl.ac.uk/micromet/index.htm

Results for the radiation (Figure 67,Figure 68) components include outgoing shortwave radiation (K↑), incoming longwave radiation (L↓), outgoing longwave radiation (L↑), and net all-wave radiation (Q*). The modelled values for K↑ and L↑ for individual surfaces include paved surfaces (PAV), buildings (BLD), coniferous trees/shrubs (CT), deciduous trees/shrubs (DT), irrigated grass (GI), non-irrigated grass (GU), and water (W) are shown. However, the instrument for the observed radiation is located on the KSS tower, wherein the field of view is primarily of buildings and paved area. From Figure 66, one can see that the vegetation and water are limited to a small compact area within this grid.

The diurnal monthly averages for the components of radiative fluxes for Runs 1 and 2 (Figure 67), as well as Runs 3 and 4 (Figure 68), for the London Grid 3004 (Figure 66) show generally good performance for the model. The assessment of the runs covers both L↓ option and the albedo values. The modelled L↓ (Runs 1 and 3; Figure 67 and Figure 68) are underestimated especially during winter, making it apparent that using observed L↓ is probably the better option for running SUEWS v1.0. However for the DSS, it will be necessary to assess if the forcing L↓ (e.g. from WRF modelling) or the modelled values are better to use. Since Runs 1 and 2 overestimate K↑, the albedo values for Runs 3 and 4 (Table 31) were changed to be consistent with the observed values, resulting in better performance of the modelled K↑ and Q*.

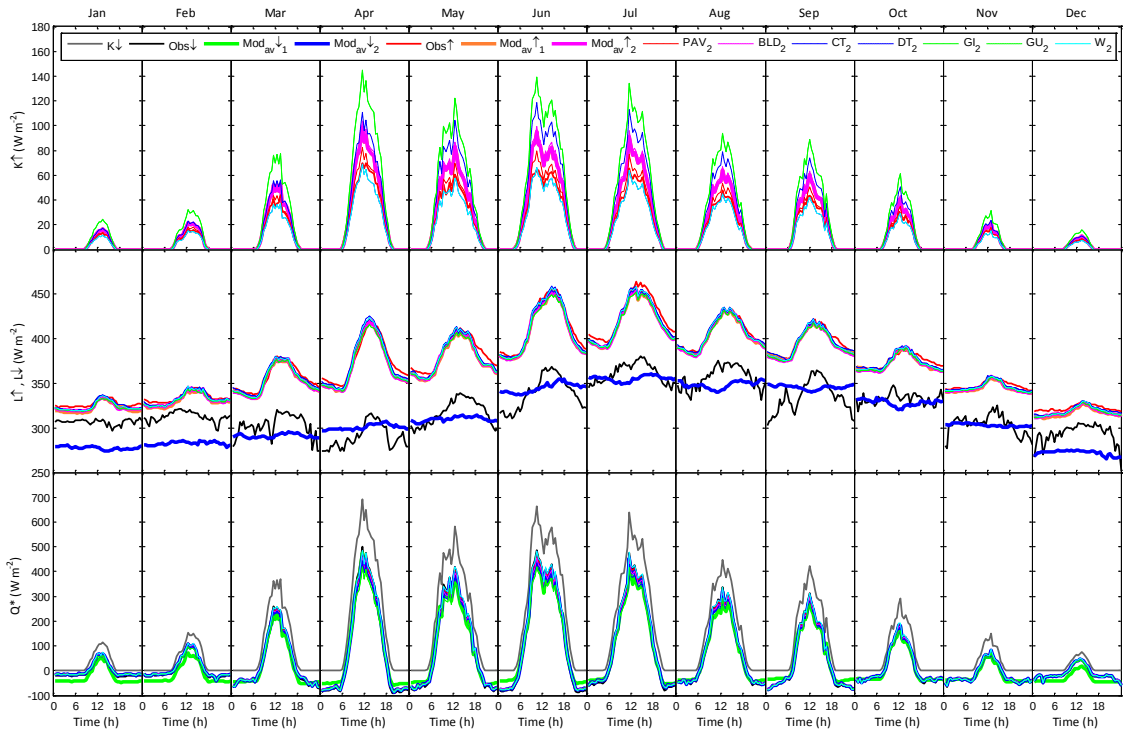

Figure 67: SUEWS v1.0results for London grid 3004 (Figure 66; Runs 1 and 2): diurnal monthly averages of the components of radiative fluxes, including those for the different surfaces.

The comparison between the modelled values for Q*, L↓, K↑, and L↑from SUEWS v1.0 and observations for the individual 30 min periods are shown in Figure 69, Figure 70, Figure 71, and Figure 72, respectively. Generally, all runs behave consistently with the observation data. Overall, Run 4 has the best fit with the observation data. The best RMSE for Q*, which is for Run 4, is 12 W

m^{-2} (Figure 69). For Run 4 the RMSE for K↑ is 5 W m^{-2} (Figure 71) and for L↑ is 6 W m^{-2} (Figure 72).

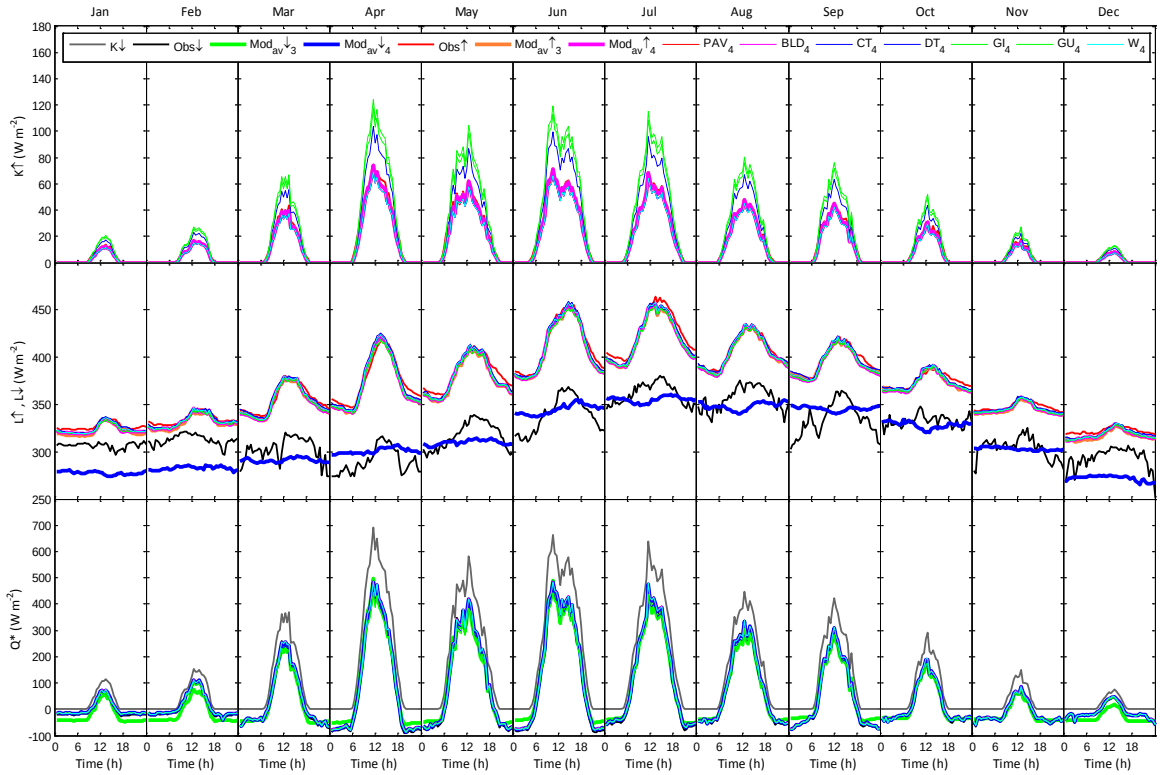

Figure 68: SUEWS v1.0 results for London grid 3004 (Figure 66; Runs 3 and 4): diurnal monthly averages of the components of radiative fluxes, including those for the different surfaces.

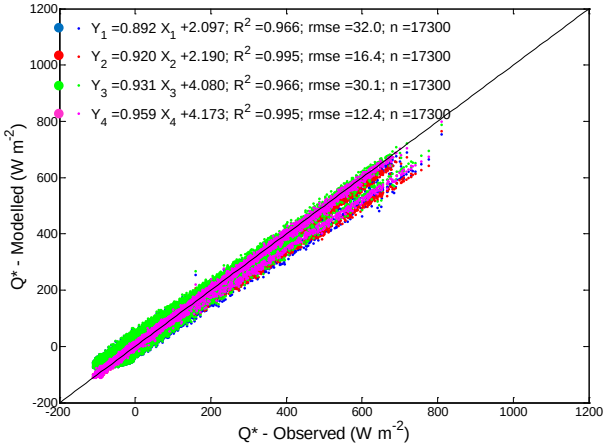

Figure 69: Evaluation of SUEWS v1.0 results for London grid 3004 (Figure 66; Runs 1-4): net all-wave radiation.

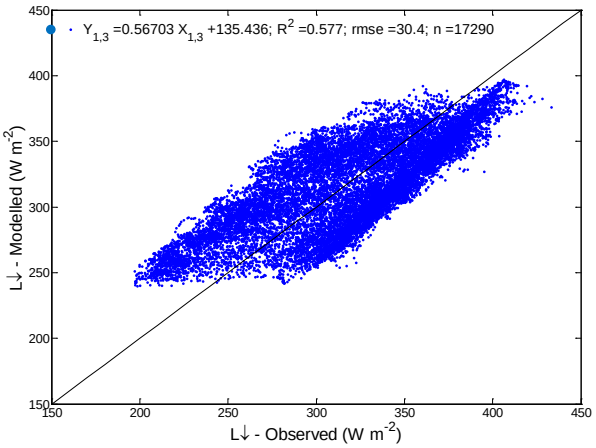

Figure 70: Evaluation of SUEWS v1.0 results for London grid 3004 (Figure 66; Runs 1 and 3): incoming longwave radiation.

Using observed L↓ as an input variable reduces the RMSE for Q* (Figure 69) from 32 to16 W m^{-2} (R1, R2) or 30 to 12 W m^{-2} (R3, R4). The impact of modelling L↓is clearly seen in when the mean time series plot are compared (Figure 67 and Figure 68) and in the scatter of the modelled L↓ for Runs 1 and 3 (Figure 70).

Changing the albedo values for Runs 3 and 4 to be consistent with the observed values improves the slope of Q relative to the 1:1 line (Figure 69). This obviously is driven by the change in K↑ (Figure 71) with RMSE reduction of more than half from 11 to 5 W m-2 (R1/2 to R3/4). Even with this improvement for modelled K↑, the lower range of modelled values (K↑< 50 W m-2) suggest that the albedo values*

(Table 31) are too low. One area for development for SUEWS is to no longer treat the albedo as constant but as a function of zenith angle and transmissivity.

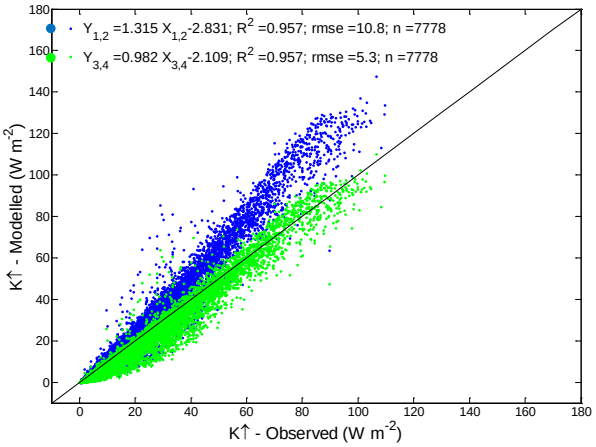

Figure 71: Evaluation of SUEWS v1.0 results for London grid 3004 (Figure 66; Runs 1-4): outgoing shortwave radiation K↑.

Although the impact of the differences in the runs is not as obvious for L↑ (Figure 72), the results still confirm that L↓ option as input variable is a better choice for SUEWS v1.0. The RMSE for Runs 2/4 is 6 W m^{-2} (Figure 72). The energy balance for a typical winter day (DOY 42) and summer day (DOY 154) for 2010 are shown in Figure 73.

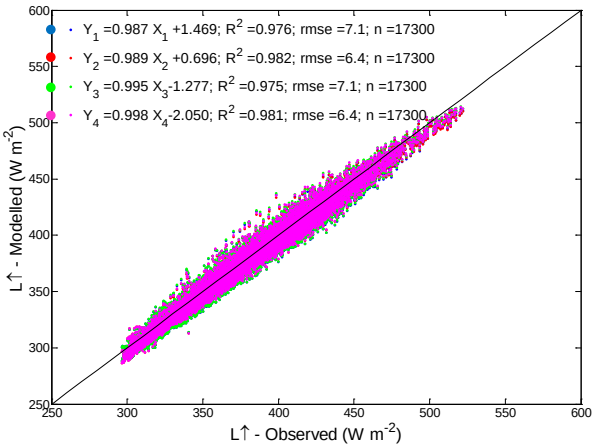

Figure 72: Evaluation of SUEWS v1.0 results for London grid 3004 (Figure 66; Runs 1-4): outgoing longwave radiation L↑.

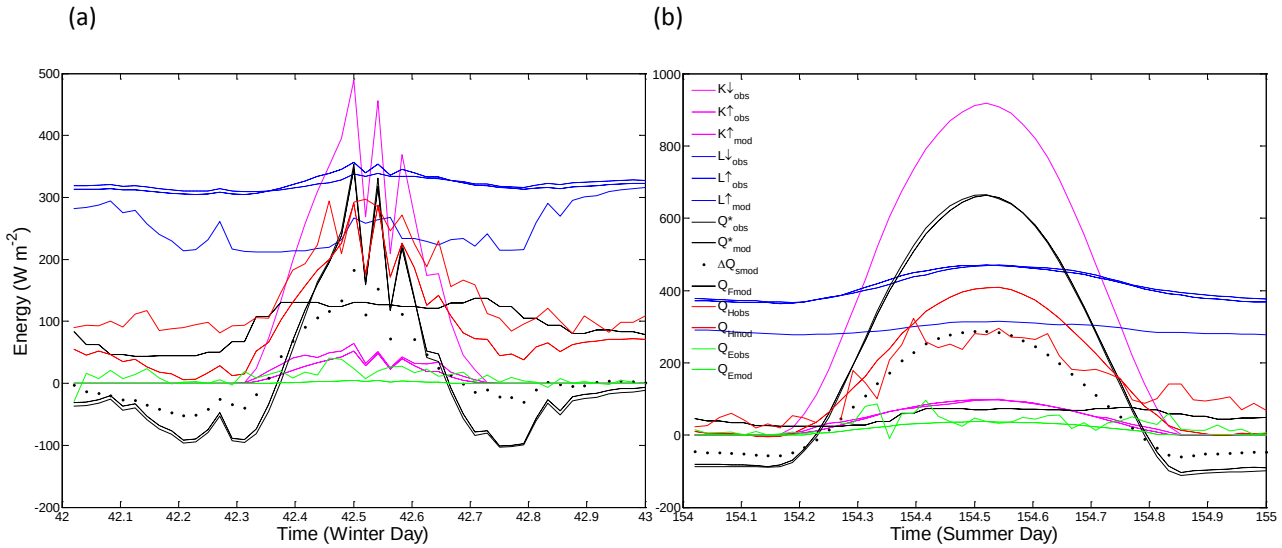

Figure 73: Evaluation of SUEWS v1.0 results for London grid 3004 (Figure 66; Run 4): (a) winter day (DOY 42 of 2010) and (b) summer day (DOY 154 of 2010) energy balance.

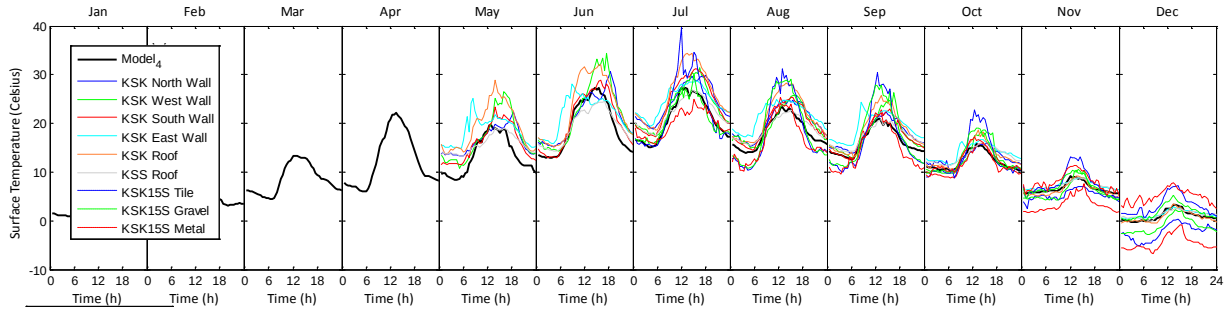

Figure 74: Evaluation of SUEWS v1.0 results for London grid 3004 (Figure 66; Run 4): diurnal monthly averages of surface temperature.

The model performance for surface temperature is evaluated based on diurnal monthly averages (Figure 74) and for the 30 min periods (Figure 75) available for the year. Surface temperature observations began in May 2010 and are presented here as diurnal monthly averages (Figure 74) and the 30 minute period data as the mean of the available surface temperature data (Figure 75). The data are observed for a number of different facets but one bulk value is modelled. The model results (R4) and observed surface temperature values are in good agreement for both the monthly diurnal behavior (Figure 74) and the mean of available surface temperature data at their 30 min period (Figure 75). With the RMSE being equal for all runs (2.3 °C), and the R^2 values being 0.973 for Runs 1 and 2 and 0.972 for Runs 3 and 4, the differences for the modelled surface temperature among the runs are not statistically significant. The model slightly underestimates the highest surface temperatures (Figure 75).The observed surface temperatures have a larger scatter and higher variability (Figure 74) compared to the modelled values. The spatial scales of the observations and the model are quite different. The sensors (IRT) measure individual surface facets with a small field of view (~1 m), while SUEWS v1.0 computes the bulk value. Thus, the local scale modelled values are smoother and have a smaller ranger than the observations, as the model does not capture all variability at the micro scale.

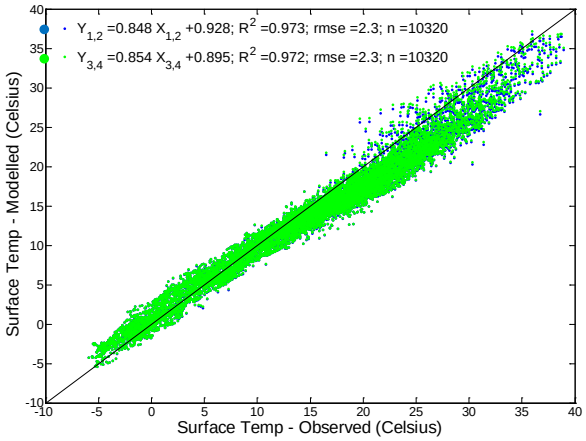

Figure 75: Evaluation of SUEWS v1.0 results for London grid 3004 (Figure 66; Runs 1-4): Mean of available surface temperature (note number of observed data points in the mean varies with data availability).

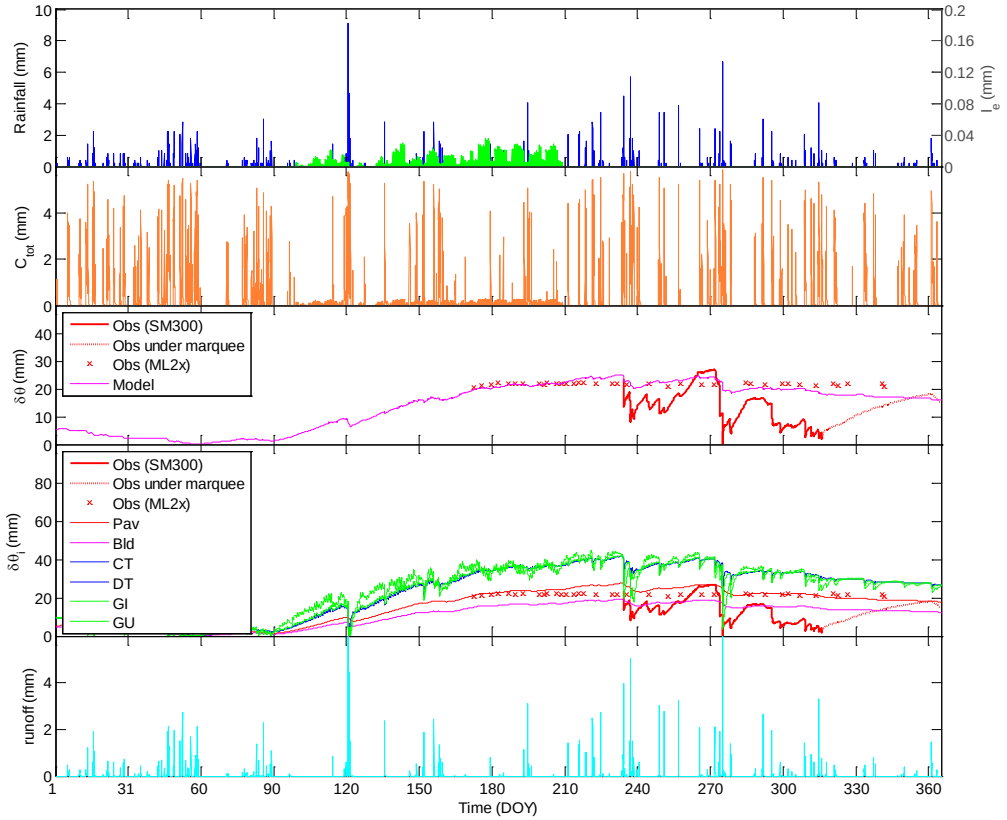

Figure 76: SUEWS v1.0 results and evaluation for London grid 3004 (Figure 66; Run 4): components of water balance: rainfall, external water use, canopy stores, soil moisture deficit, and runoff.

The components for water balance are presented in Figure 76. The behaviour of rainfall, runoff, irrigation and canopy stores seem generally consistent. Two types of soil moisture sensors were used for the different sites within and near Grid 3004: the continuous in situ SM300, and the hand-held ML2x. The response of the SM300 measurements to the rainfall events seems more variable than both the modelled values and those from the hand-held ML2x, the latter two in turn are in good agreement. The variability of the SM300 data is probably due to the nature of continuous measurement and to the *actual* irrigation activities (versus estimates in the model) not accounted for in the model. There may be a need to investigate the actual water use behaviour in the measurement sites used for soil moisture.

In summary, SUEWS v1.0 works well to model radiation, turbulent heat fluxes, energy balance, surface temperature, and water balance. There is still a need to develop a better parameterization schemes for anthropogenic heat, water use and albedo values as function of zenith angle and transmissivity.

5.4.5 Site Characteristics: Helsinki **[Author: Järvi& Grimmond]**

To assess the performance of the model data collected at the SMEAR III urban tower site and two catchmentsItä-Pasila and Pihlajamäki are used (Figure 77).

At the SMEAR III station comparisons between the measurements and model results are made separately for the different surface type areas (Table 32). As no proper footprint model for urban areas with topographical variations and different stabilities exists, comparisons were made with narrower wind sectors in order for the measurements to represent each surface type area. For urban, direction 340-20° was used in the comparisons, for road direction 60-160° and for vegetation direction 200-300°. Some of the differences between the model and measurements can be explained by the lack of footprint calculations as the source area of the measurements and therefore the plan area fractions change with different atmospheric stabilities.

Figure 78 shows the varying plan area fractions of buildings, paved area and vegetation as a function of the distance from the measurement tower. For the model calculations we chose the plan area fractions within the 600 m radius circle as it approximately matches with the footprints calculated using the numerical atmospheric boundary-layer modelSCADIS (Sogachev and Lloyd 2004[25]; Sogachev and Panferov 2006[26]) for neutral atmosphere (Vesala *et al.* 2008[27]).

To characterize the sites for the model the surface parameters were assigned using the default values (Table 33). Plan area fractions, roughness length (z_{0m}) and displacement height (z_d) were allowed to vary according to the prevailing wind direction (Table 32 and Table 33).
In addition, the parameter values are changed for the:
1) two catchments (Table 34)
2) DSS site (Figure 77)

[25]Sogachev A. and Lloyd J. 2004.Using a one-and-a-half order closure model of the atmospheric boundary layer for surface flux footprint estimation.*Boundary-Layer Meteorol.*112, 467–502.
[26]Sogachev A. and Panferov O. 2006.Modification of two-equation models to account for plant drag.*Boundary-Layer Meteorol.*121, 229–266.
[27]Vesala T., Järvi L., Launiainen S., Sogachev A., Rannik Ü., Mammarella I., Siivola E., Keronen P., Rinne J., Riikonen A. and Nikinmaa E. 2008. Surface-atmosphere interactions over complex urban terrain in Helsinki, Finland, *Tellus B*60: 188-199.

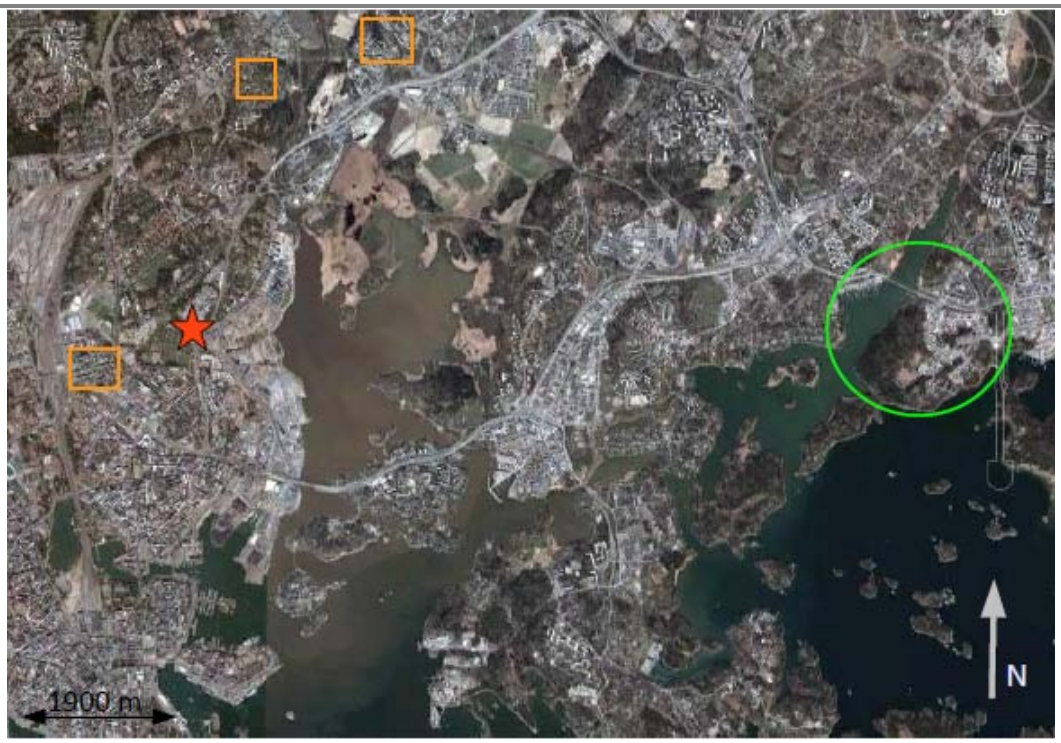

Figure 77: Locations of the observation sites. [Red star = SMEAR III, green areas = catchment areas; orange areas = (Low left corner = Itä-Pasila, Centre = Veräjämäki, top right corner = Pihlajamäki), green circle = area Meri-rastila where the DSS is to be used.]

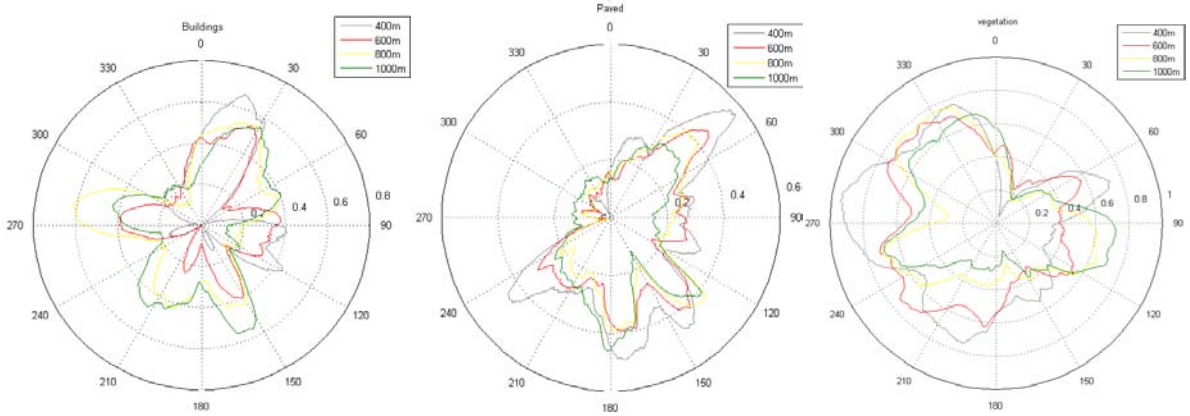

Figure 78: Plan area fraction of (a) buildings (b) paved and (c) vegetation within 400 m, 600 m 800 m and 1000 m radius circle from the measurement tower. Average values for 20° sectors.

Table 32: Surface cover fractions and mean height (z_h) within a 600 m radius circle of the SMEAR III Helsinki measurement tower. Fractions are given for the urban, road and vegetation sectors.

	Surface cover fractions			z_h
	Buildings	Paved	Vegetation	
Urban (320-40°)	0.36	0.16	0.48	4
Road (40-180°)	0.26	0.31	0.43	3.5
Vegetation (180-320°)	0.19	0.17	0.64	3.3

Table 33: Model parameters values used when modelling for 2010 for the Helsinki flux tower site (SMEAR III) (a) by surface type and b) general model run options.

a)	Units	Building	Pavement	Conif. Trees	Decid. trees	Irrigated grass	Unirrigated grass	Water
S_i	mm	0.25[a]	0.48[b]	1.3[c]	0.3-0.8[c]	1.9[c]	1.9[c]	0
$S_{soil,i}$[d]	mm	150	150	150	150	150	150	-
$D_{0,i}$	mm	10	10	0.013	0.013	10	0.013	-
b	-	3	3	1.71	1.71	0.013	1.71	-
C_i[d]	mm	0	0	0	0	0	0	0
$C_{soil.i}$[d]	mm	150	150	150	150	150	150	-
α_i^e	-	0.15	0.12	0.10	0.18	0.21	0.21	0.10[e]
ε_i^e	-	0.95	0.91	0.98	0.98	0.93	0.93	0.95[e]
$g_{i,max}$	mm s^{-1}	-	-	7.4[c]	11.7[c]	40	33.1[c]	-
<u>*b) Input*</u>		<u>*Value*</u>			$K\downarrow_m$		1200 W m^{-2}	
T_{step}		300 s			T_H		40 °C	
km		0.0005 [f]			T_L		0 °C	
GDD		300 d			S_1		0.45 mm	
SDD		-450 d			S_2		15 mm	
$T_{BaseGDD}$		5°C			G_1		16.48	
$T_{BaseSDD}$		11°C			G_2		566.1 W m^{-2}	
T_{BaseQF}		18.2°C [g]			G_3		0.216	
$a_{0,\{wd,we\}}$		0.308			G_4		3.36	
$a_{1,\{wd,we\}}$		$9.86 \cdot 10^3$			G_5		11.07	
$a_{2,\{wd,we\}}$		0.0102			G_6		0.018	
$b_{0,a}$		-84.54			Location		60.20°N, 24.96°E	
$b_{1,a}$		9.96			p		20 inh. ha^{-1}	
$b_{2,a}$		3.67						
$b_{0,m}$		-25.36			z_{hv}		10.5 m	
$b_{1,m}$		3.00			A_s		113 ha	
$b_{2,m}$		1.10			z_{0m}, z_d		Rule of thumb ($0.1z_h$, $2/3z_h$)	
$r_{s,\,max}$		9999.0			f_{aut}		0.05	
$LAI_{max,con}$		5.1[c] m^2 m^{-2}			$I_e$period		152-243	
$LAI_{max,dec}$		5.5[c] m^2 m^{-2}						
$LAI_{max,grass}$		5.9[c] m^2 m^{-2}						
$LAI_{min,con}$		4 m^2 m^{-2}						
$LAI_{min,dec}$		1 m^2 m^{-2}						
$LAI_{min,grass}$		1.6[h] m^2 m^{-2}						

Falk and Niemczynowicz (1978)[28]; Davies and Hollis (1981)[29]; Breuer et al. (2003)[30]; Grimmond and

[28] Falk J, Niemczynowicz J., 1978. Characteristics of the above ground runoff in sewered catchments, in Urban Storm Drainage, edited by Helliwell P.R. Pentech, London, 1978.

[29] Davies, H., Hollis, T., 1981. Measurements of rainfall-runoff volume relationships and water balance for roofs and roads. Second International Conference on Urban Storm Drainage, Urbana, Illinois.

Oke (1986a)[31]; Oke (1987)[32]; Belthier et al. (2006)[33]; Sailor and Vasireddy (2006)[34]; Grimmond (1988)[35]

Table 34: Parameters values changed for the two Helsinki catchments Itä-Pasila and Pihlajamäki.

	Itä-Pasila	Pihlajamäki
λ_b	0.202	0.122
λ_{pav}	0.416	0.329
λ_g	0.123	0.024
$\lambda_{g,irr}$	0.000	0.094
λ_{dec}	0.230	0.357
λ_{con}	0.007	0.040
λ_{unman}	0.022	0.034
λ_w	0	0
$S_{soil,build}$ (mm)	50	120
$C_{soil.build}$(mm)	50	120
$S_{soil,paved}$(mm)	80	120
$C_{soil.paved}$(mm)	80	120
Location	60.20°N, 24.94°E	60.24°N, 24.01°E
p (inh. ha^{-1})	42	45
A_s(ha)	23.8	44.8
z_h (m)	15.2	10.8
f_{aut}	-	0.10

5.4.6 Forcing and Evaluation data: Helsinki **[Author: Järvi & Grimmond]**

For all runs forcing data from SMEAR III station are used. These include: incoming solar radiation, air temperature, wind speed, station pressure, precipitation and relative humidity. For the runs for the actual SMEAR III site data from year 2010 are used while for the catchments data between 1 September 2010 and 29 January 2011 are used. For missing values excluding precipitation, the following gap filling procedure was used. If one hourly data point was missing, the value was linearly interpolated from the adjacent data points. If data gap was larger than one hour but less than one day, the missing values were replaced with averaged calculated for the same hour from adjacent days. If data gap was wider than one day, two adjacent days were used in similar manner.

[30]Breuer, L., Eckhardt, K., Frede, H.-G., 2003. Plant parameter values for models in temperate climates. Ecol. Model. 169, 237-293.
[31]Grimmond, C.S.B., Oke, T.R, 1986. Urban water balance 1. A model for daily totals. Water Resour. Res. 22, 1397-1403.
[32]Oke T.R., 1987. Boundary Layer Climates.Routledge, London, UK.
[33]Berthier, E., Dupont, S., Mestayer, P.G., Andrieu, H., 2006. Comparison of two evaporation schemes on a sub-urban site. J. Hydrology 328, 635-646.
[34]Sailor, D.J., Vasireddy, C., 2006.Correcting aggregate energy consumption data account for variability in local weather.Environ. Modell.Softw.21, 733-738.
[35]Grimmond, C.S.B., 1988. An evaporation transpiration model for urban areas.Ph. D. thesis, University of British Columbia, Vancouver.

To evaluate the model performance the energy balance fluxes from the SMEAR III site are used: the net all-wave radiation, sensible heat and latent heat flux. For the purposes of evaluation data are divided according to thermal seasons. Thermal winter is defined so that the daily temperatures needs to be below zero at least five days and similarly thermal summer as above 5°C. In 2010, winter was from 1 January to 25 March and from 17 November to end of the year. Spring was from 26 March to 11 May, summer from 12 May to 25 September and fall from 26 September to 16 November.

Runoff data collected at 10 min time interval at the two catchments are used for evaluation at these two sites.

5.4.7 Helsinki: Run with observed forcing data **[Author: Järvi& Grimmond]**

The model simulates the observed radiation at SMEAR III site well except in winter when the net all-wave radiation (Q^*) is underestimated (Figure 79 and Figure 80). This results from the underestimation of the modeled downward longwave radiation ($L\downarrow$) from air temperature and relative humidity (Loridan et al. 2011). If measured $L\downarrow$ is used in the calculation of Q^*, the model performance improves and rmse decreases from 30.9 W m^{-2} to 8.2 W m^{-2} when considering the whole year (Figure 81). However, a slight underestimation of Q^*occurs during the daytime but the model performance in different seasons improves (Figure 81). This suggests the albedo, especially in the summertime may not be correct. These current runs are conducted with default albedo values.

In spring and fall, when neither snow cover nor external irrigation occur, the model simulates both Q_H and Q_E well (Figure 83 and Figure 84). The underestimation of both fluxes in winter indicates underestimation of ΔQs and/or Q_F (Figure 85). Currently snow accumulation, which affects the availability of water in winter, is not accounted for but this is under development. Poor performance in summer is likely caused by underestimation of external irrigation. To date the irrigation sub-model has only been evaluated in a residential area in Vancouver where water consumption is likely lower than around the tower where allotment gardens and the University Botanical garden are located. Low Q_E (daytime difference on average 150 W m^{-2}) were modeled in August which was exceptionally warm and dry and likely irrigation was intense (Figure 83, Figure 86). In summer 2011, we plan to monitor water use in the Botanical garden, in order to get more realistic irrigation values for the site. The effect of modeled $L\downarrow$ on Q_E and Q_H are minor (Table 35, Q_H not shown), where the correlations between the modeled and measured values are shown when using the modeled and measured $L\downarrow$. If the albedo was corrected the Q* would increased, thus the Q_H and Q_E would increase.

Runoff has been monitored in two Helsinki catchments with different population densities (Figure 77 and Table 34). For both catchments SUEWS simulated the behaviour of measured runoff well (Figure 87, Pihlajamäki not shown), but overestimates runoff when applied in an uncalibrated manner with the default model parameters (r_{Mod}= 1.3+0.01r_{Meas}, rmse = 0.15, R^2 = 0.73 and r_{Mod}= 1.8r_{Meas} - 0.1, rmse = 0.12, R^2 = 0.32). Future work will include analysis of the site specific parameters values for soil depth, drainage coefficients and surface store.

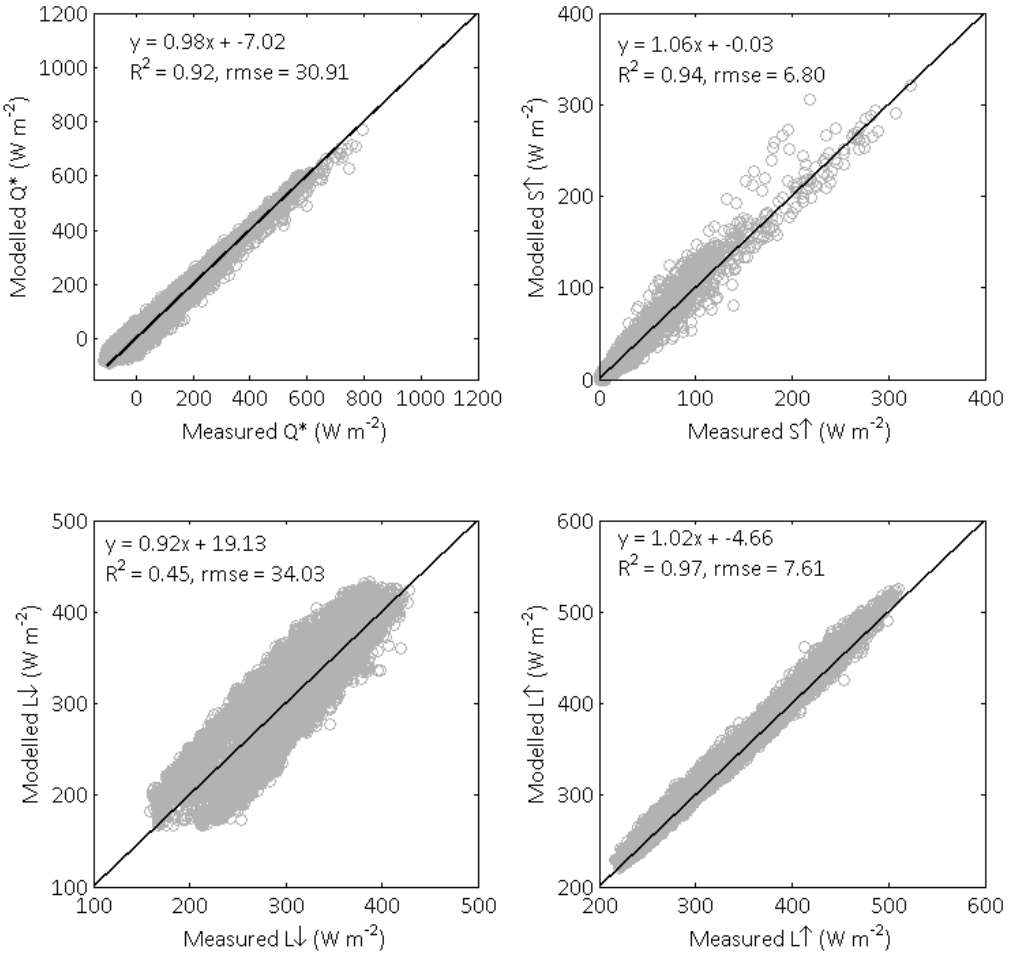

Figure 79: Hourly modeled and measured net all-wave radiation (Q), outgoing shortwave radiation (S↑), incoming (L↓) and outgoing (L↑) longwave radiation in 2010.*

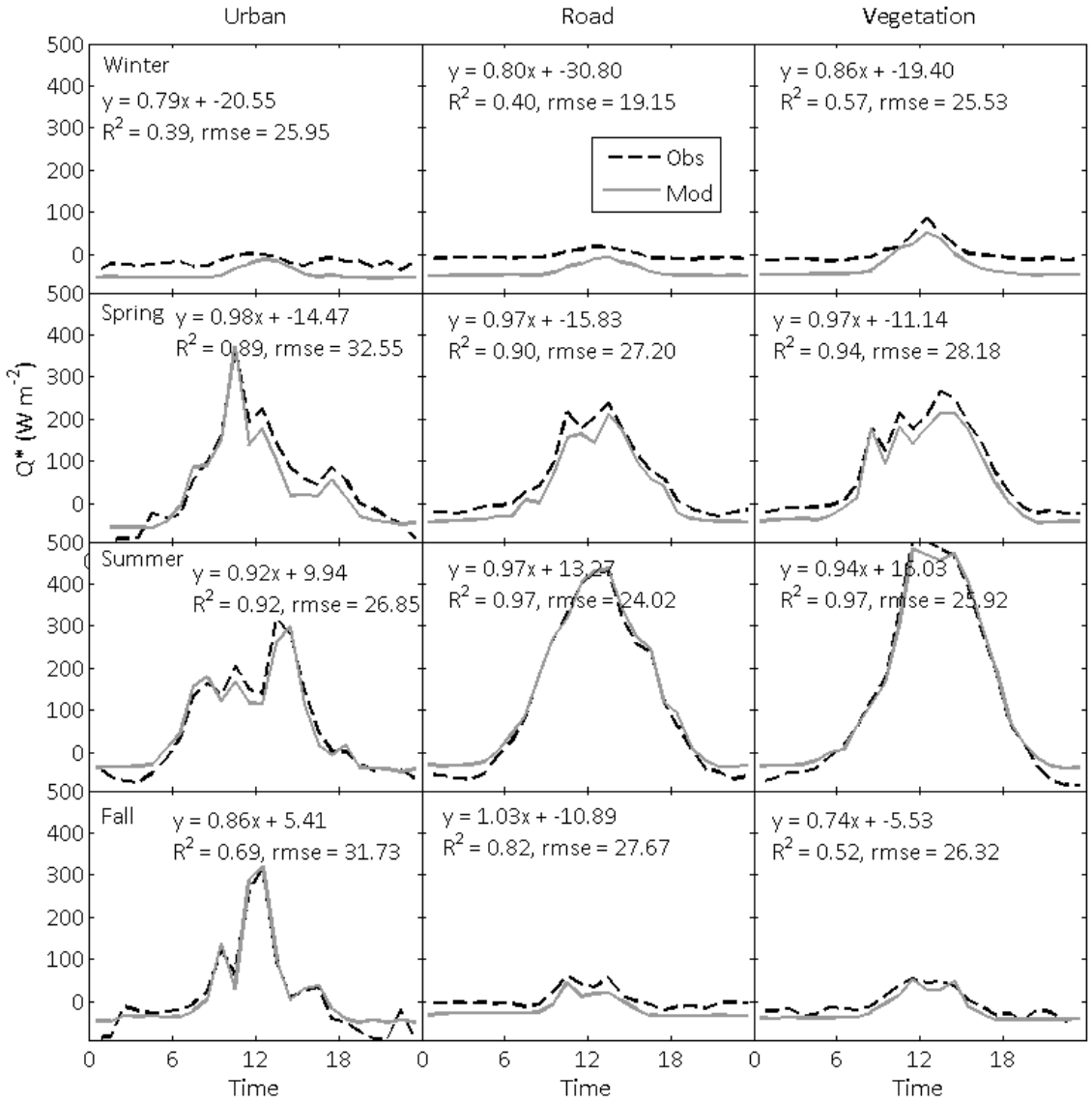

Figure 80: Mean diurnal behavior of modeled and measured net all-wave radiation (Q) by seasons and surface cover type.*

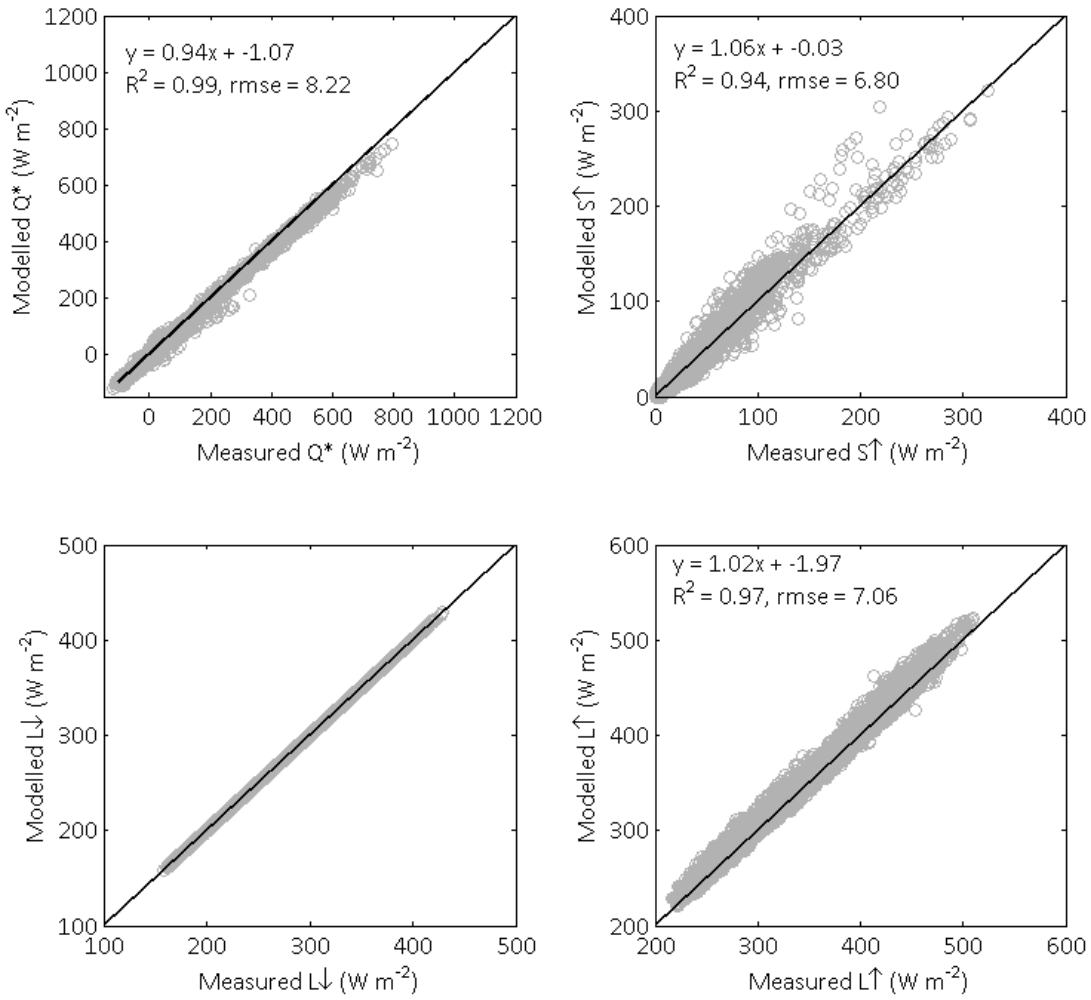

Figure 81: As Figure 79 but with measured L↓ *used.*

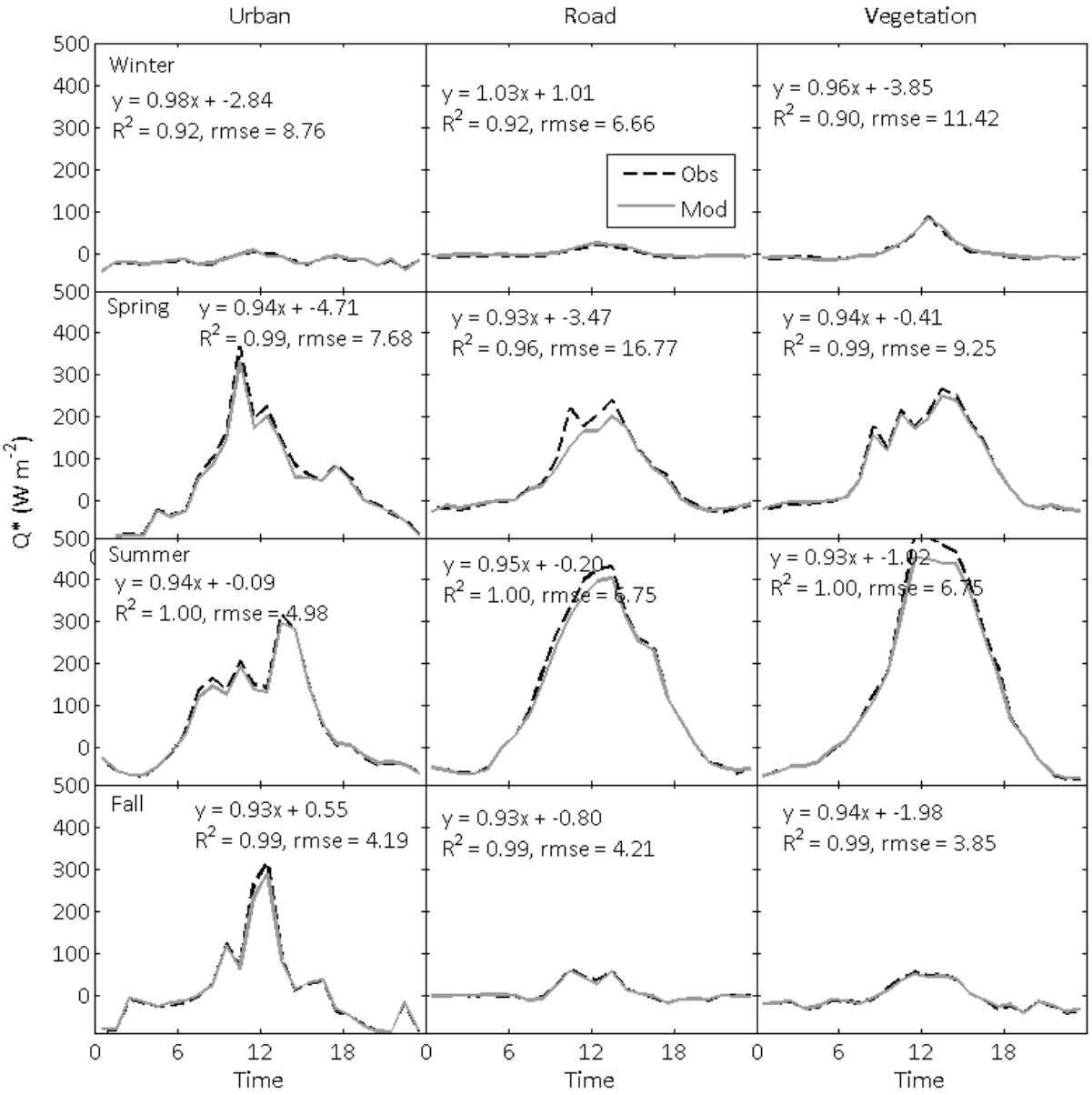

Figure 82: As Figure 80 but with measured L↓ used in the model run

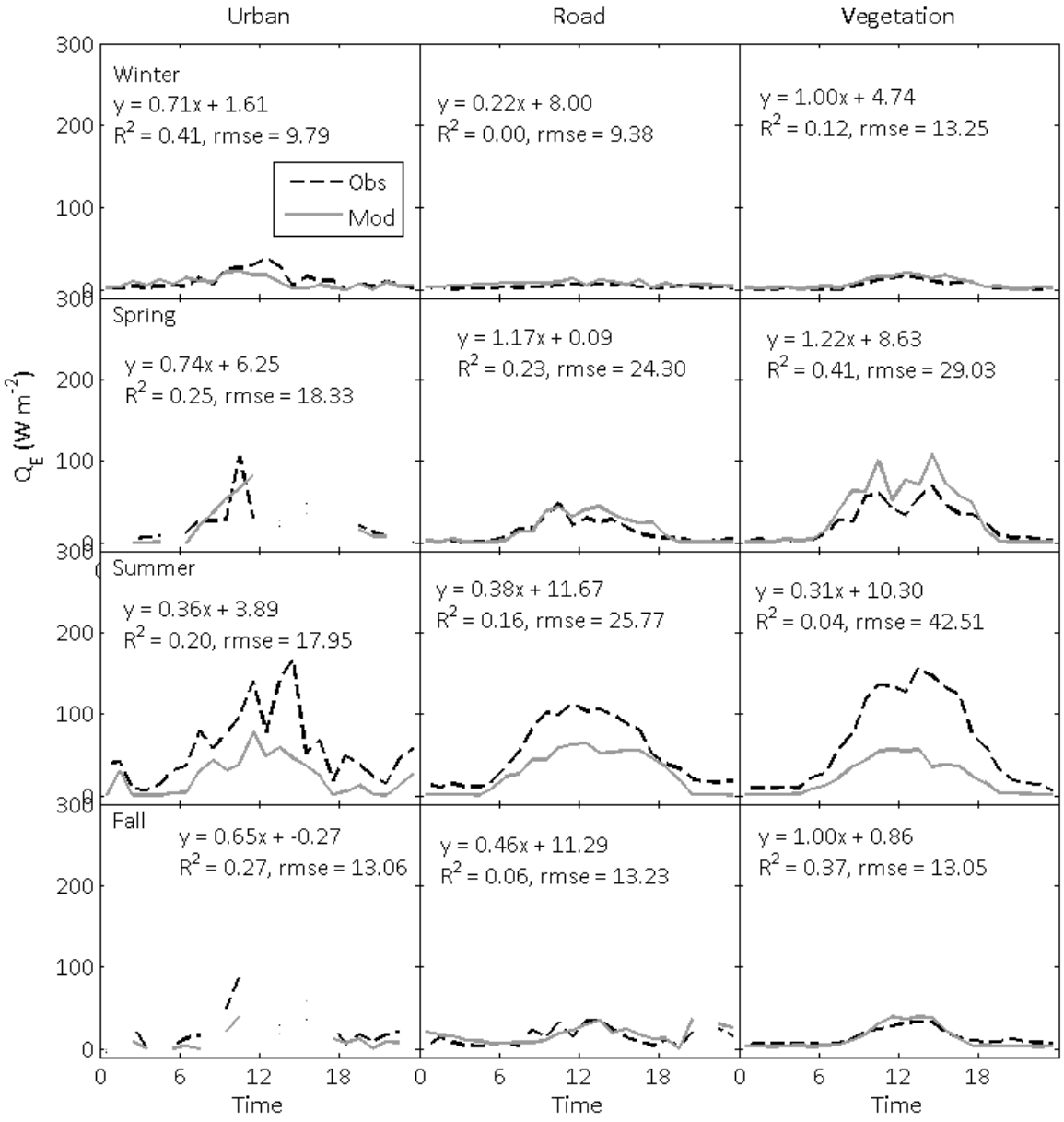

Figure 83 : Mean diurnal behaviour of modelled and measured latent heat flux (Q_E) separated by seasons and surface cover type.

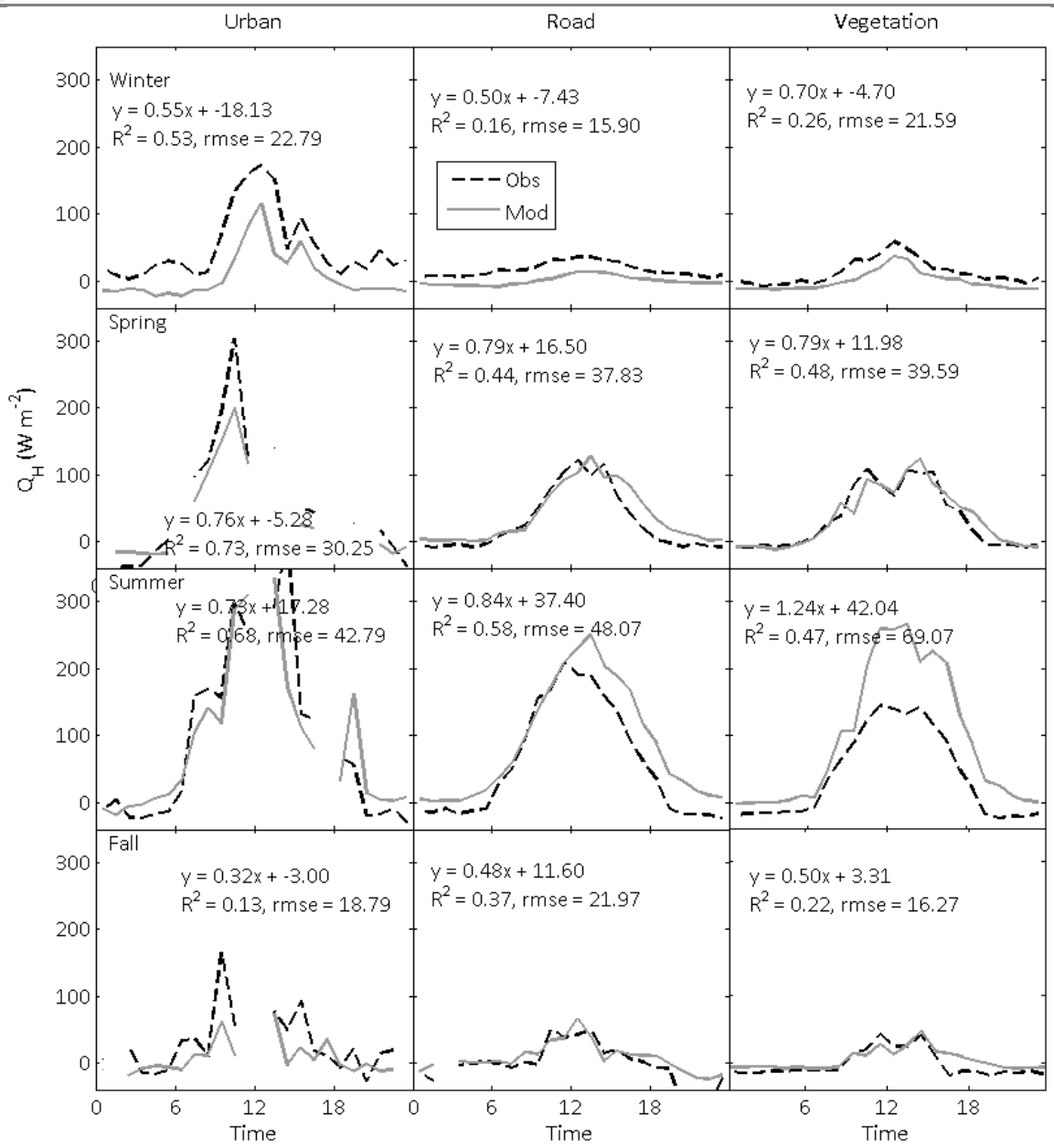

Figure 84: As Figure 83 but for sensible heat flux (Q_H).

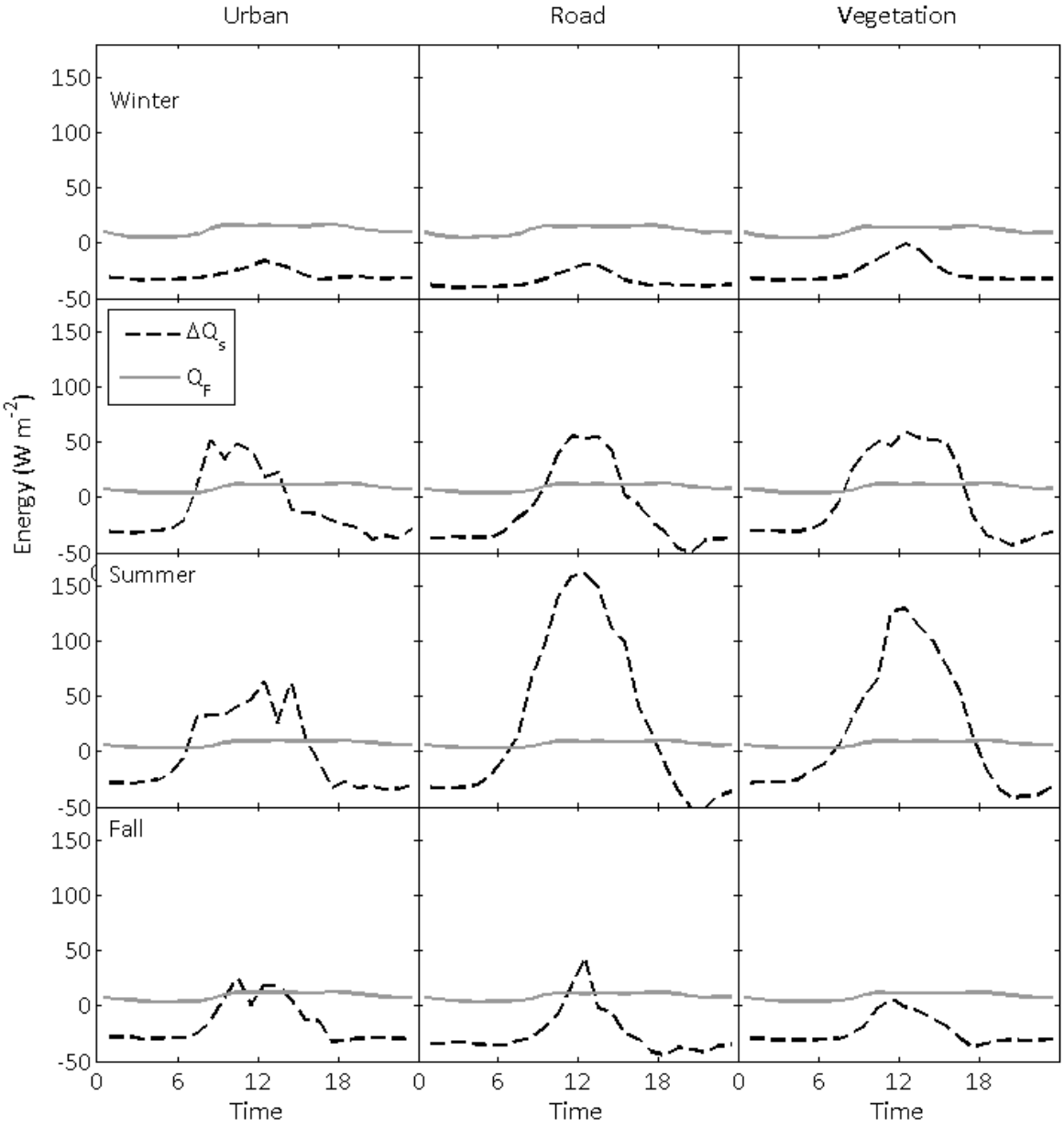

Figure 85: Mean diurnal behaviour of modelled Q_F and ΔQ_S separated by seasons and surface cover type.

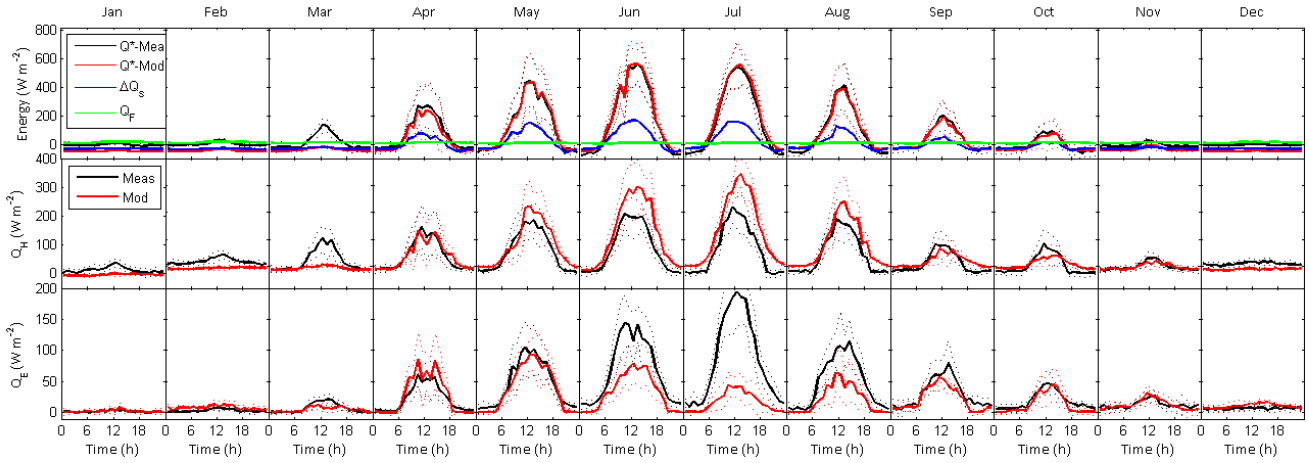

Figure 86: Mean diurnal variation of energy balance components by months.

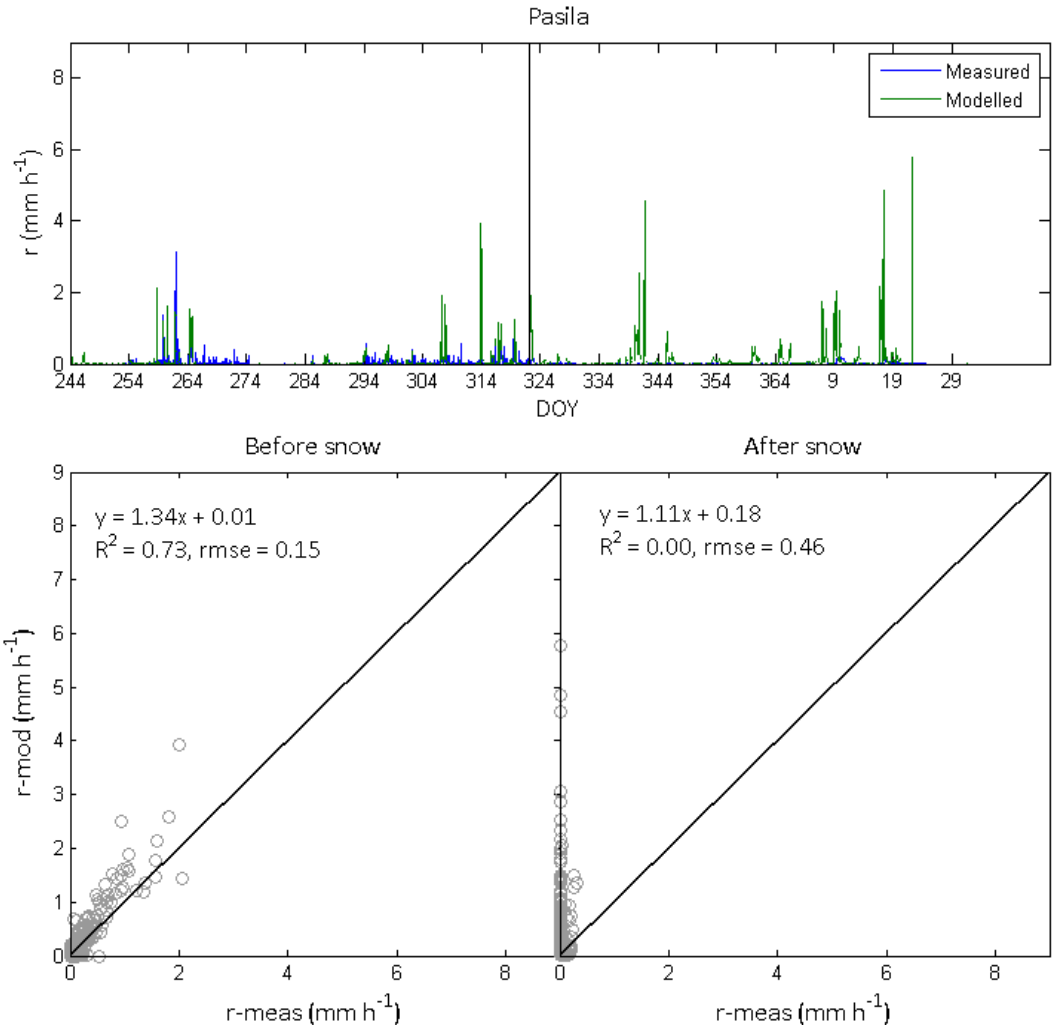

Figure 87: Comparison of hourly measured and modeled runoff at Pasila. (Upper) Time series from 2010 to early 2011. Vertical line shows when (day of year 322) precipitation started to be snowfall rather than rainfall. (lower) performance before and after the snowfall.

Table 35: The impact of using modeled L↓ *on* Q_E *results.* N = *number of datapoints in the fit.*

		Base run			Measured *L*↓ used			
		Fit	R^2	rmse (W m^{-2})	Fit	R^2	rmse (W m^{-2})	*N*
Winter	Urban	y = 0.71x+1.6	0.41	9.8	y = 0.71x+3.2	0.34	11.1	101
	Road	y = 0.22x+8.0	0.00	9.4	y = 0.19x+10.5	0.00	11.3	505
	Veg	y = 1.00x+4.7	0.12	13.3	y = 0.96x+5.9	0.10	13.7	331
Spring	Urban	y = 0.74x+6.3	0.25	18.3	y = 0.74x+5.1	0.27	17.6	17
	Road	y = 1.17x+0.1	0.23	24.3	y = 1.02x+4.0	0.06	37.0	193
	Veg	y = 1.22x+8.6	0.41	29.0	y = 1.16x+11.2	0.39	28.4	328
Summer	Urban	y = 0.36x+3.9	0.20	18.0	y = 0.36x+4.8	0.18	18.7	89
	Road	y = 0.38x+11.7	0.16	25.8	y = 0.38x+11.1	0.17	25.5	817
	Veg	y = 0.31x+10.3	0.04	42.5	y = 0.32x+9.4	0.05	41.8	868
Fall	Urban	y = 0.65x-0.3	0.27	13.1	y = 0.71x-1.5	0.32	13.3	22
	Road	y = 0.46x+11.3	0.06	13.2	y = 0.41x+16.0	0.03	14.27	86
	Veg	y = 1.00x+0.86	0.37	13.1	y = 1.04x+1.6	0.37	13.4	439

6 SURFEX. CNRM MODELS.

SURFEX and TEB in particular have along its development been comprehensively evaluated against various dataset in Vancouver, Mexico (Masson et al., 2002), Marseille (Lemonsu et al., 2004), Lodz (Offerle et al., 2005), Toulouse (Pigeon et al., 2008), Basel (Hamdi and Masson 2008) and Montreal (Lemonsu et al, 2010). During Bridge, the evaluation has focused on the representation of the buildings' indoor temperature which has been measured for a set of 10 buildings in Egaleo neighbourhood in Athens between May and October of 2009. The indoor air temperature of different residential buildings was monitored in Egaleo neighbourhood (Athens) between May and October of 2009. : Map of the monitored buildings in Egaleo neighborhood, Athens.Figure 88 shows a map of the location.

Figure 88 : Map of the monitored buildings in Egaleo neighborhood, Athens.

The parameters of the buildings used in the simulation are summarized in Table 36. Two cases are considered: Case 1 has an average building height of 9.5 and is compared to buildings 3, 4, and 5 of the experiment; and case 2 has an average building height of 15.5 and is compared to buildings 8 and 9 of the experiment.

Table 36: Simulation parameters used for the comparison between TEB-BEM and field data from the building monitoring conducted in Athens (Greece).

Parameters	**Settings**
Average building height	Case1: 9.5 m; Case2: 15.5 m
Building density	0.64
Vertical to horizontal surface ratio	1.05
Anthropogenic heat from traffic	8.0 W m^{-2}

Glazing-to-wall ratio	0.25
Window construction	Single-pane clear glass (6 mm)
Wall and roof construction	Concrete, polyurethane
Road construction	Asphalt, ground
Infiltration/ventilation air flow rate	0.5 ACH
Internal gains	Residential: 4 W m^{-2} (floor area)
HVAC system	None
Natural ventilation	3 ACH, when outdoor conditions are favorable

Figure 89 and Figure 90 represent the hourly-evolution of indoor air temperature for July and August 2009. Figure 89 corresponds to case1 and buildings 3, 4 and 5 of the experiment; and Figure 90 corresponds to case2 and buildings 8 and 9 of the experiment. It can be seen that the simulation results follow the general evolution of the measurements and agree in amplitude with the indoor air temperature measured in building 5. This agreement is mainly due to the natural ventilation model. Simulations in which this option was not activated produce considerably higher temperatures.

Note that we cannot expect an exact agreement between simulations and measurements in this particular experiment. Indoor air temperatures are very sensitive to factors that we ignore; like, for example, occupants' behavior. Even within the two sets of buildings we represent, the indoor performance significantly differ, although all the buildings have very similar parameters in terms of the simulation.

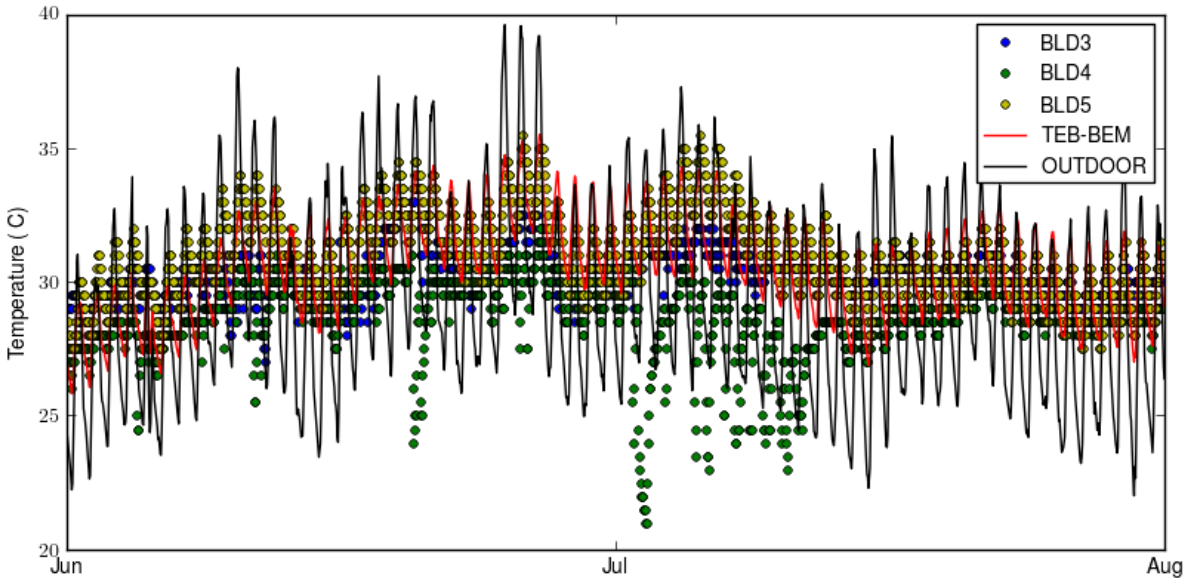

Figure 89: Hourly-evolution of indoor air temperature for July and August 2009

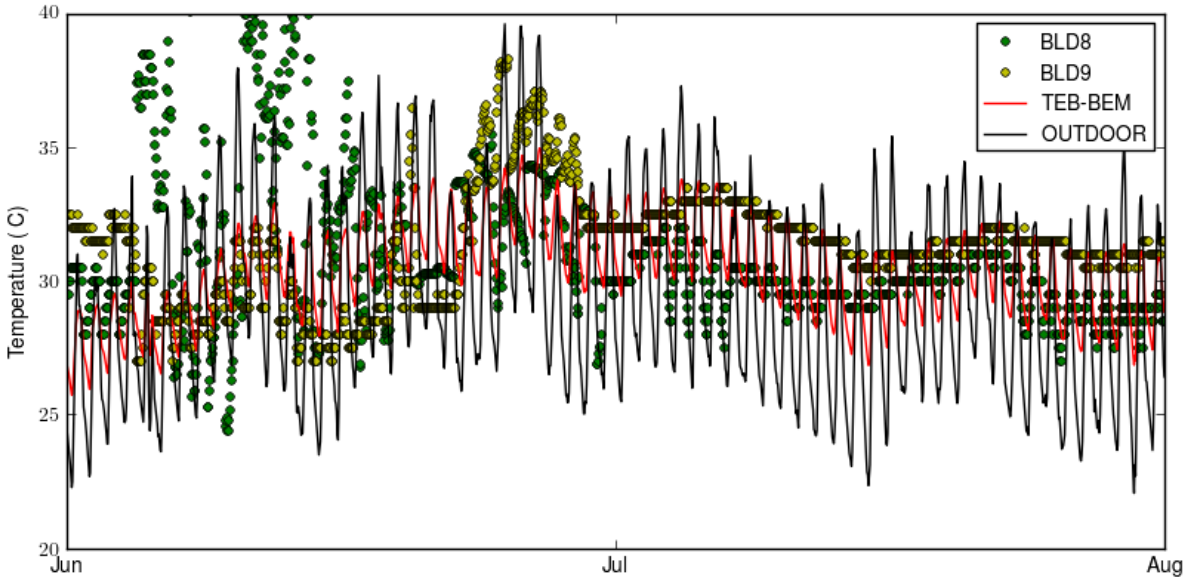

Figure 90: Hourly-evolution of indoor air temperature for July and August 2009.

7 SIMGRO. ALTERRA MODELS

7.1 SIMGRO Input data

The hydrological model SIMGRO uses data from the WRF climatological forcing, namely: precipitation, temperature, and shortwave radiation. Precipitation is used as a direct input, temperature and shortwave radiation are used to calculate a reference evapotranspiration (Makkink method). Uncertainties in the WRF outputs will lead to uncertainties in the outcomes of SIMGRO as well.

The figures below give the WRF average daily precipitation distribution for the cities of Helsinki (Figure 91a) and London (Figure 91b) (in mm). A few aspects are clearly visible in the figures. Firstly, both Helsinki and London have a boundary condition for precipitation of 0 mm. Secondly, this boundary condition appears to strongly influence the precipitation distribution for the whole grid: both for Helsinki and London a gradient in precipitation is calculated.

*Figure 91*a : WRF precipitation forcing for Helsinki

Figure 91*b: WRF precipitation forcing for London*

Spatial presentations of the different water balance outputs of SIMGRO show the same boundary and gradient characteristics as the precipitation input (Figure 92: runoff). This was concluded for both Helsinki and London.

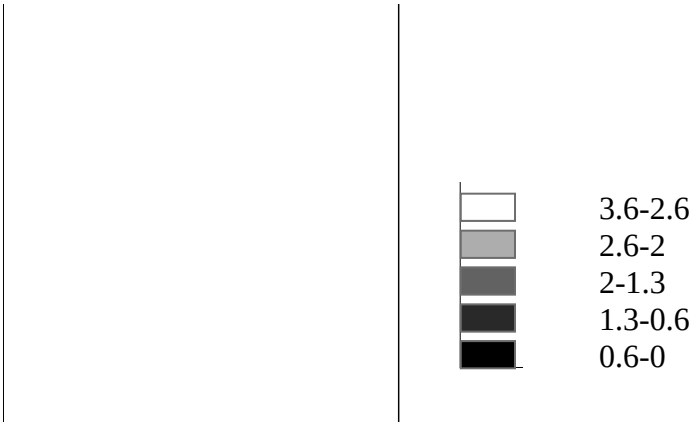

Figure 92: Simulated runoff, Helsinki

Not only does the spatial precipitation pattern show some typical characteristics, also the temporal distributions show some features. The measured precipitation for 2008 (data available at Helsinki Meteo) is compared with the WRF precipitation data (Figure 93a). The precipitation sums of the winter months (September – February) are underestimated. The WRF model calculates large peaks for April and August which are not measured. The occurrence of individual rain events seems to be calculated well (Figure 93b), but the magnitude is sometimes overestimated. Similar patterns are found in the London case.

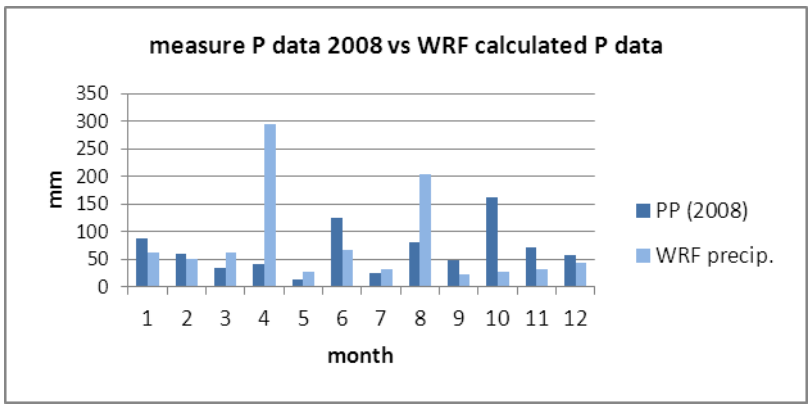

*Figure 93*a: Measured precipitation data, Helsinki Meteo (PP 2008) vs WRF precipitation

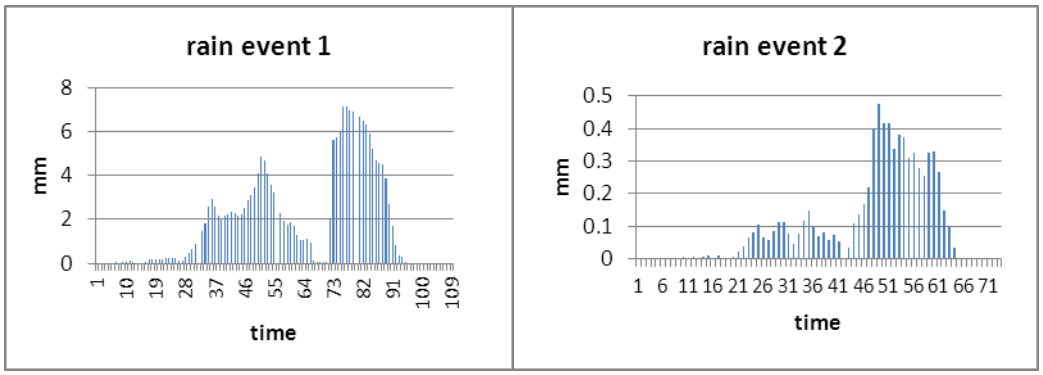

Figure 93*b : Two rain events in April 2008 show a realistic image*

The water balance time line shows the typical features as well (Figure 94). The precipitation forcing leads to extreme runoff peaks and influence actual evapotranspiration as well.

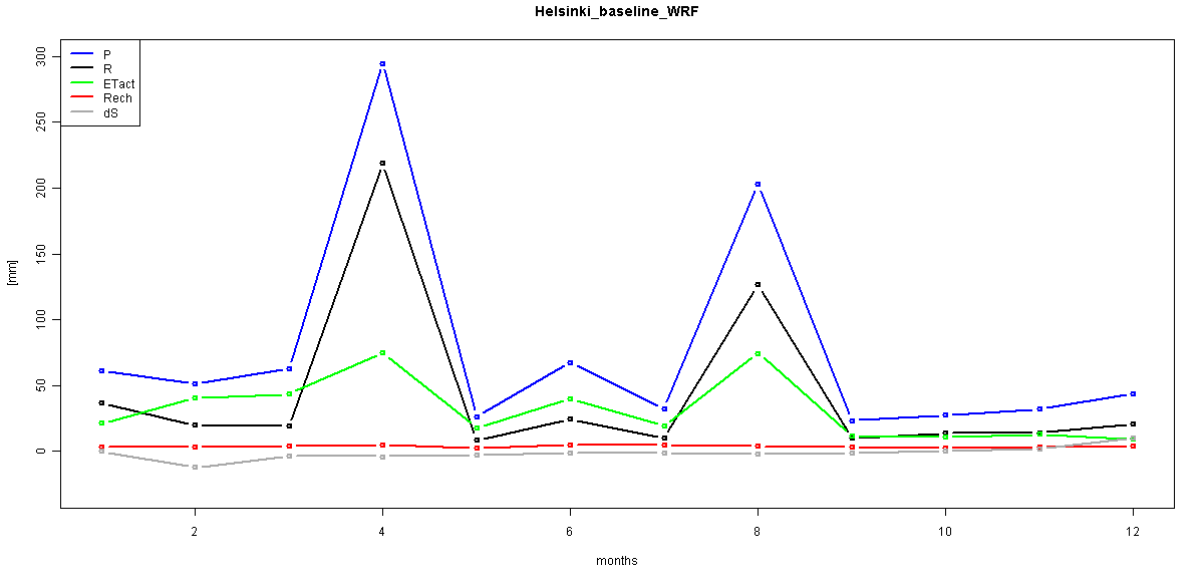

Figure 94: Water balance Helsinki baseline. P: precipitation, R: runoff, Etact: actual evapotranspiration, Rech: recharge to groundwater, dS: change is soil water storage.

Solution: average values

During the progress meeting in Gliwice (May 2011), it was decided to use the spatially averaged values of the WRF forcing for precipitation. The assumption made here is that, precipitation sums does not vary (much) over a small grid of 5.4 x 5.4 km, when looking at a longer time period. During the meeting the uncertainty in the calculation of the total precipitation sum (per hour, day, month, season, or year) was not discussed.

The SIMGRO outputs are obviously influenced by the proposed spatially averaged precipitation values. The difference in general with the 'old' yearly water balance of Helsinki is that with average precipitation values, less runoff, more actual evapotranspiration, and more changes is soil water storage are calculated (Figure 95a). More evapotranspiration is being calculated. Consequently the changes in soil water storage are bigger than in the 'old' model run. The amount of precipitation falling on sealed surface is less, resulting in less runoff.

The same conclusions can be drawn for the London case study.

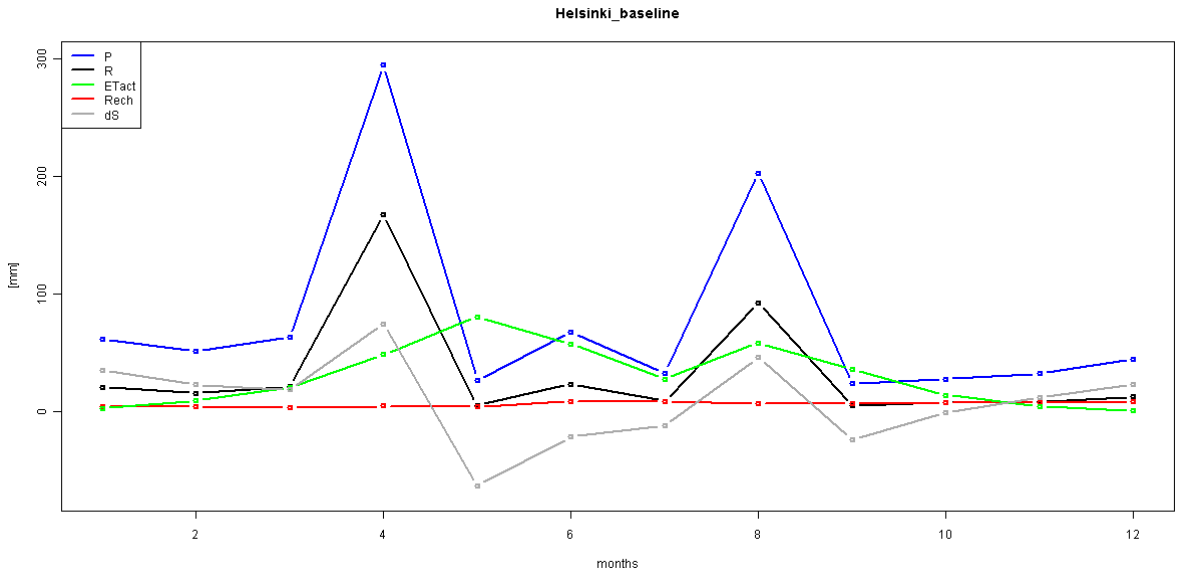

*Figure 95*a: Water balance Helsinki using WRF forcing average values.

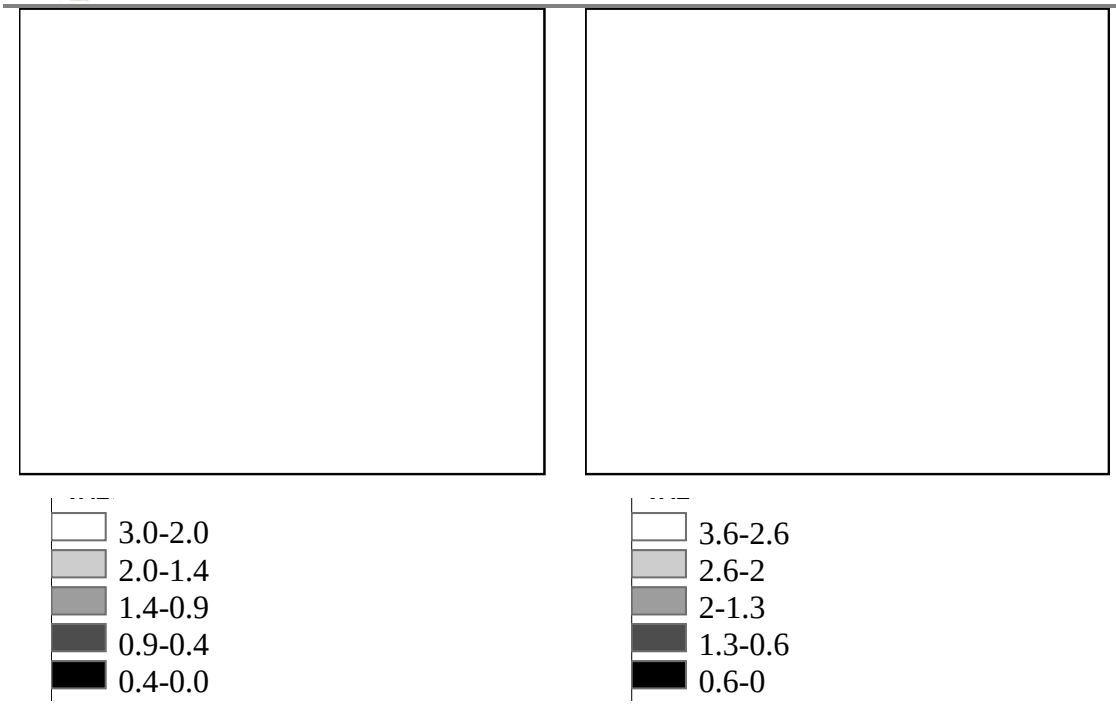

Figure 95*b: Actual evapotranspiration Helsinki baseline. Left with WRF forcing, right with Average values WRF forcing.*

7.2 Calibration and Validation

The lack of data in the urban environment makes validation of the model difficult. However, a verification based on data of comparable environments showed the results of our study are plausible.

Dependencies water balance terms

An analysis of the dependencies between runoff, recharge, actual evapotranspiration and changes in soil moisture showed that recharge and runoff are very high correlated with a strong linearity (Figure 96). This goes also for the soil moisture change and the other three parameters. The trend between recharge, actual evapotranspiration and change in soil moisture are all positive. Runoff has a negative trend, because this is the only direct outgoing term of the water balance.

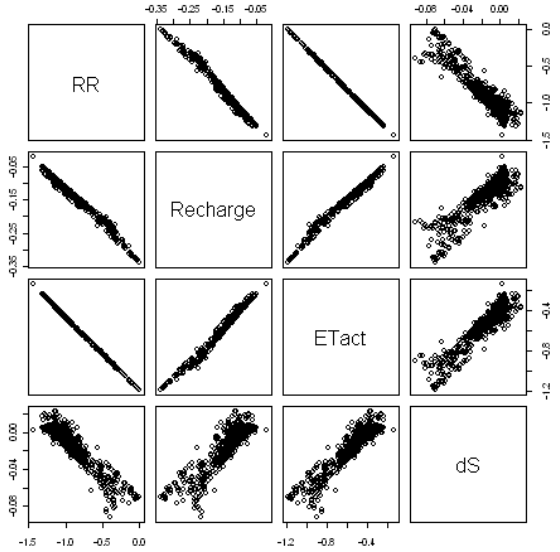

Figure 96

RR	-0.99	-1.00	-0.94
-0.99	**Recharge**	0.99	0.89
-1.00	0.99	**ETact**	0.93
-0.94	0.89	0.93	**dS**

Correlations water balance terms London baseline. Note that the KCL data-set was used here.

Urban water balance versus urban land use types

The urban land use types are defined in SIMGRO as Urban Morphological Types (UMTs). The different UMTs have specific defined reservoir characteristics and therefore represent different land uses in the urban environment (Table 1). The characteristics of the UMTs are defined in the model and are directly linked to the runoff, infiltration and evapotranspiration. A comparison is made between actual evapotranspiration, runoff, and change is micro storage per UMT in order to check whether the model gives a good presentation of the UMTs or not. For this analysis the largest and second largest UMT type per cell were used, because the influence of these UMTs will be the largest in the cell.

The results of this analysis are shown in Figure 97, Table 37 gives the legend of the x axes. The left figures give the relation with the largest occurring UMT of each of the 200 x 200 m cell. The right figures give the relation with the second largest UMT.

In general it can be concluded that cells primarily covered by buildings (UMT=1) have lowest ETact values. Cells with open water (UMT=8) have the highest ETact values. The hypothesis is set that outliers of evapotranspiration are caused by cells with open water combined with impermeable land uses. In order to verify this hypothesis the same analysis was done for the second largest UMT.

The general conclusion is that sealed surfaces (e.g. buildings and streets) have low evapotranspiration, high runoff values, and have a positive decrease of the soil water storage. This means there is more outgoing water than incoming water. Cells combined with open water have lowest runoff values, and secondly the green cells. The open surfaces have the potential to have an increase in soil water change. The results are considered plausible.

Table 37: UMT index

#	**Name UMT**
1	Building
2	Undefined
3	Broad-leaved trees
4	Conifer trees
5	Grassland
6	Streets
7	Streets with vegetation
8	Surface water

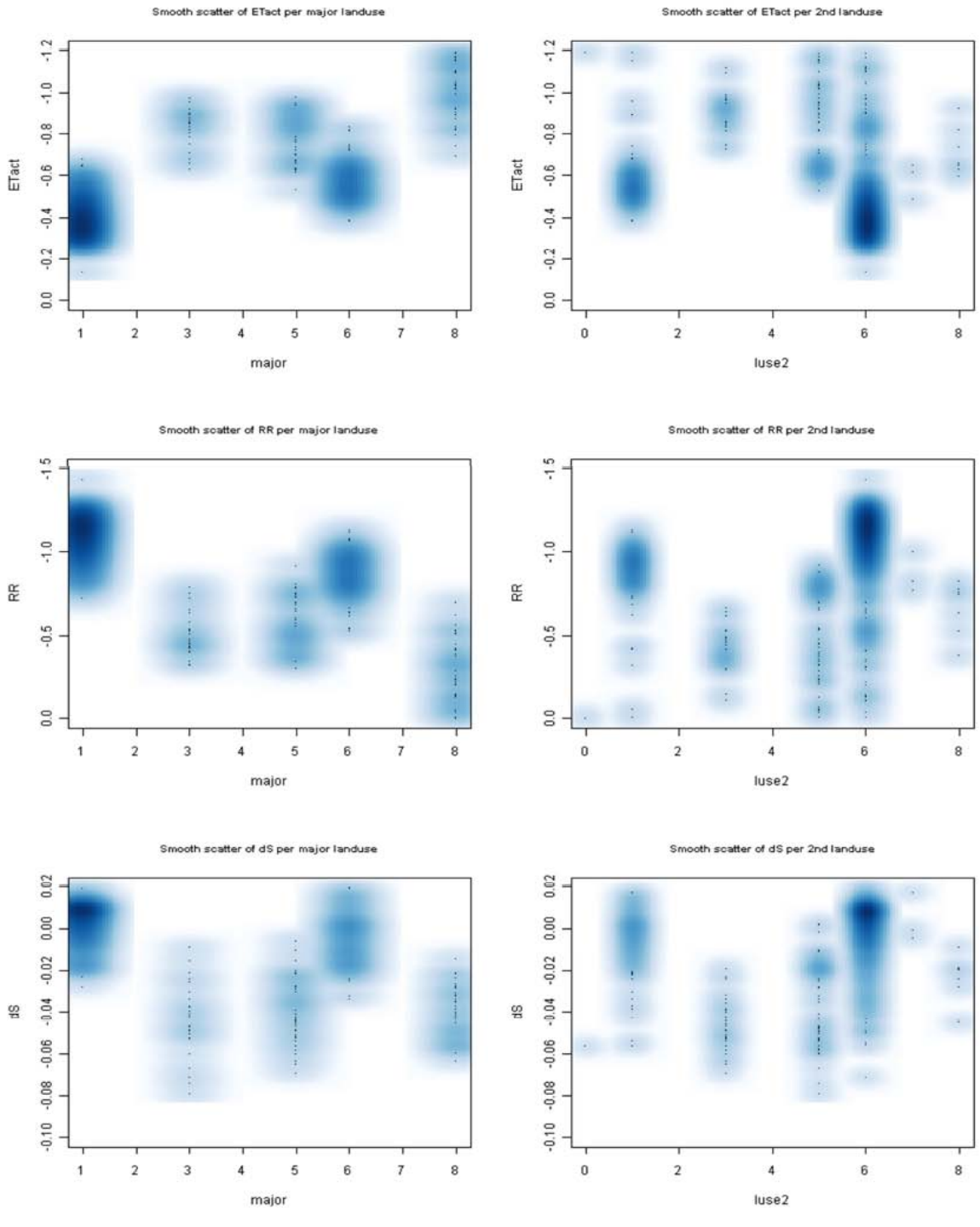

Figure 97: (top) ETact versus largest and second largest UMT. (middle) R versus largest and second largest UMT: (bottom) dS versus largest and second largest UMT.

8 ANN. NKUA MODELS

The ANN model developed by NKUA predicts urban heat island phenomenon using a limited data series. The Athens case study was used to demonstrate the feasibility and accuracy of the overall approach. The methodology and results for testing and validation that was followed for the selection of the appropriate neural network and training function is described in detail in Deliverable 4.2. In this section, the validation process of the final model is presented.
Both the training and verification of the ANN is performed using the data collected by the NKUA meteo station network during the period from 06/04/2009 to 07/09/2009. The data are fed into the ANN as blocks of 24 values corresponding to each hour of the day. The neural network has a training period of 40-60 days. The remaining data are used to verify the quality of network and adaptation of the neural network to the new data.

The quality of the model results have been validated for the following aspects:
- diurnal fluctuation of temperatures
- temperature prediction accuracy due to seasonal variations
- response to different weather conditions or during weather changes
-UHI prediction accuracy

In order to examine the quality of the model against the above mentioned aspects direct comparisons of measured and calculated data have been used as well as the calculation of the standard deviation between measured and predicted temperatures. The UHI prediction accuracy is demonstrated by the calculation of the RMSE and the R^2.

Indicative results are discribed below:
Figure and Figure 99 show the measured and predicted temperatures of 5 different locations (i.e. Ilion, Zefyri, Petoupoli, Aegaleo and Agii Anargyri) and for two different dates 19-20/06/2009 and 05-06/07/2009 respectively.

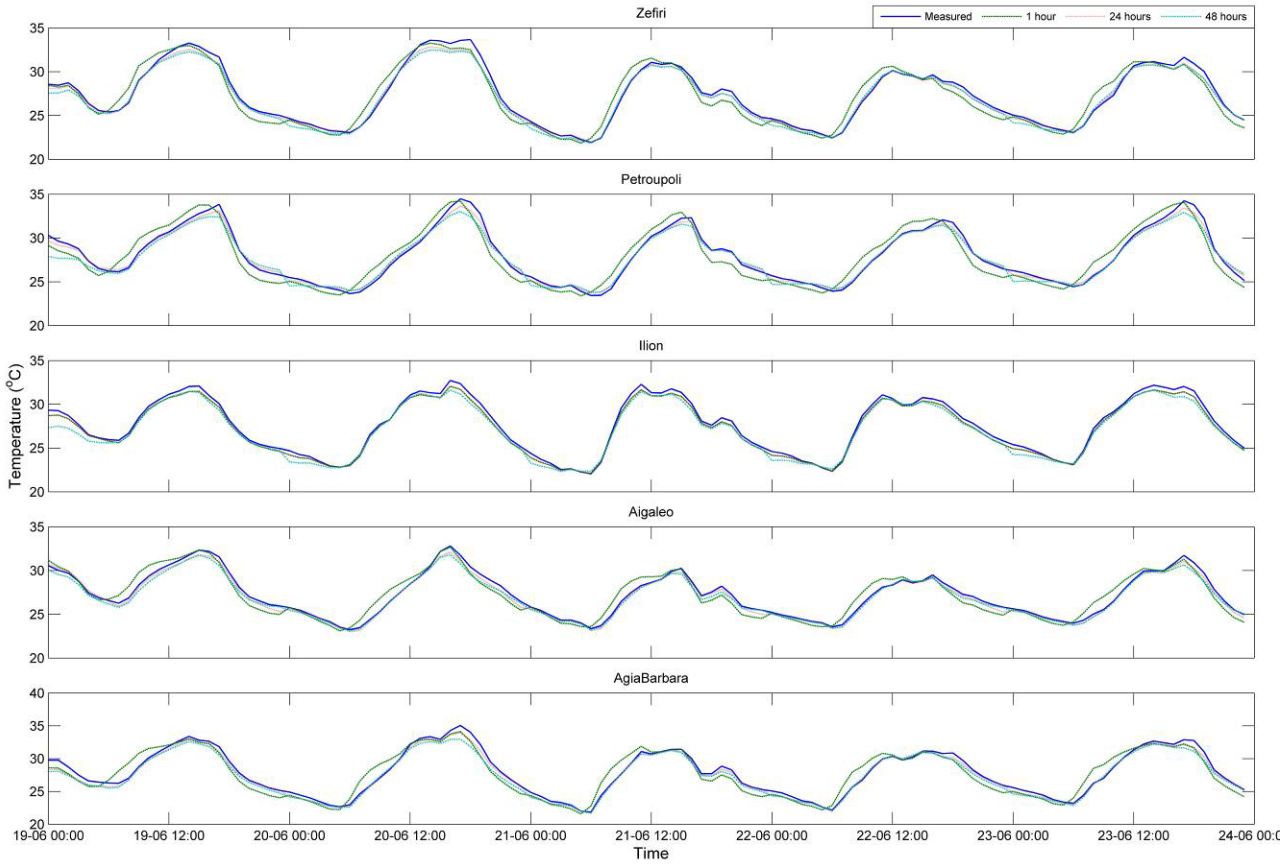

Figure 98 ***Measured – predicted temperatures for 19-20/06/2009***

As we can see in Figure , the diurnal fluctuation of temperatures is very smooth and is followed by the 1 hour and 24 hours Elman prediction algorithms quite accurately. Furthermore, although the daily temperature fluctuations depicted in Figure 99 are not as smooth and predictable, the Elman NN manages to follow the measured data most of the time.

Another significant aspect of the proposed neural network architecture that should be examined is the alterations in prediction accuracy due to seasonal variations and the necessity to retrain the network when the season changes.

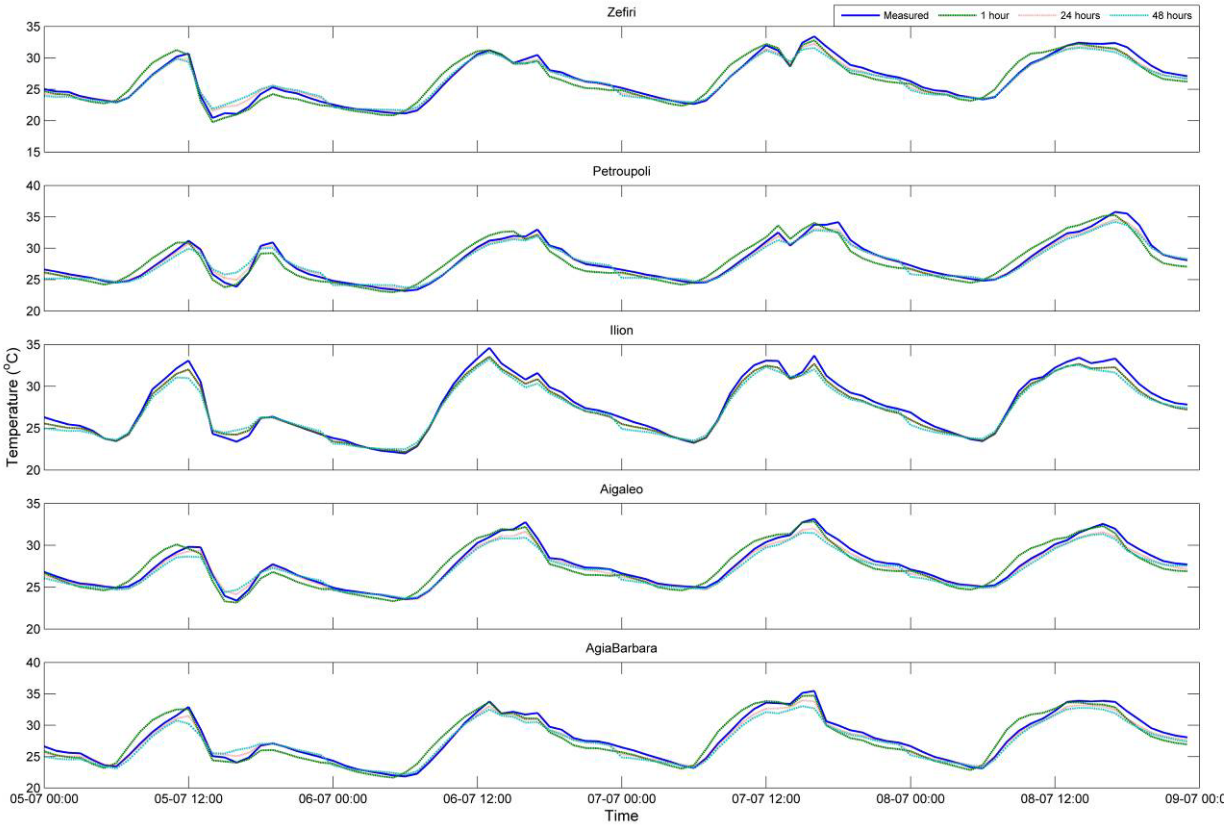

Figure 99: *Measured – predicted temperatures for 05-06/07/2009*

In Figure 100 and Figure 101 the measured and predicted temperatures are depicted for Haidari and Agia Barbara experimental sites. Although the prediction accuracy is not always the highest possible, especially for the 48 hours prediction horizon, the overall prediction accuracy does not change significantly with the seasonal changes. The seasonal changes of the standard deviation between the measured and predicted values for Haidari and Agia Barbara sites are tabulated in Table 38.

Table 38 *Seasonal variations of standard deviation between measured and predicted temperatures for Agia Barbara and Haidari sites*

	Agia Barbara			**Haidari**		
Prediction horizon	**1h**	**24h**	**48h**	**1**	**24**	**48**
12/5/2009-31/6/2009	0.5516	0.9301	0.7581	0.5532	1.4003	1.0013
1/6-30/6/2009	0.4392	0.8087	0.733	1.0013	1.0267	0.5104
1/7-31/7/2009	0.7787	0.793	1.2449	0.5767	0.8057	0.9998
1/8-31/8/2009	0.4127	0.5587	0.9892	0.5326	0.5731	1.0996
1/9-6/9/2009	0.4682	0.5061	0.93	0.7029	0.7274	1.1727

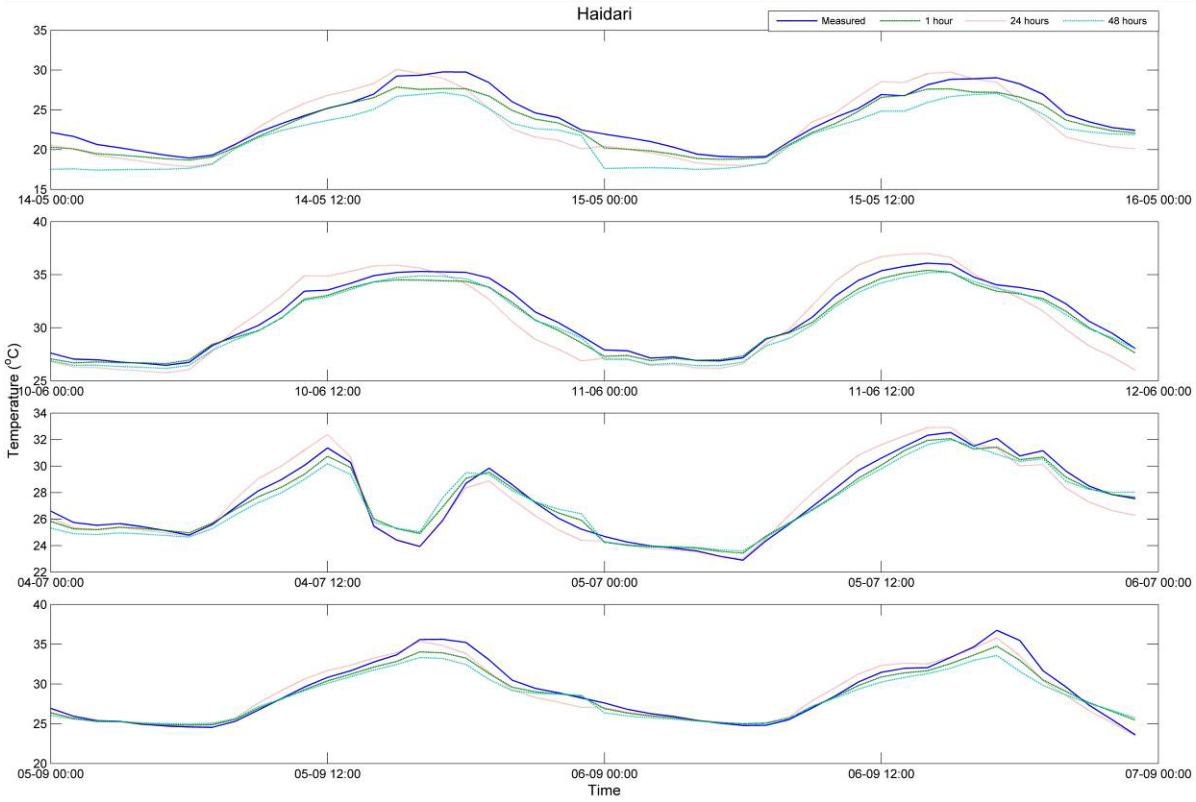

Figure 100 Monthly comparison for measured – *predicted temperatures of Haidar*i meteo station

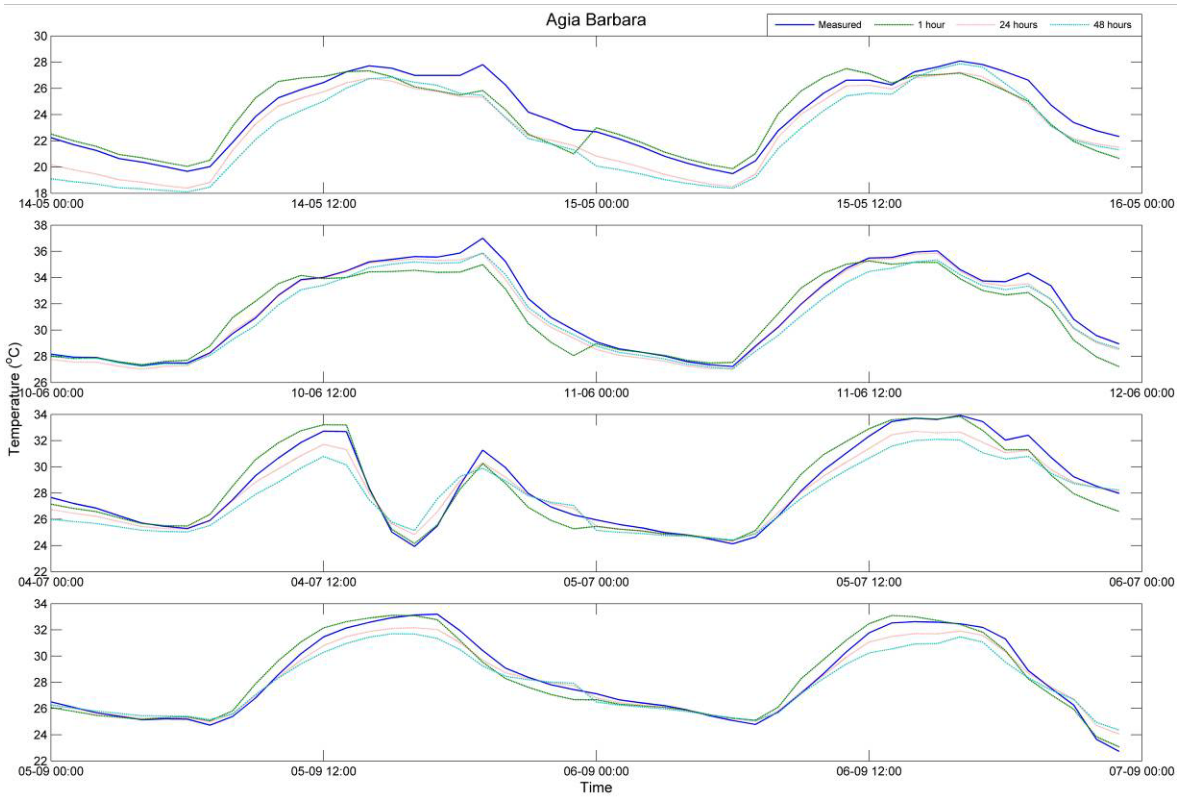

Figure 101 ***Monthly comparison for measured – predicted temperatures of Agia Barbara meteo station***

Another significant aspect is the methodology's response to different weather conditions or during weather changes. For this reason the ANN's response is studied for two experimental sites i.e. Koridalos and Haidari as well as for day to day temperature changes (Figure 102).

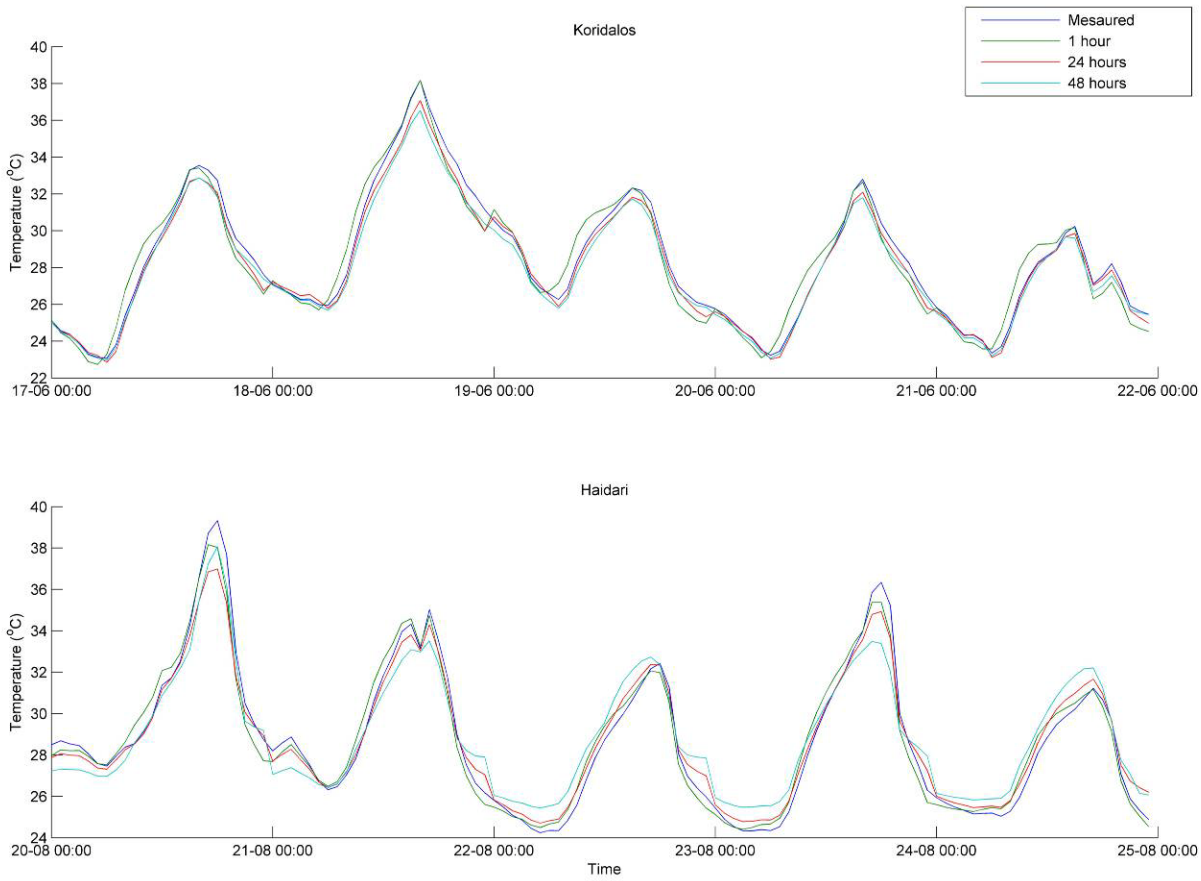

Figure 102 ***Response of the ANN to weather changes***

As we can see in the specific figure, although outdoor temperature is considerably decreased from 19/6/2009 to 20/6/2009, and also increased from 23/8/2009 to 24/8/2009, the ANN follows this change in a successful manner especially for the 24 hours prediction horizon.

The predicted versus the measured urban heat island intensity for three sites (i.e. Agia Barbara, Egaleo and Halandri) and for 24hours prediction are depicted in Figure 103, Figure 104 and Figure 105, respectively. The figures show a satisfactory fitting with a RMSE less than 0.3 and R^2 to be close or higher than 0.9 for all three sites which represents a good prediction of the urban heat island intensity.

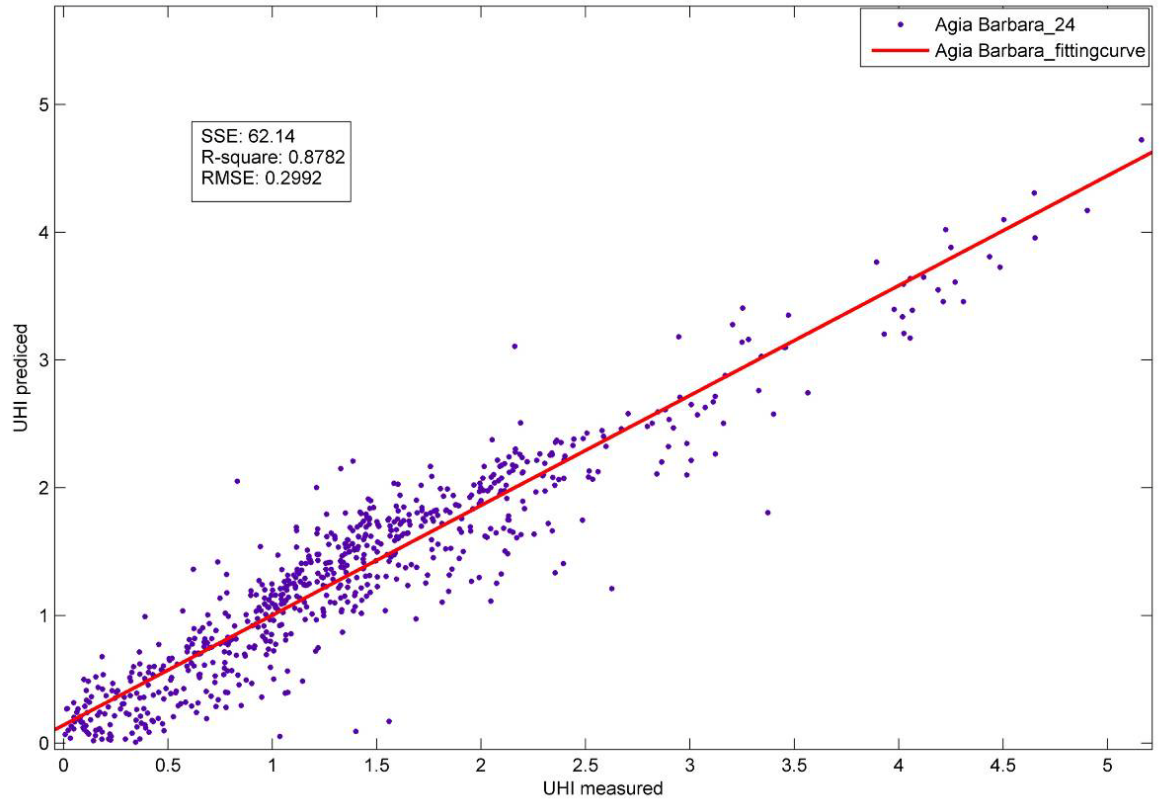

Figure 103 *The UHI measured versus UHI 24 hour predicted for the Agia Barbara site*

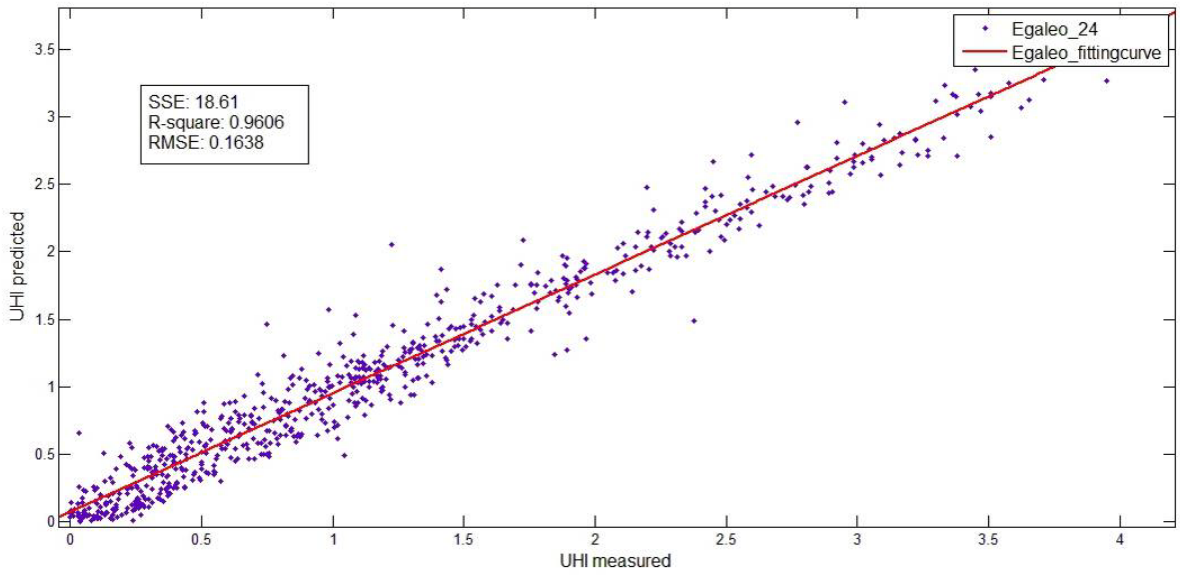

Figure 104 *The UHI measured versus UHI 24 hour predicted for the Egaleo site*

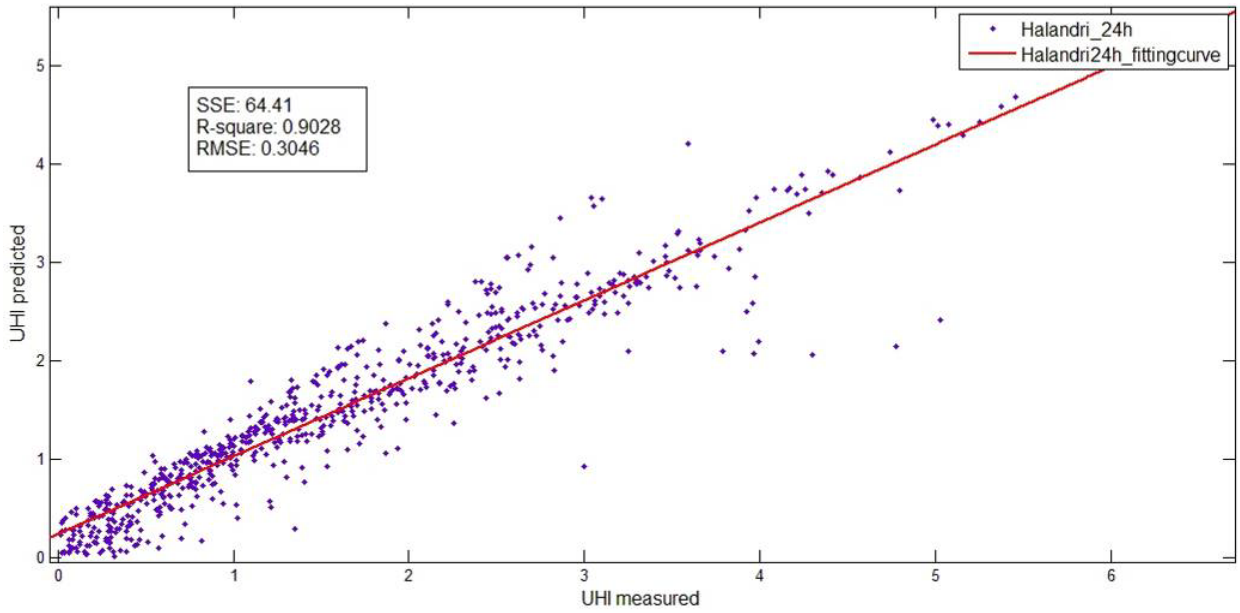

Figure 105 The UHI measured versus UHI 24 hour predicted for the Halandri site

An additional verification process has been performed using data collected in 2010 from each test site. Using the Elman Artificial Neural Network (ANN), and the data set from 19-6-2010 to 29-9-2010, the temperature at the experimental test sites is predicted. In order to verify the results from the ANN, the percentage error between the predicted and the measured temperature is used.

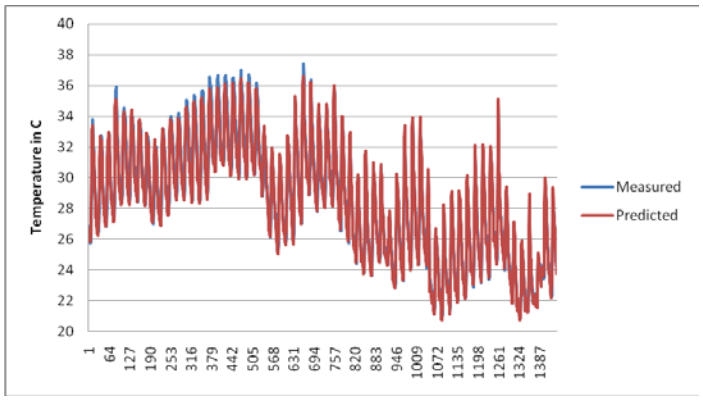

A

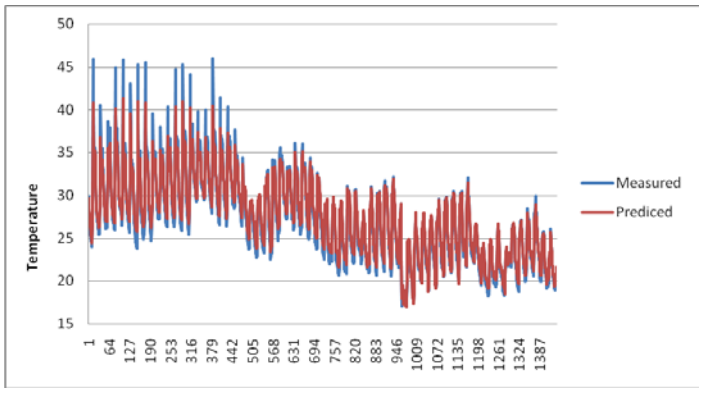

B

Figure 106 Predicted vs measured values of urban air temperature for the 2010 data set at Vyronas (A) and Ilioupoli (B) sites (1h prediction).

The mean value, standard deviation and mean square error (MSE) for 9 sites and for the 3 prediction horizons (1, 24, 48 hours) is shown in Table 38. It can be observed the ANN behaves very well to the new data and predicts the temperature accurately enough taking into account the limited set of data used for the prediction.

Table 39 Seasonal variations of standard deviation between measured and predicted temperatures for Agia Barbara and Haidari sites

Site	PredictionHorison	MeanValue	Standard Deviation	MSE
Vyrwnas	1	1.59	1.31	4.23
	24	0.85	0.60	1.07
	48	1.93	1.45	5.84
Elliniko	1	2.08	1.72	7.28
	24	2.10	1.52	6.72
	48	3.02	2.24	14.13
Glyfada	1	1.09	0.90	2.00
	24	1.35	0.88	2.58
	48	2.42	1.81	9.13
Ilioupoli	1	1.59	1.21	4.01
	24	2.51	1.80	9.51
	48	5.16	3.42	38.29
Kaisariani	1	2.08	1.59	6.84
	24	1.66	1.21	4.21
	48	3.10	2.41	15.43
Kalithea	1	2.28	1.47	7.33
	24	1.47	1.13	3.43
	48	2.39	1.63	8.36
Mosxato	1	1.79	1.81	6.45
	24	1.23	1.15	2.83
	48	2.00	1.53	6.34
Renti	1	2.53	1.98	10.32
	24	1.46	1.13	3.41
	48	2.18	1.69	7.60
Zografou	1	2.37	1.93	9.35
	24	1.43	1.12	3.31
	48	2.89	2.30	13.62

9 WRF-ACASA AND ACASA. CMCC MODEL

9.1 ACASA

The **Advanced Canopy-Atmosphere-Soil Algorithm** (**ACASA**) model, was first developed as a generalized Soil-Vegetation-Atmosphere-Transport (SVAT) scheme at University of California, Davis ((Pyles et al., 2000; 2003)) from the predecessor Higher Order Closure Model (HOCM) from Meyers (1985) and Meyers and Paw U (1986,7). The model simulates the exchanges of heat, water vapour and CO_2 within and above a canopy, It treats the surface and associated fluxes as an interconnected system, and the atmosphere, the urban surface, and the soil are represented as a multilayer system (10 layers above the canopy, 10 layers within the canopy, and 15 layers into the soil). Turbulent fluxes are calculated using third order equations (Meyers and Paw U 1986; 1987). To properly work in urban environment, the model has been modified to account for the anthropogenic contribution to heat exchange and carbon production (Marras et al., 2010). A more detailed model description is reported in the deliverables 4.1 and 4.2.

9.2 Applications

ACASA was applied by CMCC over Firenze and Helsinki case studies and used to simulate urban energy and mass fluxes at 30 minute time steps. The simulation period covered one year from January to December 2008, and a three months period in 2010 (July-September).

Model accuracy was evaluated using four different statistical indices. The first index used was the root mean squared error (RMSE) between predicted and observed data (descript earlier). Small values of RMSE indicate better model predictions. A second index used to test the accuracy of modeled flux data is the mean absolute error (MAE).

$$MAE = \frac{\sum_{i=1}^{N} \left| Pi - Oi \right|}{N}$$

where Pi is the predicted data, Oi is the observed data, and N is the number of data.
A small value is indicative of a better match along the 1:1 line comparison of predicted and observed values. The mean bias error (MBE) indicates the percentage of error of modeled data and it was calculated as

$$MBE = \sum_{i=1}^{N} \frac{Pi - Oi}{N}$$

Positive values of MBE indicate a model overestimation with respect to measured data, while negative values indicate a model underestimation. Model results were also evaluated by the index of agreement (d). This index determines the degree to which magnitudes and signs of the observed value about the mean of observed values are related to the predicted deviation about mean predicted value, and allows for sensitivity toward differences in observed and predicted values as well as proportionality changes.

$$d = 1 - \frac{\sum_{i=1}^{N}(Pi - Oi)^2}{\sum_{i=1}^{N}(\left|Pi - \overline{O}\right| + \left|Oi - \overline{O}\right|)^2}$$

Linear regression between simulations and observations were also used to evaluate model performance. The regression provides two pieces of information: the slope indicates whether or not there is a bias, and the coefficient of determination (R^2) assesses scatter, or how well the time-series shape of the simulation matches the time-series shape of the measured data. Regression significance between simulated and measured net radiation, sensible heat, latent heat, soil heat, and CO2 fluxes were evaluated by the F test. Significance was tested at 0.95 and 0.99 levels.
Also the relative error was calculated per each flux as the ratio between RMSE and the range of the measured flux variation. All statistical indices were calculated using all 30-min points. For all analysis, non gap-filled flux data were used.

9.2.1 Firenze

January-December 2008

Model evaluation was made by comparing simulated fluxes with Eddy Covariance flux measurements collected by CNR at the Ximeniano tower in the period January-April 2008. The period May-December 2008 could not be evaluated because no measured data were available for the model output comparison. The main results of the analyses have been presented in the deliverable 3.4. Here is reported a brief description of the main results and the statistical analysis of the data.

In general, differences between modeled and observed fluxes were not statistically significant and the model was able to capture trend and magnitude of sensible heat (H), latent heat (LE), and carbon (NEE) fluxes. Figure 107 and Figure 108 show the comparison between modeled and observed fluxes during the month of April 2008.

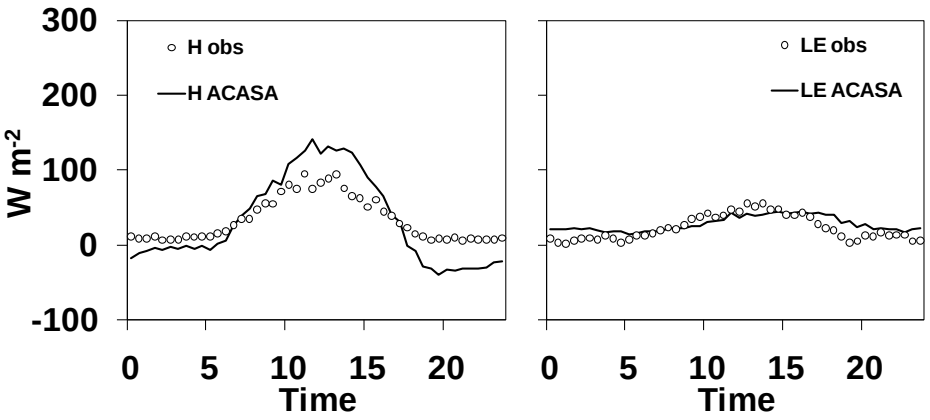

Figure 107: Comparison between simulated (solid line) and observed (dots) sensible heat flux (H) and latent heat flux (LE) data in April 2008. Data are sorted by time and averaged.

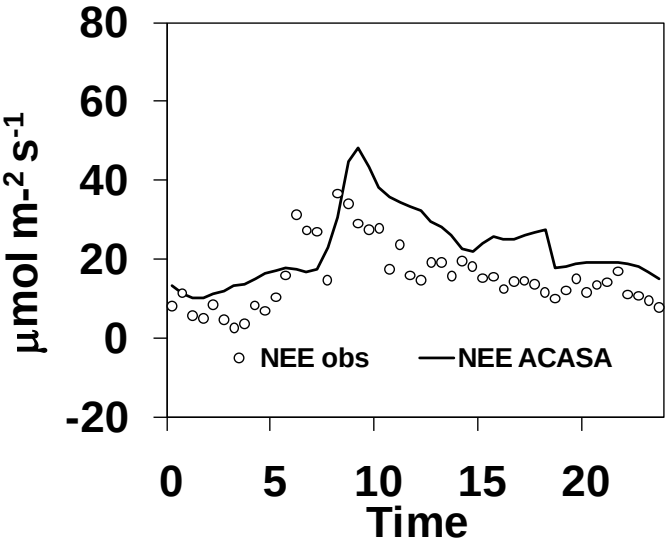

Figure 108: Comparison between simulated (solid line) and observed (dots) Net Ecosystem Exchange (NEE) flux data in April 2008. Data are sorted by time and averaged.

Measured traffic data every half-hour (number of vehicles per Km^2) were included as a model input to simulate the diurnal variation of CO_2 flux. Two peaks in CO_2 flux typically arise in the early morning and late afternoon in correspondence of the rush traffic hour. The model was able to capture this trend. The general model underestimation of CO_2 flux was mainly due to a lack of information about energy consumption for heating/cooling process to be accounted by the model.

Values of the statistical indices are reported in Table 40. Errors are generally low and the differences in simulated and observed data are not statistically significant at 95 % confidence level. A more detailed analyses is necessary to better investigate on the small differences between modeled and measured data.

Table 40. Linear regression and statistical indices for the period January-December 2008.

Flux	a	b	R^2	RMSE	Relative Error (%)	MAE	MBE	d	N
H (Wm^{-2})	1.45	-18.04	0.53	52.4	10.24	39.56	-4.36	0.74	1302
LE (Wm^{-2})	0.15	22.89	0.07	30.13	11.42	20.64	6.71	0.48	1915
NEE ($\mu molm^{-2}s^{-1}$)	0.12	19.94	0.08	26.05	8.33	16.25	2.55	0.4	1846

July-September 2010

ACASA was run for a three months period of 2010 (July to September) and simulated fluxes were compared with observations collected at the Ximeniano flux tower every half hour.
In general, small differences were observed between modeled and measured fluxes during July and August. In September, few observed data (only three days) were available for the comparison, so the evaluation of model performance was not possible for the entire month.

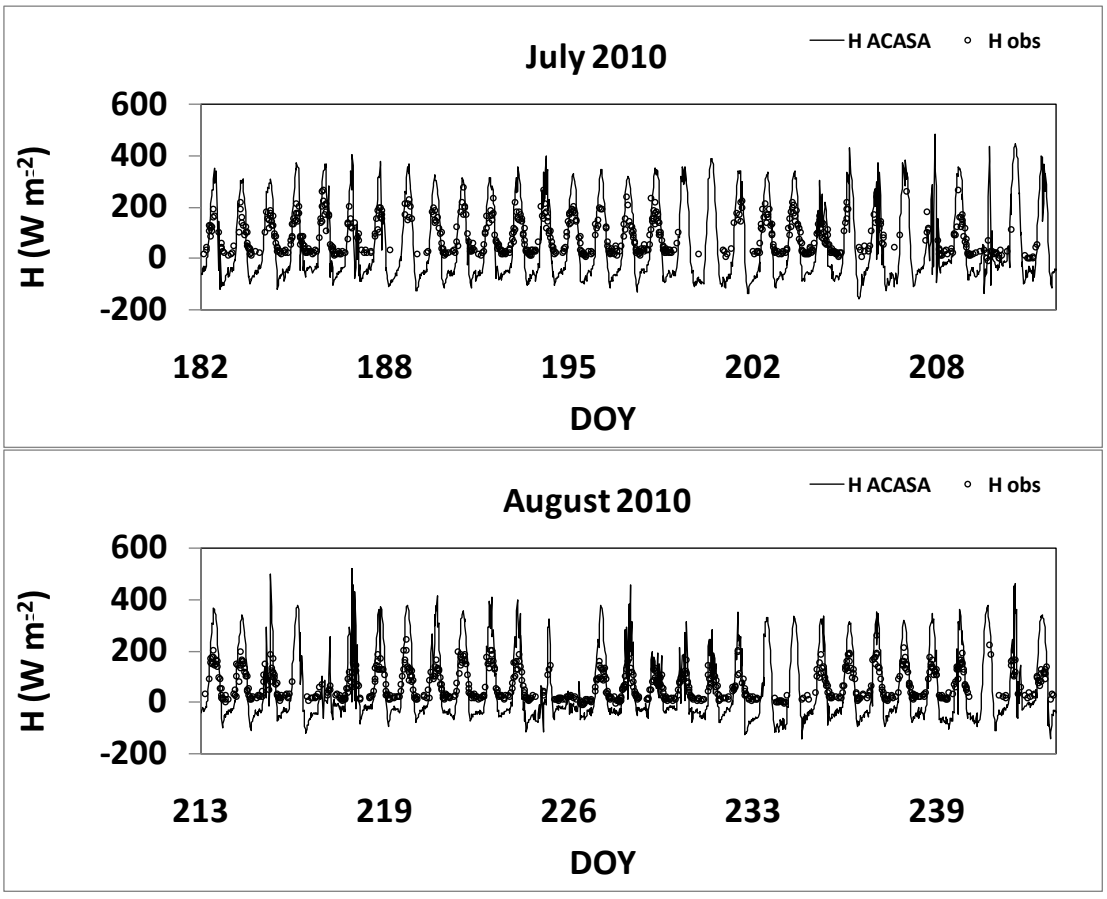

Figure 109. Comparison between simulated (solid line) and observed (dots) sensible heat flux (H) data in July and August 2010.

The model overestimated H (Figure 109) and underestimated LE (Figure 110) during the night. Many spikes were present in the observed H and LE data, so the measured data were despiked before the comparison. At the end, more the 60% of the measured data were lost.

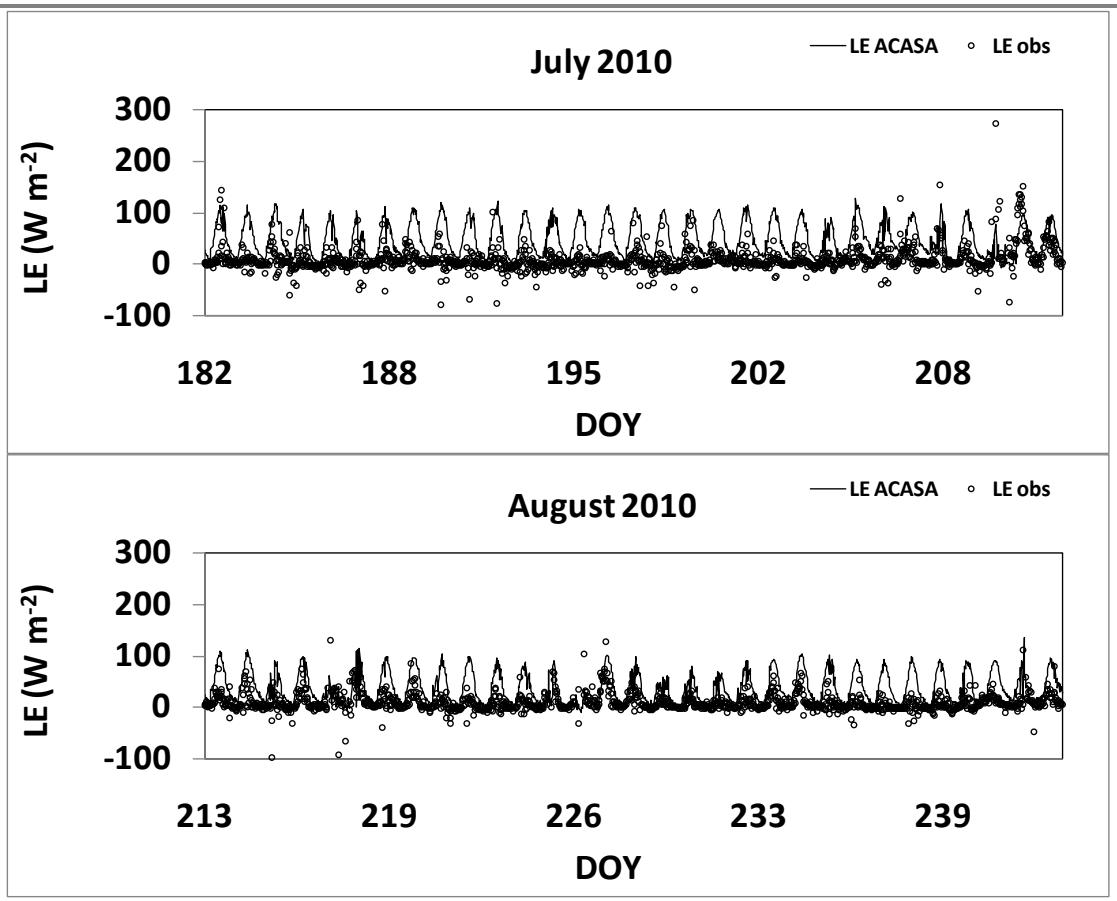

Figure 110. Comparison between simulated (solid line) and observed (dots) latent heat flux (LE) data in July and August 2010.

Measured traffic data every half-hour were not available for the 2010 period, so data of the number of vehicle per Km^2 collected in 2007 were used to simulate the diurnal variation of CO_2 flux. The model was able to capture the decrease of CO_2 flux in August where people is commonly on vacation and there is less traffic in the city (Figure 111).

Linear regression and statistical indices are reported in Table 41. Model performance in LE estimation were reduced because of the large variation in measured data, while NEE was estimated using not traffic data of the 2010 period.

Table 41:. Linear regression and statistical indices for the period July-September 2010.

Flux	a	b	R^2	RMSE	Relative Error (%)	MAE	MBE	d	N
H (Wm^{-2})	2.16	-88.91	0.77	100.71	34.87	85.98	-0.77	0.76	1551
LE (Wm^{-2})	0.54	38.21	0.12	46.18	10.32	36.37	34.04	0.42	2986
NEE ($\mu molm^{-2}s^{-1}$)	0.51	16.71	0.14	15.41	11.05	13.39	13.17	0.38	2996

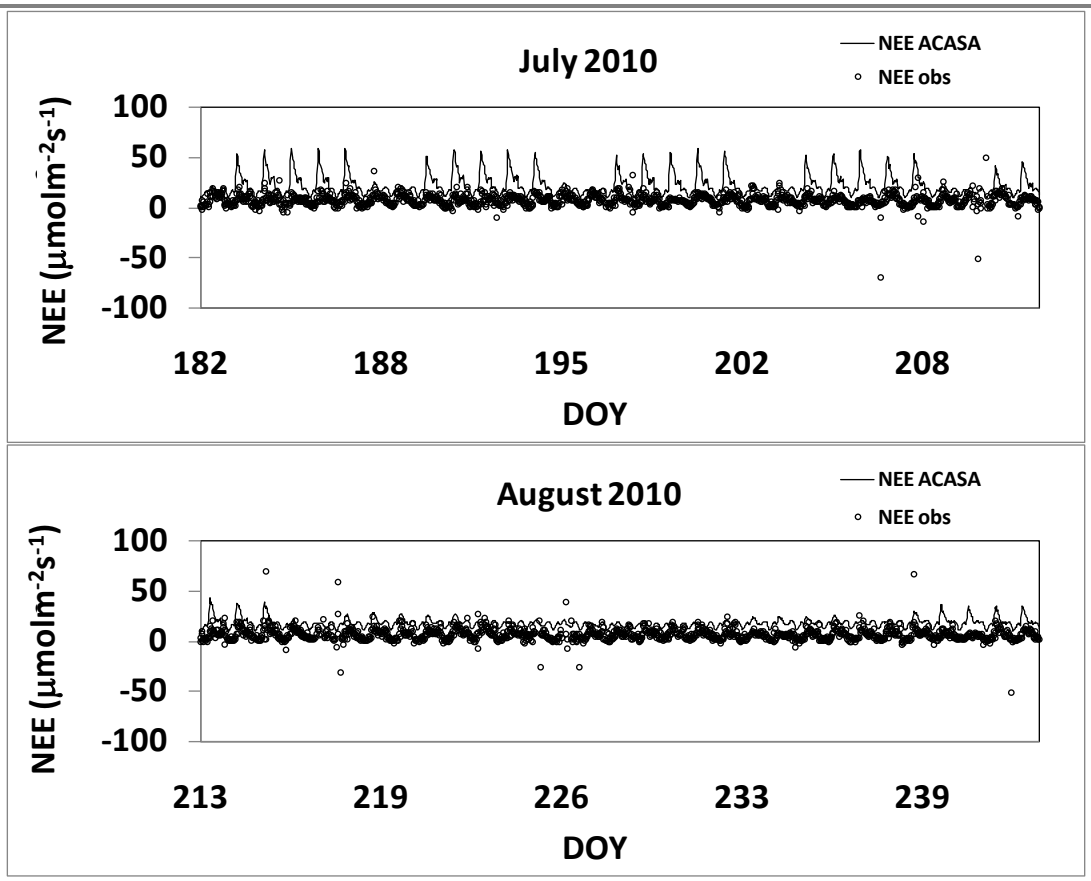

Figure 111. Comparison between simulated (solid line) and observed (dots) Net Ecosystem Exchange (NEE) data in July and August 2010.

9.2.2 Helsinki

January-December 2008

Simulated fluxes were compared with Eddy Covariance flux measurements collected by UHEL at the Kumpula site in the period January-December 2008. As for Firenze, the main results of the analyses have been presented in the deliverable 3.4. Here are reported a brief description of the main results and the statistical analysis of the data.

In this city, measured fluxes of net radiation (Rn) were available for model evaluation. Simulated net radiation (Rn) flux perfectly matched the observed flux during the entire year (Figure 112).

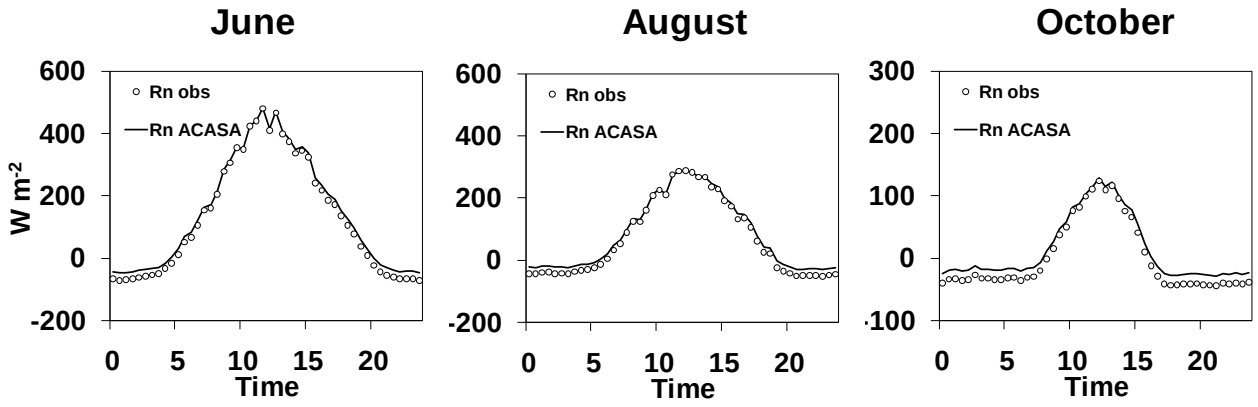

Figure 112. Comparison between simulated (solid line) and observed (dots) net radiation flux (Rn). Data are sorted by time and averaged.

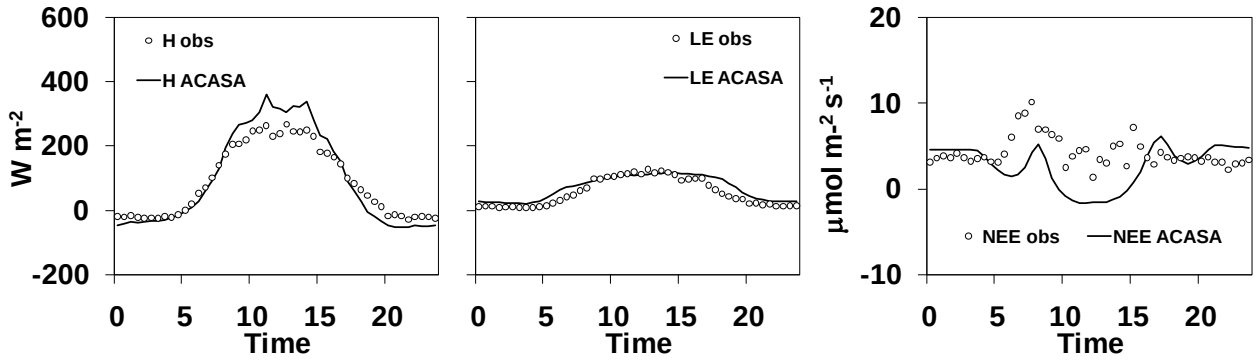

Figure 113. Comparison between simulated (solid line) and observed (dots) sensible het (H), latent heat (LE) and carbon (NEE) fluxes during May 2008. Data are sorted by time and averaged.

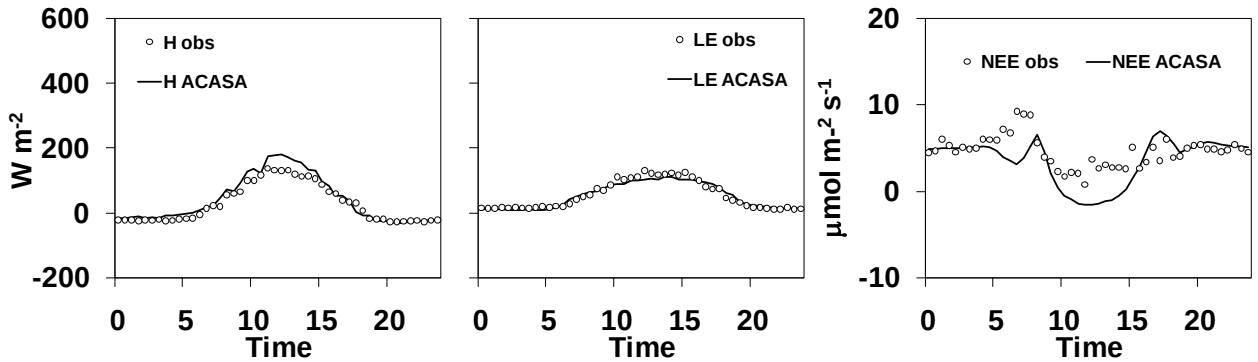

Figure 114. Comparison between simulated (solid line) and observed (dots) sensible het (H), latent heat (LE) and carbon (NEE) fluxes during August 2008. Data are sorted by time and averaged.

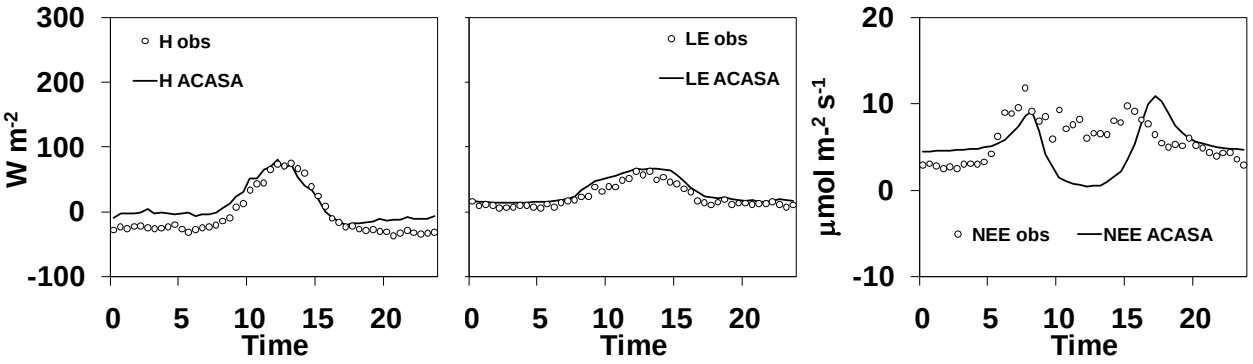

Figure 115. Comparison between simulated (solid line) and observed (dots) sensible het (H), latent heat (LE) and carbon (NEE) fluxes during October 2008. Data are sorted by time and averaged.

In general, the model was able to adequately reproduce the sensible heat flux (H) during the year (Figure 113, Figure 114, Figure 115), even if a slightly overestimation of H was observed in spring and in September. In Helsinki, vegetation is present in the investigated area and the model takes it into account in reproducing the trend and magnitude of LE flux all over the year. Simulation of the diurnal cycle of carbon flux were made using the emission curve of CO in Helsinki for the model parameterization.
In general, the model was able to capture the diurnal trend of CO_2 flux. Major differences between observations and model results were observed during the fall, when foliage in the trees fall down. A constant LAI value is set in the model, so adjustment are needed to take into account for the LAI seasonality.

Values of the statistical indices are reported in Table 42. As for Firenze case study, the errors are generally low and the differences in simulated and observed data are not statistically significant at 95 % confidence level. Best results were obtained in simulating the net radiation (Rn), while the error was similar for other fluxes.

Table 42. Linear regression and statistical indices for the period January-December 2008.

Flux	a	b	R^2	RMSE	Relative Error (%)	MAE	MBE	d	N
Rn (Wm^{-2})	0.98	15.90	1.00	18.08	1.8	15.57	14.81	1	17282
H (Wm^{-2})	1.21	13.57	0.71	73.19	9.08	47.09	21.81	0.87	10688
LE (Wm^{-2})	0.64	26.88	0.63	35.12	6.29	25.32	12.11	0.86	10002
NEE ($\mu molm^{-2}s^{-1}$)	0.47	3.03	0.04	6.64	7.6	4.29	-0.63	0.41	12689

July-September 2010

The period July-September 2010 was also used for model evaluation in Helsinki. In this city, the measured data consistency and quality were higher than in Firenze and simulated fluxes matched better the observations. The model matched well the observations all over the months. Comparison between simulated and measured Rn was also possible for the three months. An example of simulated and observed Rn, H, and LE fluxes is given in Figure 116 in August 2010. The trend and magnitude of the measured fluxes were captured by the model for the three fluxes, even if better performance were obtained with Rn. In September, the measured LE data were not available for the entire month, so the comparison is not shown.

Simulated CO_2 flux was compared with observations during the three months (Figure 117). Also in this case, measured data do not cover the 30 days of September. As for 2008, simulation of the diurnal cycle of carbon flux was made using the emission curve of CO in Helsinki for the model parameterization and a constant LAI value was used for the three months.
Table 43 reports the linear regression and statistical indices calculated for the period July-September 2010. Also, in this period, errors are generally low and the differences in simulated and observed data are not statistically significant at 95 % confidence level. Further analyses is necessary to better investigate on the small differences between modeled and measured data.

Table 43. Linear regression and statistical indices for the period July-September 2010.

Flux	a	b	R^2	RMSE	Relative Error (%)	MAE	MBE	d	N
Rn (Wm^{-2})	0.97	18.25	1.00	18.18	1.89	16.62	15.71	1.00	4261
H (Wm^{-2})	0.97	-2.74	0.61	76.68	12.41	52.36	-4.07	0.87	2429
LE (Wm^{-2})	0.71	36.13	0.52	55.90	13.45	39.19	13.45	0.84	2029
NEE ($\mu molm^{-2}s^{-1}$)	0.11	3.18	0.07	7.04	10.90	4.79	-0.21	0.47	2011

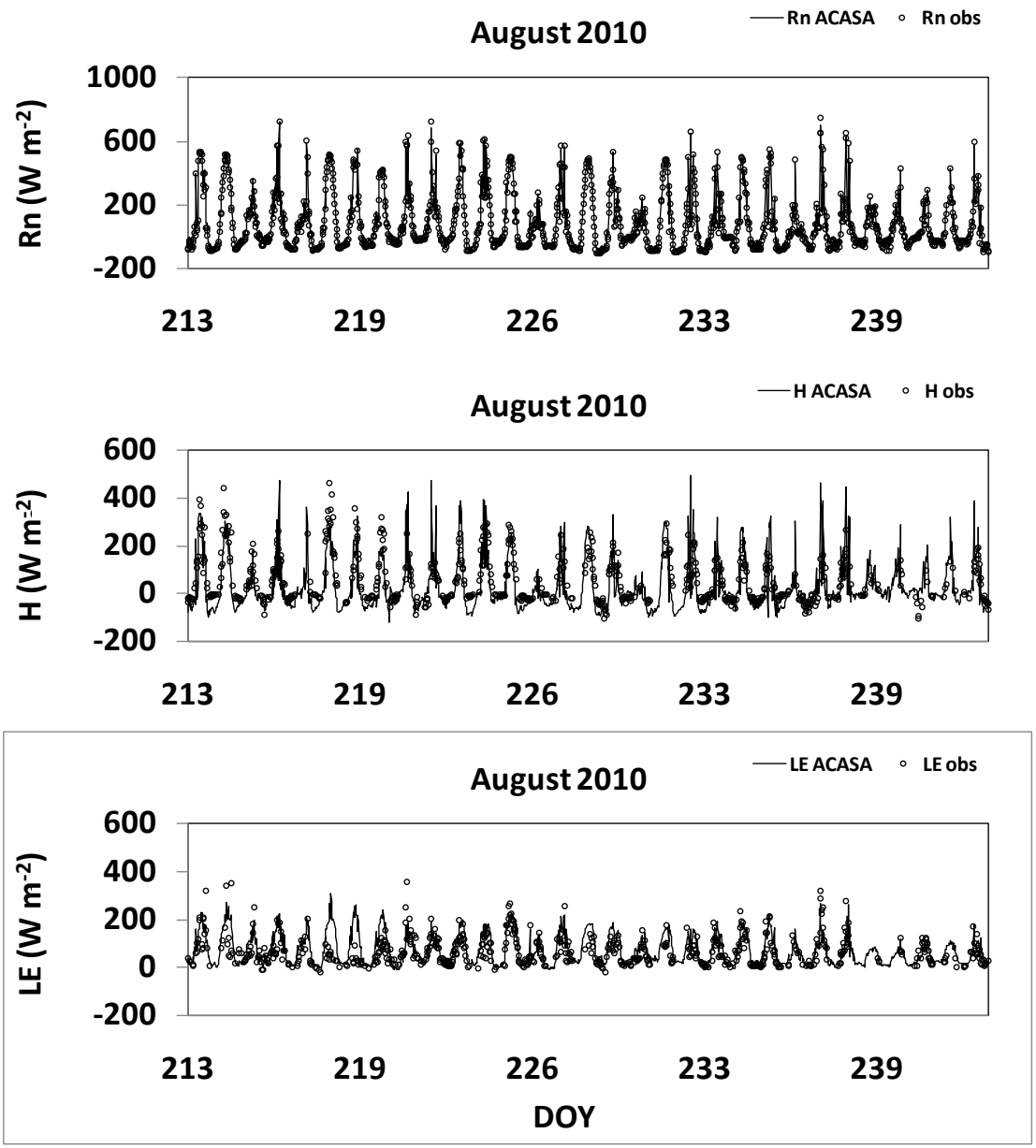

Figure 116 Comparison between simulated (solid line) and observed (dots) net radiation (Rn), sensible heat (H), and latent heat (LE) flux in August 2010.

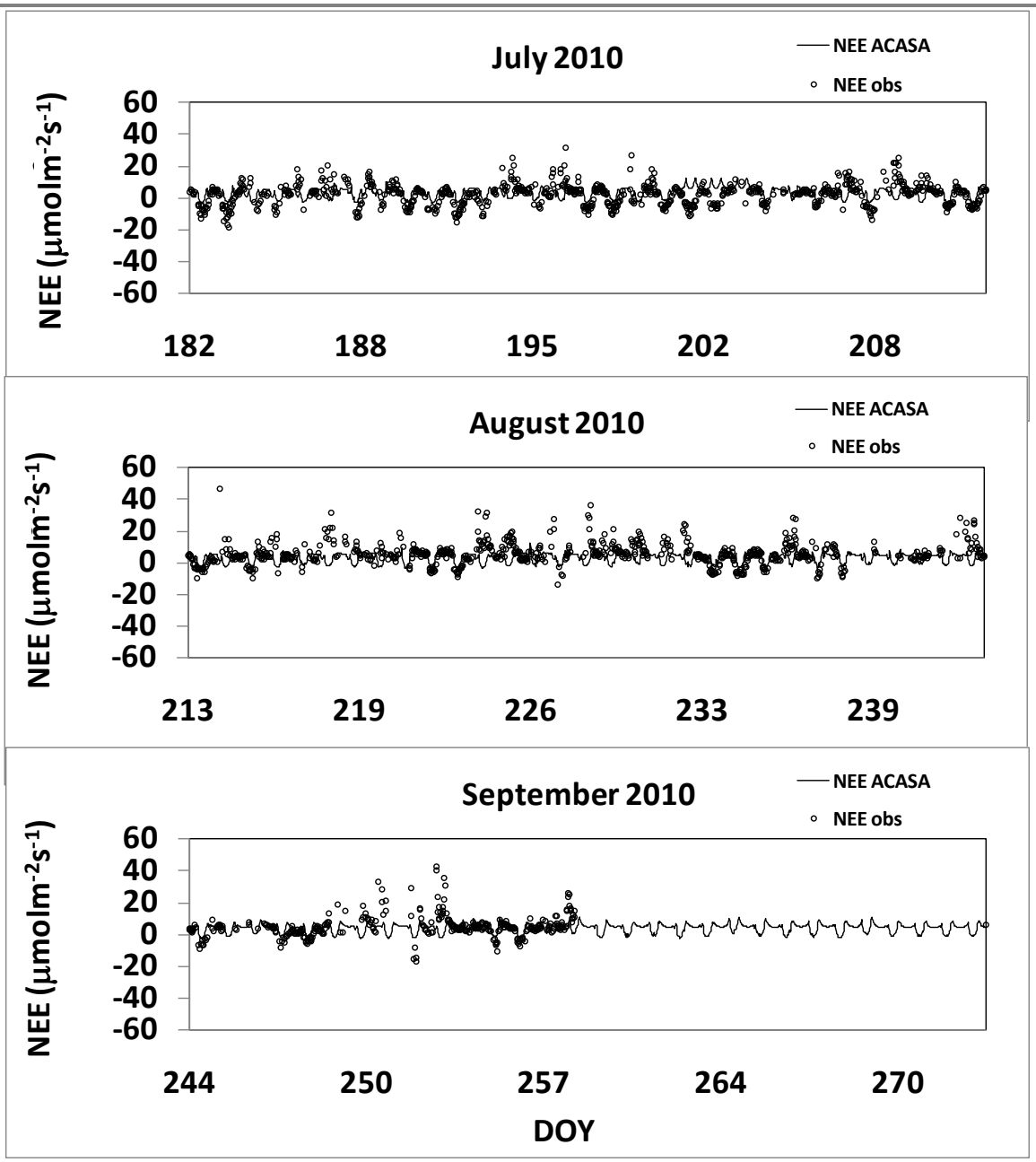

Figure 117. Comparison between simulated (solid line) and observed (dots) Net Ecosystem Exchange (NEE) flux data from July to September 2010.

In general, we can say that the model was able to adequately reproduce urban fluxes in both cities. Anyway, improvements are needed to better simulate NEE and LE fluxes. The introduction of carbon emission factors per type of vehicle could improve the estimation of CO_2 flux. Also, LAI value changes with season could improve the LE and NEE estimation.

9.3 WRF-ACASA

WRF-ACASA non-nested configuration

For the Firenze and Helsinki case studies, the mesoscale model WRF (Weather and Forecast model) was run at 200 m horizontal grid spacing for a total of 27:27:28 points (x:y:z), which gives an effective horizontal resolution of about 600-800 meters. Initial and boundary conditions updated every 3 hours were provided for all of 2008 by UPM. In addition, a special set of surface characteristics were provided at 200m grid spacing to drive the simulations, as the standard WRF package contains these at 1x1 km only. The model was run for a single (non-nested) domain (using "*ndown"*).

For these simulations, WRF was run with ACASA (Advanced-Canopy-Atmosphere-Soil Algorithm) embedded as a column physics module that provides both the physical state and forcing between the surface-layer and the rest of the WRF atmosphere. This communication is fully dynamic in that WRF provides the meteorological and morphological forcing for ACASA, while ACASA responds back to WRF in a manner that alters the atmospheric state. ACASA was implemented in WRF using a similar subroutine calling architecture as that used by the existing NOAHLSM surface-layer module, since that particular platform provided needed morphological information while enabling the usage of fluxes directly as output. This architecture was chosen over the other three options in WRF due to the fact that it is easier for ACASA to "communicate" back to WRF with little modification to its output.

As is the case with Earth's actual surface-atmosphere system, WRF simulations of the same depend very heavily on the exchange of heat, mass, and momentum between the surface and atmosphere. For this to occur, ACASA specifically requires the following variables from WRF: temperature, humidity, wind speed, downwelling long- and short-wave radiation flux densities, precipitation rate and form, air pressure, and the surface morphology characteristics (LAI, soil type, minimum stomatal resistance, background albedo and background roughness length). Other quantities needed by ACASA, such as the canopy architecture index, mean leaf diameter, basal respiration rate, etc. are "hardwired" with the same values at each point.

ACASA updates sensible heat flux density, latent heat flux density, friction velocity (related to momentum flux density), turbulence kinetic energy, and the effective surface "skin" temperature, and bulk thermal emissivity every 30 minutes. As is done with NOAHLSM and other surface-layer packages, WRF uses this information to translate the ACASA forcing into the radiative transfer modules and the time-tendency components of wind velocity, temperature, and humidity in the lowest atmospheric layers.
In addition, the soil and/or snow and/or canopy thermal and hydrological states are stored at each point between time steps in order to estimate the ACASA suite of thermal storage fluxes and water retention, etc., all of which are needed for ACASA to estimate the main fluxes (and surface emissivity) properly. Included here are albedo modifications whenever snow or soil moisture is present. Other ACASA quantities are also used by WRF, but these are mainly diagnostic only, as surface (water) runoff, underground runoff, soil surface infiltration rate, carbon-dioxide flux density.

9.4 Applications

WRF output for the estimated flux footprint surrounding the tower location (9x9 grid points, or 3.4 km2) were averaged spatially to achieve a single time series, with hourly temporal resolution. This hourly averaged model output for the 3.4 km area (specifically, points P(12,12) through P(14-14) were compared against simultaneous single-point measurements, both representing the same or similar spatial footprints. The issue of 200-m gridpoints in WRF being smaller than the Reynold's averaging scale for turbulent parameterizations has not been resolved, as of yet. Similar averaging areas were used for Helsinki and Firenze, although the EC flux tower for which observations at Helsinki were made is outside of the 200m by 200m grid.

Observed values were every 30- minutes. The frequency of WRF output is every 60 minutes. Thus it was necessary to synchronize each time series to having points representing 60 minutes each. Results involve WRF-ACASA simulations representing the baseline cases for 2008 for both Firenze and Helsinki. Model values were generated from simulations lasting one year for each case. All available observations (post-QC) were used in the comparisons. Time-series (graphical) and statistical (graphical and quantitative) comparisons were performed to compare model and observed values.

For the composite-averages, only data where both observations and model values were available were used. For Helsinki, this involved several hundred points used to calculate each composite hourly value, an adequate number for statistical analyses. For Firenze, each composite point involves averages of 35 to 45 points each, which is much less than for Helsinki but which is still sufficiently large for statistical tractability.

Observed and model composite values (24 total representing one composite 'day') were linearly regressed to quantitatively assess model performance over time. Slope and coefficients of determination (r^2) from these regressions are given in the plots. Error bars applied to observed composite points indicate 95% confidence limits applied to each composite point. The choice of using an average of multiple model grid points, instead of one, rests on the notion that in turbulent environments with significant 'canopies' (buildings and/or vegetation), that in turbulent environments, information gets 'smeared out' over one or several square kilometers over time scales of about 30 minutes. This means that the 200-meter spacing of points in the current WRF configuration is almost always smaller than the (measured) flux footprint. This means that one WRF point cannot represent what one would measure at a tower, that an average of points sufficiently surrounding the measurement site might be more appropriate. Specific footprints vary with time depending on thermal stability, among other things.

9.4.1 Firenze

Sensible Heat Flux density (H, HFX). There are roughly 5 weeks of observed data that were available for the comparison, therefore only simultaneous WRF-ACASA results were used in the statistical comparisons. Observations were available for three periods: two sets of several days in January and February, the third spanning most of April. In general, WRF-ACASA values reflect a much higher radiation environment than what was observed, with ACASA values climbing well

past 500 Wm^{-2} during midday on most days in April. Graphical representations of simultaneous observations, on the other hand, show H having difficulty getting past 200 Wm^{-2} during all days whenever data are available. This is due most likely to the WRF simulations supporting clear skies during the period over Firenze, while clouds were observed. Results from in-situ comparisons (see previous section) indicate that ACASA can indeed provide estimates of H for this time periods for this city, provided that the observed forcing meteorological data are available. Only results for January and February (Figure 118) show a similarity between observed and WRF-ACASA values of HFX in magnitude of the diurnal cycle, which is probably due to model and observed similarities in wintertime radiative forcing. Composited values for both February and April, along with linear regression statistics, are presented (Figure 119) which also shows a clear discrepancy between model and observed daytime values described above. Although coefficients of determination (R^2) are very high, there are discrepancies in the amplitude revealed in the value of the slope for this quantity.

Latent Heat Flux density (LH, LE). In sharp contrast to sensible heating, model and observed values are in much better agreement, with all but ~10 hourly points differing by less than 30 Wm^{-2}, which is commonly considered to be near the limit of observational certainty for this quantity (Figure 119). Composited results indicate that the diurnal cycle of LE is also captured reasonably well by the model than is H, with a slight overestimation during the middle of the day (Figure 119).

Carbon Dioxide Flux density (NEE, FCO2). Model values for this quantity are clearly 'flat' in relation to observed values, with composite values indicating a lack of model representation of both the magnitude and character of the diurnal cycle (Figure 119). Model estimates, on average, are as well too low at most times, indicating an underestimation of anthropogenic fluxes. We are resolving scaling issues that are related to representing anthropomorphic emissions on 200m grid, as contrasted with concepts used for in-situ model parameterization, which necessitate 'footprint' values of carbon flux sourcing for an airshed. Since vehicle flux data were not used in this set of WRF-ACASA simulations, the model anthropogenic component of the CO_2 flux was proxied by population density alone (1000 people km^2 for urban land use type 1, 1500 and 2000 people km^2 for intensity categories 2 and 3, respectively. Results could be improved using population density parameterizations that better match actual values for Firenze (e.g.: 3000 people per km^2 for intensity level 1, 3500 and 4000 people per km^2 for levels 2 and 3, respectively). Temporal variations of CO_2 flux density are parameterized in WRF-ACASA as having 2 peaks, one during the morning, and the other during the evening. Observations, however, show one main peak, indicating perhaps different kinds of emission and traffic patterns for this city related more to tourism and less to morning and evening commutes and homeothermy. Whenever vehicle flux data become incorporated into WRF-ACASA as one of the 'driving variables', then CO_2 flux estimates will improve dramatically. We also expect improvement upon 'intensifying' the CO_2 fluxes from pixels whose scales are less than that of a flux footprint, since using 'citywide' values leads to underestimations.

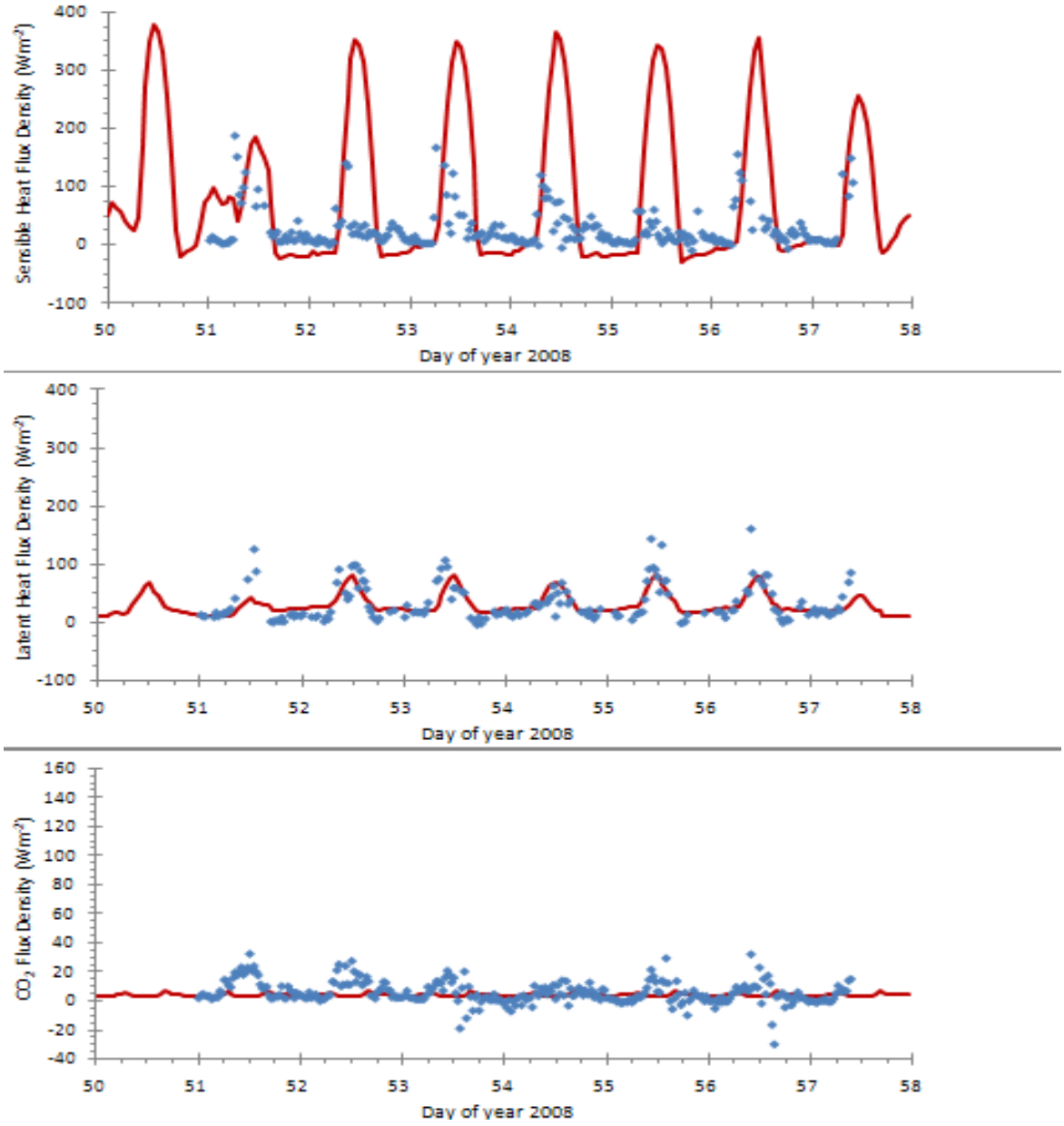

Figure 118. Comparison between simulated (solid line) and observed (dots) sensible heat flux (H), latent heat flux (LE) and CO_2 flux for a week in February 2008.

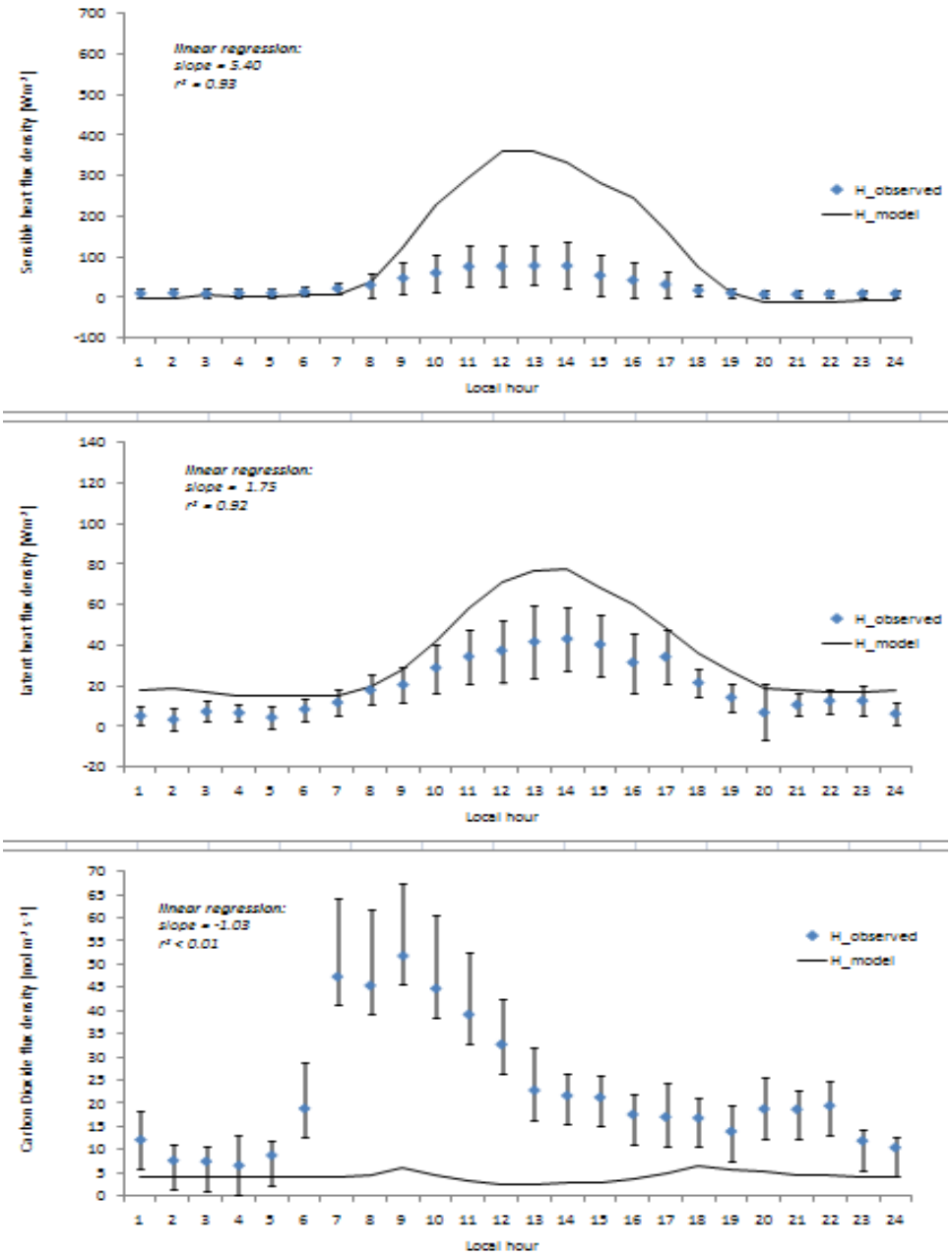

Figure 119. Comparison between composed values of simulated (solid line) and observed (dots) sensible heat flux (H), latent heat flux (LE) and CO_2 flux.

9.4.2 Helsinki

Roughly 70% of all hourly periods in the year 2008 were available for comparison (> 5000 points for each quantity) in contrast to Firenze, which involved a smaller set of points (< 1000) for comparison.

Sensible Heat Flux density (HFX, H). In all aspects, mean model values of HFX compared better with observations for this city, despite the difference in the locations of each (Figure 120). Part of this is due to there being more available data throughout the year from which to compare. The several- hundred Wm^{-2} model overestimation seen in the Firenze results is largely absent for this city. Composite values indicate only minimal discrepancies exist between model and observed diurnal cycles (Figure 121). At night, WRF-ACASA results overestimated sensible heating by roughly 10 to 30 Wm^{-2}. It is surprising, actually, how close these sets of values are given the differences in location. Hourly values show periods of time, on the scale of weeks at a time, where observed and model values match more so than others, which is probably due to WRF simulating a different set of cloud patterns from observed, and therefore different sets of down-welling radiation to drive large daytime surface heat fluxes.

Latent Heat Flux density (LH, LE). Hourly values throughout the year indicate a generally 'good' agreement with observations (Figure 120). As is the case with sensible heat flux density, model daytime composite values are within 30 Wm^{-2} of observations during most daytime hours (Figure 121). During nighttime hours, however, the agreement is less, with model values hovering past 80 Wm^{-2} while observations were 20 Wm^{-2} or less. Evaporation at night over open water (WRF-ACASA) was figured in to the model average, including near-shore values elevated due to land-sea breeze dynamics, which could largely explain this nighttime overestimation. During the day, such a spatial bias of water vs. land points would be less pronounced.

Carbon Dioxide Flux density (NEE, FCO2). Like the results for Firenze, model values for this quantity are clearly 'flat', with composite values indicating, again, an apparent lack of model representation of both the magnitude and character of the diurnal cycle. Model estimates are again overestimated, indicating an underestimation of anthropogenic fluxes at 200m pixels. The manner in which both the magnitude and character of the diurnal cycle are based on data from Helsinki, and thus it is hoped that when scaling issues are resolved and the final simulations completed, there will be better agreement between observed and model results for this quantity.

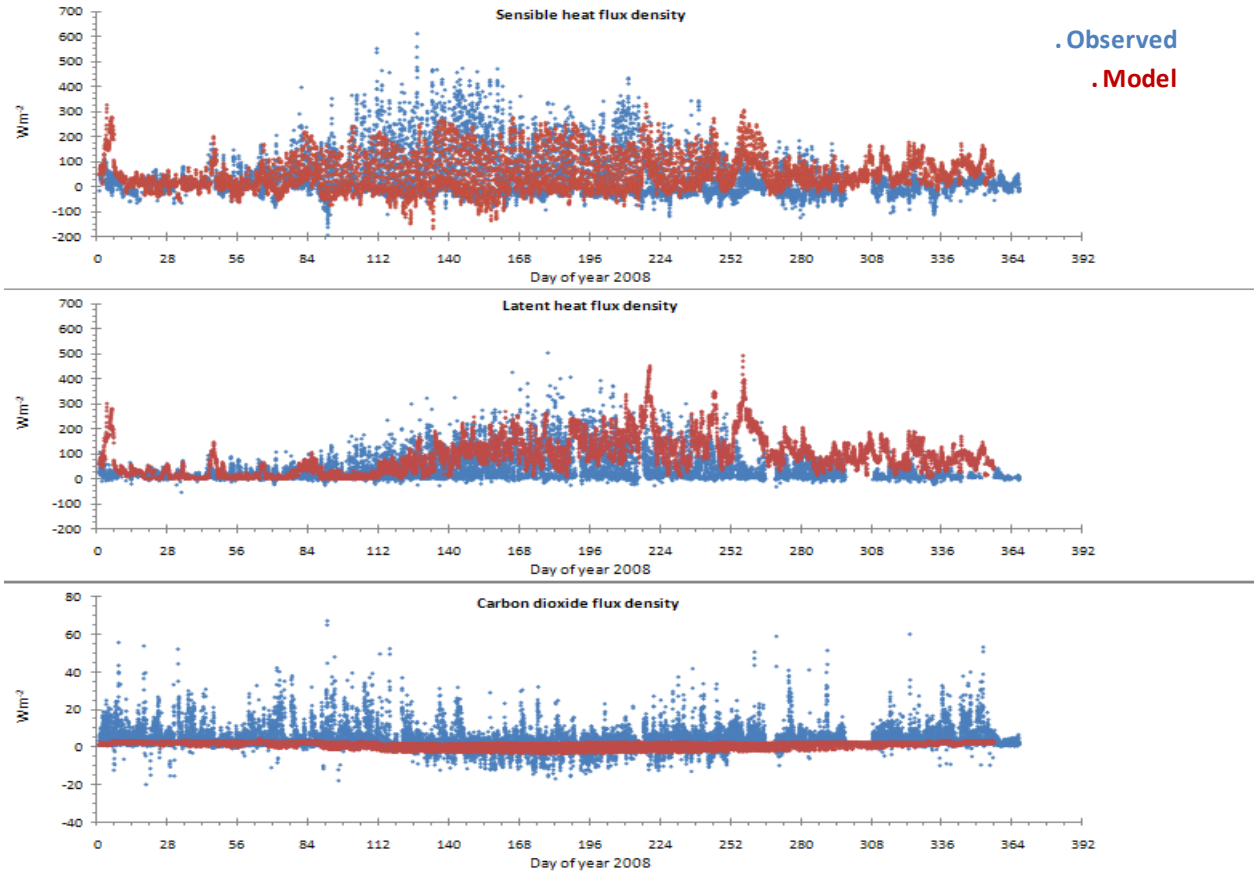

Figure 120. Comparison between simulated (solid line) and observed (dots) sensible heat flux (H), latent heat flux (LE) and CO_2 flux for the year 2008.

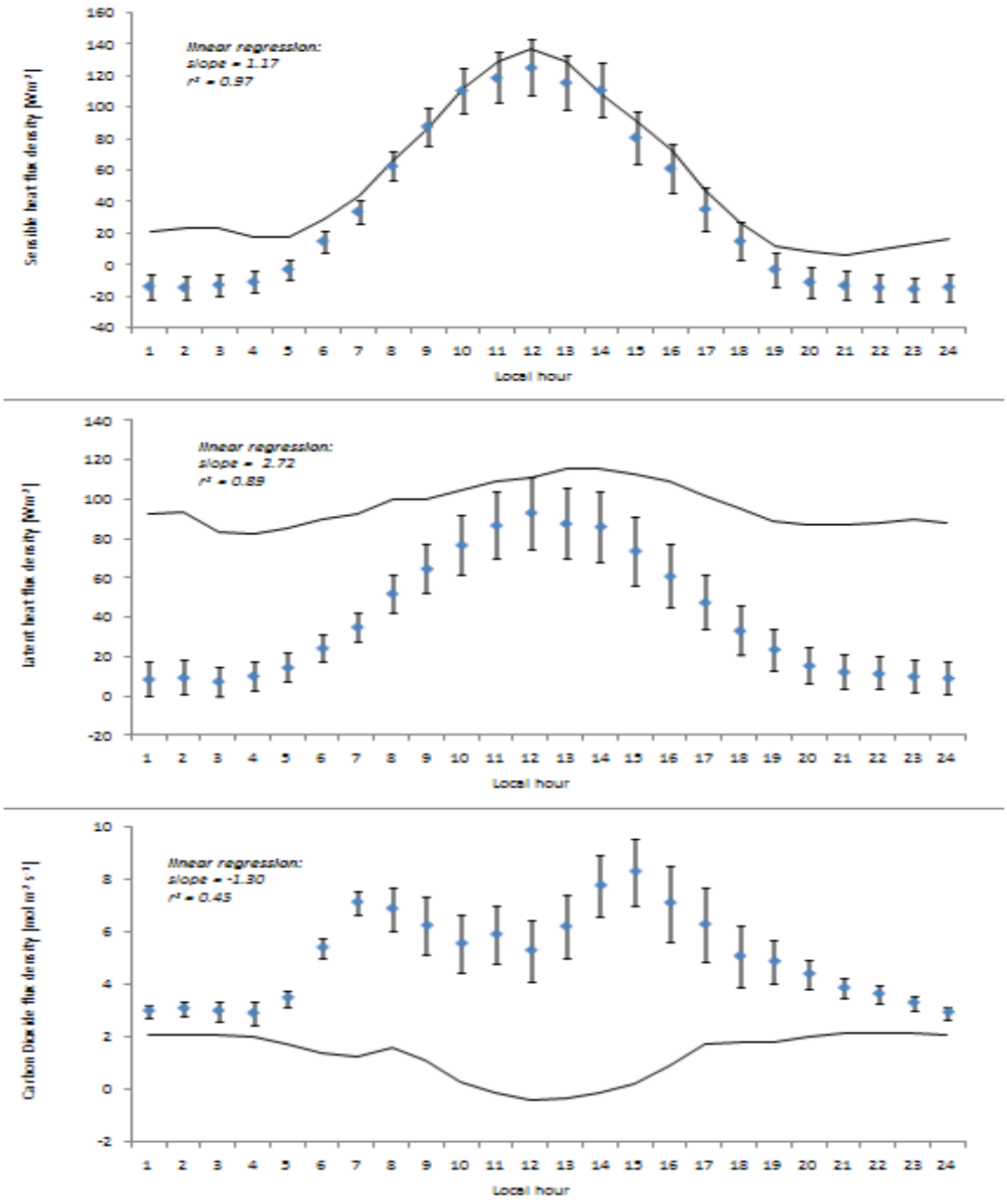

Figure 121. Comparison between composed values of simulated (solid line) and observed (dots) sensible heat flux (H), latent heat flux (LE) and CO_2 flux.

WRF-ACASA nested configuration (simulations in addition to the previously listed set)

We have configured and run WRF using 4 concentric nests for April 2008 for Firenze, initializing the model once at 12:00 31 May 2008 and running it continuously for 30 days. The largest domain covers most of Europe and surrounding waters at 48 km horizontal grid spacing. Nests proceed using the recommended 1:3 ratio (16 km, 5.4 km, 1.8 km). Nests are concentric and centered

around Firenze.This nesting design has a greater number of grid-points in each of the smaller domains than the previous simulations. We did this to ensure proper handling of mesoscale structures propagating through the region. Too small an inner domain and one will miss important structures; the innermost domain's features artificially dominated by the shape of the box being run.

Preliminarily, WRF-ACASA was invoked in the innermost two domains only. The outer domains were run with WRF-standard ("Simple") surface layer physics ("Option 1") We went with the "Simple" flux scheme because it allowed us to quickly run a 30-day simulation for all of Europe without the need for a daily re-start of the model. We found WRF-NOAHLSM running for all 4 nests to crash sometimes upon running for 30 days. The "Simple" scheme, which is theoretically similar to NOAHLSM, did not crash for 30 days. Results from preliminary simulation (April 2008, Firenze, Baseline) are presented in this document.In particular, selected results from the innermost domain (x:y:z : 37:37:50, centered around Firenze area of Tuscany) are presented here. We chose 37 instead of 27 grids on a side for the inner domain, since WRF keeps a 'buffer' that is 5 grid points wide, gradually blending in conditions from the next-larger domain to prevent numerical instabilities from building up at the boundaries with the inner. When presenting WRF results, the proper procedure is to ignore the outermost 5 points when considering the interior domain. Diagnosing the effect of numerical artifacts at the nesting boundaries is usually accomplished by looking graphically at the output fields, in particular squarish distortion around some or all of the outside of the innermost nested domain, in one or more fields. Harsh contrasts at the edges are symptomatic of potential WRF numerical instability. One should look at HFX and LH in particular, also incident solar radiation flux (SOLDN) during the day for these patterns. What alerted us to 27 x 27 grids at 200m being too fee was the simulated cloud features (Figure 122) indicating boundary issues in the 200m simulations. Numerical artifacts appear at edges of 27x27 Km domain for the two plots on the right, indicating presents (or absence) of clouds in the inner (outer) domain. This is manifest as high values of incident solar radiation at the edges. This has the potential to affect cloud development in the model and lead to errors in energy available for sensible and latent heating in the domain, particularly for the domain that are of few grids.

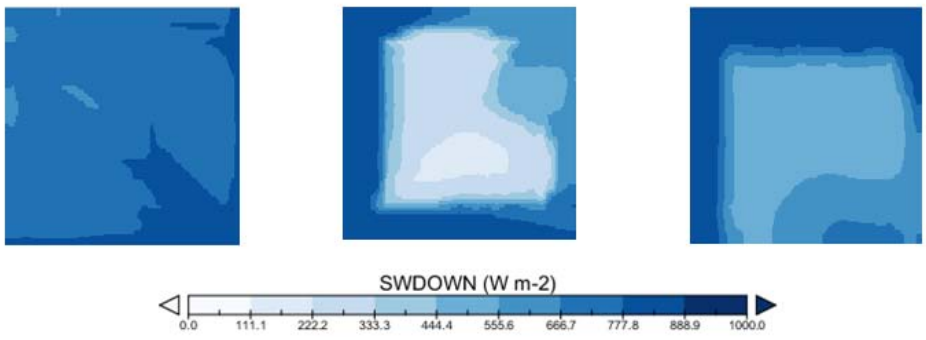

Figure 122. WRF-ACASA incident solar radiation for the 200m grid (12.00 PM local time) from 4th to 6th April 2008 (from left to right) in Firenze.

The horizontal domain for the smallest grids (1.8 km by 1.8 km) is 50 km on a side, which we admit is significantly coarser than the 200m by 200m grid domain used for the previous set of WRF-ACASA simulations.

Time steps for the inner domain were chosen to be 6 seconds each, which represents a 3-fold increase in temporal resolution relative to the time step used for the innermost domain for previous set of simulations, once scaled to the horizontal grid size differences in each set. This is due to an increased vertical resolution, which is theoretically necessary particularly in the lowest several kilometers of the atmosphere. Shorter relative time steps were also invoked to prevent aliasing and numerical truncation that still can occur even when using the time step lengths suggested in the WRF user's guide.

Choice of model physics were kept as similar as possible to the previous set of simulations, but with one important difference: the Simple surface layer scheme (option 1) was used instead of NOAH-LSM scheme (option 2) for the outer domains, because we found WRF using NOAH-LSM to be unstable within several days from model initialization, preventing a continuous simulation for the month of April 2008. We cannot emphasize enough the need to take proper care in crafting the WRF model configuration, as there are many things to consider and we are pushing the limits of human experience with this tool, along with its inherent physical assumptions and numerical discretization.

We are still working out exactly how fine a resolution we can use without violating physical assumptions in the model. If we go to 0.6 km grids, we might need to extend the vertical domain to 100 layers (or more), which involves additional memory needs. The design of the current simulation presented here is an attempt to take into account both the limitations of WRF and the physics involved. Many of the WRF contributing authors (Bill Skamarock, Georg Grell, Shu-Hua Chen), as well as colleagues from UC Davis who have used WRF previously (William Gustafson), have noted that WRF cloud-convective process and precipitation parameterizations are not designed for horizontal grid scales less than 1 to 2 km. In addition, the number of vertical layers in the present simulation have been increased to 50 (from 28) to allow for proper treatment of horizontal and vertical advection, among other processes.

9.5 Applications

9.5.1 Firenze

The upper left panel in Figure 123 shows land use type for the innermost 27 x 27 points in the 37 x 37 inner domain, with each pixel representing 1.8 km x 1.8 km. The upper right panel shows the 5x5km core (zoomed-in) surrounding Firenze proper. The lower left panel shows the 200m x 200m enhanced land-use map that was used in the previous simulations for comparison. Note the similarities in the each 5km x 5km sub-domain depiction despite the coarser resolution and the use of WRF-default land use maps in the current simulation: only the Arno River and intra-city parks are absent in the new simulations due to their dimensions. This representation is approximate and may be in error by ~ 1 km.

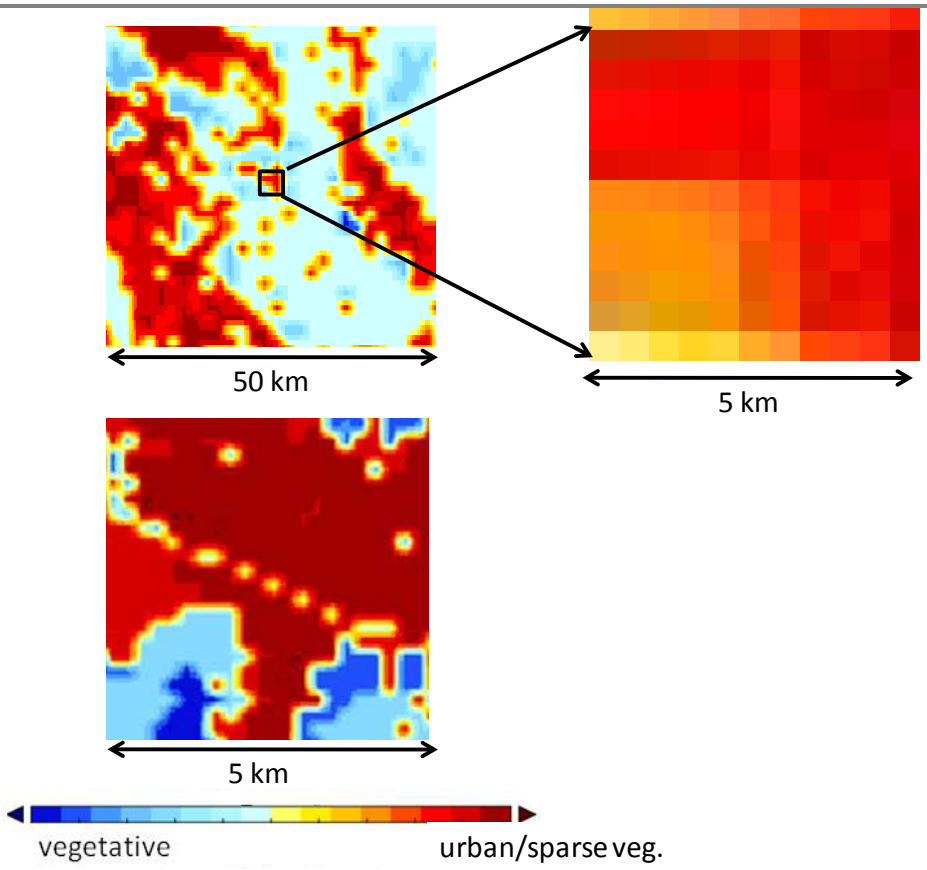

Figure 123. Land use map in the different domains

The model was initialized and results for sensible (HFX), latent (LE), 2-meter temperature (T2), and solar radiation (SWDOWN) are showed in Figure 124. Note the absence of clouds (flat blue field or 'sky') in the incident solar radiation flux density (lower right panel). WRF did not adequately produce clouds until after 24 hours into the simulation. The square in the centers of each panel represent the area of the 200m simulations; the deep blue patch in the panel for LH indicates evaporation from a lake.

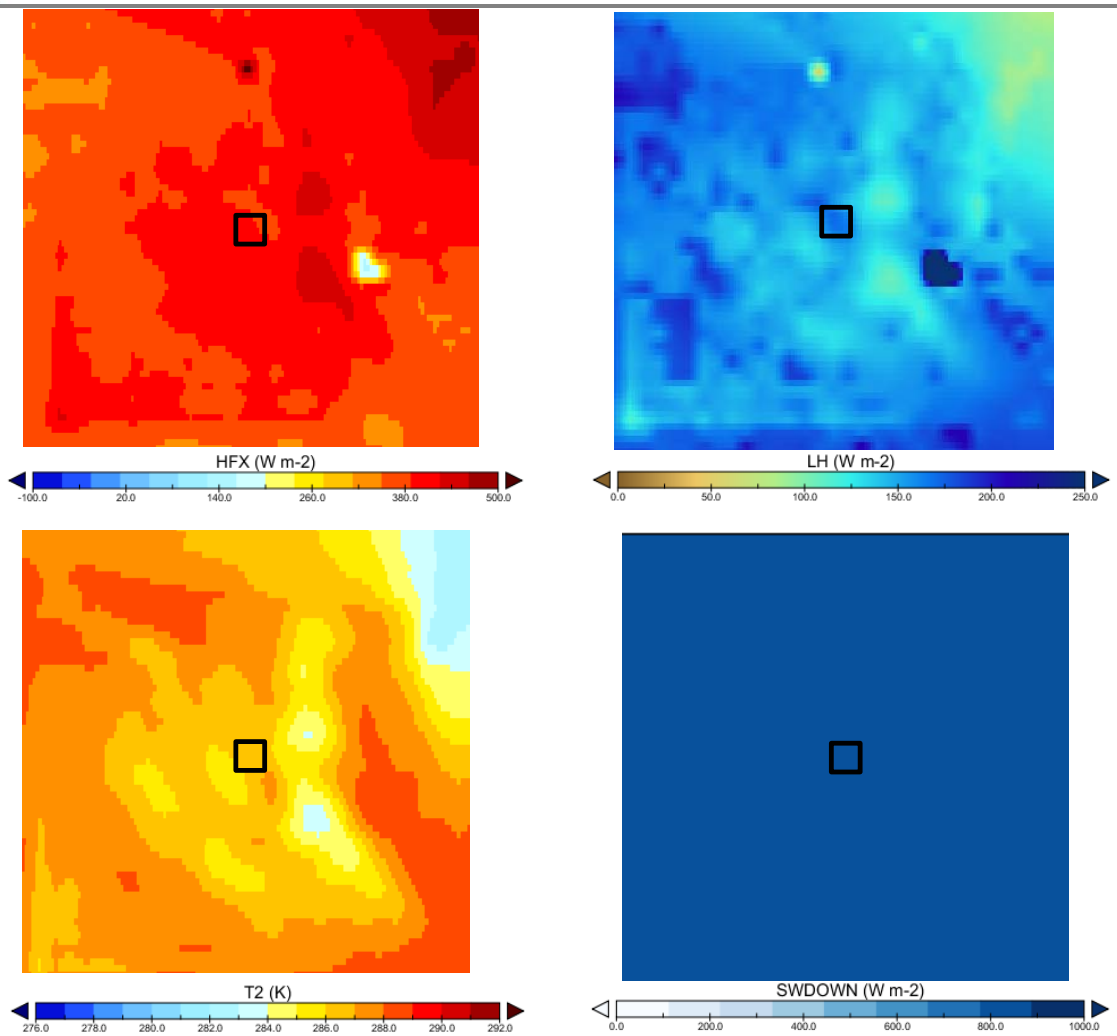

Figure 124. Maps of sensible heat flux, latent heat flux, air temperature, and solar radiation for April 1st (12.00 PM Local Time).

Maps of sensible and latent heat flux are showed in Figure 125 and Figure 126. Note low (< 200 Wm^{-2}) values for HFX in the area on 3 and 6 April. Such was not seen in the previous set of simulations. This is due to clouds appearing in a robust manner in this simulation after day 1. Note the large values of LH over the lake (deep blue area, lower set) in all days. If the Arno river were resolved, a similar process would be evident. At this scale, the Arno is absent. Values of latent heat flux density are comparable to both the previous set of runs and maxima observed for these days. These simulations appear to have captured better the overall available energy (HFX + LH) than did the previous set of 200m runs. Note additional days with low (< 200 Wm^{-2}) values for HFX in the area, particularly 8 April, where cloud cover was extensive throughout the day (Figure 128). Note also the 2 to 4 degree increase in 2m air temperature throughout the domain on 10 and 11 April (Figure 128), which is not as apparent for the same days in the previous simulations.

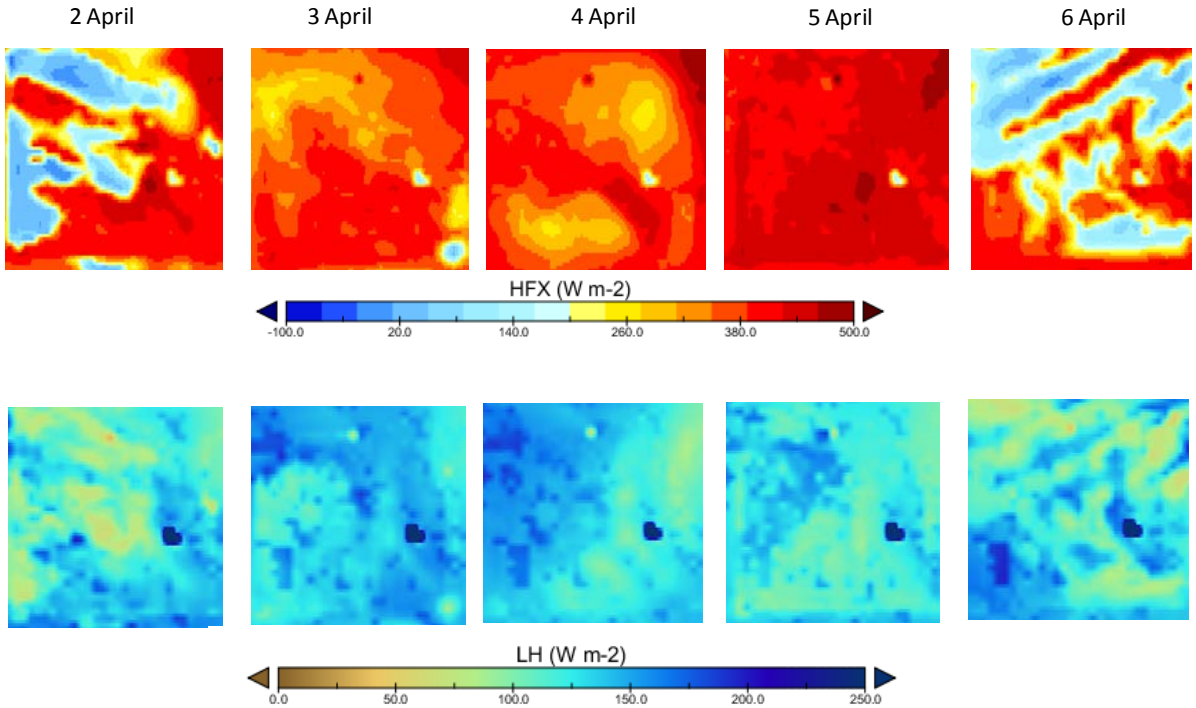

Figure 125. Maps of sensible heat flux and latent heat flux for five days of April (12.00 PM Local Time).

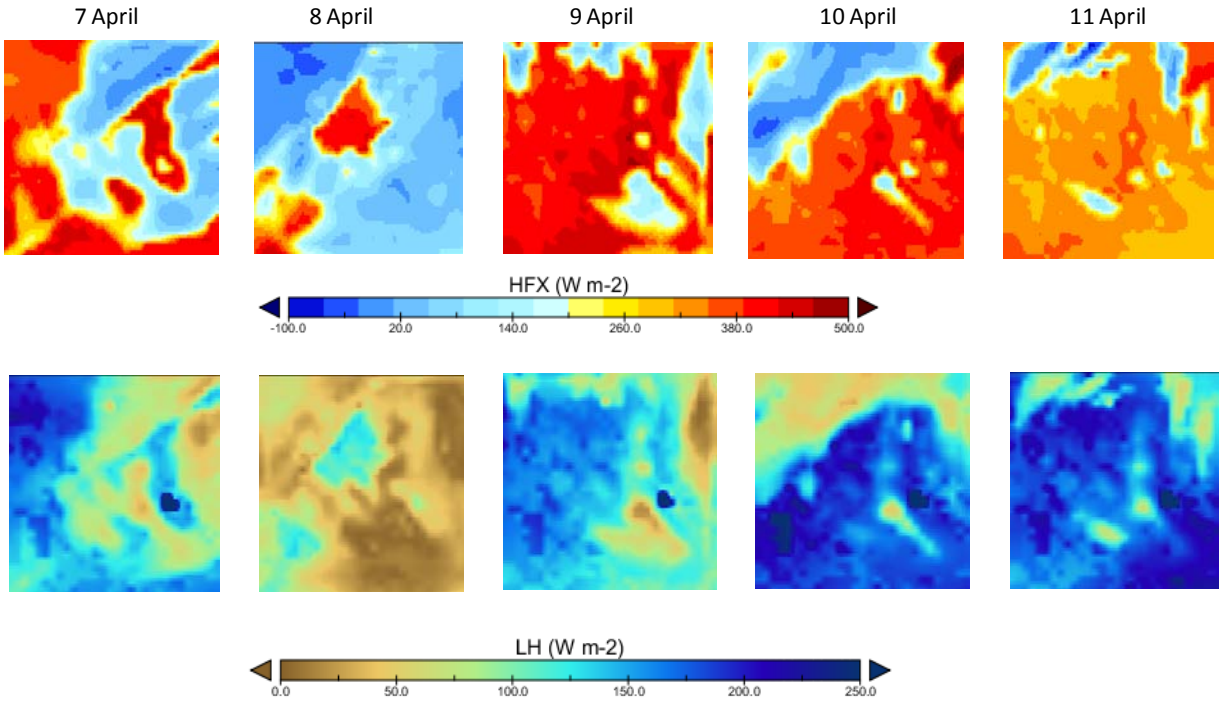

Figure 126. Maps of sensible heat flux and latent heat flux from April 7th to April 11th (12.00 PM Local Time).

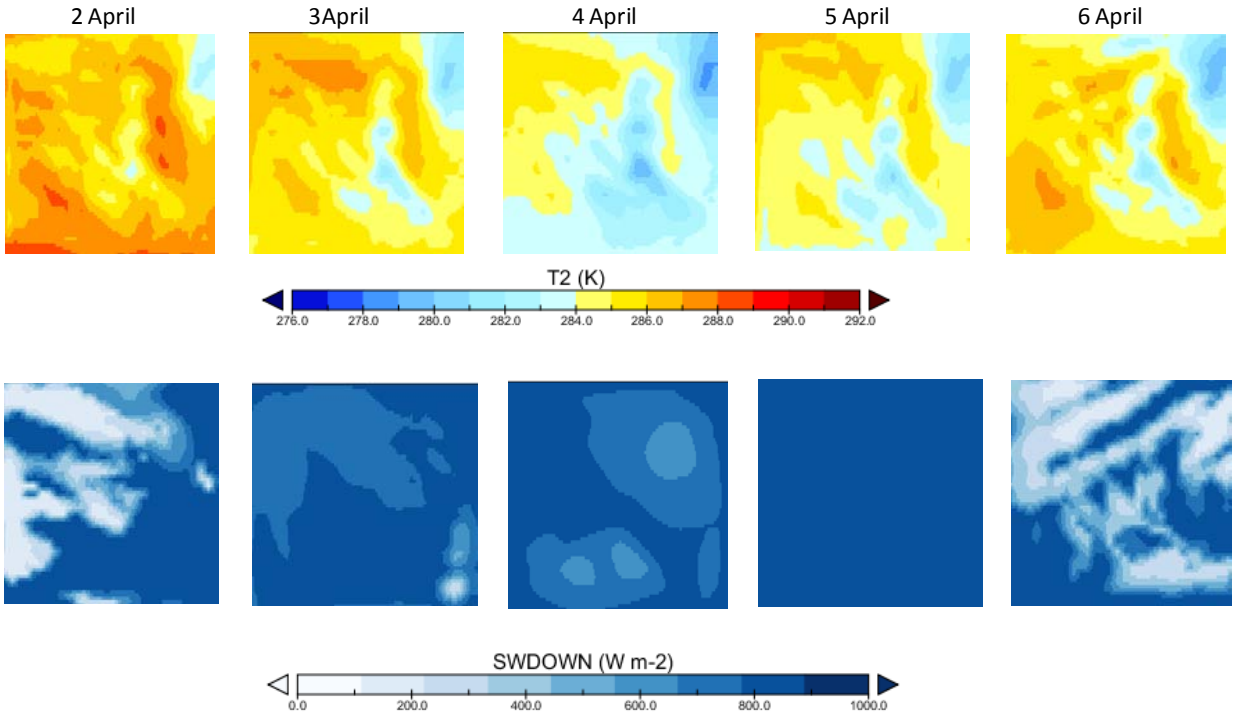

Figure 127. Maps of air temperature at 2 meters and solar radiation from April 2nd to April 6th (12.00 PM Local Time).

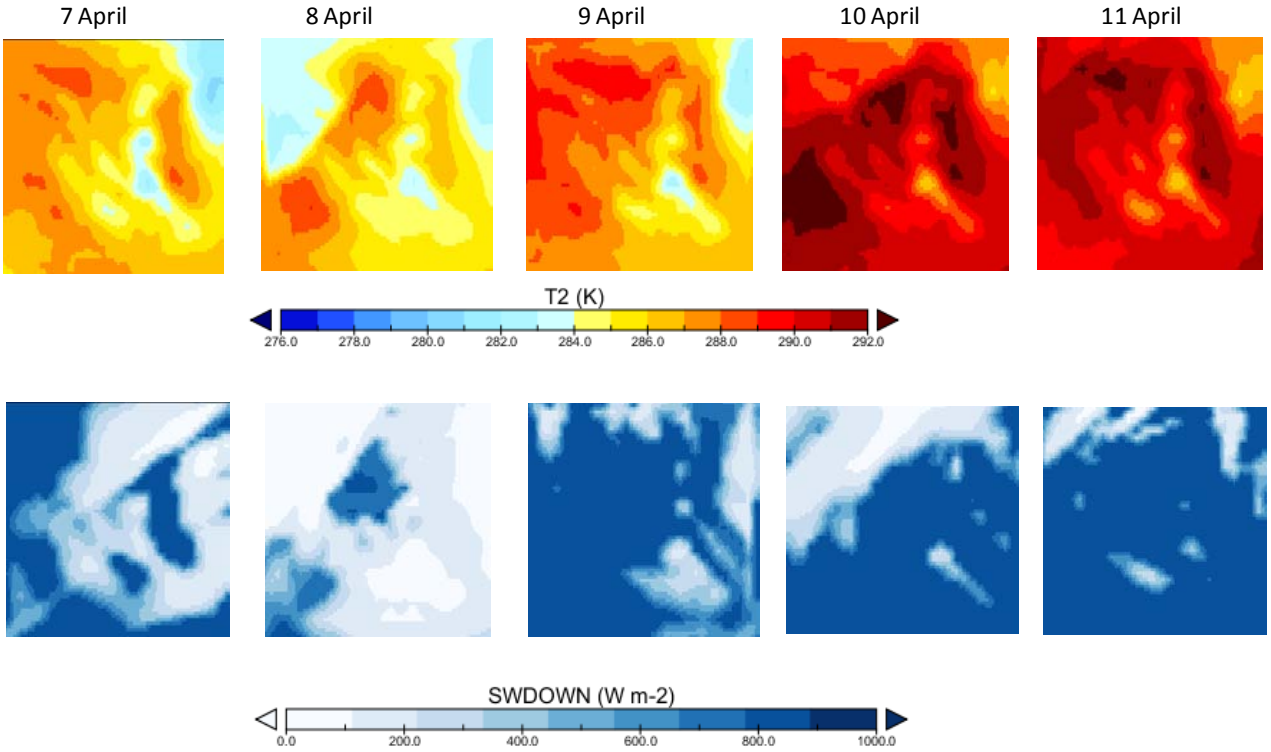

Figure 128. Maps of air temperature a t 2 meters and solar radiation from April 7th to April 11th (12.00 PM Local Time).

Statistical comparisons with tower flux (EC) observations.

Presented here are results comparing model (old and new simulations) with observed (EC) tower flux observations from the Ximeniano site for 1-9 April, 2008.
The sole urban land-use point near the center of the innermost domain of the nested (new) WRF-ACASA simulations is an abstraction of the Firenze urban center, and at this scale it made little sense to invoke the high-resolution land use dataset at the 1.8 km scale. Model results from this single point have been compared with observations in the same manner as for the WRF-ACASA-non-nested simulations. For the earlier simulation's results, recall for Firenze that we are using the average of the central set of 3x3 (9 points total) representing the flux footprint around the EC tower area. These are slightly different areal sets, but the differences in each are within the scale of a turbulent flux footprint.
To view these 2 sets of runs in context, it is also important to recall the methodology of each set of runs: it has come to our attention that the initial and boundary conditions used for the non-nested set come from WRF simulations that were re-initialized every 24 hours, representing a 'reboot' of the model physics at midnight UTC each day. For the nested runs, rather, the initialization only occurs once, and thus the model in the newer nested configuration is more dependent on the accumulated progression of its internal physics.

Due to these initialization differences, one would therefore expect model performance for the nested simulations initialized once to deteriorate with time with respect to a run that is initialized daily, regardless of the domain configuration differences. However, these preliminary results indicate a degree of parity (and in some cases a slight improvement) between the performance of both modeling configurations (Table 44). Results from the latest set of runs (April 2008) have been uploaded to the ftp site. Files are named in a self-referencing manner.

Table 44. Statistical analysis for test run of WRF-ACASA multiply nested with the new domain design, along with the similar statistics for the non-nested (200m) set up. % changes values highlighted (yellow) represent improvement using the nested WRF-ACASA version (new) at 1.8 Km configuration relative to the 200m (old) simulations.

Statistial quantity	T	T	%change	FCO2	FCO2	%change
	old	new	old-to-new	old	new	old-to-new
STDE	2.16	2.26	4	26.38	26.52	1
RMSE	3.27	2.07	-37	19.46	12.60	-35
MBE	1.57	0.07	-95	-19.79	-12.73	-36
MAE	2.51	1.69	-33	19.79	12.73	-36
slope, b	1.04	1.48	43	4.35	-61.88	-1521
coefficient of determination, r2	0.66	0.70	6	0.03	0.18	577
Standard deviation	3.39	2.99	-12	21.05	19.66	-7
95% confidence (2-tail) interval	0.52	0.46	-12	3.25	3.03	-7
N (out of 215)	215	215	/	211	211	/
notes...	all points used			4 points excluded		
				: (> +100 umol m-2 s-1)		

Statistial quantity	HFX	HFX	%change	LH	LH	%change
	old	new	old-to-new	old	new	old-to-new
STDE	136.28	132.61	-3	26.64	23.09	-13
RMSE	184.84	184.36	0	29.83	13.89	-53
MBE	79.65	19.59	-75	11.36	3.91	-66
MAE	135.41	115.32	-15	20.89	10.48	-50
slope, b	0.22	0.22	1	0.43	0.70	63
coefficient of determination, r2	0.62	0.61	-3	0.24	0.13	-47
Standard deviation	130.38	128.76	-1	26.77	19.48	-27
95% confidence (2-tail) interval	19.93	19.68	-1	4.21	3.07	-27
N (out of 215)	215	215	/	203	203	/
notes...	all points used			all points < -10 Wm-2, and		
				one positive outlier (+328 Wm-2)		

Observations used in the latest set of (1-9 April 2008) comparisons are hourly-averaged values from the Ximeniano tower dataset. Quality control allowed us to consider, as much as possible, a contiguous time series for this period. Four points of observed FCO2 were excluded due to extreme values (> 100 umol m^{-2} s^{-1}). Twelve extreme points in LE (observational record) were excluded (eleven large negative values, one large positive value).

Results highlighted in yellow indicate improvements in simulation of the nested vs. non-nested simulations. Many of these improvements were significant, and only a few changes to the summary statistics for some of the variables in question represented a 'worse' simulation. Such differences were not entirely expected and investigation into this continues.

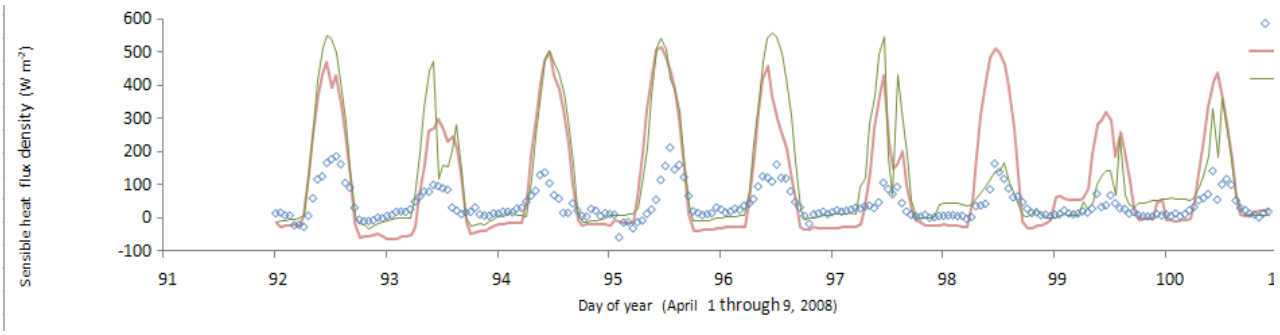

Figure 129. Comparison of observed and modeled sensible heat flux density (HFX). The red line indicates values from the non-nested (old) simulations, while the green line is from the newer (nested) set. Blue diamonds represent observed values. Observations were provided every 15 minutes, while WRF output occurs every hour. Therefore hourly means were calculated for each for the comparisons.

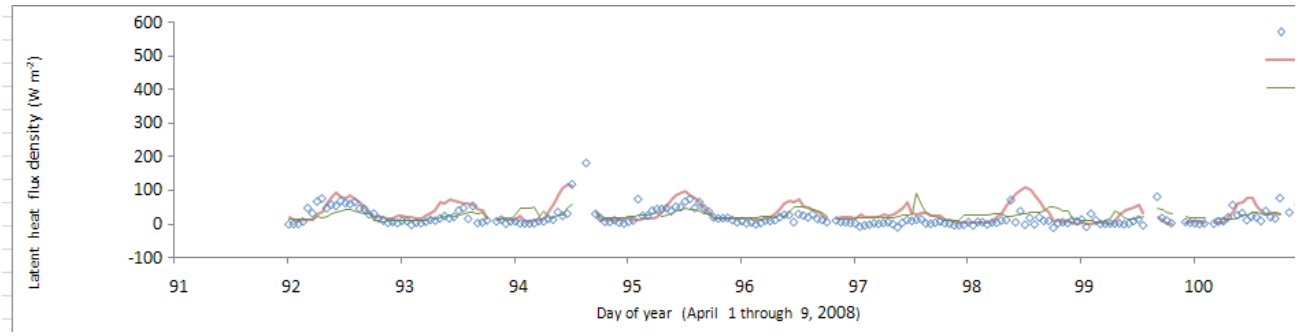

Figure 130. Comparison of observed and modeled latent heat flux density (LH).

Figure 129 and Figure 130 show the comparison between observed and simulated (WRf-ACASA nested and non-nested versions) sensible and latent heat fluxes, respectively. Note relatively low values in LH in relation to HFX (Figure 130), indicating 'urban desert' conditions. The low range of values in relation to observational uncertainty should be considered when examining slope and R^2 values (Table 44). There do appear to be fewer 'spikes' in the newer results, showing improvement. Also note the better match between observations and new simulation of HFX in the day 98 (Figure 129).

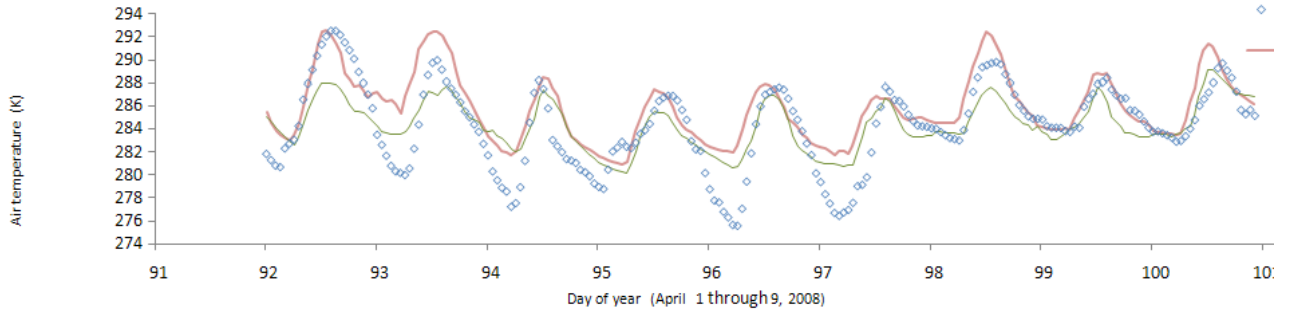

Figure 131. Comparison of observed and modeled air temperature (K).

Results for air temperature are showed in Figure 131. Note both improved phase and trending of the newer nested results despite these simulations invoking largely the same physics. We believe this has mainly to do with model set-up and configuration.

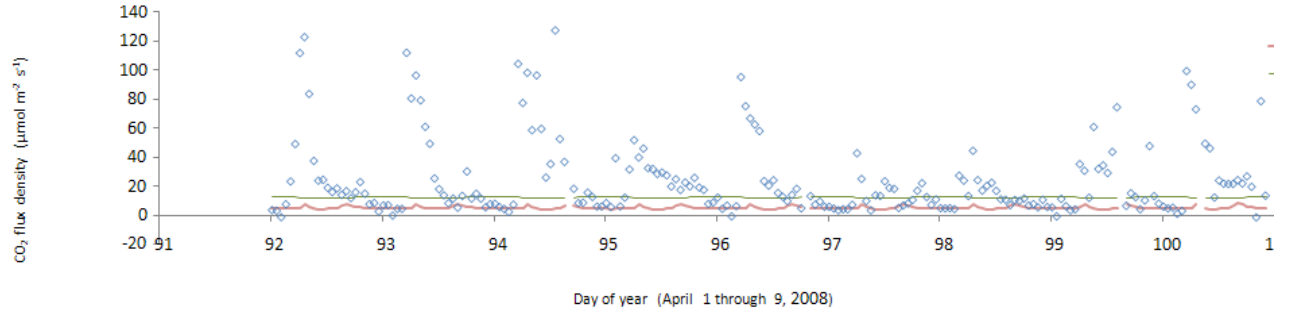

Figure 132 Comparison of observed and modeled CO_2 flux density.

Model results for CO_2 flux (Figure 132) both still look quite different from the observed time series. We still have yet to establish a consistent geographical time-coordinate from WRF to use for calculating the diurnal cycle of CO_2 flux density. We are also proceeding with the same method as was used for the nested simulations. This method does not use vehicle flux density as an input. We have already shown in the in-situ results for Firenze 2008 and 2010, that improvements can arise in predicting CO_2 flux density upon use of actual vehicle flux density as a driving variable. Until this is accomplished, we should take both the old and new model results in context. At least for the newer simulations, the average value is higher, which is more consistent with the observations (Table 44).